# Studies on parameters influencing field induced microstructures in magnetic fluids and its influence on optical properties

*By*

**DILLIP KUMAR MOHAPATRA**

**Enrolment No: PHYS 02 2015 04 025**

**Indira Gandhi Centre for Atomic Research, Kalpakkam**

***A thesis submitted to the***

*Board of Studies in Physical Sciences*

***In partial fulfillment of requirements***
***for the Degree of***

**DOCTOR OF PHILOSOPHY**

***of***

**HOMI BHABHA NATIONAL INSTITUTE**

**February, 2021**

## Homi Bhabha National Institute

## Recommendations of the Viva Voce Committee

As members of the Viva Voce Committee, we certify that we have read the dissertation prepared by Dillip Kumar Mohapatra entitled "**Studies on parameters influencing field induced microstructures in magnetic fluids and its influence on optical properties**" and recommend that it may be accepted as fulfilling the thesis requirement for the award of Degree of Doctor of Philosophy.

T R Ravindran 7.10.2021

Chairman: **Dr. T. R. Ravindran** Date:

John Philip 07.10.2021

Guide/ Convener: **Dr. John Philip** Date:

for Awadhesh Mani

External Examiner: **Dr. V. A. Raghunathan** Date: 07/10/2021

R. Raman 7/10/21

Member 1: **Dr. R. Ramaseshan** Date:

Gnanasekar 7/10/2021

Member 2: **Dr. K. I. Gnanasekar** Date:

Final approval and acceptance of this thesis is contingent upon the candidate's submission of the final copies of the thesis to HBNI.

I hereby certify that, I have read this thesis prepared under my direction and recommend that it may be accepted as fulfilling the thesis requirement.

Date: 07/10/2021
Place: Kalpakkam

John Philip
**Dr. John Philip** 7/10/21
(Guide)

## Statement by Author

This dissertation has been submitted in partial fulfillment of requirements for an advanced degree at Homi Bhabha National Institute (HBNI) and is deposited in the Library to be made available to borrowers under rules of the HBNI.

Brief quotations from this dissertation are allowable without special permission, provided that accurate acknowledgement of source is made. Requests for permission for extended quotation from or reproduction of this manuscript in whole or in part may be granted by the Competent Authority of HBNI when in his or her judgment the proposed use of the material is in the interests of scholarship. In all other instances, however, permission must be obtained from the author.

Dillip Kumar Mohapatra

(Dillip Kumar Mohapatra)

# Declaration

I, hereby declare that the investigation presented in the thesis has been carried out by me. The work is original and has not been submitted earlier as a whole or in part for a degree / diploma at this or any other Institution / University.

Dillip Kumar Mohapatra

(Dillip Kumar Mohapatra)

# List of Publications arising from the thesis

## Journals

1. “Influence of size polydispersity on magnetic field tunable structures in magnetic nanofluids containing superparamagnetic nanoparticles", Dillip Kumar Mohapatra, Philip J Camp, and John Philip, Nanoscale Adv., 3, 3573-3592, (2021)

2. “Temporal evolution of equilibrium and non-equilibrium magnetic field driven microstructures in a magnetic fluid”, Dillip Kumar Mohapatra, Junaid Masud Laskar and John Philip, J. Mol. Liq. 304, 112737 (2020)

3. “Effect of surface charge screening on critical magnetic fields during field induced structural transitions in magnetic fluids”, Dillip Kumar Mohapatra and John Philip, J. Appl. Phys. 125, 244301 (2019)

4. “Investigations on magnetic field induced optical transparency in magnetic nanofluids”, Dillip Kumar Mohapatra and John Philip, Opt. Matter. 76, 97 (2018)

## Conferences

1. “Effect of magnetic field ramp rate on microstructure formation in magnetic nanoemulsion”, Dillip Kumar Mohapatra and John Philip, at International Conference on Nano Science and Technology (ICONSAT 2020) organized by S. N. Bose National Centre for Basic Sciences at Biswa Bangla Convention Centre, New Town, Kolkata, India, during 5-7 March, 2020 **(*Best poster award*).**

2. “Magnetic field induced light transmission through magnetically polarizable nanoemulsion”, Dillip Kumar Mohapatra and John Philip, at International Conference on Advanced Materials (ICAM 2019) organized by Department of Physics, Nirmalagiri College, Kannur, Kerala, India, during 12 -14 June, 2019.

3. "Magnetic field induced structural transitions in charged magnetic nanoemulsion”, Dillip Kumar Mohapatra and John Philip, at CompFlu – 2018, organized and hosted at IIT Roorkee, Uttarakhand, India, during 6-9 December, 2018.

4. Indo-US Workshop on Soft Matter (IUWSM), organized by IIT Roorkee, Uttarakhand, India, during 9–11 December, 2018

5. “Probing disorder-order transitions in magnetic fluids using light scattering”, Dillip Kumar Mohapatra and John Philip, at CompFlu – 2017, jointly organized by IIT, Madras, IIT, Palakkad and ISR at IIT Madras, Chennai, India during 18-20 December, 2017.

## Other publication not included in the thesis

1. Dillip Kumar Mohapatra, Andrey Zubarev, Alexander Safronov and John Philip, “Reconfiguring nanostructures in magnetic fluids using pH and magnetic stimulus for tuning optical properties", J. Magn. Magn. Mater, 539, 168351 (2021).

Dillip Kumar Mohapatra

(Dillip Kumar Mohapatra)

Dedicated to my Mother

**Late Mrs. Pramila Bala Mohapatra**

# Acknowledgements

*First and foremost, I would like to express my deepest gratitude to my supervisor Dr. John Philip for his continuous guidance and encouragement, and support throughout my research work. His impressive enthusiasm, problem solving desire, high scientific perception motivated me to work harder to reach the goal.*

*My sincere thanks to the doctoral committee chairman Dr. T. R. Ravindran and members Dr. R. Ramaseshan and Dr. K. I. Gnanasekar for their constructive comments and suggestions.*

*I thank Dr. A. K. Bhaduri, Director of IGCAR, and Dr. Shaju K. Albert, Director of Metallurgy and Materials Group, for the research facilities.*

*I deeply express my heart full thanks to my seniors Dr. A W Zaibudeen, Dr. Sithara Vinod and Dr. Amit Kumar Mishra for helping in the experimental works and constructive comments.*

*I thank all research scholars/RA of SMARTS, Surojit, Manali, Srujana and Vadivel for their help and making stay in SMARTS peaceful. I express my sincere gratitude towards all other members of SMARTS for their support, kind assistance and help in numerous occasions.*

*I am thankful to all my close friends who supported and motivated me during the dreadful phases of my life and shared delightful moments during the good times. Immediately I remember the names Nithya, Santanu, Gopi, Alok, Binay, Bijay, Sita, Prasant, Padu bhai, Nila bhai, Anil, Prashant, Baba, Dhani, Abinash, Sani, Sukumar, Ajay, Arabinda, Subodh. With these friends I spend memorable periods of my life.*

*Last, but not the least, I thank my family members, especially my mother Pramila Bala Mohapatra (Late), my father Niranjan Mohapatra, my brother Deepak, my sisters Deepali and Shefali for their love, encouragement and prayers. I am forever in your debt for everything you have done for me.*

Dillip Kumar Mohapatra

(Dillip Kumar Mohapatra)

# Abstract

Magnetic fluids are a class of smart materials which alter their physical properties such as optical, rheological, and thermal properties in the presence of an external magnetic field. The magnetic field induced aggregation and de-aggregation process in magnetic fluids can alter the propagating light pathways that can give rise to interesting optical phenomena. Though field induced aggregation is rich with theoretical and simulation data, systematic experimental studies on equilibrium and non-equilibrium structures in real magnetic fluids are scarce. This was the motivation to undertake this work.

The main objectives of this thesis were to understand the parameters influencing the field driven structures in magnetic fluids (both material and magnetic field), its temporal evolution and dynamics. The fluidic parameters considered are the volume fraction, size polydispersity, and the surfactant concentration, while the magnetic field parameters examined are field ramp rate, field strength, field orientation, and switching conditions. Magnetic emulsion with droplet hydrodynamic diameter ~ 200 nm, containing superparamagnetic iron-oxide nanoparticles of diameter ~ 10 nm, is used in this study. Also, three different magnetic nanofluids of same chemical composition and volume fractions but with different size distributions were employed in this study.

In magnetic nanoemulsion, in the presence of slow magnetic field ramp rate, three distinct critical magnetic fields are identified from the changes in the field dependent transmitted forward scattering light intensity. The first critical field occurs at the commencement of small aggregate formation, the second one on completion of linear aggregation process before the commencement of lateral coalescence of individual chains, and the third one occurs when the densely packed columnar solidlike structures are formed through zippering of individual chains. As the surfactant concentration increases, the electric double layer thickness decreases and the separation between the droplets decreases in the dispersion. Therefore, the magnetic field required to induce field induced ordering and zippered structures decrease with increasing surfactant concentration. The aggregation rate was found to increase linearly with increasing surfactant concentration.

The phase contrast microscopy results show very fast lateral movement of well separated chains and interconnected frozen disordered structures at low and high magnetic fields, respectively. When the average distance among chains is greater than the escape distance, a fewer chains coalesce to form individual chains. At high field strength, more chains and complex patterns are formed within the escape distance, while at low field strengths, the average inter-chain spacing increased with time and followed a power law scaling with time. The magneto-optical measurements in the emulsion confirm that the observed field induced transparency in magnetic emulsions ($\Phi > 0.0021$) is due to the optical birefringence caused by the rod like nanostructures.

In a ferrofluid with high polydispersity indices (PDI), thin chains, thick chains, and sheets are formed on increasing the in-plane magnetic field, whereas isotropic bubbles, hexagonal and lamellar/stripe structures are formed on increasing an out-of-plane magnetic field over the same range. On the contrary, no field-induced aggregates are seen in a sample with low polydispersity under the above condition. The isotropic to hexagonal columnar to lamellar/stripe patterns observed in sample with high PDI, indicate the prominent role of larger sized particles and the applied magnetic field strength in structural transitions in ferrofluids. The observed transmitted light intensity from random particles, chains/columns, hexagonal closed pack and stripe like structures were single bright spot, circular pattern, circular ring with six bright spots and straight line, respectively.

The findings of this thesis are useful for the design of light-controllable magnetic-fluid-based devices such as light modulators and light switches. The reversible and fast response of polydisperse sample will also be beneficial for microfluidics applications such as ferrofluid-based robot and lab-on-chip devices.

# Table of Contents

# List of Figures

# List of Tables

# List of Abbreviations

| | |
|---|---|
| DLVO | Derjaguin-Vervew-Landau-Overbeek |
| IPS | Interparticle spacing |
| 1D | One dimensional |
| 2D | Two dimensional |
| 3D | Three dimensional |
| MNP | Magnetic nanoparticle |
| FCC | Face-centered-cubic |
| HCP | Hexagonal-close-packed |
| BCT | Body-centered-tetragonal |
| BCO | Body-centered-orthorhombic |
| PDI | Polydispersity indices |
| ER | Electro-rheological |
| PHE | Photonic Hall effect |
| SMB | Static magnetic birefringence |
| SDS | Sodium dodecyl sulfate |
| XRD | X-ray diffraction |
| JCPDS | Joint committee on powder diffraction standards |
| SAXS | Small angle X-ray scattering |
| DLS | Dynamic light scattering |
| PALS | Phase analysis light scattering |
| VSM | Vibrating sample magnetometer |
| TGA | Thermogravimetric analysis |
| PMT | Photomultiplier tube |
| ADC | Analog to digital converter |
| CCD | Charge coupled device |
| wt. % | Weight percentage |
| I | Isotropic |
| H | Hexagonal |
| S | stripe |
| Fig. | Figure |
| Eqn. | Equation |
| LAMMPS | Large-scale Atomic/ Molecular Massively Parallel Simulator |
| BD | Brownian dynamics |

| | |
|---|---|
| FFT | Fast Fourier transform |

# List of Symbols

| | |
|---|---|
| $k_B$ | Boltzmann's constant |
| $T$ | Temperature |
| $D_c$ | Critical size for single domain |
| $A$ | Exchange constant |
| $K_{eff}$ | Anisotropic constant |
| $\mu_0$ | Vacuum permeability |
| $M_s$ | Saturation magnetization |
| $V_p$ | Magnetic particle volume |
| $\theta_m$ | Angle between the magnetization and the easy axis |
| $D_{sp}$ | Critical size for superparamagnetic size |
| $\tau_N$ | Neel relaxation time |
| $\tau_B$ | Brownian relaxation time |
| $\tau_0$ | Attempt time |
| $\eta$ | Viscosity of carrier or base fluid |
| $V_h$ | Hydrodynamic volume |
| $\tau_{eff}$ | Effective relaxation time |
| $H$ | Applied magnetic field |
| $\nabla^2$ | Laplace operator |
| $\varepsilon_0$ | Dielectric constant of vacuum |
| $\rho_e$ | Local electric charge density |
| $z_+$ | Valency of cations |
| $z_-$ | Valency of anions |
| $e$ | Elementary charge |
| $n$ | Concentration of ions per unit volume |
| $\Psi$ | Electric potential |
| $n_+(n_-)$ | Bulk concentration of salt |
| $E_+(E_-)$ | Energy of positive(negative) ion |
| $\kappa$ | Inverse Debye length |
| $I$ | Ionic strength |
| $h$ | Distance between the charged particles |
| $W_E$ | Interaction energy of the electric double layer |
| $W_V$ | Van der Waals interaction energy |
| $C_{vdw}$ | Coefficient of dispersion interaction between the atoms of the colloidal particles |

| | |
|---|---|
| $W_T$ | Total interaction energy between two charged particles |
| $W_{max}$ | Energy barrier |
| $\chi$ | Magnetic susceptibility |
| $M_v$ | Volume magnetization |
| $\chi_v$ | Volume susceptibility of the particle |
| $m$ | Magnetic moment of the particle |
| $a$ | Radius of the magnetic particle |
| $d$ | Diameter of the magnetic particle |
| $\chi_{eff}$ | Effective volume susceptibility of ferrofluid |
| $U_{ij}$ | Magnetic interaction energy between particles i and j |
| $\mu_f$ | Permeability of environment (carrier fluid) |
| $r_{ij}$ | Distance between particles i and j |
| $\theta_{ij}$ | Angle between distance vector $r_{ij}$ and $H$ |
| $N^*$ | Aggregation parameter |
| $\Phi$ | Volume fraction |
| $\Phi_\mathrm{m}$ | Maximum particle packing fraction |
| $\Lambda$ | Magnetic coupling constant between particles |
| $\rho$ | Inter-chain/column spacing |
| $L$ | Sample thickness/ path length |
| $\lambda$ | Wavelength of light |
| $n_r$ | Order of Bragg reflection |
| $\lambda_{X-ray}$ | Wavelength of X-ray |
| $d_{hkl}$ | Interplanar spacing of the crystal |
| $\theta$ | Bragg angle |
| $\beta_{FWHM}$ | Full width at half maximum |
| $N_p$ | Total number of particle |
| $S(q)$ | Structure factor |
| $P(q)$ | Particle form factor |
| $q$ | Wave vector |
| $\Delta\rho_e$ | Electron density difference between the solute and the solvent |
| $I(q)$ | Scattered intensity |
| $B^*$ | Damping factor |
| $g^1(\tau)$ | Electric field autocorrelation function |
| $g^2(\tau)$ | Intensity autocorrelation function |
| $\tau$ | Delay time |

| | |
|---|---|
| $A_1$ | Amplitude of correlation function |
| $B$ | Baseline |
| $D$ | Translational diffusion coefficient |
| $R_h$ | Hydrodynamic radius of the dispersed particle |
| $\varepsilon$ | Dielectric constant of the suspending medium |
| $\zeta$ | Zeta potential |
| $U_E$ | Electrophoretic mobility |
| $f(\kappa a)$ | Henry's function |
| $M$ | Magnetization |
| $a_s$ | Head area of single surfactant molecule |
| $\rho_{MNP}$ | Density of magnetic nanoparticles |
| $N_A$ | Avogadro number |
| $M_w$ | Molecular weight of oleic acid |
| $s$ | Standard deviation |
| $z_D$ | Mean average size |
| $H_{c1}$ | First critical magnetic field |
| $H_{c2}$ | Second critical magnetic field |
| $H_{c3}$ | Third critical magnetic field |
| $m_0$ | Magnetic moment of oil droplet |
| $a_1$ | Radius of oil droplet |
| $d_1$ | Diameter of oil droplet |
| $\Lambda_1$ | Magnetic coupling constant between oil droplets |
| $r$ | Inter-droplet separation |
| $F_m$ | Magnetic attractive force |
| $\Lambda_{c1}$ | Coupling constant corresponding to first critical magnetic field |
| $\Lambda_{c2}$ | Coupling constant corresponding to second critical magnetic field |
| $\Lambda_{c3}$ | Coupling constant corresponding to third critical magnetic field |
| $H^*$ | Magnetic field around an infinite chain |
| $F_c$ | Total free energy of chain |
| $U$ | Interaction energy per unit length $d_1$ |
| $U_q$ | Coulomb interaction energy |
| $q_m$ | Effective charges of column |
| $U_i$ | Binding energy produced by an infinite nucleation chain |
| $U_f$ | Fluctuation energy in a chain produced by Peierls-Landau instability |

| | |
|---|---|
| $\gamma$ | Sensitivity |
| $G$ | Geometric factor |
| $F_{vdw}$ | Van der Waal's force |
| $A_H$ | Hamakar constant |
| $F_r$ | Electrostatic repulsive force |
| $d_{c1}$ | Critical inter-droplet spacing corresponding to 1st critical magnetic field |
| $d_{c2}$ | Critical inter-droplet spacing corresponding to 2nd critical magnetic field |
| $d_{c3}$ | Critical inter-droplet spacing corresponding to 3rd critical magnetic field |
| $t$ | Time |
| $I_{max}$ | Maximum intensity at $t = 1000$ s |
| $I_{min}$ | Minimum intensity at $t = 100$ s |
| $\Delta I$ | Difference in intensity (i.e., $I_{max} - I_{min}$) |
| $t_c$ | Time required to form doublet of oil droplets |
| $F_{max}$ | Maximum magnetic force between two droplets |
| $F_d$ | Viscous force |
| $v$ | Flow velocity relative to droplet |
| $I_t$ | Transmitted light intensity |
| $I_0$ | Incident light intensity |
| $n_s$ | Scatterer number density |
| $\alpha_{ext}$ | Extinction coefficient |
| $Q_{ext}$ | Scattering extinction efficiency |
| $C_{ext}$ | Extinction cross section |
| $n_e$ | Refractive index of carrier fluid |
| $a_n$ and $b_n$ | Mie scattering coefficients |
| $\zeta_c$ | Angle between the incident light and the cylindrical axis |
| $j_x$ | Diffusion flow |
| $\mu$ | Chemical potential of droplets |
| $f(\Phi)$ | Friction coefficient |
| $\kappa_f$ | Coefficient of hydrodynamic interaction |
| $\mu_H$ | Chemical potential due to magnetic contribution |
| $L(\xi)$ | Langevin function |
| $L^{'}(\xi)$ | First derivative of Langevin function |
| $\Lambda^{*}$ | Reduced parameter of dipolar interaction |
| $\gamma_c$ | Effective field constant |

| | |
|---|---|
| $D_{\perp}$ | Lateral diffusion coefficient of emulsion droplets |
| $N$ | Number of droplets in a chain |
| $r_e$ | Escape distance |
| $(D_{\perp})_{\mathrm{chain}}$ | Lateral diffusion coefficient of chain |
| $\delta(\rho)$ | Fluctuation amplitude |
| $\zeta(5)$ | Zeta function |
| $U_{tot}$ | Interaction energy between two chains |
| $C_s$ | Surfactant concentration |
| $\delta_p$ | Phase difference |
| $\Delta n$ | Birefringence |
| $\alpha$ | Angle between the analyzer and polarizer |
| $I_R$ | Resultant intensity |
| $A_2$ | Anisotropy constant |
| $\beta$ | Proportionality constant |
| $E_a$ | Anisotropic energy |
| $\chi_{\perp}$ and $\chi_{\parallel}$ | Effective dielectric susceptibility |
| $\Delta n_0$ | Maximum birefringence |
| $\Delta n/\Delta n_0$ | Reduced birefringence |
| $N(d)$ | Particle size distribution |
| $u_{ij}^{WCA}$ | Weeks-Chandler-Andersen (WCA) potential |
| $d_{ij}$ | Mean particle diameter |
| $\sigma_S$ | Diameter of small magnetic particles |
| $\sigma_L$ | Diameter of large magnetic particles |
| $m_S$ | Magnetic moment of small magnetic particle |
| $m_L$ | Magnetic moment of large magnetic particle |
| $\Lambda_{LL}$ | Magnetic coupling constant corresponding to large-large particles |
| $\Lambda_{LS}$ | Magnetic coupling constant corresponding to large-small particles |
| $\Lambda_{SS}$ | Magnetic coupling constant corresponding to small-small particles |
| $\mu_{eff}$ | Effective magnetic permeability of magnetic medium |
| $U_H$ | Potential energy of a dipole moment in an external magnetic field |
| $F_H$ | Magnetic packing force |
| $\Phi_L$ | Volume fraction of large particles |
| $\Phi_S$ | Volume fraction of small particles |
| $x'$ and $y'$ | Exponents of power law |

| | |
|---|---|
| $g(r)$ | Radial distribution function |
| $\varepsilon_1$ | Energy parameter |
| $l$ | Characteristic length scale |
| $n(r, r+\delta r)$ | Number of pairs of particles separated by a distance between $r$ and $r + \delta r$ |
| $J_0(qr)$ | Bessel function of the first kind |

# *Chapter 1*

# Introduction

## 1.1. Soft matter

Soft matter plays an important role in nearly every aspect of our daily lives. Everyday materials like food, medicines, cleaning agents, paints and polymers are highly complex at the microscopic and molecular scale. These materials are often consist of tiny particles, which are held together by weak intermolecular interactions (typically of the order of thermal energy $k_B T$, where $k_B$ is the Boltzmann's constant and $T$ is the temperature). Therefore, these materials can be easily deformed under stress, hence known as 'soft matter' [1, 2]. Soft matter is highly multidisciplinary area, where physicists, chemists, biologists and engineers involved.

In general, soft matter exhibit three characteristic features. First, the molecules form a far more disordered structure than the atoms or molecules in the crystal lattice of a true solid. Second, the structures of soft matter are both flexible and stable. Third, through self assembly, soft matter can spontaneously form supramolecular structures. The typical length scales of hard matter are in the scale of size of the atoms or molecules (i.e., Angstroms to nanometers) whereas, the typical length scales of soft materials are between several nanometers to micrometers. The number density of particles that form a soft matter structure is several orders (~12 orders) of magnitude smaller than that of a hard material due to the broad structural length scale. In addition, the time scales of soft material motions is much larger (ns to seconds) than atomistic time scales (Femto-seconds). Soft matter shows a large response to an external perturbation as compared to solids/crystals. Examples of soft materials include colloids, surfactants, liquid crystals, blood, milk, ink, paints, gels, glue, detergents, certain biomaterials and polymer in the melt or the solution, etc. These materials flow under certain conditions because of their low molecular kinetic energy (i.e., close to $k_B T$).

The name colloid is derived from the word 'gluey' in Greek. Colloids consist of microscopically small particles dispersed in another substance, the dispersion medium. These systems are also known as complex fluids or colloidal systems as they are inhomogeneous in structure at a resolution of 100 or even 1000 Å. The dispersed particle diameter varies between a few nanometers and tens of micrometers. Colloids have enormous economic and technical importance because of their industrial application.

Emulsion is a biphasic system of two immiscible liquids. Depending on the nature of the dispersed phase and dispersion medium, emulsion is divided into two types: oil-in-water (O/W) and water-in-oil (W/O) [3-9]. Emulsions are metastable colloids that require specific entities at the interface to remain stable. Emulsions are prepared by shearing two immiscible liquids. It favors (O/W) emulsification if the main surfactant is water soluble and, conversely, if the surfactant is oil soluble, it favors W/O emulsification. Surface active molecules such as surfactants, polymers, proteins, etc., are used as a stabilizer to reduce interfacial tension and prevent aggregation of droplets. In the oil-water interface, stabilizers adsorb at the O/W interface and provide steric or electrostatic, or dual electro-steric stabilization. Surface active species not only play an important role in emulsion size and stability, but it often also determines its toxicity, pharmacokinetics, and pharmacodynamics [10-12]. Some colloids that respond to external stimuli (i.e., temperature, light, voltage, stress, pH, electric field, magnetic field, etc.) and alter their physical properties are called SMART colloids [13-17].

## 1.2. Ferrofluids

Ferrofluid (magnetic fluid) is a stable colloidal dispersion containing functionalized superparamagnetic nanoparticles dispersed in a carrier fluid. Three important components of a magnetic fluid are single-domain magnetic particles, carrier liquid, and stabilizing molecule. In the presence of an external magnetic field, magnetic fluids alter their physical properties such as optical, rheological, and thermal properties and hence come under the category of smart colloids [18-21]. Magnetic fluids have been finding applications in many fields due to field-tunable physical properties. In 1963, Steve Papell developed ferrofluid at the National Aeronautics and Space Administration (NASA) while doing space research programs for fluid control in space. Using oleic acid surfactant and kerosene dispersant media, he prepared a stable concentrated magnetic fluid suspension in 1965 [22]. Later, Rosensweig and other coworkers developed sub-200 Å particles for dispersion, using various solvents, including water, aliphatic and aromatic hydrocarbons [23].

Bulk ferri- or ferro-magnetic material consists of domains, that are separated by domain walls to minimize the net energy of the system. The magnetostatic energy increases proportionally to the volume of the material, while the domain wall energy increases with the surface area. Thus, because of the domain wall energy, below a critical size domain formation become energetically unfavorable, and hence the particle become a single uniformly magnetized domain and functions as a tiny permanent magnet. The size of the single-domain particle depends on the material and contribution from different anisotropy energy terms. The critical size below which a particle acts as a single domain particle is given by [24-26] $D_c \approx 18\frac{\sqrt{AK_{eff}}}{\mu_0 M_s^2}$, where $A$ is the exchange constant, $K_{eff}$ is the anisotropy constant, $\mu_0$ is the vacuum permeability, and $M_s$ is the saturation magnetization. Single domain magnetic particle diameter typically lies in the range of few tens of nanometers and depends on the material. Typical values of $D_c$ for iron, cobalt, and nickel are ~ 19, 96.4, and 53.6 nm, respectively [27]. The magnetic anisotropy energy per particle, which is responsible for holding the magnetic moments along a certain direction, can be expressed as $E(\theta_m) = K_{eff}V_p sin^2\theta_m$, where $V_p$ is the particle volume and $\theta_m$ is the angle between the magnetization and the easy axis. The energy barrier, $K_{eff}V_p$ separates two energetically equivalent easy directions of magnetization. As the thermal energy exceeds the energy barrier for the sufficiently small particle of size $D_{sp}$, the particle's magnetic moment shifts spontaneously and rapidly in the absence of a magnetic field. Thus, the magnetization of the particles is easily flipped, which is known as Neel relaxation [28]. The Neel relaxation time of the moment of a particle, $\tau_N$ is given by

$$\tau_N = \tau_0 exp\left(\frac{K_{eff}V_p}{k_B T}\right) \tag{1.1}$$

The system is in a superparamagnetic state if the magnetic moment of the particle reverses at times shorter than the experimental time scales. For superparamagnetic particles, the timescale of the Neel relaxation process, $\tau_N$, is much smaller than the timescale of the magnetic measurement. Therefore, due to the rapid rotation of the magnetic moment of the particle, the net magnetization observed is zero in the absence of an applied field. For $k_B T > K_{eff}V_p$, the system acts like a paramagnet in the presence of a magnetic field and within each particle, there is now a giant (super) moment, therefore it is called superparamagnet. Such a system shows no hysteresis. When prepared as a liquid suspension, single-domain nanoparticles (with size larger than $D_{sp}$ but smaller than $D_c$) can act effectively as superparamagnetic particles [29] where the rotation of the entire particles can be achieved against the carrier fluid's hydrodynamic resistance, known as the Brownian relaxation given by [30]

$$\tau_B = \frac{3\eta V_h}{k_B T} \tag{1.2}$$

where $\eta$ is the viscosity of the carrier or base fluid, $V_h$ is the hydrodynamic volume (volume of the particle along with the surfactant layer). Neel and Brownian relaxation are schematically shown in **Fig. 1.1.** For a non-uniform distribution of particle size, relaxation occurs via a combination of the above two mechanisms and the effective relaxation time is given as

$$\frac{1}{\tau_{eff}} = \frac{1}{\tau_B} + \frac{1}{\tau_N} \tag{1.3}$$

For various applications, the relaxation mechanism is highly relevant. At most frequencies used in non-biomedical applications, particles that relax through the Neel mechanism will usually react in phase with the applied field.

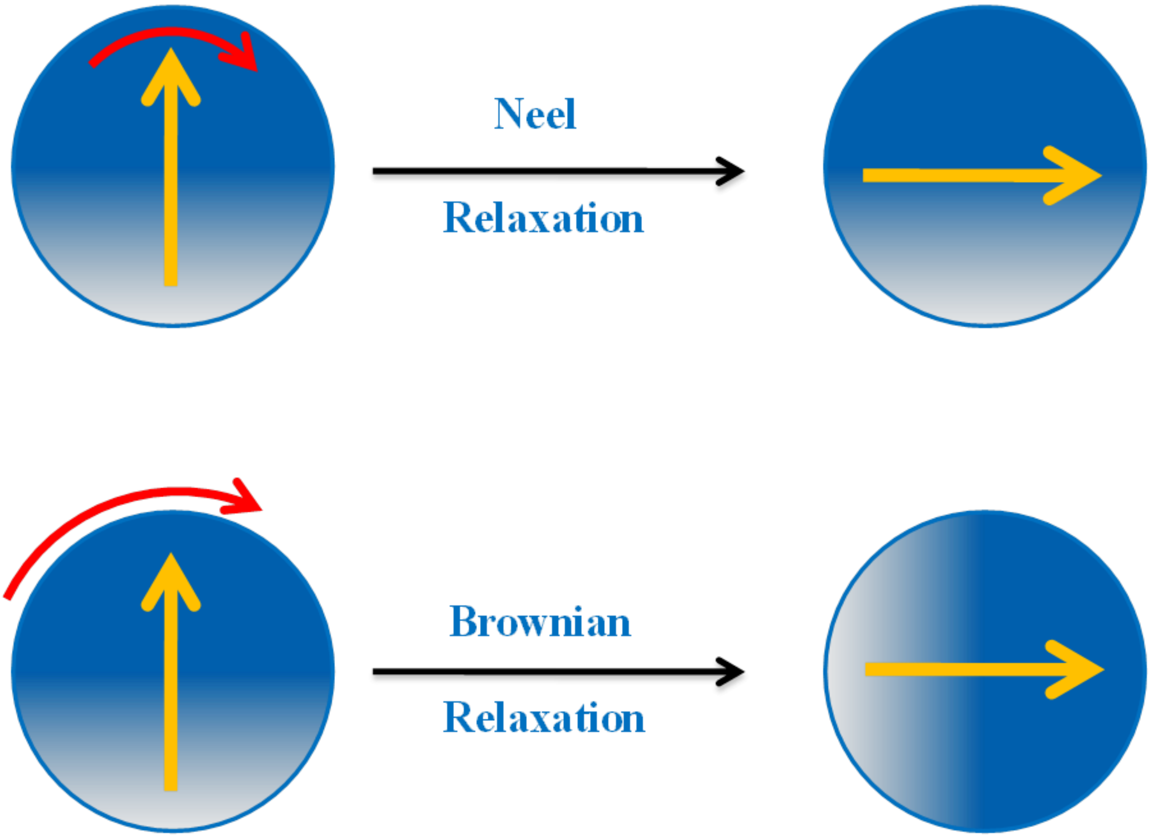

*Figure 1.1 Schematic showing Neel and Brownian relaxation of magnetic particle.*

The origin of the magnetic response of a ferrofluid is depicted schematically in **Fig. 1.2**. When applied magnetic field, $H = 0$, the nanoparticles (NPs) in the fluid have an unstable magnetic moment due to Neel relaxation, which rotates freely in all directions. A colloid containing a large number of such NPs has a net magnetic moment of zero. At low magnetic field strength, the moment of the nanoparticles fluctuates around the direction of the external field. As a consequence, in the direction of the applied field, the fluid has a net magnetization. The magnetic moments of the nanoparticles are fully aligned to the applied external field under a strong magnetic field. In all these cases, the magnetic response can be represented by a magnetic dipole associated with the external field, with an amplitude that increases with the amplitude of applied magnetic field.

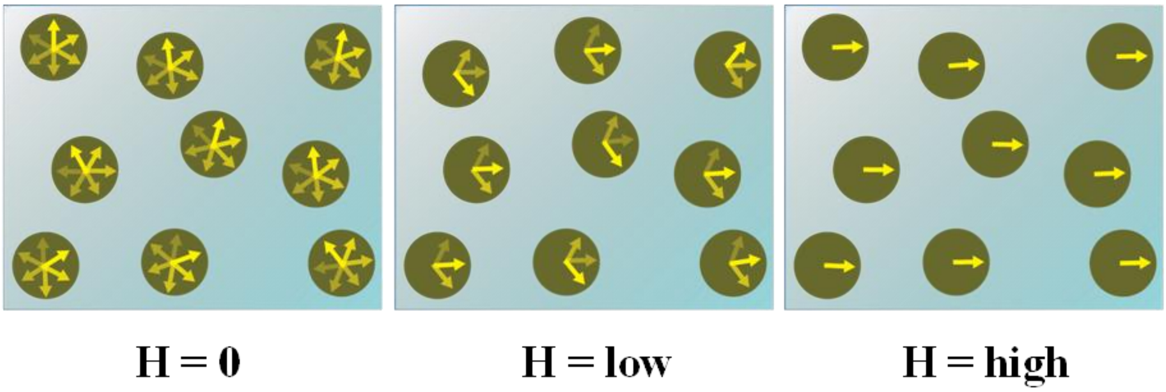

*Figure 1.2 Illustration of the nanoscopic origin of the magnetic behavior of superparamagnetic colloid in the absence and the presence of a magnetic field.*

As the particle size decreases, the surface-to-volume ratio increases as a consequence the percentage of surface atoms increases, which means that surface and interface effects become more significant. The particles in dispersions have a strong tendency to aggregate due to van der Waals forces [31, 32]. By balancing different interparticle forces such as the attractive dipole-dipole interactions, repulsive steric/ electrostatic/ electro-steric interactions, and gravitational forces, the stability of ferrofluid is achieved [33]. The high surface energy of magnetic nanoparticles, higher dipole-dipole interaction between the larger particles, relatively low particle surface stabilizer and stabilizer-carrier liquid chemical compatibility, cause the instability of ferrofluids [34]. The object of the use of stabilizers are (1) to prevent oxidation of the magnetic nanoparticle surface, (2) to prevent particle agglomeration by providing electrostatic or steric repulsion between the particles,

(3) to improve the stability of the dispersion, and (4) to increase the possibilities for surface functionalization and other molecular conjugation [35, 36].

To stabilize a colloidal dispersion there are three general methods, namely electrostatic stabilization, steric and electro-steric stabilization, are used. Electrostatic stabilization is based on the repulsive force occurring between electrical charges with an equal sign. The stability of the particles is usually achieved by coating the surface of the particle with charged groups, giving the particle a net surface charge and creating a repulsive force between them, capable of overcoming the forces of van der Waals. Particles can also acquire electric charge due to the presence of ions.

Steric stabilization is achieved by covering the particles with short or long chain molecules (typically surfactant or polymers) to prevent aggregation of the particles. The surfactant molecules in the medium interpenetrate as the particles move toward each other and the particles are repelled from each other because of the increased osmotic pressure in the region [37]. Electro-steric stabilization is the combination of both electrostatic and steric stabilization. It occurs as a result of charged polymer (i.e., polyelectrolytes) adsorption that ionizes like electrolytes but has one of their ions bound in the backbone and one free in the solution. Owing to the dissociated charge molecules, electrostatic interaction occurs, but steric interaction occurs due to the polymer chains. Polyelectrolyte geometry depends heavily on the ionic strength of the environment. The behavior of polyelectrolytes is regulated by long-range electrostatic interaction at low or zero salt levels. However, short-range excluded volume interaction dominates over long-range electrostatic force under the maximum screening of charge at high salt concentration. **Fig. 1.3** displays a diagram describing electrostatic, steric, and electro-steric repulsion.

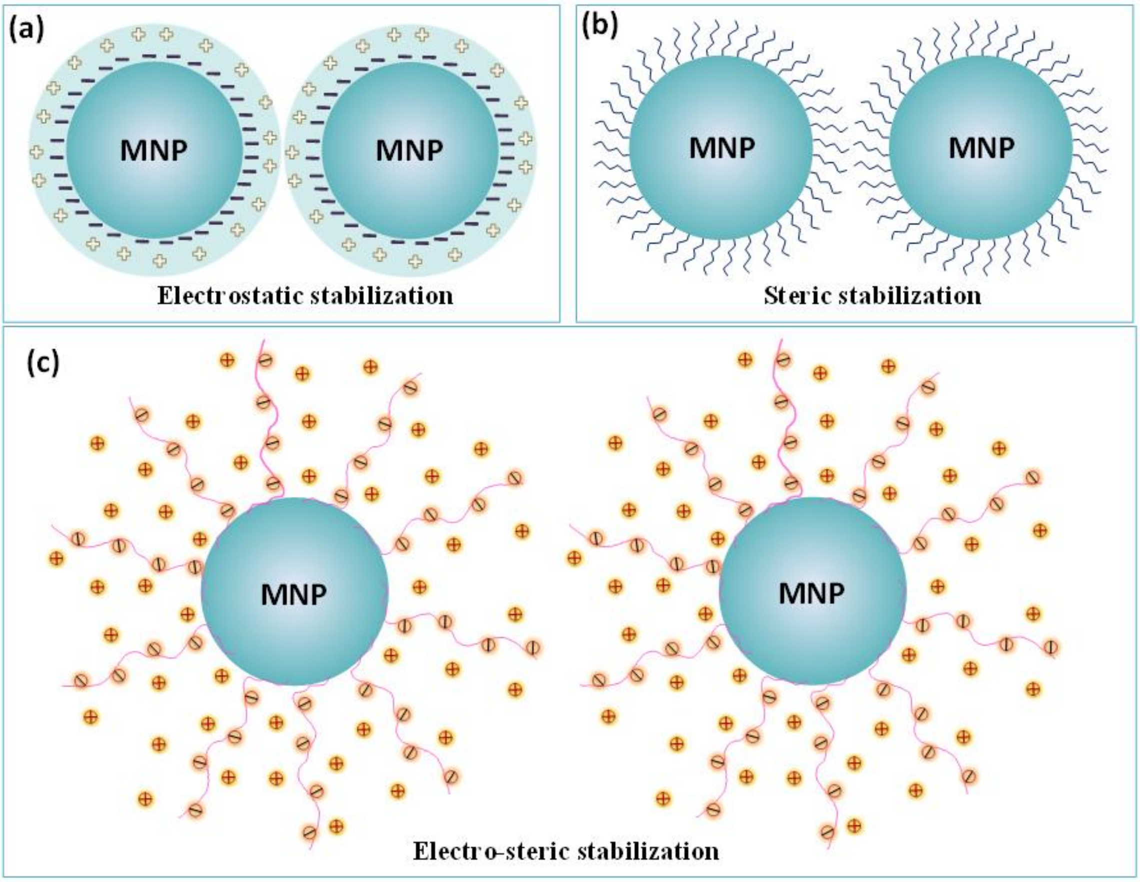

*Figure 1.3 Schematic showing electrostatic, steric, and electro-steric stabilization of magnetic nanoparticles.*

The carrier liquid in a ferrofluid can be either a polar (water, ethylene glycol) or nonpolar solvent (kerosene, silicon oil, vegetable oils, mineral oil). The synthesis of high-quality superparamagnetic nanoparticles can be done by using techniques such as co-precipitation [38], solvothermal decomposition [39], hydrothermal synthesis [40], microwave-assisted synthesis [41], sol-gel synthesis [42], etc.

Recently, owing to their interesting properties, such as melting point, density, hydrophobicity, and viscosity, ionic liquids as base fluid have been attempted by adjusting a combination of anion and cation to suit a specific requirement [43]. They are robust and eco-friendly because of their negligible vapor pressure, non-flammability, and wide liquid temperature range [44]. In ionic aqueous ferrofluids, the particles are charge stabilized and the repulsive electrostatic interactions between them can be controlled by adding salt or changing pH. The second class of aqueous ferrofluids is stabilized by a combination of steric and electrostatic effects, where the particles are surface-functionalized with molecules containing ionizable groups and the electro-steric interaction is tuned by varying solvent properties such as pH or ionic strength or temperature.

## 1.3. Ferrofluid emulsion

Ferrofluid emulsion, also known as magnetic nanoemulsion, where ferrofluid oil, containing single domain ferro- or ferri-magnetic nanoparticles of typical size $\leq$ 10 nm, coated with a surfactant or polymer, is dispersed in water. The dispersed phase possesses a zero net magnetic moment in the absence of a magnetic field, but in the presence of a magnetic field, the induced magnetic moments are oriented in the direction of the magnetic field thereby, experiencing an attractive force along the direction of the magnetic field and a repulsive force normal to it. The field induced self-assembly of nanoemulsions dramatically modify their physical properties leading to many applications such as developing tunable photonic structures [45], optical limiters [46], optical filter [47], artificial swimmers [48], colloidal gels [49], biomolecular recognization probe [50, 51], defect sensor [52], cation sensors [53], etc.

## 1.4. Stabilization mechanisms in magnetic nanofluid

The attractive van der Waals and dipole-dipole forces present in the dispersion tend to destabilize the magnetic nanofluid. A net repulsive force is necessary in order to keep them stable. Emulsions can be stabilized by electrostatic double-layer repulsion, where the interaction between like charges is always repulsive. There are many mechanisms that lead to the surface charging, such as direct surface groups ionization, specific ion adsorption, differential solution of surface ions, surface ion substitution or charges from specific crystal structures [54, 55]. In general, colloidal systems are electrically neutral, which means that any surface charge on a particle is balanced by an equal amount of opposite charge (counterions) in the surrounding phase. The charges on the surface of the particle are attached physically or chemically and to stay there more or less indefinitely. By comparison, the surrounding (balancing) charge is associated much more loosely with the particle. This countercharge is dispersed in a diffuse layer due to the thermal motions of the solvent molecules and ions, which spreads from the particle surface up to a certain distance (order of nanometers). The oppositely charged ions appear to congregate around the particle and due to the repulsion of the charges on the particle, very few negatively charged co-ions can get close to the surface. A non-uniform distribution of ions in the vicinity of the surface evokes potential across the interface, and the surface charges along with counterions are known as electric double layers. The adsorbed charged moieties give rise to an electric field that attracts the counterions balanced with the equal number of surface co-ions, as shown in **Fig. 1.4**.

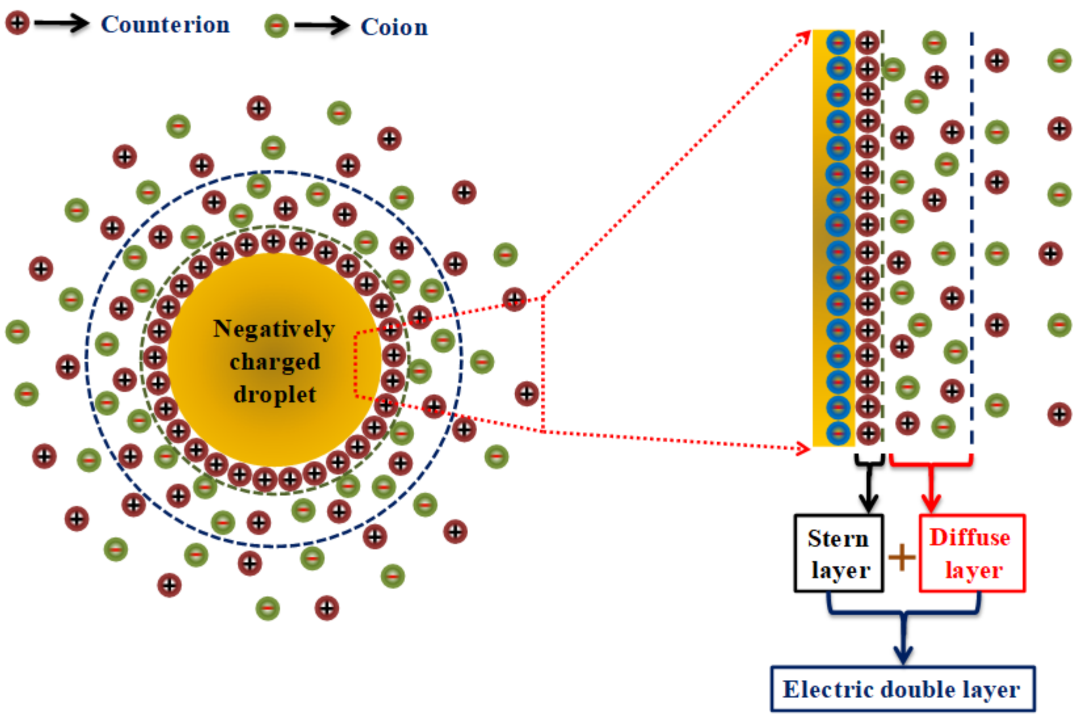

*Figure 1.4 Schematic representation of electric double layer.*

### 1.4.1. The Poisson-Boltzmann theory of diffuse double layer

The electric potential $\psi$ near a flat uniformly charged surface depends on the distance $x$ from that surface. The potential is constant in planes parallel to the surface due to the planar geometry of the surface under consideration. In general, the potential distribution $\psi(x, y, z)$ in the solution is given by the Poisson equation

$$\nabla^2\psi(x, y, z) = -\frac{\rho_e}{\varepsilon_0\varepsilon} \tag{1.4}$$

where $\nabla^2$ denotes the Laplace operator, $\varepsilon_0$ is the dielectric constant of vacuum, and $\rho_e$ stands for the local electric charge density [C/m$^3$], which is determined by the distribution of ions within the electric double layer

$$\rho_e = z_+ e n_+ + z_- e n_- \tag{1.5}$$

The valency of ions (cations or anions) is denoted here by $z_+$ and $z_-$, respectively, $e$ is the elementary charge and $n$ is the concentration of ions per unit volume. For a spherical particle, potential distribution is a function of the radial component $r$ only i.e., $\psi = \psi(r)$. Using spherical polar coordinates Eqn. (1.4) can be written as

$$\nabla^2\psi(r) = \frac{1}{r^2}\frac{d}{dr}\left(r^2\frac{d\psi}{dr}\right) = -\frac{\rho_e}{\varepsilon_0\varepsilon} \tag{1.6}$$

Since the ions are free to move, their local ion density can be estimated using the Boltzmann distribution

$$n_+ = n_{+,0}exp\left(-\frac{E_+}{k_B T}\right) \tag{1.7}$$

$$n_- = n_{-,0}exp\left(-\frac{E_-}{k_B T}\right) \tag{1.8}$$

where, $n_+(n_-)$ is the bulk concentration of the salt and $E_+(E_-)$ denotes the energy of positive (negative) ion in the given position. In the Poisson-Boltzmann theory, it is assumed that these energies are equal to the work required to bring an ion from an infinite distance to the considered point.

$$E_+ = z_+ e\psi,\ \ E_- = z_- e\psi \tag{1.9}$$

On substitution of Eqn. (1.5), Eqn. (1.7), Eqn. (1.8) and Eqn. (1.9) into Eqn. (1.6) for a spherical particle, one obtains

$$\frac{1}{r^2}\frac{d}{dr}\left(r^2\frac{d\psi}{dr}\right) = -\frac{1}{\varepsilon_0\varepsilon}\left[z_+ e n_{+,0} exp\left(-\frac{z_+ e\psi}{k_B T}\right) + z_- e n_{-,0} exp\left(-\frac{z_- e\psi}{k_B T}\right)\right] \tag{1.10}$$

The above equation is known as the Poisson-Boltzmann equation. For the condition, $\left(z_{+/-} e\psi / k_B T < 1\right)$; for an equivalent electrolyte, the potential is smaller than 25 mV, and the equation can be written as

$$\frac{1}{r^2}\frac{d}{dr}\left(r^2\frac{d\psi}{dr}\right) = \left[\left(z_+^2 n_{+,0} + z_-^2 n_{-,0}\right)\frac{e^2}{\varepsilon_0\varepsilon k_B T}\right]\psi = \kappa^2\psi \tag{1.11}$$

where $\kappa$ is the inverse Debye length

$$\kappa = \sqrt{\left(z_+^2 n_{+,0} + z_-^2 n_{-,0}\right)\frac{e^2}{\varepsilon_0\varepsilon k_B T}} \tag{1.12}$$

Taking into account the boundary conditions, i.e., $\psi(r = 0) = \psi_0$ and $\psi(r \to \infty) = 0$, a solution of the linearized Poisson-Boltzmann equation takes the following form

$$\psi(r) = \psi_0 \exp(-\kappa r) \tag{1.13}$$

From the above equation, it is clear that the potential decreases exponentially with increasing distance $r$. The Debye length ${}^{1}/_{\kappa}$ describes the range of electrostatic interactions and the thickness of the electric double layer in the dispersed systems. The more ions present in the solution, the charge screening is more effective. The ionic strength $I$ of a given solution is written as

$$I = \sqrt{\frac{1}{2}\sum_{i=+,-} n_i z_i^2} \tag{1.14}$$

The inverse Debye length is expressed as

$$\kappa = \sqrt{\frac{2e^2 I}{\varepsilon_0 \varepsilon k_B T}} \tag{1.15}$$

Therefore, as the salt concentration increases, the Debye length decreases. For example, the Debye length of $10^{-4}$ M NaCl solution is equal to 30.4 nm, while it decreases to 0.96 nm at 0.1 M and to 0.3 nm at 1 M solution [56, 57]. Coulomb's law determines the repulsion in a vacuum, whereas the interactions are screened by the ionic atmosphere in a polar liquid. The double layers begin to overlap and repulsion occurs when particles are at distances smaller than twice the double layer extension. For two spherical particles of radius $a$ and condition $\kappa a < 3$, the expression for the electric double layer repulsive interaction is given by [58]

$$W_E(h) = \frac{4\pi\epsilon_r\epsilon_0 a^2 \Psi_0^2 \exp(-\kappa h)}{2a + h} \tag{1.16}$$

The interaction energy decreases exponentially with the distance. The higher is the electrolyte concentration, the steeper is the decay.

### 1.4.2. Total interaction energy between two charged particles

The total interaction energy between two charged particles is the summation of the interaction energy due to van der Waals attraction and electric double layer repulsion and is given by

$$W_T(h) = W_V(h) + W_E(h) \tag{1.17}$$

where $W_V(h) = -\frac{C_{vdw}}{h^6}$ is the van der Waals interaction energy, $C_{vdw}$ is the coefficient of dispersion interaction between the atoms of the colloidal particles. Minus sign is due to attractive nature of van der Waals interaction. The Eqn. (1.17) was developed by Derjaguin, Landau, Verwey and Overbeek for stable colloidal dispersion and is now referred to as the DLVO theory [59, 60]. **Fig. 1.5** shows the variation of interaction energy with the distance $h$ between the charged particles in the conditions of low electrolyte concentration (strong electrostatic repulsion). The interaction energy of the electric double layer decays exponentially with the distance ($W_E \rightarrow 0$), while the van der Waals energy decreases with the sixth power of the distance and does not disappear. At very short distances, $W_V \gg W_E$, the total interaction energy is negative, resulting in a deep primary minimum of the energy. Particles on such a distance are subjects of the irreversible aggregation. At large separation, $W_V > W_E$, a shallow secondary minimum appears which corresponds to a weak and reversible flocculation of the particles. At the intermediate distance, $W_V < W_E$, resulting in energy maximum $W_{max}$. That is the electrostatic barrier, which prevents the particles from aggregation. The height of $W_{max}$ depends on the value of $\psi_0$, as well as on the electrolyte concentration and the ion valency. In order to ensure satisfying colloidal stability, $W_{max}$ has to be greater than $25k_BT$. The higher is the valency and the electrolyte concentration, the lower is the energy maximum. A barrier of $25k_BT$ is reached when the electrolyte concentration is smaller than $10^{-2}$M (monovalent electrolyte) and the zeta potential is around ±40 mV [58].

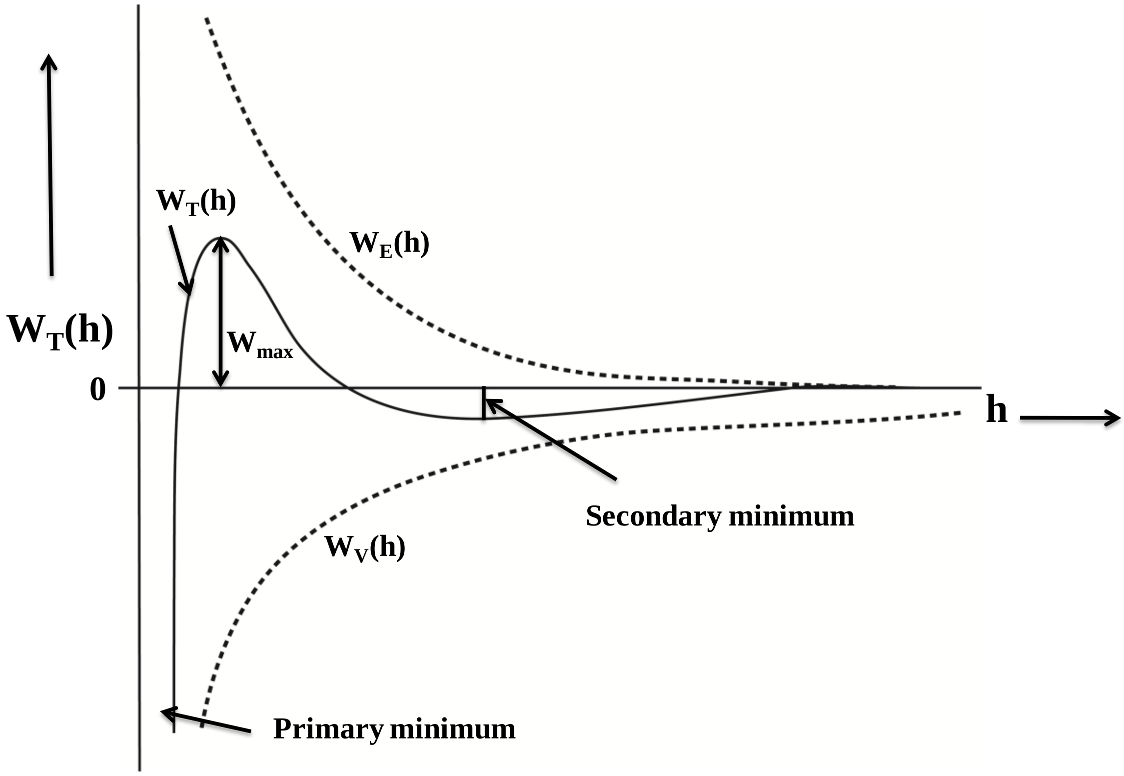

*Figure 1.5 Schematic representation of interaction energy between two charged colloidal particles according to the DLVO theory. The top dotted line represents electric double layer repulsion between charged particles, the bottom dotted line represents van der Waals attraction and the solid line represents the total interaction energy.*

## 1.5. Magnetic interactions between particles

The magnetic property of a material and its response to an external magnetic field is defined by the magnetic susceptibility $(\chi)$. Magnetic susceptibility indicates whether a substance is attracted into a magnetic field or repelled from it. The relationship between volume magnetization and an applied magnetic field is given in the Eqn. (1.18)

$$M_v = \chi_v H \tag{1.18}$$

where $\chi_v$ is the volume susceptibility of the particle ($\chi_v < 0$ for diamagnetic material, $\chi_v > 0$ for paramagnetic material and $\chi_v >> 0$ for ferro-, ferri- and superparamagnetic materials). The materials with $\chi_v > 0$ are attracted by the magnetic field, while diamagnetic materials are repelled from the field. The typical value of $\chi_v$ for $Fe_3O_4$ ~ 3.2 [61] The typical value of $\chi_v$ is $10^{-5}$ for diamagnetic material, $10^{-5}$-$10^{-2}$ for paramagnetic material and $10^2$-$10^6$ for ferromagnetic materials [62]. Superparamagnetic nanoparticles greatly respond to the external magnetic field with higher susceptibility values. Hence, the superparamagnetic nanoparticle is a suitable candidate for the ferrofluid system. On exposure to an external magnetic field, magnetic moments of superparamagnetic nanoparticles align with the magnetic field direction. The magnetic moment of each particle is given as

$$m = \frac{4\pi}{3} a^3 \chi_{eff} H = \frac{\pi}{6} d^3 \chi_{eff} H \tag{1.19}$$

where $a$ is the radius of the particle, $d$ is the diameter of the particle, $\chi_{eff}$ is the effective volume susceptibility of the ferrofluid. The anisotropic interaction energy, $U_{ij}$, between two particles is given by

$$U_{ij}(r_{ij}, \theta_{ij}) = \frac{\mu_f}{4\pi {r_{ij}}^3} \left[ m_i . m_j - \frac{3(m_i . r_{ij})(m_j . r_{ij})}{{r_{ij}}^2} \right] \tag{1.20}$$

where, $\mu_f$ is the permeability of environment (for vacuum, $\mu_0$ = 4π × $10^{-7}$ H.m$^{-1}$), $m_i$ and $m_j$ are the magnetic moments of $i^{th}$ and $j^{th}$ particles, and separated by a distance $r_{ij}$ (see **Fig. 1.6**). Assuming that the two magnetic particle are identical ($m_i = m_j = m_1$). For this case, the magnetic interaction energy and corresponding interaction force between two particles can be written as [63]

$$U_{ij} = \frac{\mu_0 m_1^2}{4\pi r_{ij}^3} \left[ 1 - 3cos^2\theta_{ij} \right] \tag{1.21}$$

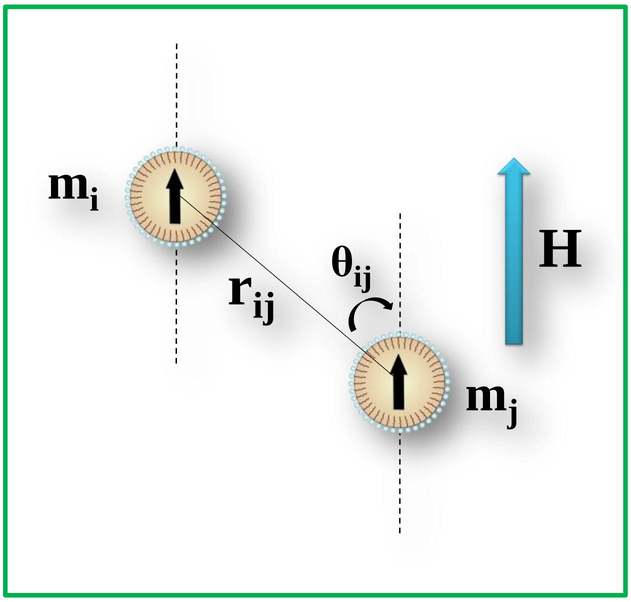

*Figure 1.6 Schematic showing the geometry of the interaction between two magnetic particles in an external magnetic field direction.*

$$F_{ij} = -\nabla U_{ij} = \frac{3\mu_0 m_1^2}{4\pi r_{ij}^4}\left[\left(1 - 3cos^2\theta_{ij}\right)e_r + 2sin\theta_{ij}cos\theta_{ij}e_\theta\right] \tag{1.22}$$

where $\theta_{ij}$ is the angle between the vector $r_{ij}$ and external field vector, the direction of the magnetic field, $e_r$ represents the coordinate variable along the linking line of the two particles and $e_\theta$ in a cylindrical coordinate system. The magnetic force component along $e_r$ has a negative value when $0^o \leq \theta_{ij} \leq 54.73^o$, showing the interparticle interaction is attractive. Inversely, the interparticle interaction is repulsive when $54.73^o \leq \theta_{ij} \leq 90^o$.

## 1.6. Magnetic field induced aggregation in magnetic fluids

Magnetic field induced aggregation in a magnetic fluid has been an area of interest due to the technological applications. Magnetic field induced aggregation depends on multiple parameters such as particle magnetic response, the concentration of particles, and the viscosity of carrier fluid or thermal energy. Field induced aggregation is due to the energy decrease in the magnetic association and the loss of entropy in the solution associated with the formation of structures of various sizes must be taken into account in a colloidal dispersion. Faraudo et al. [64] introduced a dimensionless quantity, called aggregation parameter $N^*$, that includes both the magnetic properties of the colloids and thermodynamic variables such as volume fraction and temperature, is given by

$$N^* = \sqrt{\Phi e^{\Lambda-1}} \tag{1.23}$$

where $\Lambda$ is the magnetic coupling parameter, which is the ratio between dipolar magnetic interaction energy to the thermal energy is given by

$$\Lambda = -\frac{U(d,0)}{k_B T} = \frac{\pi \mu_0 d^3 \chi_{eff}^2 H^2}{72 k_B T} \tag{1.24}$$

and $\Phi$ is the volume fraction of magnetic nanoparticles in the solution, which gives the information about the interparticle spacing in the dispersion. The interparticle spacing (IPS) of a monodisperse colloidal dispersion for a given $\Phi$ is given by

$$IPS = 2a\left[\left(\frac{\Phi_m}{\Phi}\right)^{1/3} - 1\right] \tag{1.25}$$

where $\Phi_m$ is the maximum particle packing fraction. $\Phi_m \sim 0.63$ for random dense packing. As the volume fraction increases, the IPS decreases. According to Eqn. (1.23), the actual condition determining the formation of structures ($N^* > 1$) involves not only $\Lambda$ but also the volume fraction. If thermal agitation is stronger than magnetic interaction ($\Lambda < 1$) and $N^* < 1$ and no field induced self assembly will occur due to weak magnetic interaction or the too large interparticle spacing. Values of $\Lambda$ larger than 1 imply that the magnetic interaction between particles in contact is stronger than thermal energy, but self-assembly is not guaranteed in this case. The magnetic nanoparticles self assemble to form linear aggregates in the direction of the magnetic field at $\Lambda > 1$ and $N^* > 1$. In ferrofluid, when the magnetic force overcomes the thermal force, the magnetic moment of the particles align along the direction of the magnetic field. As a result, one dimensional (1D) linear short and long chains formed in the direction of the magnetic field from the Brownian fluids [65-67]. When the concentration of the particle increases, due to the sufficiently strong inter-chain repulsive forces, shifting of the neighboring chain by a distance of half particle radius in the vertical direction occurs, then the chains start to aggregate laterally and form zippered structures (magnetic sheets) which are two dimensional (2D) in nature [68]. Zhang et al. showed that 1D to 2D transitions is mainly due to minimizing the repulsive potential under the conditions of a strong magnetic field gradient and high volume fraction of large particles [69]. When the particle concentration is above a certain critical value, two chain assembly is more stable than the one chain [70]. This 2D structure is considered as the intermediate state between 1D and three dimensional (3D) structures [71]. The 2D structures gradually developed into crystalline 3D structures as the concentration of particles and the interparticle potential increased further. The schematic representation of the transformation from homogeneous dispersion to one-, two-, and three-dimensional assemblies is shown in **Fig. 1.7.**

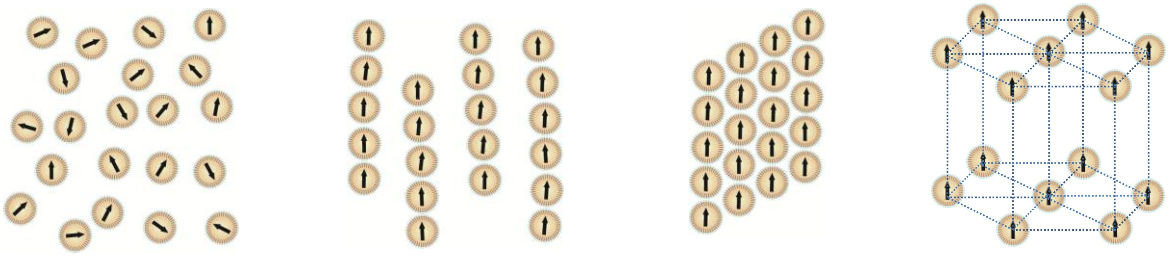

**Magnetic fluid** **1D Chains** **2D sheet** **3D crystal**

*Figure 1.7 Illustration of magnetically induced phase transitions between colloidal fluids, 1D particle chains, 2D sheets, and 3D structures.*

Various theoretical simulation methods were used to understand the effect of various parameters such as temperature, magnetic moment, field strength, particle concentration, sample thickness, etc., on the assembling process of magnetic nanoparticles and their assemblies' morphology. The transition from the one-dimensional particle chains into two-dimensional sheets are observed in the presence of magnetic field with an increasing number of particles in the system [72]. Hynninen and Dijkstra used the Monte Carlo simulation for the equilibrium packing of well dispersed homogeneous dipolar spheres responsive to external fields (electric or magnetic field) [73]. Coupling constant determines the extent of the external field on the formation of the anisotropic structures. Coupling constant and the particle volume fraction were used as scaling parameters in equilibrium phase diagram. The phase diagram for dipolar sphere shows fluid, face-centered-cubic (FCC), hexagonal-close-packed (HCP), body-centered-tetragonal (BCT) and body-centered-orthorhombic (BCO) phases. For $\Lambda > 1$, thermal diffusivity is suppressed by dipolar interactions which govern the assembling process and stabilize the structure. Swan, et al. later studied the kinetics of assembling of paramagnetic iron oxide coated polystyrene latex particles in pulsed magnetic field with toggling frequencies 0.33-10 Hz [74]. Assembled particle chains gradually merge laterally and gives rise to large, regular, crystalline domains with an increasing the time. Asher et al. reported the formation of FCC structures from highly-charged monodisperse superparamagnetic particles due to the minimization of interparticle electrostatic repulsive potential [45, 75]. Studies show that the magnetic fluids undergo several interesting structural transitions depending on the applied magnetic field strength, concentration of the particles, particle size polydispersity [76-79]. It has been shown that for particle sizes in the range 5 nm-8 nm and with a narrow size distribution (< PDI = 0.017 ), the columns are isolated and well defined with closely packed nanoparticles inside the columns [80], and no transition is observed from columnar to a labyrinthine pattern. In contrast, for broader size distributions (> PDI = 0.017) defects at the ends and the edges of the columns, resulting from a cohesion of the nanoparticles inside the columns, favor the fusion of columns into labyrinthine structures. Field induced structures in magnetic fluids also depend on the ramp rate of the magnetic field. When they are subjected to an external magnetic field at a slow ramp rate, three distinct critical magnetic fields are identified [66]. Bent wall or lamellar and labyrinthine pattern is observed for a highly concentrated sample in the case of a high field ramp rate [81]. The formation of field induced structures (columns, bent-wall or labyrinthine) is explained by minimization of free energy comprising magnetic, interfacial, and entropic contributions [82-85].

## 1.7. Application of magnetic fluids

The magnetic field induced structural transitions in magnetic fluids have been a topic of interest from both fundamental and practical point of view [86-90]. The self assembly of magnetic nanoparticles under an external magnetic field show interesting optical properties that are exploited for application such as magneto-optical wavelength filter [91], optical limiters [46], optical switches [92], optical grating [93], sensors [94, 95], optical fiber modulator [88, 89], magneto-optical waveguide [96], holographic optical tweezers [97], tunable photonic devices [98, 99], etc. The self assembled dipolar nanoparticles in base fluids are used in field induced heating [100], thermal transport [101, 102], magnetic fluid hyperthermia [103-105], magnetic resonance imaging [106], etc. Magnetic nanofluids are also used in various mechanical and microfluidic applications [107, 108]. **Fig. 1.8** summarizes the most important applications of magnetic nanofluids.

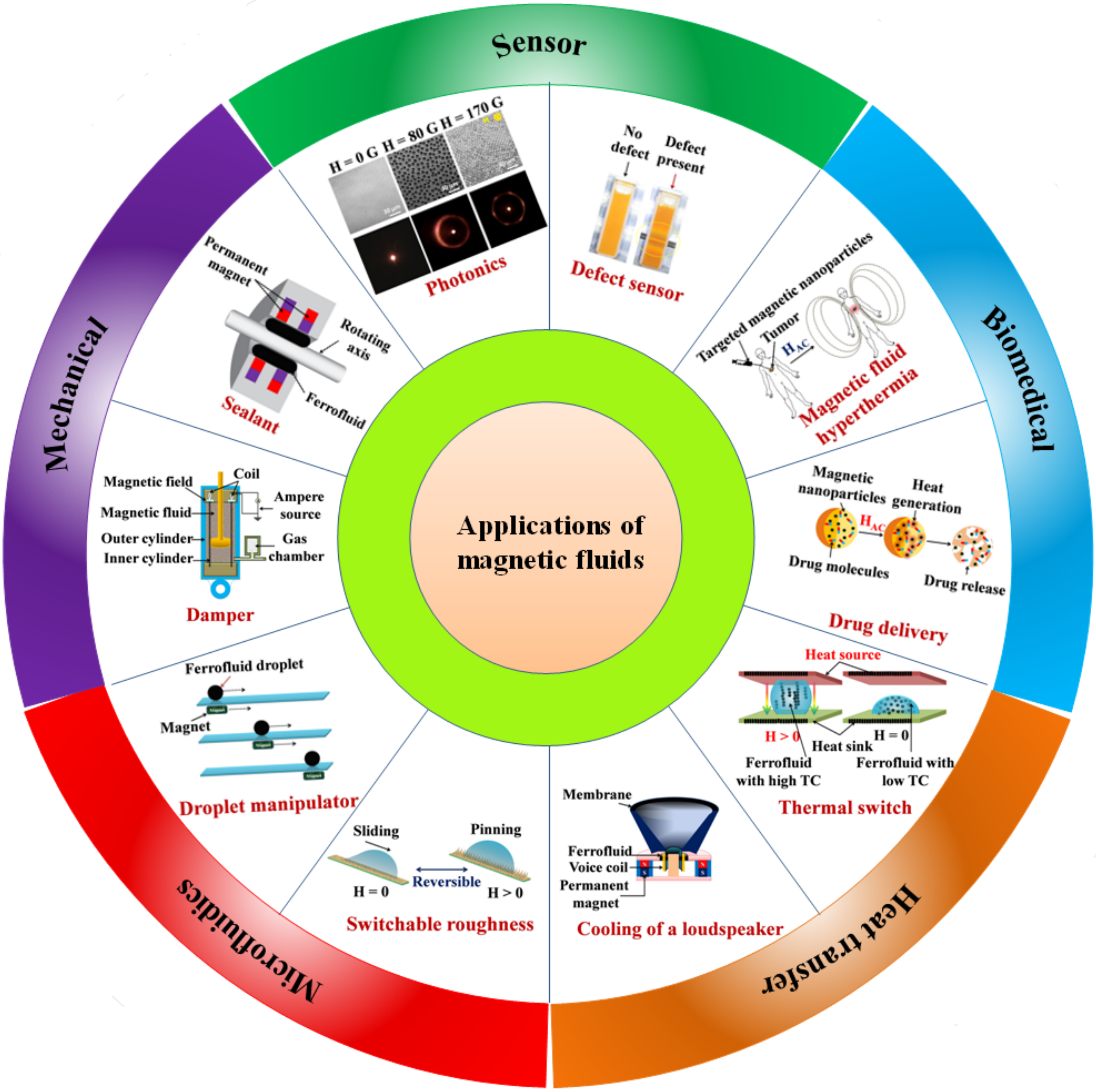

*Figure 1.8 Schematic representation of various applications of magnetic fluids.*

## 1.8. Probing internal structures in magnetic fluids

Various techniques have been used to understand the field induced structural transitions and their kinetic in magnetic fluids [76, 109-111]. Among these, light scattering techniques are widely used to investigate the aggregation kinetics of magnetic nanoparticles in magnetic fluid. Small angle neutron scattering [112-115], small angle X-ray scattering [116, 117], scattering dichroism [118], Raman spectroscopy [119], optical microscopy [120, 121], etc., have also been used to characterize the magnetic fluids.

Several robust theoretical and numerical formalisms have been developed to understand the inter-particle interaction under an external magnetic field in magnetic nanofluids under different conditions [122]. Followed by the pioneering numerical simulations work by Tao et al. [123, 124] on field induced structural transitions in electro-rheological (ER) fluids, several studies have been performed on structural formation in magnetic fluids using Brownian dynamics [125], Monte Carlo simulation [126-129], molecular and stochastic dynamic simulation [130-132], mutual dipole model based on thermodynamic theory [133] and computer model [111]. **Fig. 1.9** shows the various techniques used to probe the internal structures in magnetic fluids.

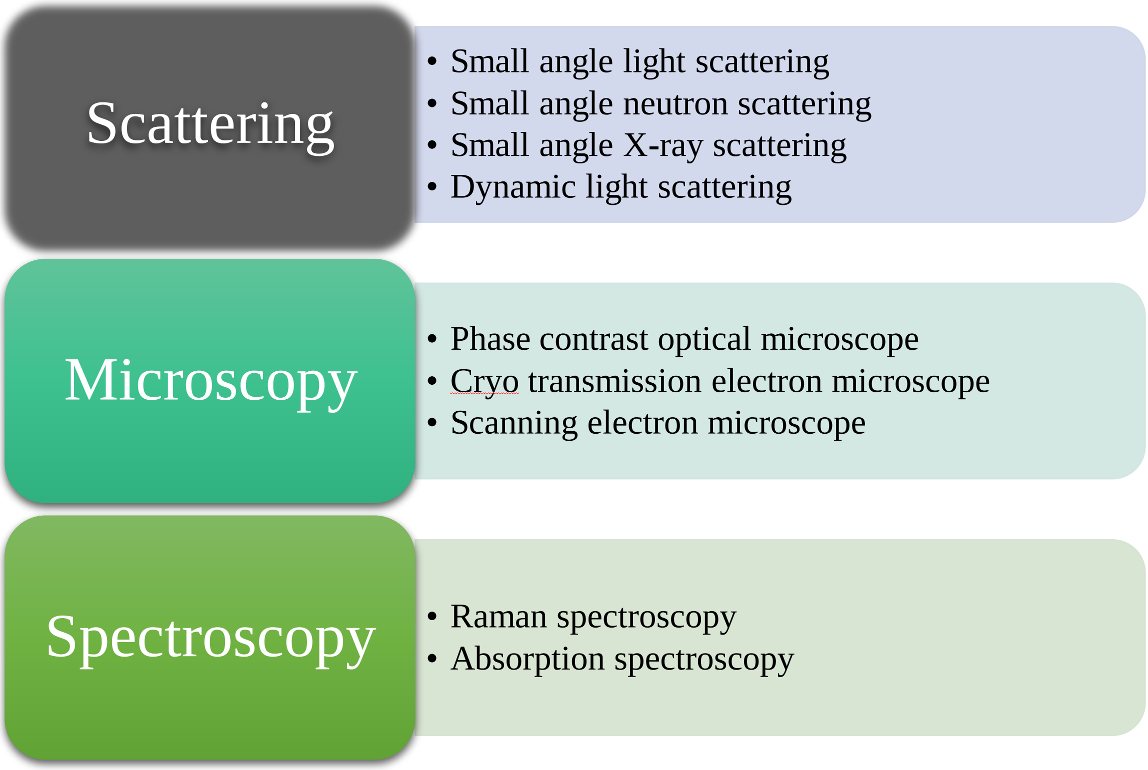

*Figure 1.9 Schematic representation of various techniques used to probe the internal structures in magnetic fluids.*

## 1.9. Light scattering studies in magnetic fluids

The field induced structural transitions in the ferrofluid, ferrofluid emulsion and mixed magnetically tunable soft systems have been studied using light scattering techniques [86, 109, 134-140]. The optical anisotropy caused by the magnetic field in magnetic fluids contributes to many exceptional magneto-optical properties such as magnetic birefringence, linear dichroism, Faraday rotation, Faraday ellipticity, circular dichroism, etc. [141-143]. Photonic Hall effect is also reported in magnetic nanofluid [144].

Light scattering was also used to assess aggregation kinetics of magnetic fluids [145]. From the variation of forward scattered light and the scattered pattern, aggregation times at various external fields were probed [86]. Also, by measuring the transmitted light intensity, the aggregation rate at various external magnetic fields was evaluated [146, 147]. Light scattering used to probe structural transitions in magnetic fluids under external magnetic fields [144, 148, 149]. The phenomena of scattering and diffraction of light in magnetic suspension and mixtures of magnetic and nonmagnetic scatterers were also investigated in the past [76, 150]. Details of some important studies along with key findings on magnetic field induced structures in water, oil based magnetic fluids and ferroemulsions using light scattering techniques are given in Table 1.1, 1.2 and 1.3, respectively**.**

*Table 1.1 Key findings of a few selected works on magnetic field induced structures in water-based ferrofluids using light scattering techniques.*

| **Particle/Base fluids** | **Size (nm)** | **Volume fraction (Φ )** | **Key findings** | **[Ref]** |
|---|---|---|---|---|
| $Fe_3O_4$/water | 11.9 | 0.002 | ✓ Particle size and the magnetic dipole moment were determined from the transmitted light intensity. | [151] |
| $Fe_3O_4$/water | 10 | 0.0309 | ✓ Optical dichroism in ferrofluid was studied.<br>✓ Found magnetic field induced anisotropic structures as the origin of the dichroic effect. | [152] |
| γ-$Fe_2O_3$/water | 3 - 30 | 0.0006 | ✓ Found birefringence is due to the magnetic field induced aggregation<br>✓ After switching off the magnetic field, the birefringence is reduced to zero with a characteristic time proportional to the solution's viscosity. | [153] |
| γ-$Fe_2O_3$, | 6- | 0.0006- | ✓ The optical birefringence measured as a | [109] |

| | | | | |
|---|---|---|---|---|
| $MnFe_2O_4$, $CoFe_2O_4$/water | 15.6 | 0.056 | function of temperature showed the presence of nematic-type order of magnetic particles in the absence of a magnetic field.<br>✓ Found anisotropic charge distribution in the ferrofluid grains was responsible for the nematic order.<br>✓ The measured optical anisotropy was explained in terms of shape anisotropy and the classical light depolarizing factors.<br>✓ Birefringence was proportional to the concentration of the magnetic particles. | |
| $Fe_2CoO_4$/water | 12 | 0.00025 | ✓ Photonic Hall Effect (PHE) as a function of concentration, magnetic field, and polarization of the incident light was studied.<br>✓ The PHE was due to the orientation of the particle's magnetic moments in the Faraday effect. | [144] |
| $\gamma$-$Fe_2O_3$ | 10 | 0.015 | ✓ Static magnetic birefringence (SMB) was studied.<br>✓ SMB was found to be proportional to the square of the applied magnetic field at low field limit and remained constant at high magnetic field limit. | [154] |
| $CdFe_2O_4$/water and $\gamma$-$Fe_2O_3$/water | 9.2 and 10.2 | 0.008 - 0.072 | ✓ Static magnetic birefringence was studied.<br>✓ Transmissivity and birefringence of the $CdFe_2O_4$ based sample was several times greater than $\gamma$-$Fe_2O_3$ based sample. | [134] |
| $Fe_3O_4$/water | 13 | 0.001 – 0.003 | ✓ Light transmission through a thin ferrofluid film modulated by an applied magnetic field is studied.<br>✓ The behavior of transmission coefficient was dependent on the particle chains forming, lengthening, moving, and breaking in the ferrofluid film. | [155] |
| $Fe_3O_4$/water | 6 | 0.01 | ✓ Time and magnetic field dependent optical anisotropy was studied for two orthogonal He-Ne laser beams propagating through ferrofluid.<br>✓ Forward scattering light showed a non-monotonic time dependence, dropping off sharply to virtually zero intensity at short times then increased to values that strongly field dependent at long times.<br>✓ The characteristic time to zero forward scattering was found to vary inversely with the applied magnetic field strength. | [86] |
| $Fe_3O_4$/water | 11.5 | 0.012 | ✓ Magneto-optical extinction was investigated.<br>✓ Rayleigh to Mie transition was observed in the presence of a magnetic field. | [156] |

| | | | | |
|---|---|---|---|---|
| $Fe_3O_4$/water | 8.42 | 0.0017 – 0.0152 | ✓ Transmitted intensity decreased to a minimum value at a certain magnetic field related to the onset of columns of chains formed from isolated particle chains.<br>✓ The critical magnetic field decreased with increase in particle concentration and the sample's aging time. | [135] |
| $Fe_3O_4$/water | 10 | 0.0075-0.03 | ✓ The effect of field strength, particle concentration, and wavelength of incident light on birefringence was studied.<br>✓ Found magnetic field induced aggregation was the origin of the birefringence. | [157] |
| $Fe_3O_4$/water | 15 | 0.002 | ✓ Time dependent dynamic behavior of diffraction pattern in the presence of a magnetic field was investigated.<br>✓ When the magnetic field was parallel to the light propagation direction, the size of the diffraction ring varied with time due to the variation of lattice like structures. | [158] |
| $Fe_3O_4$/water | 15 | 0.001-0.005 | ✓ Time- and wavelength-dependent light scattering under an external magnetic field was probed.<br>✓ Characteristic inversion time was found to follow a power law with the wavelength of the incident light. | [159] |
| $Fe_3O_4$/water | 15 | 0.00816 | ✓ Continuous evolution of backscattered speckle pattern as a function of magnetic field was studied.<br>✓ The speckle contrast was found to increase linearly with the external magnetic field due to the evolution from highly dynamic to static scatterers in the dispersion.<br>✓ Backscattered light intensity completely reversed after switching off the magnetic field. | [99] |
| $Fe_3O_4$/water | 15-46 | 0.00916 | ✓ Effect of hydrodynamic size on field induced transmission was investigated.<br>✓ Critical magnetic fields followed a power law decay with the applied magnetic field with increasing hydrodynamic size. | [160] |
| $Fe_3O_4$/water | 10 | 0.0079 | ✓ Laser self induced birefringence of magnetic fluid was investigated and a linear increase in birefringence with the laser power was observed. | [161] |

*Table 1.2 Key findings of a few selected works on magnetic field induced structures in oil-based ferrofluids using light scattering techniques.*

| **Particle/Base fluids** | **Size (nm)** | **Volume fraction (Φ)** | **Key findings** | **[Ref]** |
|---|---|---|---|---|
| $Fe_3O_4$/Decalin | 7.5 | 0.0014 | ✓ Magneto-optical birefringence was studied.<br>✓ Birefringence was found to be proportional to the square of the applied magnetic field at low fields. | [162] |
| $Fe_3O_4$/Kerosene | 9 | 0.06 | ✓ Time dependent transmission was observed.<br>✓ The transmitted light intensity increased with the power of the incident light.<br>✓ The peak of transmitted power decreased with an increase in the magnetic field. | [163] |
| $Fe_3O_4$/hydrocarbon fluid | 9 | 0.12 | ✓ Field strength and time dependent linear dichroism was studied in ferrofluid film.<br>✓ Dichroism observed at low field indicated the presence of small, ‘primary’ linear aggregates.<br>✓ Rapid disappearance of the diffraction pattern upon removal of the field was observed. | [164] |
| $Fe_3O_4$/hexane | 10 | 0.0046 | ✓ Dynamic thermally induced diffraction patterns coupled with the effect of gravity and an external magnetic field were investigated.<br>✓ The observation of diffraction patterns in zero fields was correlated to the thermally lensing effect. | [150] |
| $Fe_3O_4$/Kerosene | 6.7 | 0.0016-0.0276 | ✓ Magnetic field induced extinction of light was observed.<br>✓ Transmitted light intensity extinct at a certain magnetic field, which followed a power law decay with the volume fraction.<br>✓ Light transmission was reversible. | [165] |
| $Fe_3O_4$/Octane | 6.5 | 0.00649 | ✓ Several critical fields were observed based on the variation of transmitted light intensity.<br>✓ Critical fields observed at a regular interval of 20 G.<br>✓ The observed critical fields were attributed to the zippering transitions of the chains. | [68] |
| $Fe_3O_4$/Kerosene | 6.5 | 0.00649 | ✓ Influence of field ramp rate on the kinetics of field induced chain like structure was investigated.<br>✓ The variation of transmitted light intensity at different ramp rate was explained based on initial aggregation time. | [138] |

| | | | | |
|---|---|---|---|---|
| | | | ✓ Disappearance of the ring like pattern and the reappearance of the original spot, upon removal of the magnetic field, confirmed the perfect reversibility of the linear aggregates. | |
| $Fe_3O_4$/kerosene | 6.5 | 0.00155 | ✓ Influence of temperature and incident wavelength on magnetic field induced light transmission was investigated.<br>✓ The rate of extinction of normalized transmitted light intensity decreased linearly with increasing sample temperature. | [166] |
| $Fe_3O_4$/Kerosene | 6.7 | 0.01713 | ✓ Path length dependent magnetic field induced scattering pattern was investigated.<br>✓ A single corona like light scattered ring was observed for the longer path length (1 mm) and a concentric diffraction ring pattern was observed for a shorter path length (80 μm).<br>✓ 2D hexagonal to 3D hexagonal structure is seen when 10 μm < path length < 80 μm. | [167] |
| $Fe_3O_4$/hydrocarbon carrier fluid | 10 | 0.0106 | ✓ Faraday rotation in the terahertz regime (0.2 - 0.9 THz) at room temperature was reported. | [168] |

*Table 1.3 Key findings of a few selected works on magnetic field induced structures in ferrofluid emulsion using light scattering techniques.*

| **Particle/Base fluids** | **Size (nm)** | **Volume fraction, (Φ)** | **Key findings** | **[Ref]** |
|---|---|---|---|---|
| Ferrofluid emulsion | 500 | 0.0004 | ✓ The field induced structures in a monodisperse ferrofluid emulsion were studied.<br>✓ The equilibrium structure consists of equally sized and locally ordered columns of magnetic droplets.<br>✓ Column spacing ($\rho$) followed a power law rise with the cell thickness (i.e., $\rho = 1.33L^{0.37}$) in the range of 3 ≤ thickness ≤ 800 μm). | [76] |
| Ferrofluid emulsion | 466 | 0.00007 | ✓ The structure formation and dynamics of dilute, monodisperse ferrofluid emulsion under an external magnetic field were investigated.<br>✓ Field induced chain formation was observed for $\Lambda > 1$, and was found to be a diffusion limited process. | [169] |
| Ferrofluid emulsion | 200 | 0.003-0.1 | ✓ Magnetic field induced structural transitions were observed.<br>✓ Gas to solid transitions observed with the increase of the magnetic field. | [66] |

| | | | | |
|---|---|---|---|---|
| | | | ✓ Three structural transitions were found. | |
| Ferrofluid emulsion | 220 | 0.0033 | ✓ Fano-like resonance was observed in presence of magnetic field.<br>✓ By varying the magnetic field, the Fano profile and the transmittance were turned. | [170] |
| Ferrofluid emulsion | 220 | 0.0014-0.0067 | ✓ Magnetic field dependent near infrared photon absorption was studied.<br>✓ The absorption was found to depend on the volume fraction and applied magnetic field. | [171] |

## 1.10. Motivation

When the size of particles or droplets of soft matter is in the nano range ($d$ < 10 nm), due to limited experimental tools available, probing structural transitions and their kinetics in-situ under an external magnetic field is very challenging. Magnetically tunable soft matter is an excellent model system to study scattering phenomenon in various regimes because the size of the scatterers can be tuned from the Rayleigh regime ($d << \lambda$) to the Mie regime ($d \sim \lambda$) and eventually to the geometric regime ($d >> \lambda$) by simply varying the strength of the external magnetic field. Magnetically tunable soft matter is also ideal system for studying electromagnetic wave scattering and propagation through ordered, weakly ordered media and order-disorder transition, which has been a topic of interest for quite a long time.

Though field induced aggregation is rich with theoretical and simulation data, systematic experimental studies on equilibrium and non-equilibrium structures in real magnetic fluids are scarce. Insights into such field induced structures and order-disorder transitions in magnetic fluids are very important for developing practical applications. The purpose of this work were to understand the parameters influencing the field driven structures in magnetic fluids (both material and magnetic field), its temporal evolution and dynamics. The fluidic parameters considered are the volume fraction, size polydispersity, and the surfactant concentration, while the magnetic field parameters examined are field ramp rate, field strength, field orientation, and switching conditions.

## 1.11. Objectives

The objectives of the thesis are the following:

- ✓ To investigate the surface charge screening on critical magnetic field associated with field induced structural formation in a charged magnetic nanoemulsion.
- ✓ To study the temporal evolution of equilibrium and non-equilibrium magnetic field driven microstructures in a magnetic nanoemulsion.
- ✓ To study the magnetic field induced transparency and the magneto-optical birefringence in magnetic nanoemulsion.
- ✓ To study the effect of size polydispersity on magnetic field induced equilibrium and non-equilibrium structures in ferrofluids.

## 1.12. Overview of thesis

The thesis consists of seven chapters. **Chapter 1** gives a brief introduction to soft matter, smart colloids, ferrofluids, ferrofluid emulsion, stabilization mechanisms, magnetic interactions between particles in different environments, magnetic field induced aggregation and the factors affecting magnetic field tunable physical properties of magnetic fluids. A detailed literature survey on field induced structural transitions studies in magnetic fluid and magnetic nanoemulsion by various techniques, motivation and objectives of the present work, are also provided here.

**Chapter 2** briefly discusses the details of various samples used for the experimental studies. The details of characterization techniques such as powder X-ray diffraction, small angle X-ray scattering, dynamic light scattering, vibrating sample magnetometer, thermogravimetric analysis, and phase contrast optical microscope are provided. Details of light scattering setup for probing the structural transition in magnetic fluids (ferrofluids and ferrofluid emulsion) using transmitted light intensity and scattered pattern are also discussed.

**Chapter 3** describes the field assisted structural transitions in magnetic nanoemulsion of average droplet size of 200 nm containing superparamagnetic iron oxide nanoparticles of diameter ~ 10 nm. The role of surface charge screening on critical magnetic fields for various structural transitions in magnetic nanoemulsion of different volume fractions is studied. Three distinct critical magnetic fields are identified, which correspond to the commencement of small aggregate formation, complete formation of linear aggregates before the commencement of lateral coalescence of individual chains, and the formation of densely packed columnar solid-like structures through zippering of individual chains. During the structural transitions, the transmitted light spot is transformed into a ring, with distinct speckle characteristics, due to scattering from self-assembled linear aggregates. The speckle pattern was fully reversible, and the aggregation rate was found to increase linearly with increasing surfactant concentration.

**Chapter 4** presents the temporal evolution of magnetic field driven microstructures in a magnetic nanoemulsion under different experimental conditions such as volume fraction, surfactant concentration, magnetic field strength, and ramp rate. For low volume fractions and applied magnetic fields, transmitted light intensity showed a rapid decrease, followed by an increase with elapsed time, while at high field strengths transmitted light intensity was low and time independent. The critical magnetic field followed a power law decay with the volume fraction. The phase contrast microscopy results show very fast lateral movement of well separated chains and interconnected frozen disordered non-equilibrium structures at low and high magnetic fields, respectively. When the average distance among chains is greater than the escape distance, a fewer chains coalesce to form individual chains. At high field strength, more chains and complex patterns are formed within the escape distance, while at low field strengths, the average inter-chain spacing increased with time and followed a power law scaling with time.

**Chapter 5** provides magnetic field induced optical transparency and its origin in magnetic nanoemulsion. Beyond a certain volume fraction ($\Phi > 0.0021$) of magnetic nanoemulsion and a critical magnetic field ($H_{c1}$), the transmitted light intensity increases drastically and reaches a maximum at another critical magnetic field ($H_{c2}$), beyond which the transmitted light intensity decreases and reaches a plateau. The transmitted light intensity at $H_{c2}$ is found to increase linearly with $\Phi$ and the critical magnetic fields ($H_{c1}$ and $H_{c2}$) follow a power law decay with volume fraction. The light intensity recovers to its initial value when the magnetic field is switched off, indicating a perfect reversibility of the field induced transparency process. The observed straight line scattered patterns above $H_{c2}$, on a screen placed perpendicular to the incident beam, confirms the formation of rod like anisotropic nanostructures perpendicular to the direction of light propagation. The magneto-optical measurements in the emulsion confirm that the observed field induced transparency in magnetic emulsions ($\Phi > 0.0021$) is due to optical birefringence caused by rod like nanostructures.

**Chapter 6** presents the effect of particle polydispersity on field induce aggregation and structural transitions in ferrofluids. Three different ferrofluids, containing oleic acid capped superparamagnetic nanoparticles of different polydispersity indices (PDI), namely M1 (PDI = 0.22), M2 (PDI = 0.23) and, M3 (PDI = 0.79), are used in the present study. Ferrofluid confined between two glass plates showed no field induced aggregates in a ferrofluid with a PDI of 0.22, up to a magnetic field strength of 550 G. In the sample with PDI ~ 0.79, single chains, thick chains and sheets are formed on increasing in-plane magnetic field from 0 to 550 G, whereas isotropic bubbles, hexagonal and lamellar/stripe structures are formed on increasing the magnetic field in out-of-plane. In M3, bubbles were formed at a very low magnetic field strength of 30 G with an average inter-column spacing of 3 μm, which is found to decrease with magnetic field and hexagonal close packed columnar structures were formed with an inter-column spacing of 0.6 μm at H = 170 G. The average inter-column spacing is found to vary inversely with the external magnetic field up to a field strength of 170 G, beyond which the columns coalesce and form a stripe patterns. At very high magnetic field strength, the undulation due to long range magnetic coupling interaction between stripes caused a zig-zag pattern. The isotropic to hexagonal columnar to lamellar/stripe patterns observed in sample M3, indicate the prominent role of larger sized particles and the applied magnetic field strength in structural transitions in ferrofluids. The inter-column spacing decreases with the volume fraction of large particles ($\Phi_L$) and follows a power law dependence, and the magnetic field required to form hexagonal and stripe like patterns is found to decrease with PDI and $\Phi_L$. The observed transmitted light intensity from random particles, chains/columns, hexagonal closed pack and stripe like structures were single bright spot, circular pattern, circular ring with six bright spots and straight line, respectively, which further confirm the microscopic results. Based on the observed microstructures, a phase diagram is constructed with volume fraction of larger particle and the applied magnetic field strength.

**Chapter 7** summarizes the overall results, conclusions, and the scope for future work.

## *Chapter 2*

## Materials and methods

### 2.1. Materials

The chemicals used, ferric chloride hexahydrate ($FeCl_3.6H_2O$), ferrous chloride tetrahydrate ($FeCl_2.4H_2O$), 25% ammonium hydroxide, 35% hydrochloric acid, oleic acid, acetone, and hexane, were purchased from E-Merck and GR grade with 99% purity. The anionic surfactant, sodium dodecyl sulfate ($C_{12}H_{25}SO_4Na$), was obtained from Sigma Aldrich. All reagents were used as received without further purification. MilliQ water of resistivity 15 MΩcm was used to make solutions throughout the experiments.

### 2.2. Synthesis of ferrofluid

The magnetite nanoparticles were synthesized by co-precipitation method using freshly prepared iron salts, 0.2 M $FeCl_2.4H_2O$ and 0.4 M $FeCl_3.6H_2O$, mixed in 1:1 ratio at a constant stirring (i.e., 1000 rpm) [38, 172, 173]. The mixture was heated in a water bath until it reached a temperature of 60 ºC. The pH of the solution was increased rapidly to 10.5 by adding 25% aqueous ammonia. After the solution turned black, indicates the formation of magnetic nanoparticles, 20 mL of oleic acid was added. The pH and the temperature of the solution were adjusted to 9.5 and 70 ºC, respectively. At the same pH, temperature, and stirring speed, the solution was kept for 30 minutes to ensure surfactant binding on the nanoparticle surface. The temperature was increased to 79 ºC to remove the excess ammonia and the protonation of adsorbed and unabsorbed ammonium oleate as oleic acid. The surfactant coated particles were washed with triply distilled water at 60 ºC until the pH became 7 and removed the ionic impurities and later dispersed in water. The hexane dispersion was treated with acetone to induce aggregation of particles. The resulting mixture was centrifuged at 2500 rpm for about 30 minutes to separate aggregated particles from the dispersion. The precipitate magnetite nanoparticles were again dispersed in hexane for further treatment. The hexane, acetone mixture washing procedure was repeated a few times. The oleic acid coated $Fe_3O_4$ nanoparticles were dried at 35 $^oC$ for 48 hours in an inert atmosphere and the dried particles were dispersed in kerosene. **Fig. 2.1** shows the schematic of ferrofluid sample.

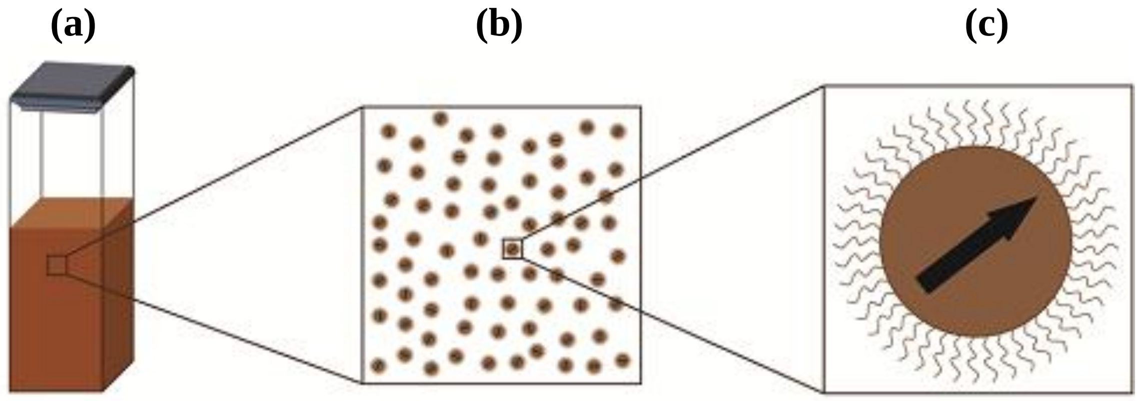

*Figure 2.1 Schematic representation of ferrofluid: (a) On a macroscopic length scale, ferrofluid resembles an ordinary liquid with a zero net magnetization, (b) On a colloidal length scale, solid nanoparticles dispersed in a liquid, (c) Each particle consists of a single domain magnetic core, e.g., iron oxide, and a surface grafted with surfactant or polymer chains. Typically particle size ~ 10 nm.*

## 2.3. Preparation of magnetic nanoemulsion

The magnetic nanoemulsion was prepared by shearing non-aqueous ferrofluid (octane containing oleic acid capped $Fe_3O_4$ nanoparticles) with surfactant (SDS) solution at ~ 1500 rpm, using IKA homogenizer [174-176], results in the formation of a highly polydisperse coarse emulsion (where droplet size varies between 0.05 and 1 μm). Monodispersed emulsion of narrow size distribution is obtained from coarse emulsion using fractionation technique, where excess surfactant solution is added into the continuous medium to induce an attractive interaction between droplets (depletion flocculation) and to phase separation between a dilute phase with smaller droplets and a dense phase with larger droplet size [7]. The dilute phase is removed and the dense phase is diluted with surfactant solution further. By repeating this process, a highly monodisperse ferrofluid emulsion was obtained.

The aqueous ferrofluid emulsion droplets were stabilized using an anionic surfactant: SDS. In aqueous solutions, SDS is dissociated with a negatively charged $DS^-$ head group, which is hydrophilic in nature. At the emulsion interface, the hydrophobic alkyl chain buried deep into the oil droplet and the $DS^-$ is exposed to water. The dissociated $Na^+$ (counter-ion) and $DS^-$ (surfactant head group) at the interface form an electrical double layer and provide electrostatic stabilization. **Fig. 2.2** shows the schematic of the magnetic nanoemulsion sample.

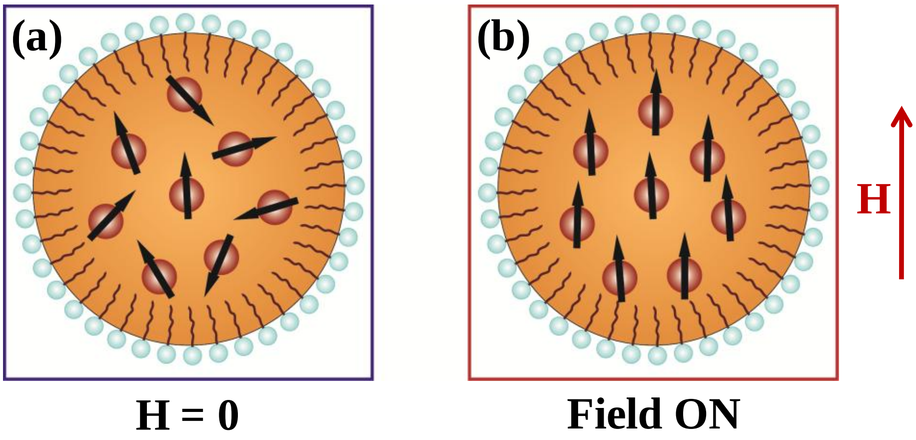

*Figure 2.2 Schematic representation of magnetic nanoemulsion. Each droplet contains single domain iron oxide nanoparticles of size ~10 nm. (a) The magnetic moment of each nanoparticles are randomly oriented in the absence of magnetic field. (b) In the presence of magnetic field, the magnetic moment of magnetic nanoparticles align in the direction of the magnetic field.*

## 2.4. Characterization techniques

### 2.4.1. Powder X-ray diffraction

Powder X-ray diffraction is the most widely used diffraction method to determine the structure of crystalline solids as the wavelength of the radiation is on the same scale as the atom spacing in a crystal [177]. X-ray diffraction is based on constructive interference of monochromatic X-rays scattered from the crystalline plane. The interaction of the incident rays with the crystalline plane produces constructive interference when diffraction conditions satisfy Bragg’s law:

$$2d_{hkl}sin\theta = n_r\lambda_{X-ray} \tag{2.1}$$

where, $n_r$ is an order of Bragg reflection, $\lambda_{X-ray}$ is the wavelength of X-ray, $d_{hkl}$ is the interplanar spacing of the crystal, and $\theta$ is the Bragg angle. In a typical XRD pattern, the diffracted intensities are plotted versus the detector angle $2\theta$. Each peak is then assigned a label indicating the spacing of a crystal plane. The average crystalline size is calculated using Debye-Scherrer equation,

$$d_{crystal} = \frac{K\lambda_{X-ray}}{\beta_{FWHM}cos\theta} \tag{2.2}$$

where $K$ is a constant (~ 0.9 for spherical particle), $\beta_{FWHM}$ is the full width at half maximum of the highest intensity peak measured in radians.

In the present study, powder XRD characterization was carried out using Rigaku Ultima IV X-ray diffractometer with Cu-K$_\alpha$ radiation, $\lambda_{X-ray}$ of 1.5418 Å and an applied voltage and current of 40 kV and 30 mA, respectively. The scanned $2\theta$ range was 20 – 80$^0$ with a step size of 0.02$^0$ and a scan rate of 2$^0$/minute, respectively. Data acquisition and preliminary analyses were performed using PDXL software and the obtained diffraction pattern was compared with the database of Joint Committee on Powder Diffraction Standards (JCPDS).

### 2.4.2. Small angle X-ray scattering

Small angle X-ray scattering (SAXS) is a characterization technique to study the size and shape of the inhomogeneities in the material at length scales much larger than the X-ray wavelength. Primary experimental requirements of SAXS are a well collimated X-ray beam with a small cross-sectional area and an extended sample-detector distance to reduce X-ray background. Typical length scales probed with SAXS are in the 1-100 nm range.

In SAXS, the scattered intensity can be written as [178]

$$I(q) = N_p S(\vec{q}) P(\vec{q}) \tag{2.3}$$

where, $N_p$ is the total number of particles, $S(\vec{q})$ is the structure factor which describes the interparticle interference, $P(\vec{q})$ is the particle form factor, and $q = (4\pi/\lambda_{X-ray})sin\theta$ is the wave vector. For a dilute solution, $S(\vec{q}) \sim 1$ (where there is no interaction between the particles), the total intensity is proportional to $P(\vec{q})$. For a spherical magnetic particle of radius $a$ the scattering intensity is given in the following equation [178]

$$I(q) = (\Delta\rho_e)^2 {V_p}^2 \left[3\frac{\sin(qa) - qa\cos(qa)}{(qa)^3}\right]^2 \tag{2.4}$$

where $\Delta\rho_e$ is the electron density difference between the solute and the solvent. From the decay of scattered intensity (*I(q)*) at small $q$, size of the particles is estimated and the region is called Guinier region. The *I(q)* at high $q$ limit is called Porod region, which gives the information about Fractal dimension. The distance distribution function is obtained by the Fourier transform of the scattering curve and is given in Eqn. (2.5) [179], which gives information about the shape of the particles.

$$p(r) = \frac{2}{\pi}\int_0^\infty I(q)qr\sin(qr)\exp(-B^* q^2)\,dq \tag{2.5}$$

where $B^*$ is the damping factor to remove the termination effect of the Fourier transform.

In the present study, the small angle X-ray scattering studies were carried out using a Rigaku Ultima IV instrument equipped with a Cu-$K_\alpha$ source and scintillation detector. SAXS measurements are performed in transmission geometry in the $2\theta$ range of 0-2.2$^0$ in steps of 0.01$^0$. Data analysis is performed using NANO-solver software.

### 2.4.3. Dynamic light scattering

Dynamic light scattering (DLS) is a non-invasive and non-destructive technique used for measuring hydrodynamic size of dispersed particles that are in the submicron range in dilute solution. This technique measures the time dependent fluctuations in the intensity of the scattered light at a constant angle that occurs because of the Brownian motion of particles [180, 181]. This time varied intensity is studied through autocorrelation function, which determines the translational diffusion coefficient of particles. The correlation function depends on the size of the nanoparticles, i.e., for smaller particles, the correlation function decays faster due to their rapid motion as compared to the larger sized particles (see **Fig. 2.3**).

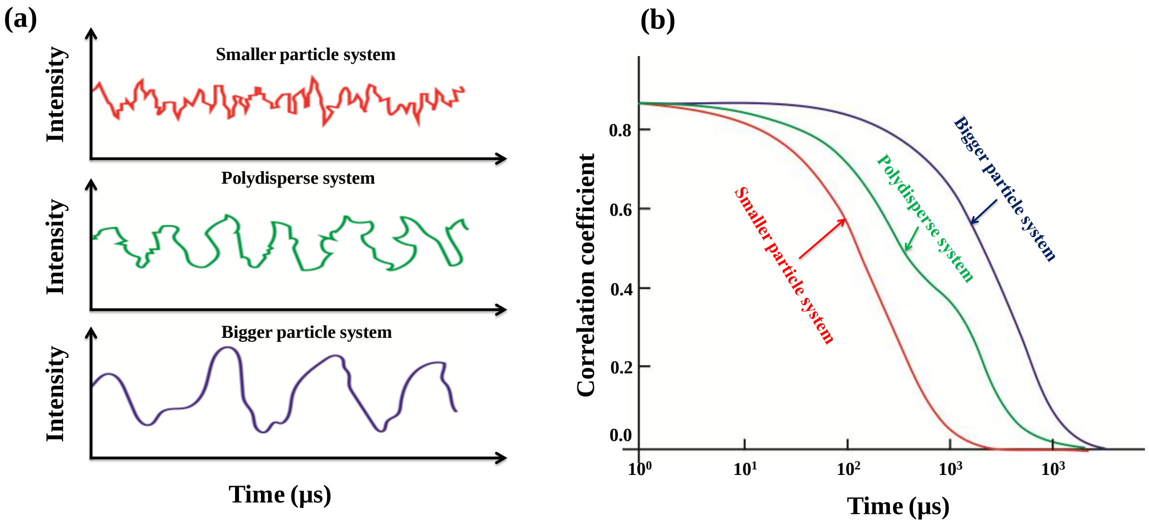

*Figure 2.3 (a) The scattered light intensity fluctuates faster for smaller particles than for larger particles. The resulting correlation coefficient therefore decays faster for smaller particles than for larger particles.*

The intensity autocorrelation function is given by

$$g^2(\tau) = \frac{\langle I(t)I(t+\tau)\rangle}{\langle I(t)\rangle^2} \tag{2.6}$$

where, $I(t)$ is the scattered intensity at an arbitrary time, $t$, and $I(t+\tau)$ is the scattered intensity after a delay time, $\tau$. The intensity autocorrelation function decays exponentially with time since the particles in the suspension are in Brownian motion. The intensity autocorrelation function, $g^2(\tau)$, is related to the electric field autocorrelation function, $g^1(\tau)$ by Siegert's relation, which is given by,

$$g^1(\tau) = [g^2(\tau) - 1]^{0.5} \tag{2.7}$$

For a suspension of monodisperse spherical particles, the autocorrelation function decays exponentially with delay time $\tau$ and is given as

$$g^1(\tau) = A_1 . e^{-Dq^2\tau} + B \tag{2.8}$$

where $A_1$ is the amplitude of the correlation function, $B$ is the baseline, $D$ is the translational diffusion coefficient. The electric field autocorrelation function is fitted with the Eqn. (2.8) to obtain the translational diffusion coefficient. The hydrodynamic size of the droplet was obtained from translational diffusion coefficient using Stokes-Einstein equation,

$$D = \frac{k_B T}{6\pi\eta R_h} \tag{2.9}$$

where $R_h$ is the hydrodynamic radius of the dispersed particle. In the present study, hydrodynamic size is measured using Zetasizer Nano ZS (Malvern Instrument, UK). The experiments were performed in the backscattering geometry ($173^0$) at an ambient temperature of 25 °C for measuring hydrodynamic size.

### 2.4.4. Zeta potential measurement

The development of a net charge at the particle surface affects the distribution of ions, resulting in an increased concentration of counter ions close to the surface. There are two parts of the liquid layer covering the particle. First, the compact layer is also known as the Stern layer, which comprises counter ions tightly bound to the surface and the outer layer is called the diffuse layer, where they are attached less strongly. There is a notional boundary within the diffuse layer under which the ions and particles form a stable entity. This boundary is called the slipping plane; as a particle travels, ions within the boundary move with it, but any ions outside the boundary do not migrate with the particle. The potential at the slipping plane is known as the zeta potential. The zeta potential was obtained by using Henry's equation,

$$U_E = \frac{2\varepsilon\zeta f(\kappa a)}{3\eta} \tag{2.10}$$

where $\zeta$ is the zeta potential, $U_E$ is the electrophoretic mobility, $\varepsilon$ is the dielectric constant of the suspending medium, and $f(\kappa a)$ is Henry's function. $f(\kappa a) \approx 1.5$ by Smoluchowski approximation for particles larger than 0.2 µm dispersed in an electrolyte containing more than $10^{-3}$ M salt. For small particles in low dielectric constant media, $f(\kappa a)$ becomes 1 by Huckel approximation for non-aqueous measurements. Particles with a zeta potential of greater than ± 30 mV are considered to be a stable dispersion.

The electrophoretic mobility of the particle is measured using a combination of laser Doppler velocimetry and phase analysis light scattering (PALS), which allow one to get the zeta potential for particle with lower mobility with high precision. Zetasizer Nano ZS (Malvern Instrument, UK) is used for zeta potential measurement.

### 2.4.5. Vibrating sample magnetometer

Vibrating sample magnetometer (VSM) system is used to measure the magnetic properties of materials such as magnetic moment, blocking temperature, susceptibility, etc., as a function of the magnetic field, temperature, and time. VSM is based on Faraday's law of induction, which states that an electromagnetic force is generated in a coil when there is a change in flux through the coil [182]. The magnetic sample to be studied is placed between two electromagnetic pieces that produce a constant magnetic field, which allows the magnetic moments or spins of the sample to align in the direction of the magnetic field. Stationary pickup coils are mounted on the poles of the electromagnet. The sample oscillated sinusoidal (up and down) perpendicular to the magnetic field produced by the electromagnet induces a voltage in the coils proportional to the magnetic moment of the sample. In the present study, the magnetic properties of the magnetic sample were obtained using a cryogen-free VSM (M/s Cryogenics, U.K.) and the measurement was performed in the field range ± 2 T.

### 2.4.6. Thermogravimetric analysis

Thermogravimetric analysis (TGA) is a method of thermal analysis in which the amount and the rate of change in the mass of a sample are monitored over time as a function of temperature under a controlled atmospheric environment [183]. TGA gives information concerning the mass and composition of the stabilizers (based on their melting or evaporation temperature). TGA instrument consists of a sample pan supported by a precision balance and resides in a furnace. The furnace is programmed for a linear rise of temperature with time, which generates heat radially towards the center. In the present study, TGA of ferrofluids was carried out using Mettler-Toledo TGA-DSC-1, 1100 LF (Switzerland) under Argon atmosphere in the temperature range of 30 – 600 ℃ at a heating rate of 10 ℃/minute.

### 2.4.7. Phase contrast optical microscope

Phase contrast optical microscope uses contrast-enhancing optical technique to produce high contrast images of transparent specimens [184]. **Fig. 2.4** shows the schematic representation of phase contrast microscopy. Light from the white light source (i.e., halogen lamp) passes up through the condenser lens (located above the annular ring) and is then focused onto the specimen. Then undeviated and diffracted light was collected by the objective lens. The objective lens contains a phase plate in order to maximize differences in intensity (or contrast) between the specimen and the background in the image plane. Depending upon the different refractive indices, the object to be studied shows a different degree of contrast in the microscope.

In the present study, the microstructures of magnetic nanofluids at different magnetic field strengths were obtained using a Leica inverted phase contrast optical microscope equipped with a digital camera (ORCA-Flash4.0LT, Model - C11440-42U, Hamamatsu, Japan). The obtained images are processed using HCImageLive software. A stepper motor control stage (DPM, motor part number: DPM57SH51-1A.000) with two arms fixed with permanent magnets are brought closer at different speeds to attain the desired ramp rate and magnetic field strength. The variation in the magnetic field within the sample was ± 5%. However, the variation within the area of interest of microscope was less than 1%.

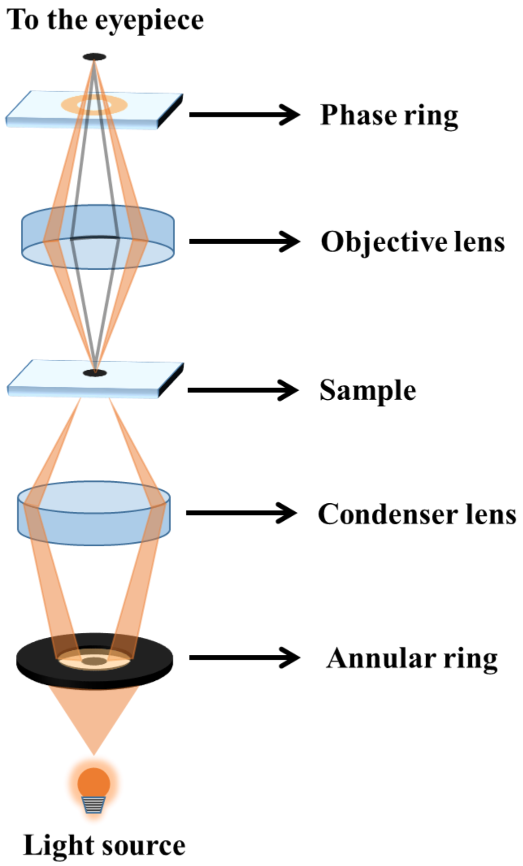

*Figure 2.4 Schematic representing phase contrast technique.*

## 2.5. Light scattering setup for probing structural transition in magnetic fluids (ferrofluids and ferrofluid emulsion) using transmitted light intensity

### 2.5.1. Light scattering experimental setup (parallel mode)

**Figure 2.5 (a)** show the schematic of the experimental setup used to probe the structural transition in the magnetic fluids using the transmitted light intensity as a function of magnetic field and time. The photograph of the experimental setup is shown in **Fig. 2.5 (b).**

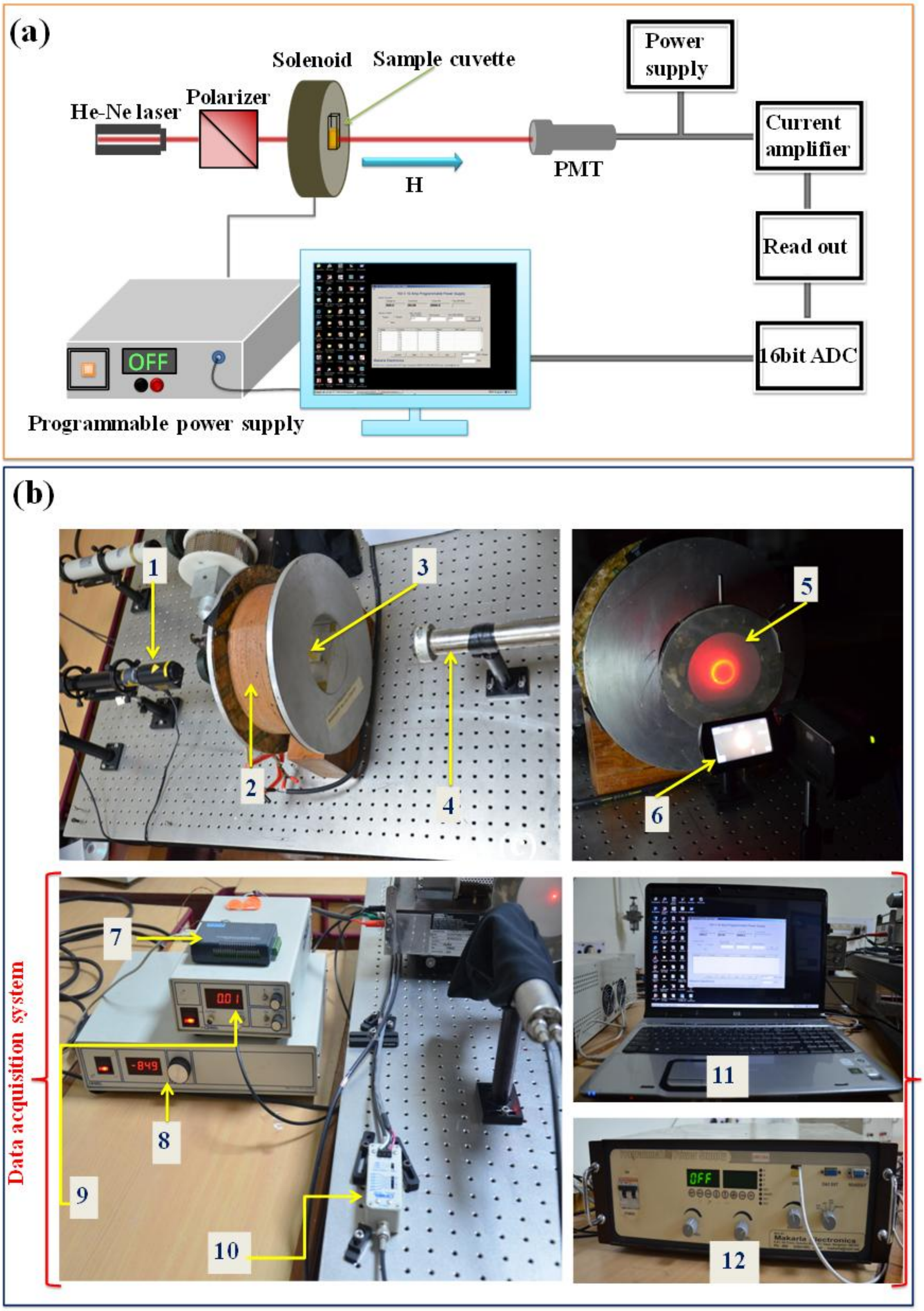

*Figure 2.5 (a) Schematic representation of the light scattering experimental setup. The applied magnetic field is parallel to the light propagation direction. (b) Photograph of the experimental setup; (1) He-Ne laser, (2) solenoid, (3) sample cuvette, (4) photomultiplier tube (PMT), (5) white screen, (6) CCD camera, (7) analog-digital converter (ADC), (8) PMT power supply, (9) PMT readout, (10) pre-amplifier, (11) software, (12) programmable power supply.*

The sample is taken in a quartz cuvette having optical path length of 1 mm. An amplitude and frequency stabilized He-Ne laser (Spectra-physics, USA, model- 117 A), with a wavelength of 632.8 nm and an output power 1 mW was used as a light source. The light beam first goes through a polarizer and then through the sample placed inside the solenoid. The magnetic field strength was controlled by changing the current using a programmable DC power supply (Makarla Electronics, Bangalore, India). The software offer to change the magnetic field in different ways, i.e., the magnetic field can be increased or decreased between two magnetic field strength with different ramp rates, different paths, etc., and also magnetic field can keep constant as a function of time. The direction of the applied magnetic field was parallel to the light propagation direction. The variation in the magnetic field within the sample was 5% and the variation within the laser spot diameter was less than 1%.

The forward transmitted light intensity was measured by using a photomultiplier tube (PMT) (Oriel Newport, model-77265). A power supply (model: 70705, Oriel instruments) supplies highly regulated voltage to the PMT. This power supply has LED displays and two high voltage BNC outputs for the photomultiplier tube (voltage range: -200 to 2000 Volts). The output of PMT was fed to a readout (model: 70701, Oriel instruments) through a current amplifier (model: 70710, Oriel instruments) with variable gain. The 70701 readout has a 3 $^{1}/_{2}$ digit LED display for calibrated output signal. There were two types of input/output connectors. The input voltage can be varied from ± 0.1 to 10 times and offset from 0 to 100%. The 70710 current amplifier is designed for use with current source as photomultiplier tube and was a low noise current-to-voltage amplifier. It converts the low current output from PMT to a voltage signal for the 70701 readout. It has six switchable amplifier selections: $10^4$, $10^5$, $10^6$, $10^7$, $10^8$, and $10^9$ volts per ampere. The analog output from the readout was connected to a 16 bit analog to digital converter

(ADC, 200 kS/s, 16 bit, 16-ch Multifunction USB Module, model: 4716, Advantech) that was interfaced with a computer through a USB port. The transmitted intensity data were acquired and saved by the software with which the ramp rate of external magnetic field was also changed using the programmable power supply. For recording transmitted intensity patterns, the light scattered from the sample was projected on a screen and were recorded using a charge coupled device (CCD) camera (digital video camera recorder, DCR SR 45 E, Sony Corporation, Japan).

### 2.5.2. Light scattering experimental setup (perpendicular mode)

**Figure 2.6 (a)** show the schematic of the experimental setup where magnetic field was applied perpendicular to the light propagation direction to probe the optical anisotropy (birefringence) in magnetic fluids by measuring the transmitted light intensity as a function of magnetic field and time. The axes of the polarizer and analyzer were set perpendicular to each other for the birefringence measurement. The photograph of the experimental setup is shown in **Fig. 2.6 (b)**.

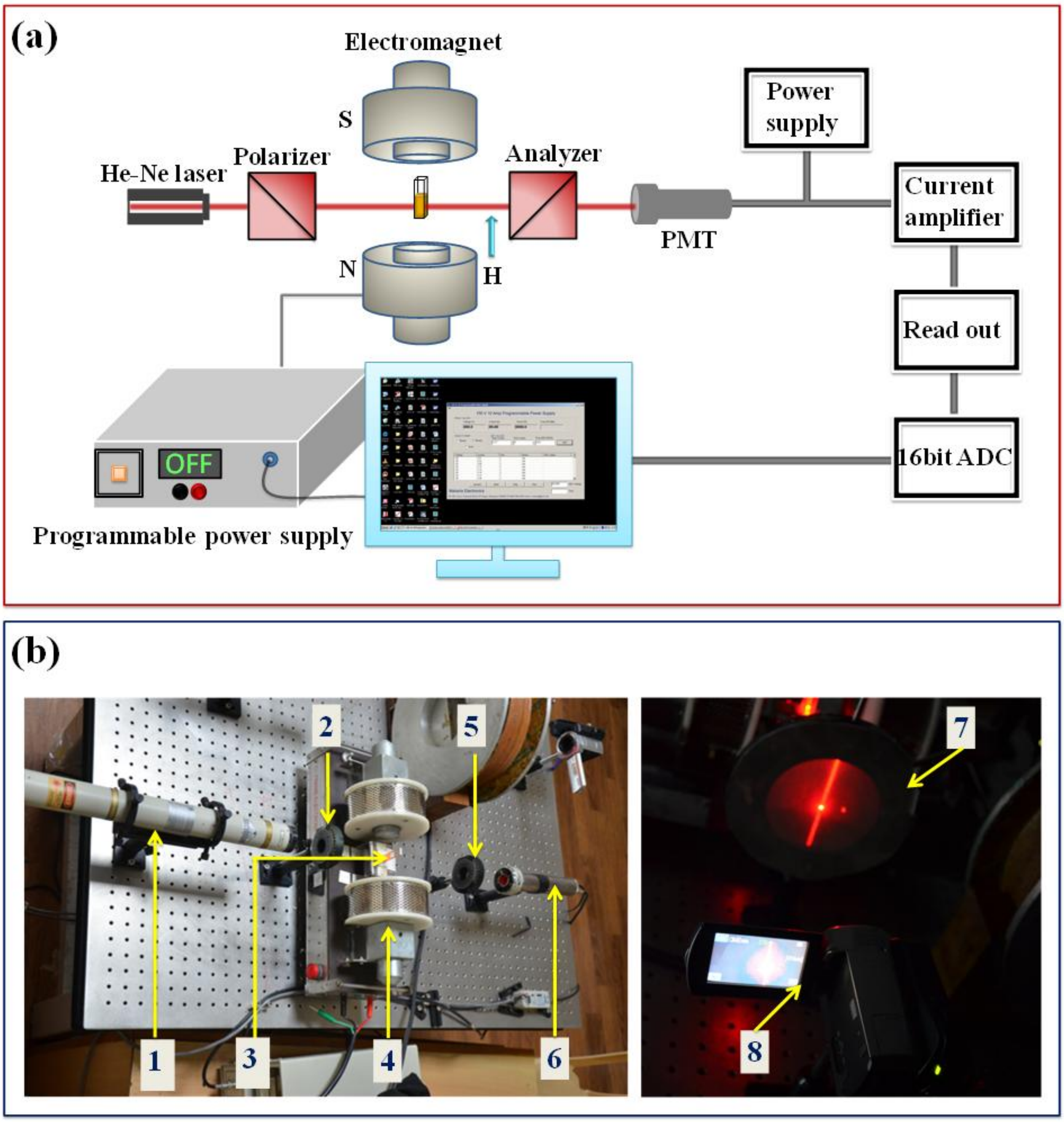

*Figure 2.6 (a) Schematic representation of the light scattering experimental setup for measuring optical anisotropy in magnetic fluid. (b) Photograph of the experimental setup; (1) He-Ne laser, (2) polarizer, (3) sample cuvette, (4) electromagnet, (5) analyzer, (6) photomultiplier tube, (7) white screen, (8) CCD camera. Data acquisition system used was the same as shown in Fig. 2.4 (b)*

## 2.6. Ferrofluids used and their properties

Three different ferrofluids are used in our study, which contains oleic acid capped magnetic nanoparticles ($Fe_3O_4$) of the same volume fraction ($\Phi = 0.037$). In all cases, the particles are dispersed in kerosene. These samples are indicated as M1, M2, and M3, respectively. **Table 2.1** shows the compiled results of the physical properties of the three samples obtained from XRD, DLS, VSM, and TGA.

*Table 2.1 Sample code, crystallite size, hydrodynamic size, polydispersity index, magnetization, and surfactant loss in samples M1, M2, and M3.*

| Sample name | Crystallite size [nm] | Hydrodynamic size [nm] | Polydispersity index | Magnetization [emu/g] | Surfactant weight loss [%] | Estimated surfactant wt% required for a monolayer |
|---|---|---|---|---|---|---|
| M1 | 9.6 ± 0.7 | 10 ± 0.6 | 0.22 | 69 ± 0.6 | 24 | 19 |
| M2 | 8.3 ± 0.8 | 11.7 ± 0.9 | 0.23 | 66 ± 0.7 | 21 | 21.4 |
| M3 | 10.5 ± 1 | 20.9 ± 1 | 0.79 | 71 ± 0.7 | 19 | 17.7 |

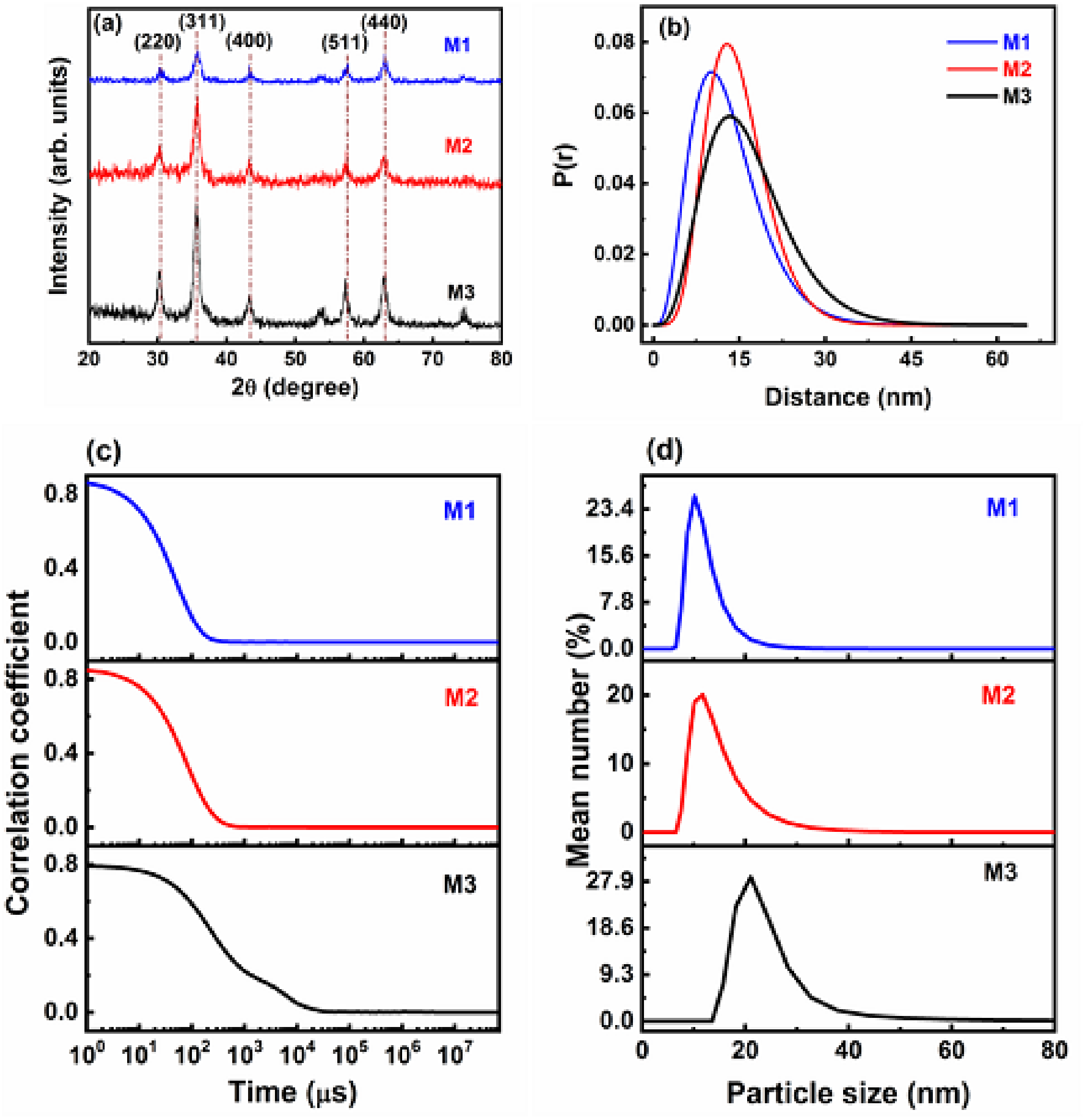

*Figure 2.7 (a) X-ray diffraction pattern, (b) distance distribution function, (c) correlation coefficient as a function of time of scattered light obtained from dynamic light scattering, and (d) hydrodynamic size distribution of M1, M2, and M3.*

**Figure 2.7 (a)** shows the XRD pattern of oleic acid coated iron oxide nanoparticles. The Bragg's diffraction peaks corresponding to (220), (311), (400), (511), and (440) planes of $Fe_3O_4$ (JCPDS file no. 19-0629) are observed. $Fe_3O_4$ has an inverse spinel structure where tetrahedral sites are occupied by $Fe^{3+}$ ions, whereas octahedral sites are shared between $Fe^{3+}$ and $Fe^{2+}$ ions. From the highest peak, corresponding to (311) plane, the average crystallite size was calculated using Debye-Scherrer equation (**Eqn.**

**2.2**) and the estimated values are found to be 9.6 ± 0.7, 8.3 ± 0.8, and 10.5 ± 1 nm for M1, M2, and M3, respectively. **Fig. 2.7 (b)** shows the distance distribution function obtained from small angle X-ray scattering. The most probable size was found to be 10.2 ± 1, 12.8 ± 1, and 13.4 ± 1 nm for M1, M2, and M3, respectively, which shows slightly bigger in size than the size obtained from XRD values due to the presence of a dead layer of oleic acid on the surface of the nanoparticle. The correlogram of M1, M2, and M3, as a function of time, were obtained from the DLS technique, are shown in **Fig. 2.7 (c)**. The correlation coefficient of M1 decaying faster than M2 and M3 indicates the presence of a larger number of smaller particles than M2 and M3. In M3, the decay follows various steps, indicating the presence of larger sized particles or larger aggregates. **Fig. 2.7 (d)** shows the number distribution curve of M1, M2, and M3. The average hydrodynamic size of M1, M2, and M3 were found to be 10 ± 0.6, 11.7 ± 0.9, and 20.9 ± 1 nm, respectively. The polydispersity index ($PDI = \frac{s^2}{{z_D}^2}$ , where $s$ is the standard deviation and $z_D$ is the mean average size) values were found to be 0.22, 0.23, and 0.79 for M1, M2, and M3, respectively. The polydispersity of M3 was high due to the presence of larger aggregates, which was evident in the correlogram profile. In comparison with the corresponding crystallite sizes, the hydrodynamic size of M3 (20.9 nm) was much larger than its crystallite size, 10.5 nm, which indicated that there was aggregation in this system. Moreover, the number distribution indicates M3 has significant amount of larger sized particles and M1 has the least.

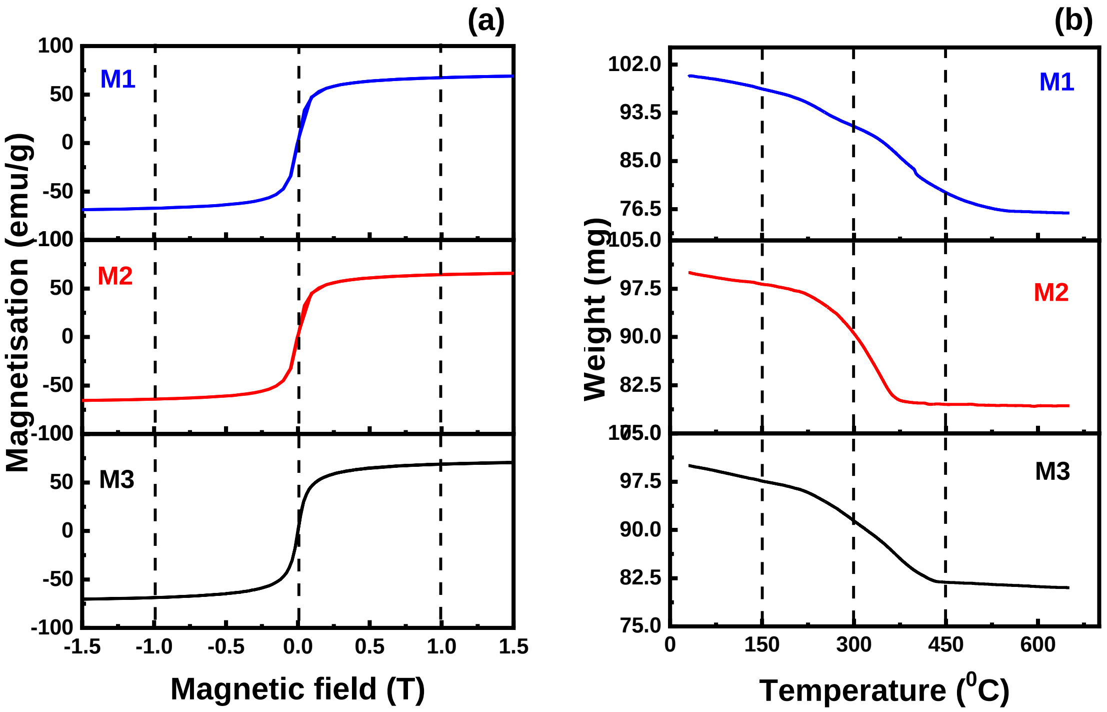

*Figure 2.8 (a) M – H curve of M1, M2, and M3. The saturation magnetization values are found to be 69, 66, and 71 emu/g, respectively. (b) Thermogravimetric weight loss curves of the dried surfactant coated magnetite nanoparticles of M1, M2, and M3.*

**Figure 2.8 (a)** shows the M – H curve of the samples M1, M2, and M3. The saturation magnetization values were found to be 69 ± 0.6, 66 ± 0.7, and 71 ± 0.7 emu/g for M1, M2, and M3, respectively. Since the average size of the magnetite nanoparticles of the three samples was similar, there was not much difference in the saturation magnetization values. However, the presence of a significant amount of larger particles in M3 lead to a higher initial value of susceptibility. The M – H curve did not show any hysteresis at room temperature, which indicates that all three samples are superparamagnetic in nature. **Fig. 2.8 (b)** shows the thermogravimetric weight loss curves of the dried surfactant coated magnetite nanoparticles of M1, M2, and M3. The weight loss percentages were approximately 24, 21, and 19% for M1, M2, and M3, respectively. The weight loss percentage of surfactant adsorbed on the surface of nanoparticles can be calculated using the formula, $\frac{100\left(\left(\frac{\pi d_{crystal}^{2}}{a_s}\right)\frac{M_W}{N_A}\right)}{\left(\frac{1}{6}\pi d_{crystal}^{3}\rho_{MNP}+\left(\frac{\pi d_{crystal}^{2}}{a_s}\right)\frac{M_W}{N_A}\right)}$, where $a_s$ is the head area of a single surfactant (oleic acid) molecule, $\rho_{MNP}$ is the density of magnetite nanoparticles, $N_A$ is the Avogadro number, and $M_w$ is the molecular weight of oleic acid [185]. Using the above equation, the calculated weight loss percentage were 19, 21.4, and 17.7% for M1, M2, and M3, respectively. In comparison, M1 showed slightly higher surfactant content than that required for a monolayer, whereas M3 seems to have a little less than that was required for a monolayer. The non-uniform coating could lead to formation of larger aggregates in the absence of magnetic field. This could lead to higher polydispersity and was the reason why the hydrodynamic size of M3 (20.9 nm) was larger than the crystallite size (10.5 nm). For M2, an adequate amount of surfactant was present to have a monolayer.

## 2.7. Characterization of ferrofluid emulsion

The ferrofluid emulsion used in this study is a dispersion of octane oil droplets in water of average size ~ 200 nm, containing oleic acid capped $Fe_3O_4$ magnetic nanoparticles of average size ~ 10 nm.

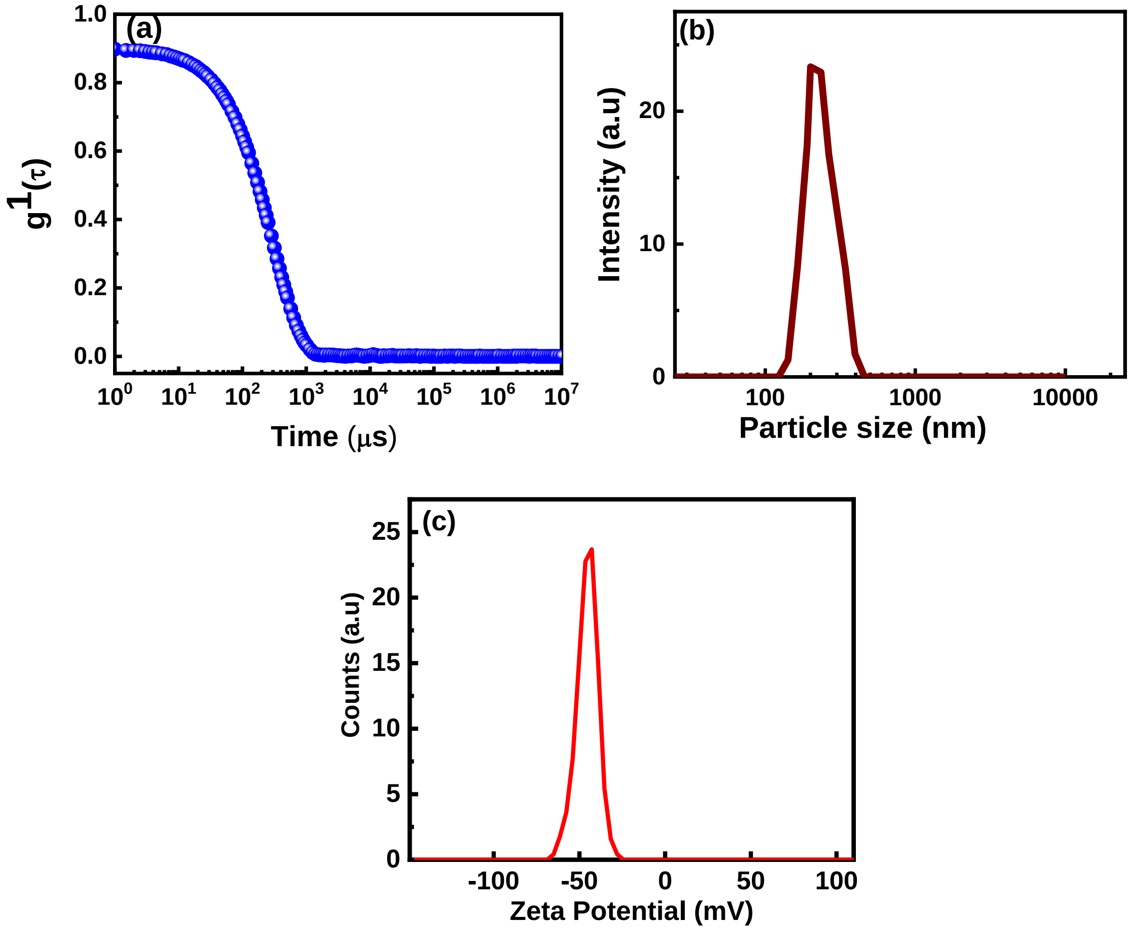

*Figure 2.9 (a) Electric field autocorrelation function as a function of time, (b) the hydrodynamic size distribution of droplets and (c) zeta potential of SDS stabilized magnetic nanoemulsion.*

**Figure 2.9 (a)** and **(b)** shows the electric field autocorrelation function as a function of time and the hydrodynamic size distribution of droplets. **Fig. 2.9 (c)** shows the zeta potential distribution of magnetic nanoemulsion.The average hydrodynamic diameter and zeta potential are found to be ~ 200 nm and -50 mV, respectively. The polydispersity index of 0.05 (PDI) indicates that the emulsion is fairly monodispersed.

## 2.8. Conclusion

The details of various samples, preparation of ferrofluid and ferrofluid emulsion are discussed briefly. The details of characterization techniques such as powder X-ray diffraction, small angle X-ray scattering, dynamic light scattering, vibrating sample magnetometer, thermo-gravimetric analysis, and phase contrast optical microscope are presented. The physico-chemical properties of iron oxide nanoparticles are presented. Details of light scattering setup and procedure to measure transmitted light intensity and scattered pattern are also discussed.

## *Chapter 3*

# Role of surface charge screening on field induced structural transitions in magnetic nanoemulsion

## 3.1. Introduction

Magnetic fluids have attracted much interest during the last few decades due to their interesting magnetic stimulus responsive optical properties and engineering applications [18, 21]. Magnetic fluids undergo several interesting structural transitions depending on the applied magnetic field strength [66, 76-79]. Being thermodynamically unstable colloid, the stability and phase behavior of magnetic fluids are strongly dependent on surface adsorbed moieties. The charged particles in a magnetic colloid create electrostatic repulsive interaction, which can be varied by changing the surfactant concentration, salt concentration, pH, etc. [186, 187]. As water-based systems are preferred for many applications, including biomedical fields, we choose a water-based system for our study, where surface charge density is varied with surfactant concentration to control the stability. Although the understanding of field induced structural transitions in magnetic fluids has steadily progressed, the role of surface charge on the critical magnetic field has not yet been studied. Owing to the wide range of applications on water-based magnetic fluids, an understanding of the phase behavior of such systems, especially the surface charge screening on critical magnetic fields associated with field induced structural transitions, is very important.

Here, we study field assisted structural transitions in magnetic nanoemulsion. The emulsion used here is stabilized with an anionic surfactant of different concentrations. The role of surfactant concentrations on the field induced structural transitions is studied systematically. We use forward light scattering, transmitted scattered patterns, speckle pattern analysis, and phase contrast optical microscopy to study the structural transitions.

The field and time dependent light transmitted intensity are measured to obtain the critical magnetic field strength. Three critical magnetic fields have been identified, and the scaling of critical fields with volume fraction is compared with existing theoretical models.

## 3.2. Materials and methods

The magnetic nanoemulsion was prepared by shearing non-aqueous ferrofluid (octane containing oleic acid capped $Fe_3O_4$ nanoparticles) with surfactant (SDS) solution at ~ 1500 rpm, using a IKA homogenizer. The synthesis procedure to produce ferrofluid emulsion and monodispersed emulsion from coarse emulsion with wider size distribution was achieved by fractionation technique, which is detailed in section 2.3 of chapter 2. Magnetic emulsion with droplet hydrodynamic diameter ~ 200 nm, containing superparamagnetic iron-oxide nanoparticles of diameter ~ 10 nm, is used in this study. The light scattering experimental set-up is shown in **Fig. 2.5**. In this case, the magnetic field was ramped slowly at 0.3 G/s, and the direction of the applied magnetic field was parallel to the light propagation direction. The detailed procedure of acquiring the transmitted light intensity through the sample and the scattered pattern as a function of external magnetic field is explained in section 2.5.1 of chapter 2.

## 3.3. Results and discussion

### 3.3.1. Concentration dependence on structural transitions

The normalized transmitted light intensity as a function of applied magnetic field for magnetically polarizable nanoemulsion of $\Phi = 0.0105, 0.0117, 0.0131, 0.0149, 0.0174, 0.0189, 0.0208, 0.0218$, and $0.0230$ is shown in **Fig. 3.1**.

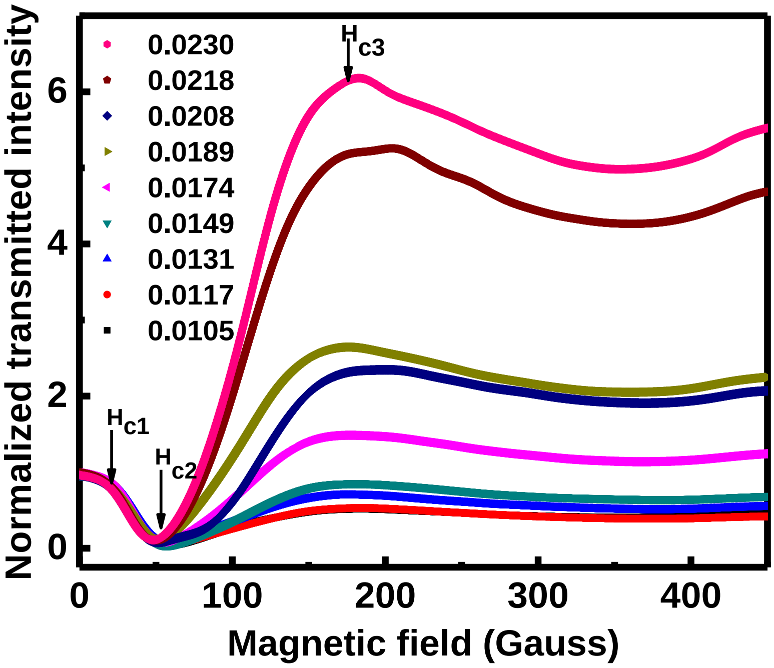

*Figure 3.1 Normalized transmitted intensity as a function of applied magnetic field for magnetically polarizable nanoemulsion of different volume fractions from 0.0105 to 0.0230.*

The ratio of transmitted light intensity with and without magnetic field is taken as the normalized transmitted intensity. The first critical magnetic field $(H_{c1})$ is defined as the field above which the transmitted intensity decreases rapidly. The second critical magnetic field $(H_{c2})$ corresponds to the next minimum intensity, and the subsequent intensity maximum is defined as the third critical magnetic field $(H_{c3})$, beyond which light intensity drops a little and saturate.

### 3.3.2. Magnetic field induced structural transitions

When magnetic energy exceeds thermal energy, the magnetic moments align along the applied magnetic field direction, and the induced magnetic moment of the droplet is given by

$$m_0 = \frac{\pi}{6} d_1^3 \chi_{eff} \mathrm{H} \tag{3.1}$$

where $d_1$ is the diameter of droplet. The effective magnetic interaction between two droplets can be expressed in terms of coupling constant $(\Lambda_1)$

$$\Lambda_1 = -\frac{U(d_1, 0)}{k_B T} = \frac{\pi \mu_0 d_1^3 \chi_{eff}^2 H^2}{72 k_B T} \tag{3.2}$$

The magnetic field directed self-assembly of magnetic droplets occurs at $\Lambda_1 > 1$. The inter-droplet spacing is inversely proportional to the volume fraction (given in Eqn. 1.25). Owing to the inverse dependence of magnetic attractive force $F_m$ ($F_m \propto 1/r^4$, where r is the inter-droplet separation), it is stronger at a smaller inter-droplet distance. As the larger particles have a large magnetic moment for a polydisperse system compared to the smaller ones, larger particles quickly form a chain at the lower magnetic field.

*Table 3.1 Details of critical magnetic fields $H_{c1}$, $H_{c2}$, and $H_{c3}$ obtained from transmitted intensity profiles corresponding to different volume fraction, IPS, and the coupling constants $\Lambda_{c1}$, $\Lambda_{c2}$, and $\Lambda_{c3}$ calculated using Eqn. (3.2).*

| Φ | IPS (nm) | $H_{c1}$ (G) | $H_{c2}$ (G) | $H_{c3}$ (G) | $\Lambda_{c1}$ | $\Lambda_{c2}$ | $\Lambda_{c3}$ |
|---|---|---|---|---|---|---|---|
| 0.0105 | 572.36 | 23.6 | 58.56 | 173.4 | 1.53 | 9.43 | 82.7 |
| 0.0117 | 545.26 | 21.8 | 57.92 | 170.6 | 1.31 | 9.23 | 80.1 |
| 0.0131 | 517.98 | 21.4 | 59 | 169.3 | 1.25 | 9.59 | 78.9 |
| 0.0149 | 488.11 | 20.7 | 56.6 | 169 | 1.18 | 8.83 | 78.6 |
| 0.0174 | 453.77 | 20 | 53.9 | 170.7 | 1.1 | 8 | 80.2 |
| 0.0189 | 436.18 | 18.2 | 52.8 | 177 | 0.91 | 7.67 | 86.3 |
| 0.0208 | 416.38 | 18 | 51.4 | 188.2 | 0.88 | 7.26 | 97.5 |
| 0.0218 | 406.90 | 17.6 | 49.4 | 193.6 | 0.85 | 6.72 | 103 |
| 0.023 | 396.26 | 16.5 | 48.3 | 190.2 | 0.75 | 6.42 | 99.5 |

**Table 3.1** shows the values of critical fields $H_{c1}$, $H_{c2}$, and $H_{c3}$ obtained from the experiments and the values of $\Lambda_{c1}$, $\Lambda_{c2}$, and $\Lambda_{c3}$ obtained using Eqn. (3.2). The first coupling constant varies from 1.1 to 1.53, as the volume fraction is varied from 0.0174 to 0.0105. As the volume fraction is increased from 0.0189 to 0.023, the coupling constant decreases from 0.91 to 0.75. This implies that even when the coupling constant is slightly lower than unity, the attractive interaction is significant at higher volume fractions due to contributions of larger droplets. With increasing Φ, the inter-droplets spacing becomes

smaller, and hence chain formation occurs at lower $H$. $\Lambda_{c1}$ indicates the first coupling constant where the individual droplets start to form small chains in the magnetic field direction. When $\Lambda_{c1} << 1$, the droplets are under random motion and behave as a disordered system, but as $\Lambda_{c1} \sim 1$, the light intensity slowly decreased up to $H_{c1}$. Droplets form small aggregates at $\Lambda_{c1} \geq 1$, and the aggregate size continues to grow with the magnetic field strength. After $H_{c1,}$ the scatterer dimension and hence the mean free path become comparable to the incident wavelength of incident light (corresponds to a region of weak localization), where the dipole resonances within the scatterers and the subsequent delay in the light propagation are considered to cause the extinction of light at $H_{c2}$ [165]. The length of the chains continues to increase with the magnetic field until they form space filling chains by attaining the path length of the cell along the field direction. Once such space filling long chains are developed, it will attract the nearest neighbor to form columns where the long chains act as a nucleation site. The magnetic field around an infinite chain (center chain or nucleation chain) of magnetic dipoles is given by

$$H^*(\rho, z) \approx -(2\pi)^2 \left(\frac{m_0}{4\pi\mu_0\rho^2 d_1}\right)\left(\frac{d_1}{\rho}\right)^{1/2} e^{-2\pi\rho/d_1} \cos\left({}^{2\pi z}/_{d_1}\right) \tag{3.3}$$

where z is the position along the chain in the field direction. According to Halsey-Toor model, Landau-Peierls fluctuations created by dipolar single chains suspended in a three dimensional fluid result in a long range attraction with a power law decay [188]. The total free energy for the chains and the mean-squared field around the fluctuating chain is given by

$$F_c(\rho) = \frac{-11.11 k_B T \Lambda_1 d_1^4}{2\pi\rho^5} \tag{3.4}$$

$$\langle H^{*2}\rangle \sim \frac{m_0^2 k_B T}{\mu_0^2 \rho^4 d_1^2 \varepsilon} \sim \frac{k_B T d_1}{\mu_0 \rho^4} \tag{3.5}$$

Therefore, the lateral interaction is independent of $H^*$. The interaction energy per unit length $d_1$ is given by [189]

$$U \sim (m_0/d_1)\langle H^{*2}\rangle^{1/2} \sim \frac{\chi_{eff} H (\mu_0 k_B T)^{1/2} d_1^{1/2}}{\rho^2} \tag{3.6}$$

It can be either attractive or repulsive and strongly dependent on $H$ as well as the separation between the chains ($\rho$). When the chains are of different lengths or shifted with respect to one another (off registry), zippering of chains can take place due to attractive energy well [190, 191]. Hence, the gap between columns increases with the external magnetic field, resulting in an increase in light transmission after reaching a minimum. At $H_{c3}$, the transmitted intensity reaches a maximum, beyond which it slowly decreases and becomes saturated. The column formation occurs between $H_{c2}$ and $H_{c3}$ regions where columns are loosely bound (with hexagonal structure) because of thermal energy [66]. Completely rigid columns are formed at $H_{c3}$. Above $H_{c3}$, columns become more rigid solid kind of structures, similar to the body-centered-tetragonal structure where the spacing between the columns remains constant [192]. As a result, not much variation in transmitted intensity was observed above $H_{c3}$. When light is incident on such kind of cylindrical structures, it scatters light in a conical direction, resulting in the formation of a ring like pattern where the total intensity (spot intensity) is distributed in the circumference of this ring. As the photomultiplier tube measures only the spot intensity and not the whole intensity of the ring pattern, the intensity decreases slowly after becoming a maximum. It then saturates due to the formation of more rigid and ordered structures.

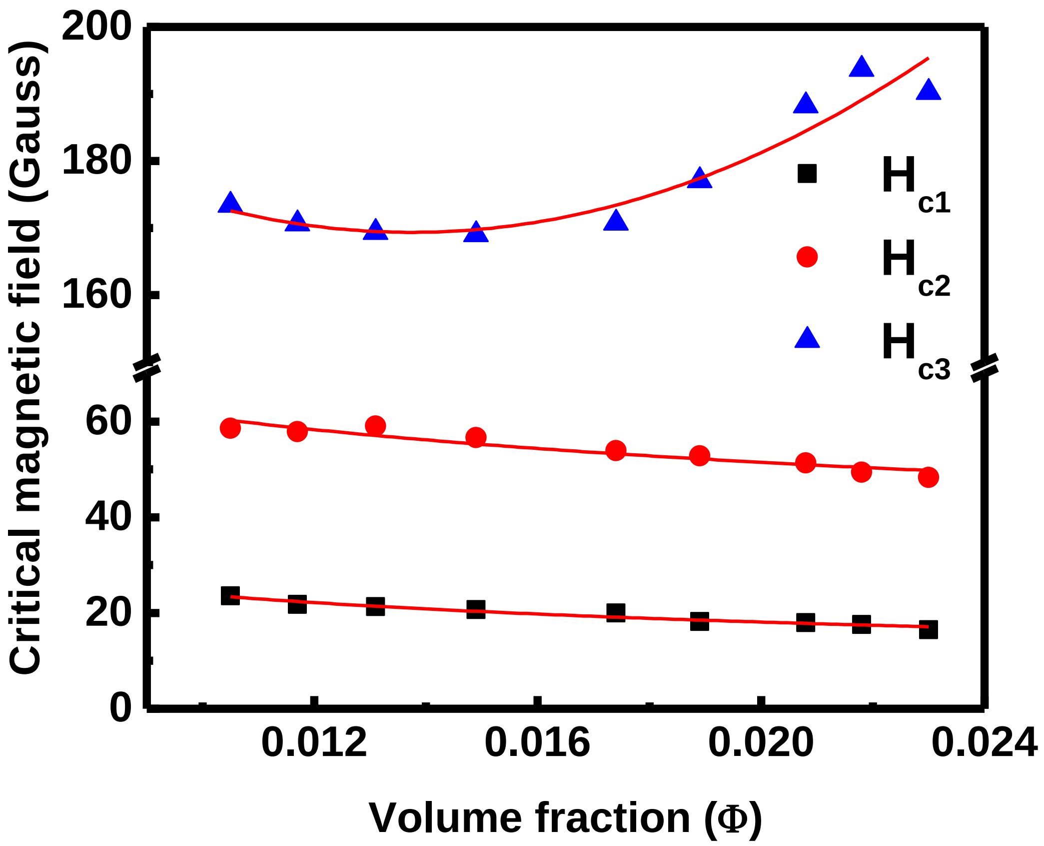

*Figure 3.2 The critical magnetic fields as a function of droplet volume fraction.*

The variation of $H_{c1}$, $H_{c2}$, and $H_{c3}$ as a function of Φ is shown in **Fig. 3.2.** With increasing Φ from 0.0105 to 0.0230, $H_{c1}$ decreases from 23.58 to 16.5 G whereas $H_{c2}$ decreases from 58.56 to 48.32 G. The $H_{c3}$ decreases from 173.4 to 169 G as the volume fraction is increased from 0.0105 to 0.0149 and then from 170.72 to 193.64 G, as the volume fraction is increased from 0.0174 to 0.0218. For Φ = 0.023, the critical field was 190.2 G. The theory behind these three critical fields and their variation with different volume fractions is elegantly derived by Ivey et al. [66] is briefly presented below.

At the first critical magnetic field, random Brownian nanodroplets start to interact with each other and form small aggregates. The favorable condition for $H_{c1}$ is $\frac{\mu_0 m_0^2}{4\pi r^3} \geq k_B T$. The relationship between the first critical magnetic field and Φ $(= \frac{\pi d_1^3}{6r^3})$, is [66]

$$H_{c1} \approx \left(\frac{24k_BT}{\mu_0\chi_{eff}^2d_1^3}\right)^{1/2}\Phi^{-1/2} \tag{3.7}$$

Therefore, according to theory, $H_{c1}$ follows power law decay with the volume fraction ($\Phi^{-x'}$), where $x'$ equals 0.5. Interestingly, the experimentally observed $H_{c1}$ also follows a power law decay with an exponent of 0.4, which is very close to the predicted value of 0.5.

At the second critical magnetic field, long chains are formed. They act as nucleation centers for the column-like structures. The long chains attract the nearest neighboring short chains and single droplets to form columns, resulting in a weak local ordering in the perpendicular direction to the magnetic field [193]. As the field increases, the local ordering in the column increases due to repulsive Coulomb interaction energy ($U_q \approx \frac{q_m^2}{\rho}$) between the effective charges $q_m$ at the end of the neighboring columns. $U_q$ favors the ordering of the long chains, whereas the thermal energy tends to destroy the local ordering, and the competition between these two energy results in the $H_{c2}$. For large volume fractions, the chains become closer (smaller IPS), and hence the field required to form columns is lower. The condition for the second critical magnetic field is given by $\frac{q_m^2}{\rho} \approx k_BT$, where $q_m \approx \frac{\pi}{6}d_1^2\chi_{eff}H$. For this state, $\Phi$ can be approximated as $\Phi \propto \left(\frac{d_1}{\rho}\right)^2$. Therefore, $\frac{\pi^2d_1^4\chi_{eff}^2H_{c2}^2}{36\rho^2} \approx k_BT$,

$$H_{c2} \approx \left(\frac{36k_BT}{\pi^2\chi_{eff}^2\rho^2}\right)^{1/2}\Phi^{-1/4} \tag{3.8}$$

Therefore, theoretically, $H_{c2}$ scales as $\Phi^{-x'}$ where $x' = 0.25$. The experimentally observed value of $x' = 0.27$ was in excellent agreement with the predicted value.

At the third critical magnetic field, loosely bound columns with liquid-like structures are transformed into densely packed columnar solid-like structures [188]. The thermal fluctuation of a long chain or thin column produces a long range field given in Eqn. (3.5). So, the long chains act as a nucleation center to attract nearby short chains or single droplets. The magnetic field around an infinite chain given by Eqn. (3.3) creates interaction energy, which is responsible for binding the columns into rigid ones [123, 194]

$$U_i \approx -(2\pi)^2 \left(\frac{m_0^2}{4\pi\mu_0\rho^2 d_1}\right)\left(\frac{d_1}{\rho}\right)^{1/2} e^{-2\pi\rho/d_1} \cos\left(2\pi z/_{d_1}\right) \tag{3.9}$$

The fluctuation energy, which is induced by Peierls-Landau instability, has the opposite effect [193]

$$U_f \approx m_0 \left(\frac{27\pi}{128}\right)^{1/2} \left(\frac{d_1^2 k_B T}{\rho^5}\right)^{1/2} \tag{3.10}$$

So the third critical magnetic field results from the competition between these two energies, i.e., $U_i \approx U_f$, and is given by

$$H_{c3} \approx \left(\frac{27\pi k_B T}{32 d_1^3}\right)^{1/2} \left(\frac{3}{2\pi^2 \chi_{eff}}\right) \frac{1}{\left|\langle\cos\left(2\pi z/_{d_1}\right)\rangle\right|} \left(\frac{d_1}{\rho}\right)^2 e^{-2\pi\rho/d_1} \tag{3.11}$$

It is assumed that, below $H_{c3}$, hexagonal structures are formed, and above $H_{c3}$ body-centered-tetragonal solid-like structures are formed, i.e., $\left(\frac{d_1}{\rho}\right)^2 \approx \frac{\Phi}{(1.21)^2}$ (for hexagonal structure) and $\left(\frac{d_1}{\rho}\right)^2 \approx \frac{1}{(1.73)^2} \approx \frac{(\Phi)^0}{(1.73)^2}$ (for body-centered-tetragonal structure).

The generalized form at $H_{c3}$ is

$$\left(\frac{d_1}{\rho}\right)^2 = \frac{\Phi^\gamma}{G^2} \tag{3.12}$$

where $\gamma$ reflects the sensitivity of $\Phi$ and depends on $\rho$. The value of $\gamma$ lies between 0 and 1. $G$ is the geometric factor that originates from the column structures.

Using Eqns. (3.12) and (3.11),

$$H_{c3} \approx \left[ \left( \frac{27\pi k_B T}{32 d_1^3} \right)^{1/2} \left( \frac{3}{2\pi^2 \chi_{eff}} \right) \frac{1}{\left| \left\langle cos\left( \frac{2\pi z}{d_1} \right) \right\rangle \right|} \right] \left[ \frac{\Phi^{\gamma}}{G^2} exp\left( \frac{-2\pi G}{\Phi^{\gamma/2}} \right) \right] \tag{3.13}$$

The best fit using Eqn. (3.13) on the experimental $H_{c3}$ value is shown by the solid line in **Fig. 3.2**. The values of $\gamma$ and $G$ obtained from the best fit are found to be 0.68 and 0.15, respectively, which were within the range of theoretical predictions. When interaction energy is sufficient to overcome the energy barrier, lateral coalesce occurs, which causes an increase in the column width that necessitates a higher magnetic field to make the columns rigid explains the reasons for the rise in $H_{c3}$ at higher volume fractions.

### 3.3.3. Effect of surface charge screening on critical magnetic fields for structural transitions

The normalized transmitted light intensity as a function of $H$ for magnetically polarizable nanoemulsion with $\Phi$ = 0.0105 of different surfactant concentrations 0.2, 2, 4, 8, and 16 mM is shown in **Fig. 3.3**. The transmitted light intensity curves follow the same trend as before, where $H_{c1}$, $H_{c2}$, and $H_{c3}$ were observed for all SDS concentrations.

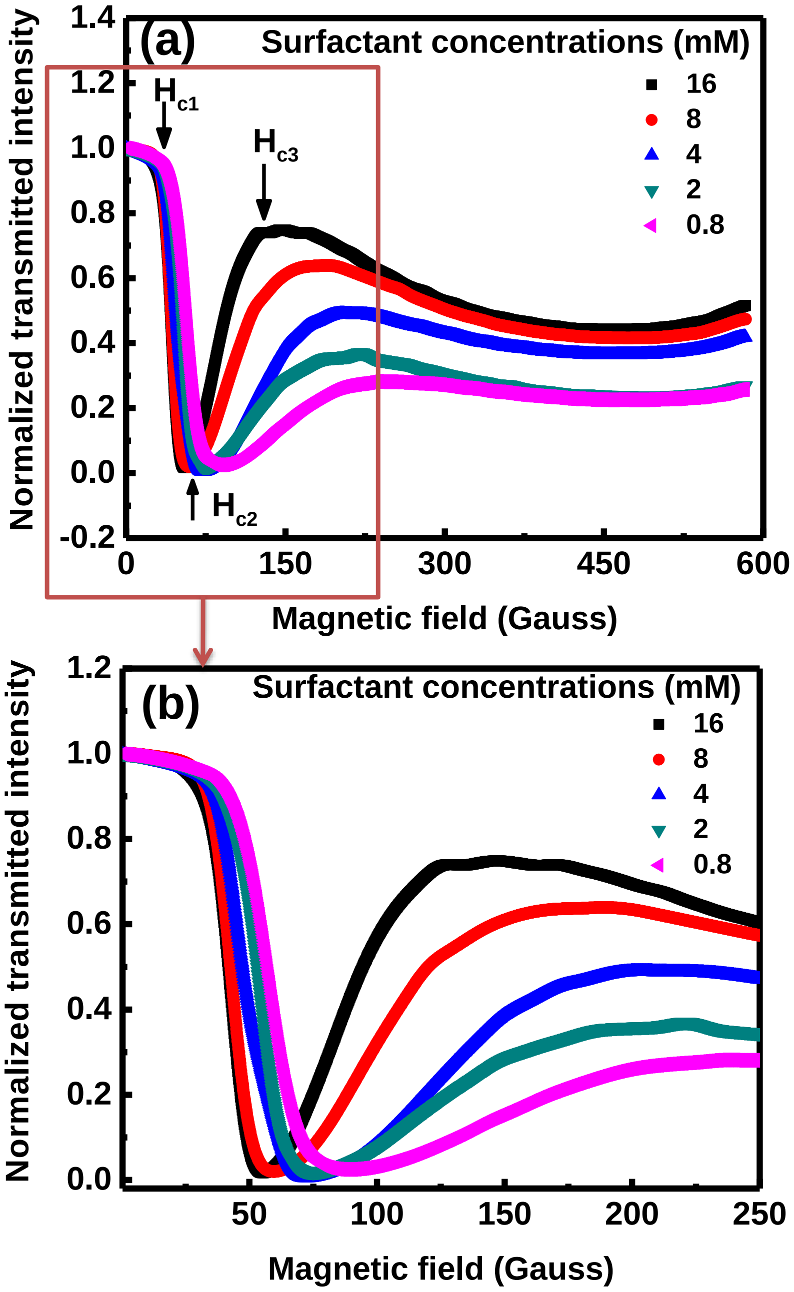

*Figure 3.3 (a) Normalized transmitted intensity as a function of the applied magnetic field. (b) The magnified view of transmitted intensity at lower* H *(0 – 250 G), for Φ = 0.0105, with different surfactant concentrations.*

Without the magnetic field, Van der Waal's attraction and electrostatic repulsion are the dominant interaction between the droplets. The attractive Van der Waal's forces for spherical particles of diameter $2a_1$ is given by

$$F_{vdw}(r) = \frac{A_H a_1}{12(r-2a_1)^2} \tag{3.14}$$

where $A_H$ is the Hamaker constant. The value of $A_H$ computed for octane-water dispersion is $10^{-20}$ J. Van der Waal's force for $a_1 \sim 100\, nm$ is negligible at $r$ > 10 nm. Here, the electrostatic repulsion force for a thin double layer $(\kappa a_1 < 5)$, is given by

$$F_r(r) = 4\pi\varepsilon\psi_0^2 a_1^2 \left[\frac{\kappa}{r} + \frac{1}{r^2}\right] exp[-\kappa(r - 2a_1)] \tag{3.15}$$

The range of repulsion is reduced significantly at high surfactant concentration due to the screening effect. When the double layer is largely extended $(\kappa a_1 > 5)$, the repulsive force is given by

$$F_r(r) = 2\pi\varepsilon\psi_0^2 a_1 \kappa \frac{exp[-\kappa(r - 2a_1)]}{1 + exp[-\kappa(r - 2a_1)]} \tag{3.16}$$

The critical magnetic fields as a function of surfactant concentration are shown in **Fig. 3.4**. As concentration increases from 0.8 to 16 mM, $H_{c1}$ decreases from 36 to 19.7 G, whereas $H_{c2}$ drops from 88 to 55 G and $H_{c3}$ decreases from 245.4 to 148.2 G, respectively. The critical fields follow a power law decay with the surfactant concentration $(C_s^{-x'})$, where the $x'$ values are 0.19, 0.15, and 0.15 for $H_{c1}$, $H_{c2}$, and $H_{c3}$, respectively.

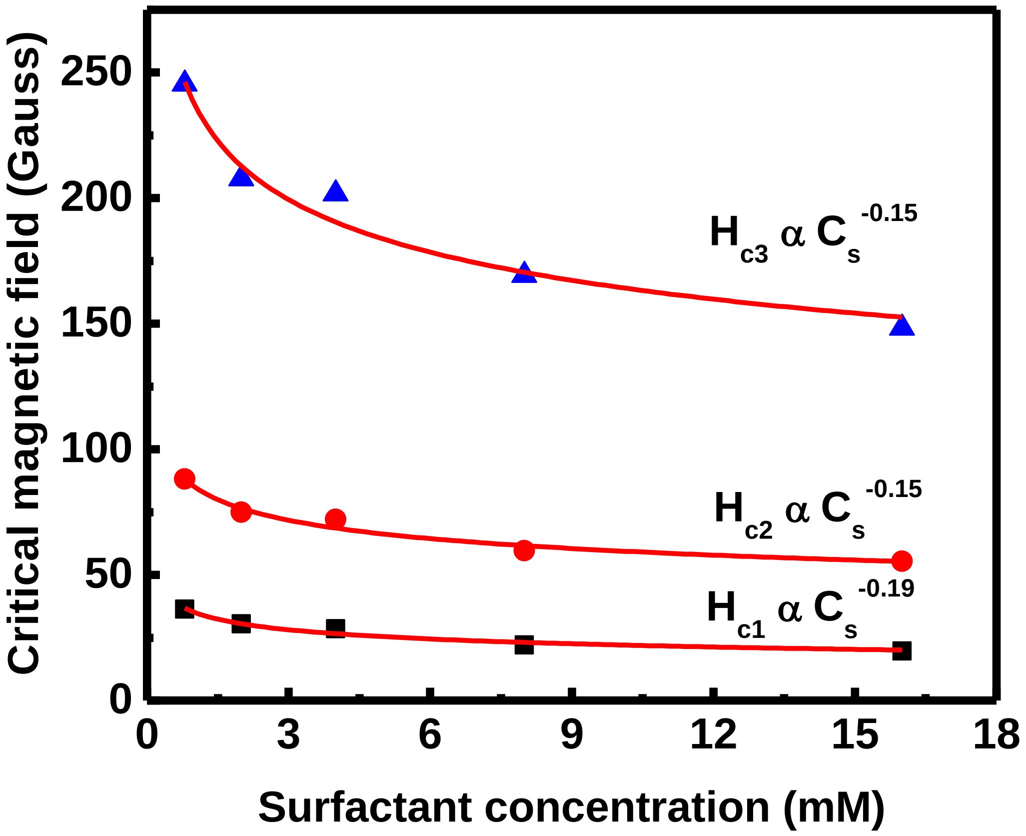

*Figure 3.4 Critical magnetic fields ($H_{c1}$, $H_{c2}$, and $H_{c3}$) as a function of surfactant concentration. The solid line represents the best fit of the experimental data.*

For the surfactant concentration of 0.8, 2, 4, 8, and 16 mM, the Debye length was found to be 10.74, 6.79, 4.806, 3.398, and 2.403 nm, respectively. As the surfactant concentration increases, the electric double layer thickness decreases, and the separation between the droplets decreases in the dispersion. Therefore, the magnetic field required to induce field induced ordering and zippered structures decrease with increasing surfactant concentration. The interdroplet distance in a chain was calculated from the force-distance measurement [195]. The force measurement was performed for a magnetic nanoemulsion with $\Phi = 0.0105$ by varying the surfactant concentration from 0.8 to 8 mM.

*Table 3.2 The experimental $H_{c1}$, $H_{c2}$, and $H_{c3}$ obtained from light scattering study and the corresponding extrapolated interdroplet separation ($d_{c1}$, $d_{c2}$, and $d_{c3}$) from force-distance curve for a ferrofluid emulsion of* $\Phi$ = 0.0105 *with different surfactant concentration of 0.8, 2, 4, and 8 mM.*

| Surfactant concentration (mM) | $H_{c1}$ (G) | $H_{c2}$ (G) | $H_{c3}$ (G) | $d_{c1}$ (nm) | $d_{c2}$ (nm) | $d_{c3}$ (nm) |
|---|---|---|---|---|---|---|
| 0.8 | 36.32 | 88.16 | 245.44 | 298.18 | 275.3 | 251.07 |
| 2 | 30.52 | 74.88 | 207.72 | 260.66 | 246.9 | 232.3 |
| 4 | 28.48 | 72.16 | 201.76 | 249.2 | 240.16 | 230.48 |
| 8 | 22.08 | 59.68 | 169.3 | 225.5 | 221.15 | 216.58 |

**Table 3.2** shows the experimental $H_{c1}$, $H_{c2}$, and $H_{c3}$ values and $d_{c1}$, $d_{c2}$, and $d_{c3}$ for a ferrofluid emulsion of $\Phi$ = 0.0105 with different surfactant concentrations of 0.8, 2, 4, and 8 mM. The first critical interdroplet separation varies from 298.18 to 225.5 nm. The second critical interdroplet separation varies from 275.3 to 221.15 nm, and the third critical interdroplet separation varies from 251.07 to 216.58 nm as the surfactant concentration is increased from 0.8 to 8 mM.

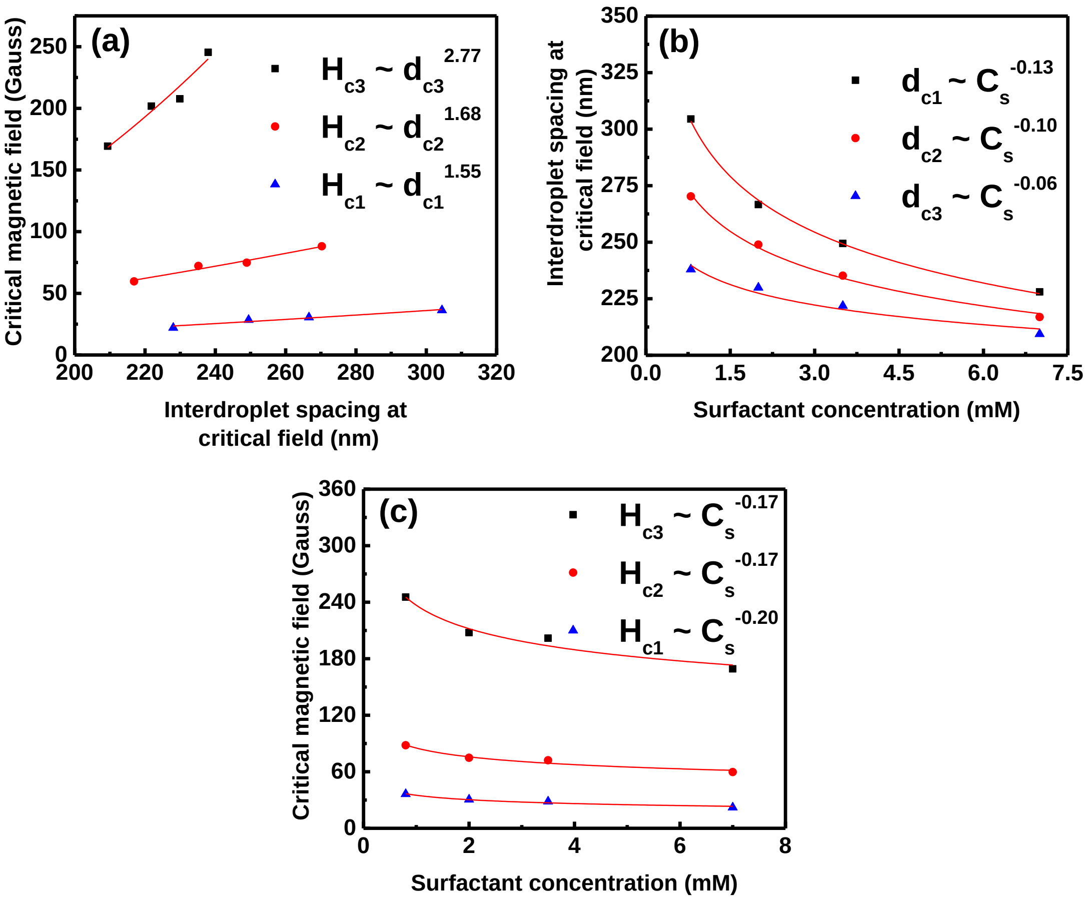

*Figure 3.5 (a) Critical magnetic fields as a function of interdroplet separation, (b) interdroplet separations as a function of surfactant concentration for different critical fields, and (c) critical magnetic field as a function of surfactant concentration for Φ = 0.0105.*

**Figure 3.5 (a)** and **(b)** show the variation of critical magnetic fields with the interdroplet separation and the interdroplet spacing as a function of surfactant concentration, respectively, corresponding to a different critical magnetic field. **Fig. 3.5 (c)** shows the critical magnetic field variation with surfactant concentration for ferrofluid emulsion of Φ = 0.0105. The solid line corresponds to the best fit with a power law equation (i.e., $Y = pX^{y'}$, where $p$ is the multiplication factor and $y'$ is the exponent), and in each case, R$^2$ was found to vary between 0.97 to 0.99. The scaling exponent with respect to the field, concentration of surfactant and interdroplet spacing are found to be $H_{c1} \sim d_{c1}^{1.55}$; $H_{c2} \sim d_{c2}^{1.68}$; $H_{c3} \sim d_{c3}^{2.77}$; $d_{c1} \sim C_s^{-0.13}$; $d_{c2} \sim C_s^{-0.10}$; $d_{c3} \sim C_s^{-0.06}$; $H_{c1} \sim C_s^{-0.2}$; $H_{c2} \sim C_s^{-0.17}$; $H_{c3} \sim C_s^{-0.17}$.

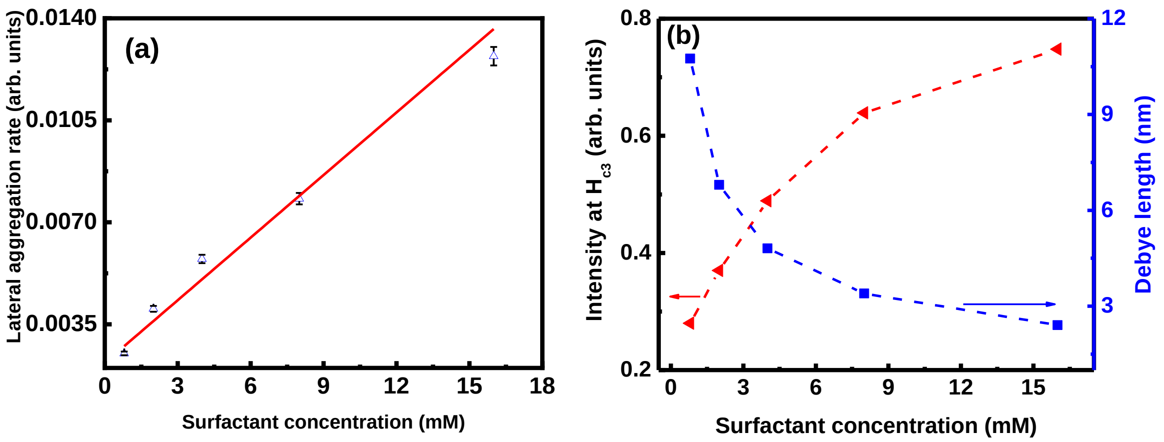

*Figure 3.6 (a) Lateral aggregation rate and (b) transmitted intensity at $H_{c3}$ and Debye length, as a function of SDS concentration with $\Phi = 0.0105$.*

The lateral aggregation rate, which was obtained from the slope of the linear region between $H_{c2}$ and $H_{c3}$, as a function of surfactant concentration, is shown in **Fig. 3.6 (a)**. The aggregation rate increases from 0.0025 to 0.0127, with an increase in concentration from 0.8 to 16 mM. The lateral aggregation rate is found to vary linearly with surfactant concentration, where the slope was $6.41 \times 10^{-4}$, with a $R^2$ value of 0.99. **Fig. 3.6 (b)** shows the Debye length and transmitted intensity at $H_{c3}$ as a function of SDS concentration. The light intensity increases from 0.282 to 0.748, as the concentration is increased from 0.8 to 16 mM. The aggregation is found to occur quickly in dispersion with higher SDS concentration than the lower one due to lower interdroplet spacing. With increasing thickness of the column, the inter-columnar spacing increases, and the intensity at $H_{c3}$ increases for dispersion with higher SDS concentration.

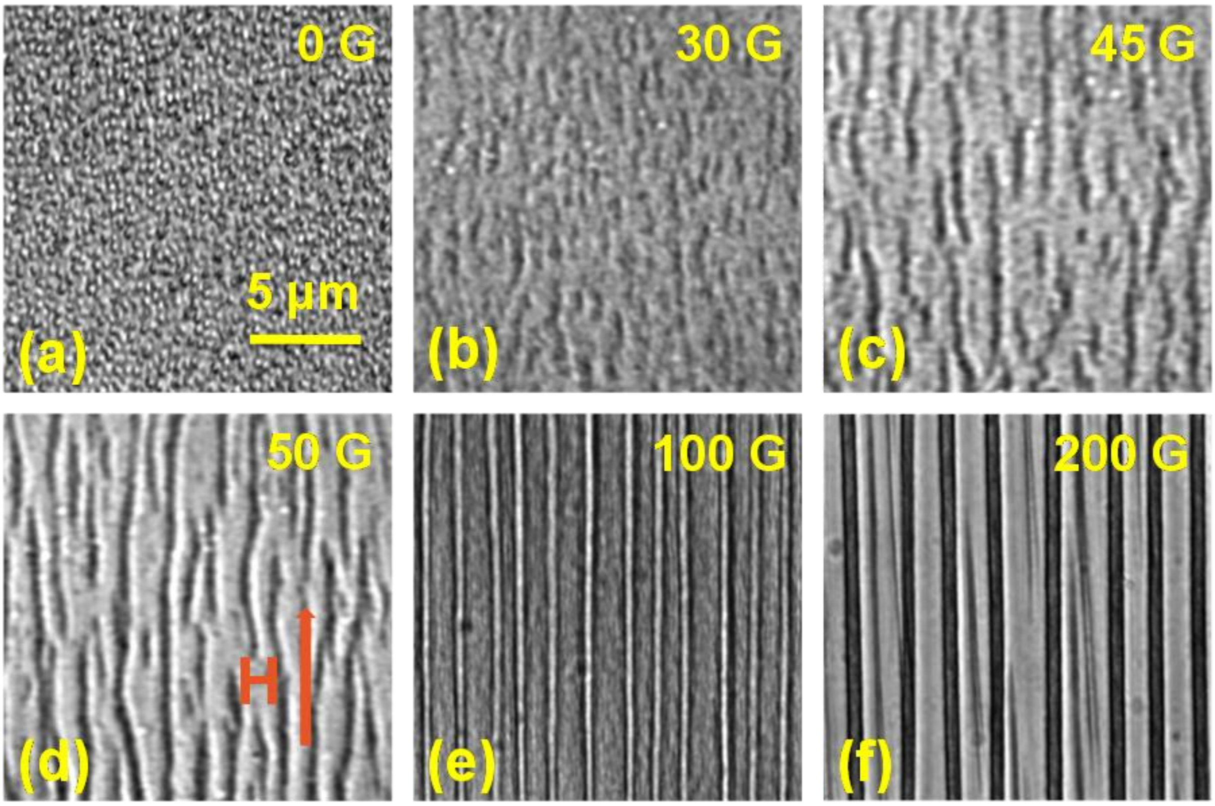

*Figure 3.7 Phase contrast microscope images of magnetic nanoemulsion at* H = *0, 30, 45, 50, 100, and 200 G. The direction of* H *is shown by the arrow.*

**Figures 3.7 (a)-(f)** show the phase contrast microscope images of the magnetic nanoemulsion at $H$ = 0, 30, 45, 50, 100, and 200 G. The direction of $H$ is shown by an arrow in **Fig. 3.7 (d)**. At zero magnetic field, the system behaves as a gas like structure, where the magnetic coupling constant was less than one, as shown in **Fig. 3.7 (a)**. **Fig. 3.7 (b)** shows the phase contrast microscopy images taken at $H$ = 30 G, where the single droplets combine to form dimers, trimers, and small chains. As the magnetic field strength increases, the aspect ratio of the chain increases. Once the chains reach the maximum length, the lateral interaction between the chains takes place under certain conditions, as shown in **Fig. 3.7 (e)** and **(f)**. When the magnetic field is weak, the assembled chains are usually short and flexible due to the fluctuation of the induced moments. The flexibility of chains depends on the magnetic field strength, volume fraction, thermal fluctuations in a chain, number of particles in a chain, etc. According to the Halsey and Toor model [194], one-dimensional structures suspended in a three dimensional fluid dipolar chain exhibit strong Landau-Peierls fluctuation. The magnitude of the fluctuation decreases as the magnetic field strength increases, indicating the stiffening of the chains due to strong inter-particle interaction.

### 3.3.4. Scattering pattern and speckle profile

**Figures 3.8 (a - i)** show the forward scattered pattern from nanoemulsion of $\Phi$ = 0.0174 at $H$ = 0, 20.8, 35.2, 53.9, 105.6, 175.2, 256, 380.8, and 448 G and **Figs. 3.8 (j - r)** show the corresponding surface plot of the scattered patterns under the same $H$. The diffused spot at zero field is transformed into a ring like pattern at higher fields. There was no change in spot intensity up to 20.8 G, which corresponds to the $H_{c1}$ for a volume fraction of 0.0174. After $H_{c1}$, the spot intensity decreases drastically and becomes minimum at 53.9 G, which corresponds to $H_{c2}$. The spot intensity reaches a maximum at 170.7 G, at the $H_{c3}$, where the spot is fully converted into the ring like pattern, beyond which the ring becomes sharper without any change, indicating the formation of well-ordered solid like structures. The formation of ring like scattered patterns can be explained by considering the scattering of light by cylindrical surfaces [196]. These scattered fields are derived for an infinite right circular cylinder of diameter '$d_1$' when it is illuminated by a plane homogeneous wave $E_i = E_0 \exp(iq\hat{e}_i.x)$, propagating in the direction $\hat{e}_i = \sin\zeta_c\,\hat{e}_x - \cos\zeta_c\,\hat{e}_z$ where, $\zeta_c$ is the angle between the incident light wave and the cylindrical axis.

The shape dependence of the conic section, on the incident angle with respect to the cylinder axis, is explained by deriving the expression of scattered electromagnetic field from the cylindrical surface [154, 197]. Therefore the wave fronts are cones of half-angle $\zeta_c$ with their apexes at $z_c = -\frac{c}{\cos\zeta_c}$ . The propagation of the scattered waves can be visualized as a cone that is sliding down the cylinder. The direction of propagation at any point on the cone or wave normal $\hat{e}_s$ is $\hat{e}_s = \nabla f = \sin\zeta_c\,\hat{e}_r - \cos\zeta_c\,\hat{e}_z$. The pointing vector is therefore, in the direction of $\hat{e}_s$. From the above equation it is evident that on placing a screen at some distance from the cylinder (perpendicular to the incident light), the scattered pattern forms a conic section. When the $\zeta_c = 0^0$, the scattered pattern will be a circle, while for $\zeta_c \leq 45^0$, ellipse is formed on the screen that becomes hyperbola for $45^0 \leq \zeta_c \leq 90^0$. When the incident light is normal to the cylinder axis, a straight line pattern is formed [134]. This explains the reason for the observed ring like pattern.

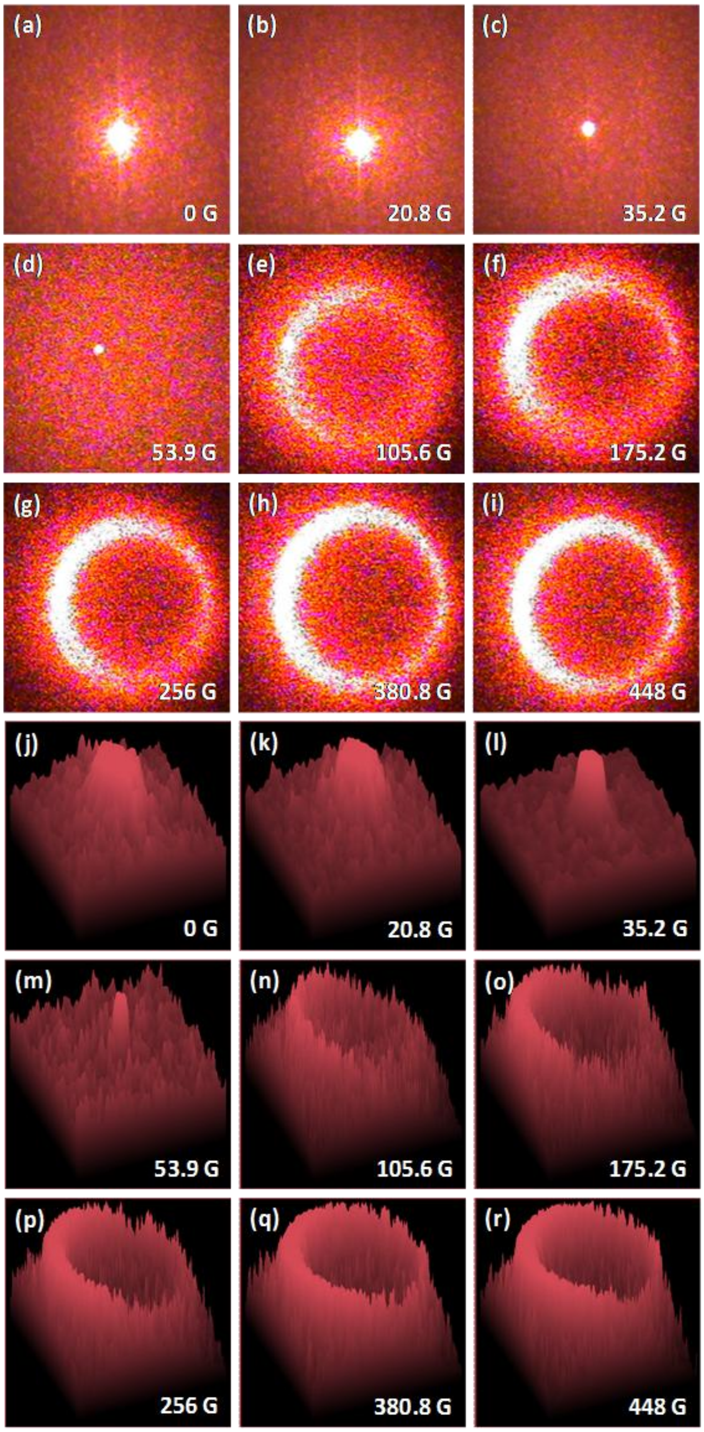

*Figure 3.8 (a) - (i) Scattered patterns from magnetic nanoemulsion for Φ = 0.0174 at field strengths 0, 20.8, 35.2, 53.9, 105.6, 175.2, 256, 380.8, and 448 G. (j) - (r) The corresponding surface plots.*

The transmitted scattered intensity pattern at $H$ = 380.8 G for Φ = 0.0174 is shown in **Fig. 3.9 (a)**. **Fig. 3.9 (b)** shows the expanded view of the lobe part. **Figs. 3.9 (c) - (g)** show the images of the lobe part at $H$ = 53.9, 105.6, 175.2, 256, 448 G and **Figs. 3.9 (h) - (l)** show the corresponding 3-D surface plots.

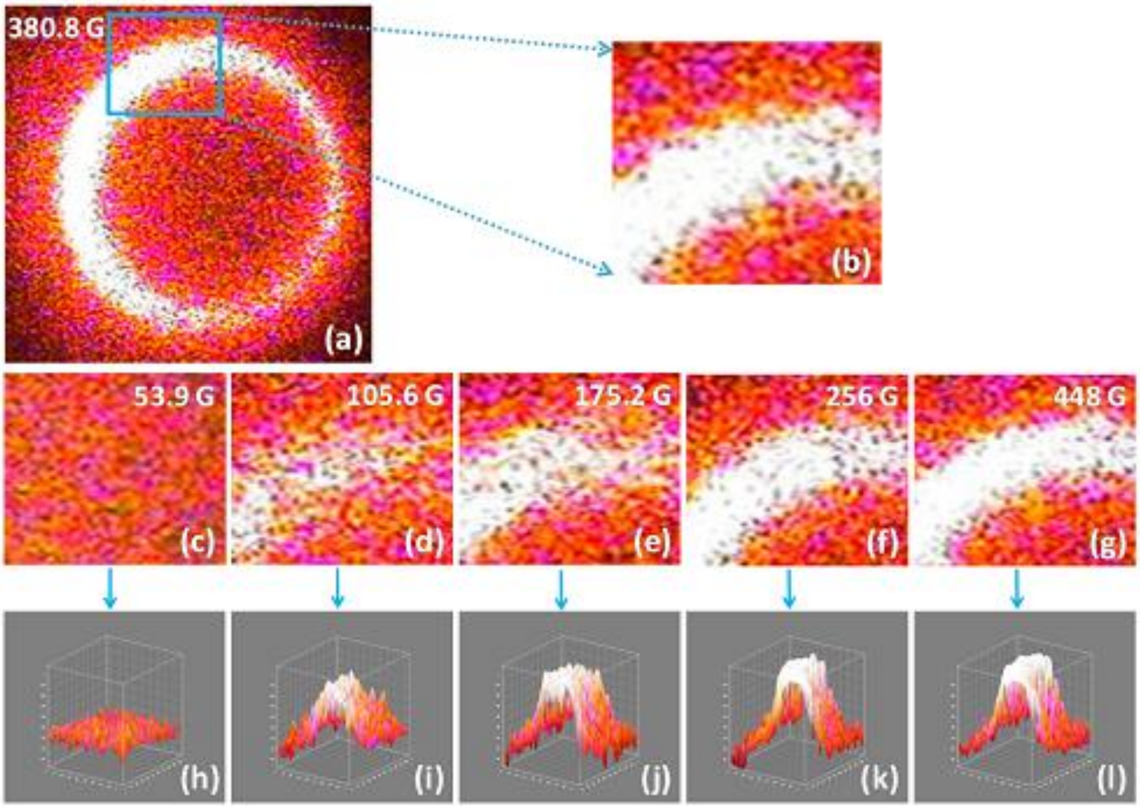

*Figure 3.9 (a) Image of the transmitted scattered pattern at* H = *380.8 G. (b) The magnified view of the speckle pattern shown in the box. (c) - (g) The speckle pattern of the same lobe part at* H = *53.9, 105.6, 175.2, 256, 448 G and (h) - (l) the corresponding 3-D surface plots.*

The lobe speckle intensity increases with the applied magnetic field only after $H_{c2}$. The scattering from single chains and columnar structures enhances the scattering intensity as well as the speckle contrast. The formation of ring like scattered pattern is due to the scattering of light by the chain like structures [196]. The anisotropic structure formation, under the influence of magnetic field, is evident from the ring like pattern observed here.

## 3.4. Conclusions

The role of surface charge on the critical magnetic field for various structural transitions in magnetic nanoemulsion of different volume fractions is studied for the first time. Three distinct critical magnetic fields are identified from the changes in the field dependent transmitted forward scattering light intensity, which correspond to the commencement of small aggregate formation, complete formation of linear aggregates before the commencement of lateral coalescence of individual chains, and the formation of densely packed columnar solid like structures through zippering of individual chains. The field induced anisotropic structure formation in the emulsion was evident from the ring like pattern observed. With decreasing Debye screening length, the aggregation rate was found to increase linearly. The experimentally observed critical fields were in good agreement with theoretical predictions at lower surfactant concentrations. These results provide better insights into the field induced structure formation and are useful in designing magnetic fluidic based optical devices.

*Chapter 4*

# Effect of field ramp rate on temporal evolution of equilibrium and non-equilibrium magnetic field driven microstructures in magnetic nanoemulsion

## 4.1. Introduction

Owing to the magnetic stimulus responsive nature, magnetic fluids (ferrofluid and ferrofluid emulsion) are ideal colloids to probe order-disorder transitions [18]. Such magnetic field induced structural transitions in magnetic fluids have been a topic of interest from both fundamental and practical point of view [86-89, 96]. Owing to their practical applications, magnetic fluids and their analogues have been studied extensively in recent years [41-46]. Magnetic colloids undergo different structural transition from gaseous phase (randomly dispersed nanoparticles) to ID, 2D, and 3D structures of aggregated nanoparticles (well separated chains, columns, bent walls or labyrinthine patterns or colloidal crystals) in the presence of magnetic field [66, 67, 77, 81, 84, 198]. Magnetic interaction energy between the chains depends on the applied magnetic field strength and the separation between the chains [199]. Lateral aggregation occurs when the magnetic interaction energy overcomes the potential energy barrier for the lateral aggregation. Parameters like thermal fluctuations, polydispersity, defects of chains, ramp rate, viscosity of carrier fluid, particle surface roughness, surface active moieties, lateral diffusion coefficient of chains, sample thickness, etc., determine the lateral aggregation [111, 199-201]. Though this field is rich with theoretical and simulation data, systematic experimental studies on equilibrium and non-equilibrium structures in real magnetic fluids are scarce.

This study is aimed at bridging this gap, to understand the field induced structural transitions, particularly their temporal evolution, dynamics, volume fraction, and the surfactant concentration on field driven structures. Here, we investigate the temporal evolution of field induced equilibrium and non-equilibrium microstructures under different surfactant concentrations in the presence of a magnetic field. The transmitted light intensity from the emulsions and optical phase contrast microscopy under different magnetic field strengths, zeta potential and hydrodynamic size distribution, are used to study the temporal evolution of structures under different conditions.

## 4.2. Materials and methods

The preparation of magnetically polarizable nanoemulsion used in this study is discussed in chapter 2. The experimental set-up is shown in **Fig. 2.5**. In this case, the magnetic field was switched on at a time, $t$ = 100 s and kept constant up to $t$ = 1000 s and, again switched off. Here, the direction of the applied magnetic field was parallel to the light propagation direction. The transmitted light intensity through the sample as a function of time is recorded through the photomultiplier tube, and the detailed procedure is explained in section 2.5.1 of chapter 2.

## 4.3. Results and discussion

### 4.3.1. Effect of SDS concentration on hydrodynamic size and zeta potential

The hydrodynamic size and the zeta potential distributions of ferrofluid emulsion for different SDS concentrations are shown in **Fig. 4.1 (a)** and **(b)**, respectively.

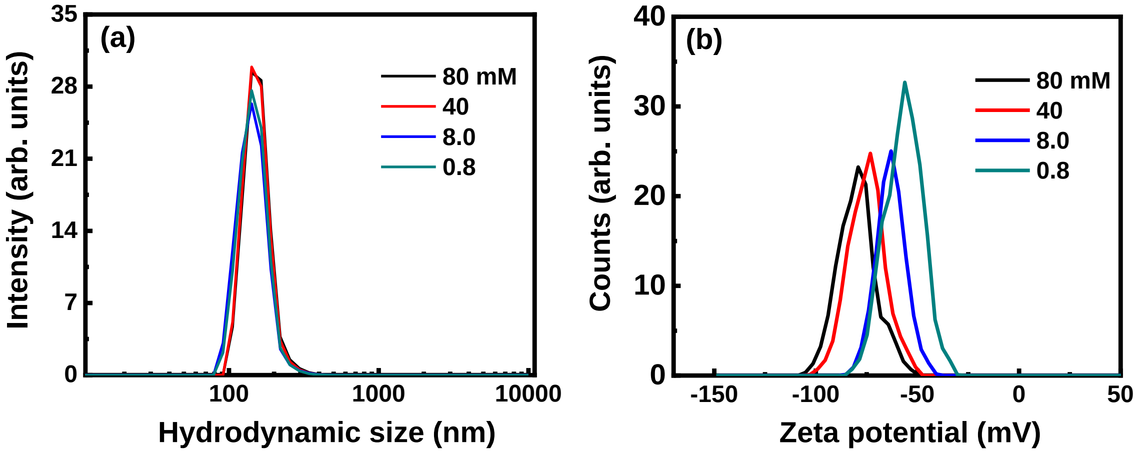

*Figure 4.1 (a) Hydrodynamic size distribution of emulsion droplets and (b) zeta potential distribution of ferrofluid emulsion at different SDS concentrations of 0.8, 8, 40, and 80 mM.*

The zeta potential of emulsion with 0.8 mM SDS was -56 mV, which was found to increase with surfactant concentrations. The average size of the droplets was unaffected by the surfactant concentrations. The lowest concentration of surfactant used here was sufficient to form a monolayer of surfactant molecules.

### 4.3.2. Effect of volume fractions and magnetic field strengths on field induced structures

The variation of the normalized transmitted intensity as a function of time, at different magnetic field strengths, for ferrofluid emulsion of different Φ with the same SDS concentration of 80 mM is shown in **Fig. 4.2**.

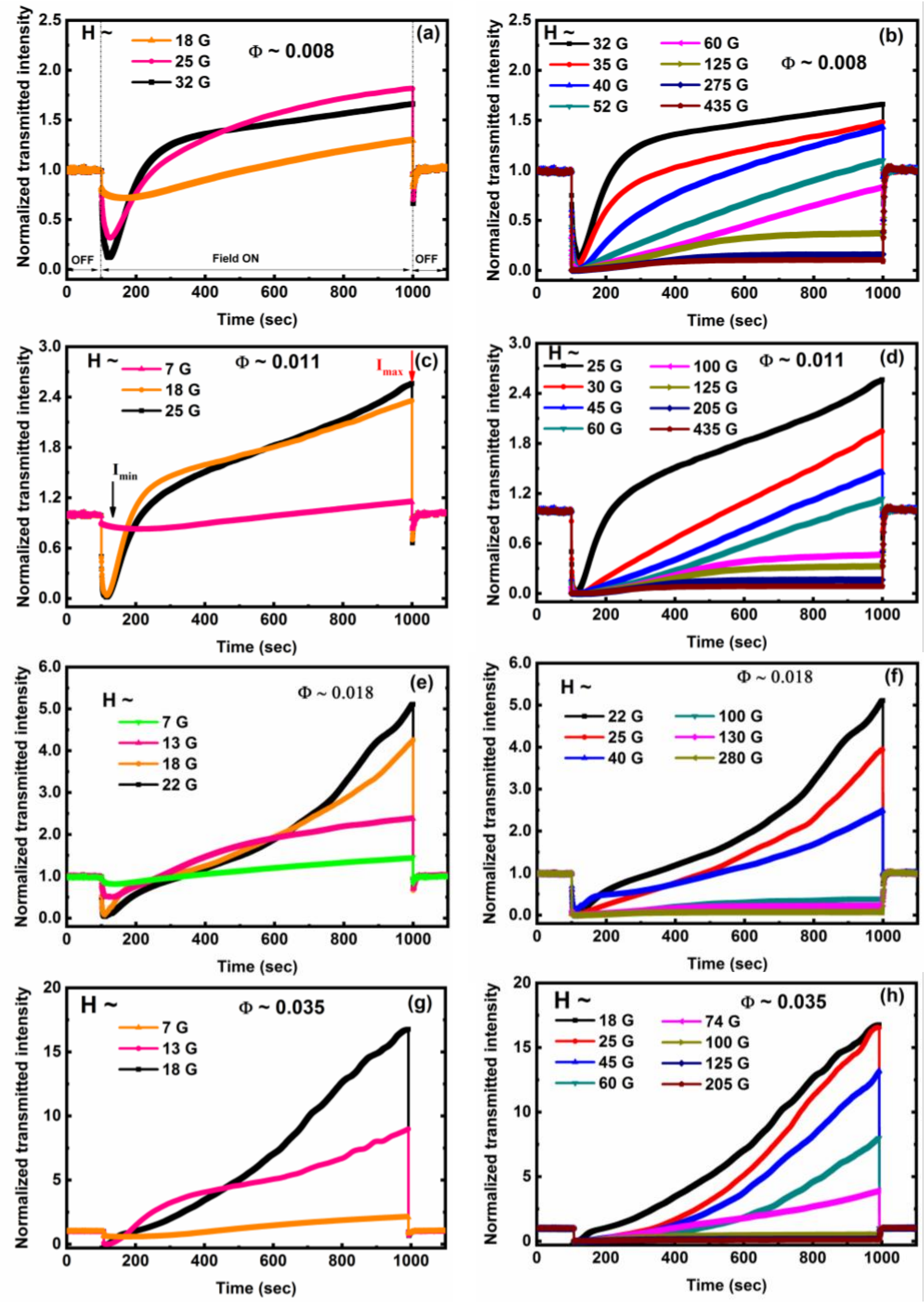

*Figure 4.2 Normalized transmitted intensity as a function of time at different magnetic field strengths for magnetically polarizable nanoemulsion of different Φ (a - b) 0.008, (c - d) 0.011, (e - f) 0.018 and (g – h) 0.035, where the SDS concentration in the emulsion was kept constant at 80 mM. Figures in the left panel are for lower magnetic fields, and the right panel is for higher field strengths.*

The transmitted light intensity remains constant during the initial time interval ($t$ = 0 - 100 s), when the magnetic field was zero. As the size of the droplet is less than the wavelength of the incident light, i.e., $d_1 < \lambda$ ($\lambda$ = 632.8 nm), the scattering is essentially due to Mie scattering. On switching the field ON, for low volume fraction (Φ = 0.008) of droplets, the transmitted intensity showed a rapid decrease in intensity for a certain time interval (~ 2 s at $H$ = 435 G for Φ = 0.008). After being in a low transmittance state (called $I_{min}$) for a short time duration of ~ 60 s, the transmitted intensity increases again and gets stabilized after 1000 s (called $I_{max}$). The magnitude of $I_{min}$ was maximum (i.e., nearly zero intensity) at an optimum applied magnetic field strength of 32 G (at Φ = 0.008) as observed in **Fig. 4.2 (a)** and **(b)**. Above 32 G, the difference in $I_{max}$ and $I_{min}$ value (i.e., $\Delta I = I_{max} - I_{min}$) starts to decrease. A similar trend in the temporal variation of transmitted intensity is observed for all volume fractions, as shown in **Figs. 4.2 (c – h)**. The most interesting observation is that the ΔI was close to zero at a sufficiently high magnetic field strength. The variation in the temporal evolution of transmitted intensity is explained as follows:

In the absence of any magnetic field, the emulsion behaves like a gas, where the droplets are under Brownian motion due to thermal agitation. When subjected to a magnetic field, linear aggregation of droplets takes place, followed by lateral aggregation at high magnetic field strength. However, under the application of a constant magnetic field, the time required for the aggregation of droplets depends on the interplay of two competing forces: the viscous drag and the magnetic force. The time required to form a doublet of droplets in the presence of magnetic field is defined as [138, 202]

$$t_c = \frac{6\pi a_1^2 \eta}{5F_{max}}\left[\left(\frac{r}{2a_1}\right)^5 - 1\right] \tag{4.1}$$

where $F_{max}$ is the maximum magnetic force between two droplets, which is given by $F_{max} = \frac{\mu_0}{4\pi}\frac{3m_0^2}{8a_1^4}$. The interdroplet spacing is considered as the average inter-particle spacing for a given Φ. The typical aggregation time to form doublets, triplets and chains of aggregating droplets of 200 nm size is ~ a few seconds. E.g. the aggregation times for Φ = 0.008, 0.011, 0.018, and 0.035 are 103, 50, 16, and 3 msec (assuming

$\eta = 0.00089\ Pa.s, a_1 = 100\ nm, \chi_{eff} = 1.09$), respectively for an external magnetic field $H$ = 50 G. This is because the aggregating droplets experience a much lower viscous force ($F_d = 6\pi\eta a_1 v$, where $v$ is the flow velocity relative to droplet) as compared to the dipolar magnetic force in an extremely low viscous carrier liquid like water.

For a ferrofluid emulsion containing dispersed random scatterers, the transmitted light intensity ($I_t$) is given by [170]

$$I_t = I_0 exp(-\alpha_{ext} L) = I_0 exp(-n_s C_{ext} L) = I_0 exp(-n_s Q_{ext} \pi a_1^2 L) \tag{4.2}$$

where $L$, $I_0$, $n_s$, $\alpha_{ext}$, $Q_{ext}$ and $C_{ext}$ are the path length, incident light intensity, scatterer number density, extinction coefficient, scattering extinction efficiency, and extinction cross section, respectively. Here,

$$C_{ext} = \frac{2\pi}{q^2} \sum_{n=1}^{\infty} (2n+1) Re\{a_n + b_n\} \tag{4.3}$$

where $a_n$ and $b_n$ are the Mie scattering coefficients. The extinction efficiency ($Q_{ext}$) is very less for emulsion droplet radius ($a_1 \sim 100\ nm$) and size parameter ($qa_1 \sim 1$). Doublets are formed when size parameter increases from $qa_1 \sim 1$ to $qa_1 \sim 2$, corresponding to a sudden increase in scattering extinction efficiency from $Q_{ext} \sim 0.7$ to $Q_{ext} \sim 5.7$. Therefore, the formation of doublets and triplets or short chains under applied field increases the scattering size parameter, which results in a sudden increase in the scattering extinction efficiency, leading to a steep decrease in transmitted intensity on the application of an external magnetic field, as observed in **Fig. 4.2** [165]. The steady and slow increase in the transmitted light intensity observed at lower applied magnetic fields is due to the longer time required for the aggregation process to attain equilibrium structure [138]. The magnetic droplets self-assemble to form a linear structure when $\Lambda_1 > 1$. The lateral coalescence of chains depends on lateral diffusion coefficient of droplets and chains, depending on the magnetic field strength, volume fraction, polydispersity and viscosity of carrier fluids [201, 203, 204].

The diffusion coefficient of a single emulsion droplet, containing superparamagnetic particle dispersed in water in the presence of magnetic field is determined by Fick's law of diffusion given by [205] $j_x = -\Phi \frac{\partial \mu}{\partial x} \frac{1}{f(\Phi)}$ . Here, $j_x$ is the diffusion flow, $\mu$ is the chemical potential of droplets, $f(\Phi) = 6\pi\eta a_1(1 + \kappa_f \Phi)$ is the friction coefficient, $\kappa_f$ is the coefficient of hydrodynamic interaction ~ 6.55 (for hard sphere) [206]. The chemical potential for droplet is $\mu = \mu(H = 0) + \mu_H$, where, $\mu\ (H = 0)$ is the chemical potential of the solution at zero magnetic field. Magnetic contribution to the chemical potential $\mu_H$ is given by $\mu_H = -k_B T ln(sinh\xi_e/\xi_e)$. In ferrofluid emulsion, magnetic droplets are assumed to be superparamagnetic in nature and in presence of magnetic field, and magnetization is given by the Langevin law, $M = \Phi M_s L(\xi)$, where, $\xi = \frac{\mu_0 M_s V H}{k_B T}$ is the Langevin parameter and $L(\xi) = coth(\xi) - \xi^{-1}$ is the Langevin function. The magnetic interdroplet interactions under the applied magnetic field can be estimated by using mean field approximation and an effective field model, where the equation for magnetization can be expressed as $M = \Phi M_s L(\xi_e)$. Here, $\xi_e$ is given by the self-consistent equation $\xi_e = \xi + \Lambda^* \gamma_c L(\xi)$, where, $\Lambda^* = \mu_0 M_s^2 V \frac{\Phi}{k_B T}$ is the reduced parameter of dipolar interaction, $\gamma_c$ is the effective field constant. If $\gamma_c = 0$, the interdroplet interaction is absent. The classical Lorentz value of $\gamma_c = 0.33$ [205]. The diffusion coefficient $(D_\perp)$ of emulsion droplets perpendicular to the magnetic field direction is equal to

$$D_\perp = D_0(\Phi) - \frac{k_B T}{f(\Phi)} \alpha_{\gamma_c}(\Phi, H) \tag{4.4}$$

Here, $\alpha_{\gamma_c}(\Phi, H) = \frac{\gamma_c \Lambda^* L^2(\xi_e)}{1-\gamma_c \Lambda^* L'(\xi_e)}$, where $L'(\xi_e)$ is the first derivative of the Langevin function $L(\xi_e)$. Assuming a magnetic droplet of the diameter of 200 nm dispersed in water with a Φ = 0.035, the $D_\perp$ is found to be $3.26 \times 10^{-12} m^2 s^{-1}$ in the absence of a magnetic field. For $H$ = 400 G, the $D_\perp$ is found to be $2.9 \times 10^{-13} m^2 s^{-1}$ clearly shows that the lateral diffusion coefficient $(D_\perp)$ of droplet decreases on increasing the magnetic field strength.

The lateral diffusion coefficient of a straight chain containing *N*, number of droplets is given by [201]

$$\frac{(D_\perp)_{chain}}{D_0} \approx \frac{A_1}{\sqrt{\Lambda_1}} g(N) q a_1 + f(N) \tag{4.5}$$

Substituting $\Lambda_1$ on Eqn. (4.5)

$$\frac{(D_\perp)_{chain}}{D_0} \approx \sqrt{\frac{9k_B T}{\pi \mu_0 a_1^3 \chi_{eff}^2}} \left(\frac{A_1}{H}\right) g(N) q a_1 + f(N) \tag{4.6}$$

Here, $A_1$ is a constant (~ 3.0 ± 0.2), $g(N)$ is a function of $N$ (= $N^{-0.7}$, for $N > 5$), $f(N) = [3\,ln(2N) + 1.254]/4N$. Since, coupling constant, $\Lambda_1$ is proportional to $H^2$, the lateral diffusion coefficient $(D_\perp)_{chain}$ of a chain is inversely proportional to the magnetic field strength as per Eqn. (4.6).

The lateral diffusion coefficient of a chain containing different number of droplets (*N*), computed as a function of the magnetic field, is shown in **Fig. 4.3 (a).** It is observed that $(D_\perp)_{chain}$ is maximum for the lowest applied field and decreases on increasing the magnetic field. **Fig. 4.3 (b)** shows the lateral diffusion coefficient as a function of number of aggregating droplets in the chains, at different magnetic field strengths.

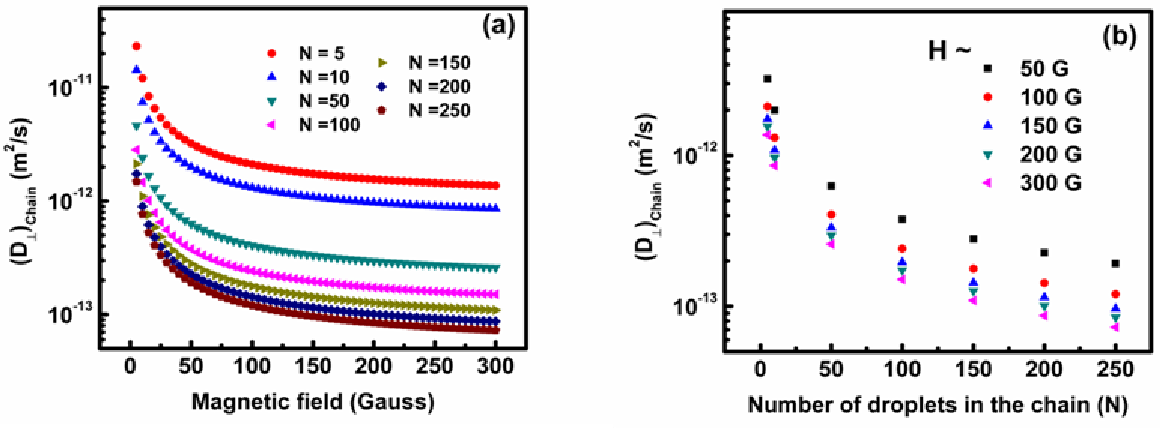

*Figure 4.3 (a) Lateral diffusion coefficient of magnetic chain, containing different number of droplets,* N, *as a function of magnetic field, (b) lateral diffusion coefficient of chains as a function of* N, *during the chain formation at different magnetic field strengths (*H = *50, 100, 150, 200, and 300 G).*

It is observed that $(D_{\perp})_{chain}$ decreases as the number of droplets in the chain (i.e., the chain length) increases, on increasing the applied magnetic field strength. When zippering aggregation is less favored, the system contains more linearly aggregated chains (i.e., more scatterers), which causes the transmitted light intensity to decrease. Therefore, due to the presence of larger number of scatterers and slow lateral diffusive motion of linear aggregates, the transmitted light intensity decreases at higher magnetic field strength, as shown in **Fig. 4.2**. According to Halsey and Toor model [194], linear particle chain structures acting as dipolar chains, suspended in a fluid exhibit strong Landau-Peierls fluctuation, which induces long range attractive interaction among the dipolar chains. The longitudinal and transverse fluctuations of wave vector $q$ in a dipolar chain can generate a local gradient in the concentration of dipoles and fluctuation in the lateral field. The total interaction energy is the sum of the interaction energy between the fluctuations of the chains and the energy of deformation required for the fluctuation mode. The strong peak at $q\rho \cong 1$ indicates that only fluctuation with wavelength comparable to the separation distance can interact strongly. The lateral interaction is independent of the applied field strength and decays as a power law. Martin and co-worker modified Halsey and Toor model to show that the lateral coalescence depends on both the applied magnetic field strength as well as thermal fluctuations of a dipolar chain [149]. A large amplitude fluctuation draws two chains together to initiate the aggregation. When the coalescence time scale $\tau_c$ is much shorter than the characteristic relaxation time of the fluctuation $\tau_f$, the fluctuation persists long enough to drive the coarsening process. For a dipolar chain that is surrounded by neighboring particles and chains, by using local-mode model developed by Krall and Weitz [207], the fluctuation amplitude is given by [199]

$$\frac{\delta(\rho)}{d_1} = \left(\frac{8}{3\zeta(5)N\Lambda_1}\right)^{1/2} \left(\frac{\rho}{d_1}\right)^2 \qquad (4.7)$$

where $\zeta(5) = \sum_{n=1}^{\infty}(1/n^5) \approx 1.037$ is the zeta function. The Eqn. (4.7) shows that the fluctuation amplitude varies with interaction energy as $\delta(\rho) \sim \Lambda_1^{-1/2}$. As magnetic field strength increases, the fluctuation amplitude decreases; hence the chains behave as a rigid system that restricts the lateral movement of chains towards each other [120, 208]. The saturation value of transmitted intensity at high magnetic field strength (**Fig. 4.2)** decreases as the volume fraction of the droplet increases. The nonlinear behavior of light transmission through ferrofluid emulsion depends on the aggregation kinetics and the diffusion coefficient of magnetic droplets and chains. In each transmitted intensity variation curve (**Fig. 4.2**), there is a minimum intensity point (i.e., $I_{min}$) and a maximum intensity point (i.e., $I_{max}$). The difference between these two intensity values is a measure of the effective transparency of ferrofluid emulsion.

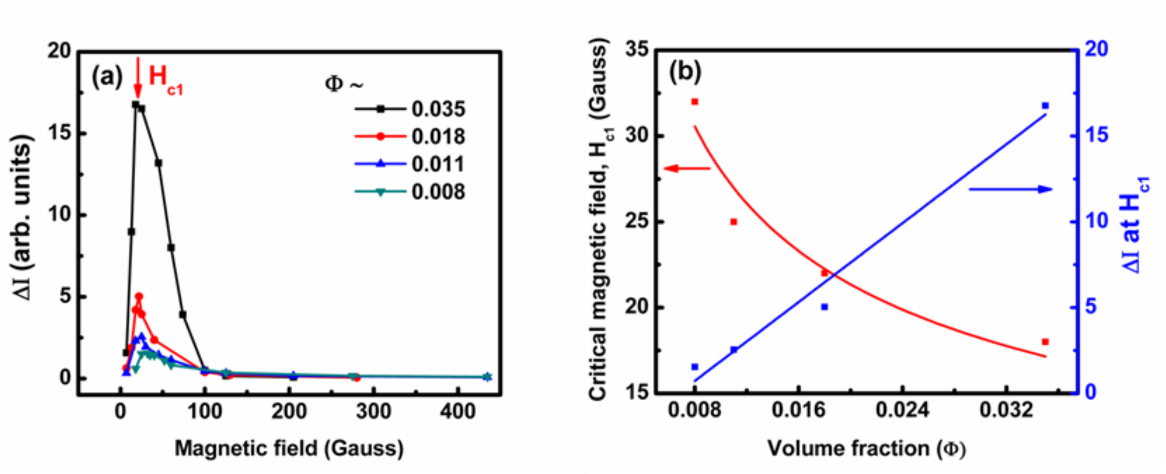

*Figure 4.4 (a) $\Delta I$ as a function of an applied magnetic field, for different volume fractions, (b) the critical magnetic field ($H_{c1}$) and $\Delta I_{max}$ ($\Delta I$ at $H_{c1}$) as a function of droplet volume fraction.*

**Figure 4.4 (a)** shows the difference in transmitted light intensity (ΔI, obtained from **Fig. 4.2**), as a function of the external applied magnetic field, for different volume fractions of the emulsion. ΔI decreases above a critical magnetic field ($H_{c1}$) and reaches a minimum at another magnetic field strength, beyond which ΔI remains constant at a minimum value. Due to excessive heating of the solenoid, application of a sufficiently large magnetic field was not attempted. Therefore, the variation of the transmitted light intensity (with the volume fraction of droplets and SDS concentration) is studied only at the first critical magnetic field. **Fig. 4.4 (b)** shows critical magnetic field and ΔI at $H_{c1}$ as a function of Φ. The $H_{c1}$ is defined as the field at which effective transparency of ferrofluid emulsion becomes maximum. $H_{c1}$ follows a power law decay with the volume fraction ($\Phi^{-x'}$), where the exponent $x'$ is found to be 0.4, with a $R^2$ value of 0.94. On the other hand, $\Delta I_{max}$ increases linearly with the volume fraction with a slope of 575 ($R^2$ ~ 0.96), due to the increase of inter-chain spacing with the volume fraction [140]. To obtain further insight into the internal microstructures, phase contrast microscopy images were obtained at different magnetic fields.

### 4.3.3. Temporal evolution of microstructures at low and high magnetic field strengths

The temporal evolution of microstructure is studied at two magnetic field strengths (50 and 300 G), at a fixed volume fraction of 0.035 and a $C_s$ of 80 mM. The phase contrast optical microscopic images of the ferrofluid emulsion (Φ = 0.035) at different time intervals, for a constant magnetic field of 50 G is shown in **Fig. 4.5.**

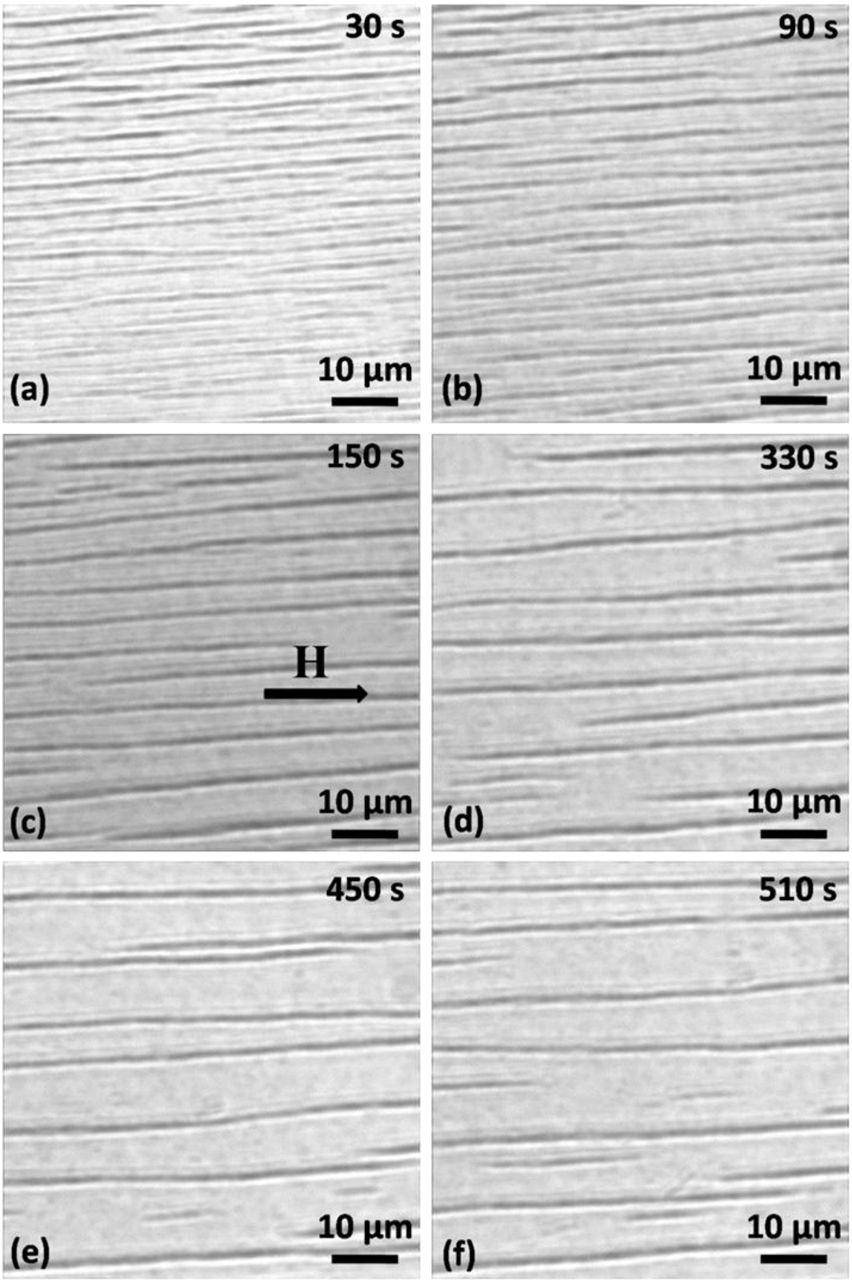

*Figure 4.5 Temporal evolution of field-induced microstructures of ferrofluid emulsion of Φ = 0.035 at* H *= 50 G, observed under a phase contrast optical microscope. The arrow in Fig. 4.5 (c) shows the direction of the magnetic field.*

It was observed that the lateral movement of chains is very fast at $H$ = 50 G. As time progresses, both the thickness of chains and the spacing between the columns increase. This increased inter-column spacing results in an increase in the transmitted light intensity as observed in **Fig. 4.2**. The flexibility of chains in the present case is attributed to the fluctuation of the induced moments [199, 200].

The phase contrast optical microscopic images of ferrofluid emulsion (Φ = 0.035) at different time intervals after applying a magnetic field strength of $H$ = 300 G, is shown in **Fig. 4.6**. Here, we observed that longer chains are formed almost immediately along the field direction within a fraction of seconds (since for Φ = 0.035, the aggregation time to from doublets was found to be $7.6 \times 10^{-5} s$, for an external magnetic field $H$ = 300 G) that spanned almost the entire length of the sample area. More rigid chains are formed at a high magnetic field ($H$ = 300 G, **Fig. 4.6**), which were not seen at low magnetic field strength ($H$ = 50 G, **Fig. 4.5**). At high magnetic field, the magnetic chains were interconnected to each other, which prevents structural rearrangement at $H$ = 300 G. The chain thickness at $H$ = 300 G was less than the thickness of chains observed at $H$ = 50 G. Moreover, the chains at the higher field were more disordered compared to the chains at lower magnetic field, due to the rapid quenching to high magnetic field [78, 209]. The observed temporal evolution of field induced structures manifests the equilibrium and non-equilibrium structures formed under different magnetic fields.

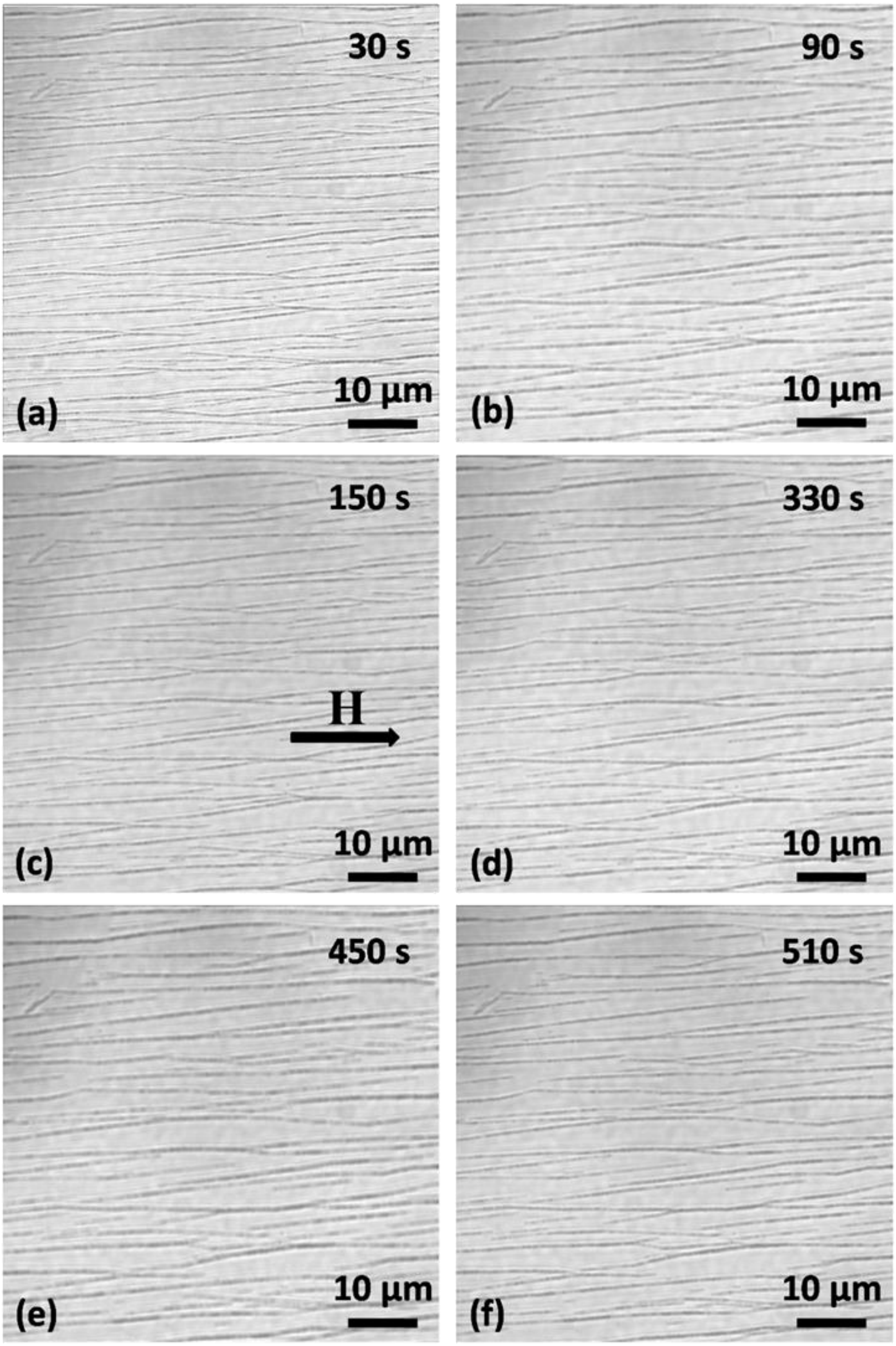

*Figure 4.6 Temporal evolution of field-induced microstructures of ferrofluid emulsion of $\Phi = 0.035$ at* H *= 300 G, observed under a phase contrast optical microscope. The arrow in Fig. 4.6 (c) shows the direction of the magnetic field.*

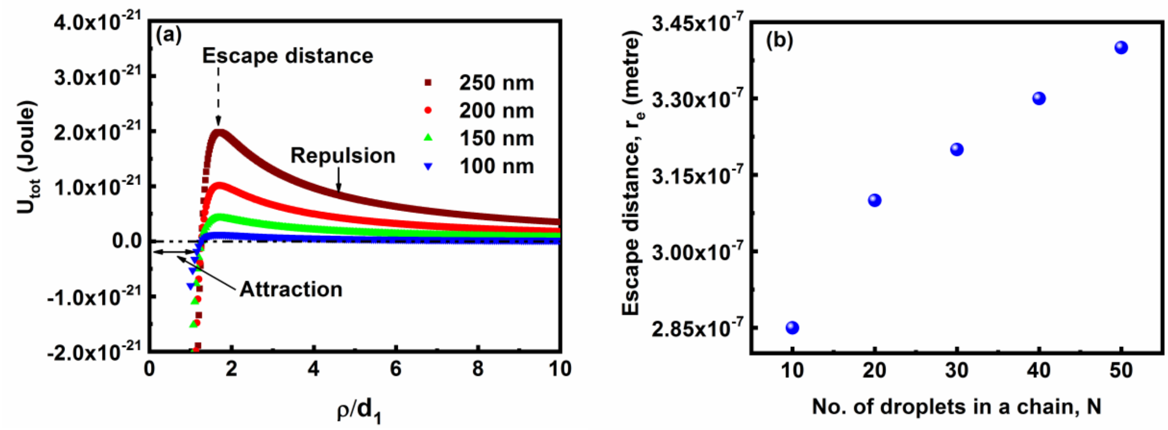

*Figure 4.7 (a) The interaction energy ($U_{tot}$) between two magnetic chains, each containing 50 magnetic droplets of different diameters, $d_1$ = 100, 150, 200 and 250 nm, as a function of lateral separation (ρ), (b) Escape distance, $r_e$ as a function of number of droplets ($d_1$ ~ 200 nm) present in a chain at an external magnetic field of 50 G.*

**Figure 4.7 (a)** shows the interaction energy between two parallel chains, each containing 50 magnetic droplets of different diameters, $d_1$ = 100, 150, 200 and 250 nm, as a function of lateral separation, $\rho$, using equation [199] $U_{tot} = \sum_i \sum_{j>i} U_{ij}^{dip} = \sum_i \sum_{j>1} \frac{\mu_0}{4\pi} \frac{m_i.m_j - 3(\hat{r}.m_i)(\hat{r}.m_j)}{r^3}$. The vertical shift in this case is constant at one droplet radius, corresponding to an off-registry position. The interaction energy curve consists of two parts: an attractive part and a repulsive one. The magnitude of the energy barrier increased from $1.2 \times 10^{-22}$ to $1.9 \times 10^{-21} J$ as the droplet diameter increases from 100 to 250 nm for a fixed chain length ($N$ = 50) at an external magnetic field of ~ 50 G. For the lateral aggregation of two chains, applied energy needs to overcome the energy barrier [191]. In the off-registry position, where the two chains are attracted at close range, there is a distance beyond which the interaction force becomes repulsive, called the escape distance. **Fig. 4.7 (b)** shows the escape distance as a function of chain length. The escape distance increases from 285 to 340 nm as the number of droplets in a chain is increased from 10 to 50. If the average distance among the chains is greater than the escape distance, a fewer chains coalesce. On increasing the droplet concentration, if the chain separation decreases to within the escape distance, more chains attract each other, resulting in the formation of columns by lateral aggregation of chains [111].

In a system with a large distribution of chains of random length, position, and relative vertical shift, the total potential energy can have a large number of local minima and maxima. At certain ramp rates, the system may get trapped in one of the local minima in the potential energy curve, which is deep enough to overcome by thermal energy of the droplets. As chains approach each other from the random position and orient at high magnetic field, they stick to one another, as a result of trapping in a local potential energy minima. For high Φ, the longer chains are formed very quickly due to the shorter aggregation time. Moreover, as there are more chains within the escape distance attracting each other, more possible pathways exist for the chains to approach the aggregation center resulting in a more complex pattern at a high field strength of 300 G, as shown in **Fig. 4.6**.

The average inter-chain spacing determined using 'IMAGE J' software from microscopic images shown in **Figs. 4.5** and **4.6**, as a function of time for ferrofluid emulsion of Φ = 0.035 at H = 50 and 300 G, respectively, are shown in **Fig. 4.8 (a)** and **(b)**.

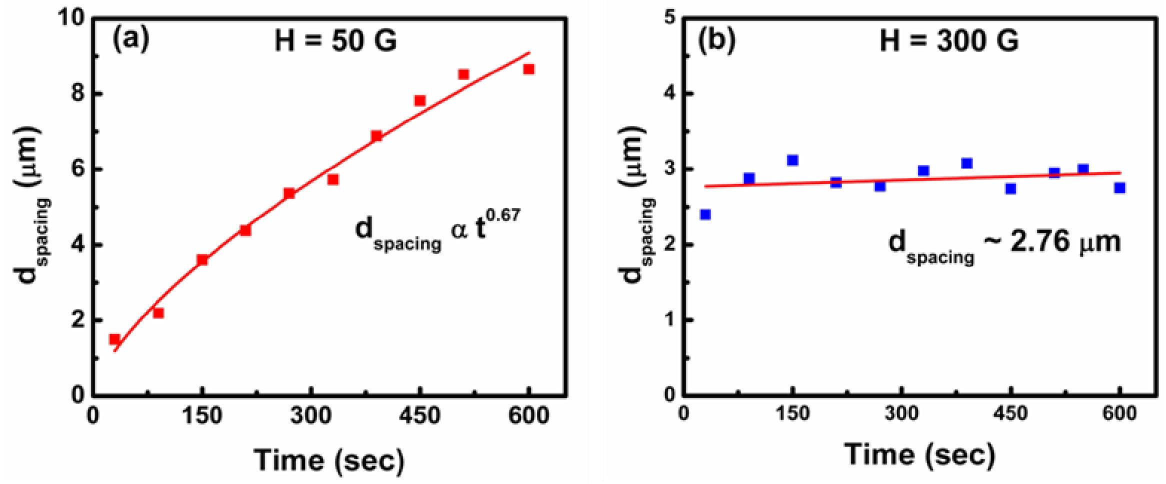

*Figure 4.8 The average inter chain spacing as a function of time for ferrofluid emulsion of Φ = 0.035 at (a) 50 G and (b) 300 G.*

For low magnetic field strength of 50 G, the average inter-chain spacing ($d_{spacing}$) increases and follows a power law rise dependence with time, i.e., $d_{spacing} \sim t^{x'}$, where the exponent $x'$ was found to be 0.67 ($R^2$ = 0.97). Interestingly, the measured power law exponent ($x'$ = 0.67) is found to be between the values (0.5 to 0.75) reported earlier [199]. For high magnetic field strength of 300 G, the average inter-chain spacing remains independent of time (i.e., $d_{spacing}$ ~ 2.7 μm), as observed in **Fig. 4.8 (b)**. The temporal variation observed in inter-chain spacing is due to the slow lateral movement of magnetic chains, which arises from the weak fluctuating thermal force [78]. Our experimental results are consistent with the previous findings, where the spacing between the chains and the thickness of the chains in a ferrofluid was inversely proportional to the magnetic field strength [78, 210].

### 4.3.4. Effect of surface charge screening on transmitted light intensity

The difference in the transmitted light intensity, as a function of external applied magnetic field for ferrofluid emulsion of Φ = 0.011, at different surfactant concentrations is shown in **Fig. 4.9**.

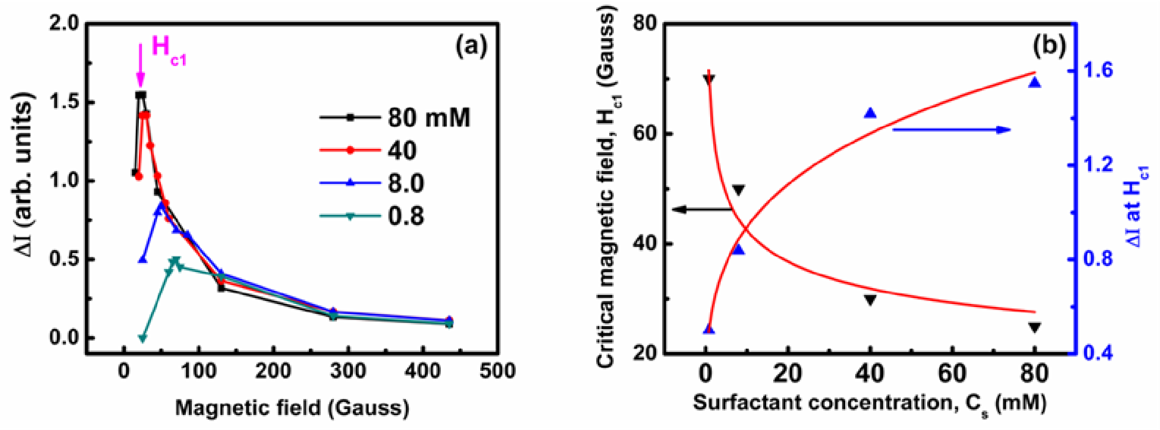

*Figure 4.9 (a) $\Delta I$ as a function of applied magnetic field at different SDS concentration, $C_s$ = 0.8, 8, 40, and 80 mM. (b) critical magnetic field, $H_{c1}$ and $\Delta I$ at $H_{c1}$ as a function of $C_s$. The emulsion volume fraction was 0.011.*

As $C_s$ increases from 0.8 to 80 mM, $H_{c1}$ decreases from 65 to 25 G, and ΔI at $H_{c1}$ increases from 0.5 to 1.55. The $H_{c1}$ follows a power law decay with the surfactant concentration ($C_s^{-x'}$), where the exponent $x'$ is found to be 0.2 ( $R^2$ ~ 0.94). For the surfactant concentration of 0.8, 8, 40, and 80 mM, the Debye screening length was obtained to be 10.75, 3.40, 1.52, and 1.10 nm, respectively, and the corresponding zeta potentials were found to be -56, -63, -73, and -79 mV, respectively. The electric double layer of droplets containing magnetic nanoparticles can be imagined as a core-shell spherical system, where the core is magnetic, and the shell is electrically charged. As the surfactant concentration increases, the surface charge is sufficiently screened, and hence, the electric double layer thickness of the droplets decreases where the magnetic interaction is dominant over the electrostatic repulsion [211]. To form a stable field induced chain, the magnetic dipolar interaction energy under an applied magnetic field must be greater than the sum of electric repulsive interaction energy and Brownian thermal energy. On increasing the SDS concentration, the interdroplets spacing becomes smaller. The onset of field induced ordering and zippered structures are formed at a lower magnetic field strength, as observed in **Fig. 4.9**. This stronger effective interaction (magnetic interaction over electric repulsive interaction and Brownian thermal energy) among the droplets at higher SDS concentration results in the formation of thicker columns through lateral aggregation, leads to increased inter-column spacing. This explains the observed increase in the ΔI with the surfactant concentration. The potential applications of these magnetic fluids are in tunable light attenuators or light switches where the magnetic field can be used to control those properties. This work demonstrates that the light transmission through magnetic emulsion can be controlled with the different parameters like volume fraction of droplet, surfactant concentration, magnetic field strength, magnetic field ramp rate. The reversible and fast response of emulsion has interesting practical applications.

## 4.4. Conclusions

The effect of volume fraction of magnetic droplets, magnetic field strength, and surfactant concentration on the temporal evolution of magnetic field induced structures, is studied using time dependent transmitted intensity measurement and phase contrast optical microscopy. The transmitted light intensity through ferrofluid emulsion is found to decrease after a certain critical field ($H_{c1}$) and reaches a minimum at a higher magnetic field. At low magnetic field strength ($H$ = 50 G), the long chains and zippered structures are formed by lateral chain aggregation where the spacing among the chains is found to increase with time. At higher magnetic field strength ($H$ = 300 G), the chains are interconnected to each other and the spacing between the chains remains constant with time, which was consistent with the observed time independent transmitted light intensity. With increased volume fraction of droplet and surfactant concentration, a larger number of individual non-zippered chains are observed at higher magnetic field strength due to the reduction of lateral diffusion of magnetic chains in the dispersion. These results confirm that the lateral diffusion of chains is hindered at high magnetic field strength due to reduced thermal fluctuation.

## *Chapter 5*

# Magnetic field induced optical transparency and magneto-optical birefringence in magnetic nanoemulsion

## 5.1. Introduction

Magnetic nanofluids are very interesting stimulus responsive materials whose optical properties can be controlled by an external magnetic field [18]. The magnetic field assisted assembly of magnetic nanoparticles show interesting optical phenomena, which is dictated by the competition between hydrodynamic and magnetic forces [87, 156, 198, 212]. Magneto optical properties like dichroism and birefringence in pure ferrofluids and ferroemulsions have been studied in the past [86, 141, 153, 213-219]. A birefringence phenomenon, in general, is widely exploited in optical devices such as light modulator, quarter wave plate, half wave plate, etc [220, 221]. The initial thinking about the origin of birefringence in ferrofluid was due to the magnetization of the particles caused by Neel rotation [217]. Subsequent studies considered nanosized linear aggregates [141, 222], spatial anisotropy [215] and shape anisotropy [217] as the cause for magnetic birefringence in ferrofluids. Pan et al.[223] considered the combined effects of field-induced orientation of shape-anisotropic scatterers and the chain-like aggregation of magnetic particles in an external magnetic field as the cause for the magnetic field-induced optical anisotropy and used the Monte-Carlo technique to simulate the field dependence of magneto-birefringence. Di et al. [157] studied magnetic birefringence in magnetic fluids as a function of volume fraction and wavelength and showed that the birefringence increases with the concentration of particles. It was also reported that the magnetic permeability of magnetic nanoemulsion increases with magnetic field due to droplet elongation in the direction of magnetic field [224]. Shape anisotropy due to elongation of droplet in the presence of a small field is considered to be one of the reasons for field induced birefringence. In the earlier studies, though field induced transparency in magnetic fluids [134, 225] was observed in some cases, the conditions for the formation of such field induced transparency and reasons for such changes in the transmitted light intensity was not fully understood.

In this chapter, we study the field induced optical transparency and magneto-optical birefringence in magnetic nanoemulsions as a function of volume fraction. We observed that such field induced transparency is seen only above a certain volume fraction and magnetic birefringence is the cause of the observed transparency, which was further confirmed from the fact that the transmitted intensity (reduced birefringence), is proportional to the square of the magnetic field in the low field region.

## 5.2. Materials and methods

The preparation magnetic nanoemulsion used in this study is discussed in chapter 2. The experimental set-up is shown in **Fig. 2.6**. In this case, the direction of the applied magnetic field was perpendicular to the light propagation direction. The axes of polarizer and analyzer were set perpendicular to each other for the birefringence measurement whereas they were parallel for during the transmitted scattered pattern measurement. The detailed procedure of acquiring the transmitted light intensity through the sample and the scattered pattern as a function of external magnetic field is explained in section 2.5.1 of chapter 2.

## 5.3. Results and discussion

### 5.3.1. Transmitted light intensity through magnetic nanoemulsions

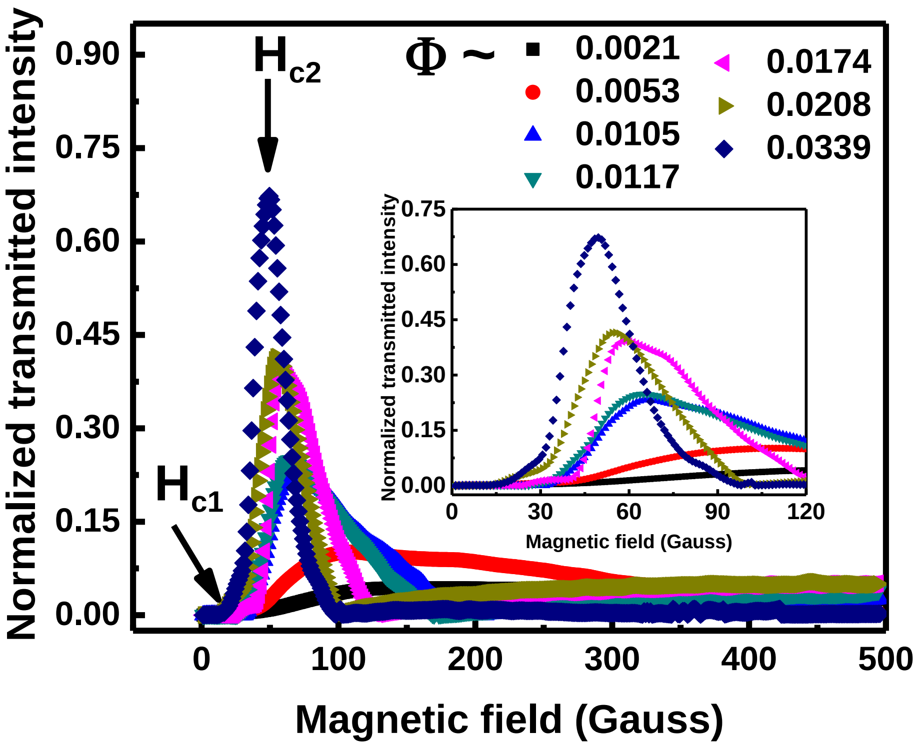

*Figure 5.1 Normalized transmitted intensity as a function of applied magnetic field. Inset shows the enlarged view of variation of light intensity at lower applied magnetic field values (0-120 G), for magnetically polarizable nanoemulsion of different volume fractions.*

**Figure 5.1** shows the transmitted light intensity measured as a function of applied magnetic field for magnetic nanoemulsion of different volume fractions 0.0021, 0.0053, 0.0105, 0.0117, 0.0174, 0.0208, and 0.0339. There was no significant increase in transmitted light intensity for the lower volume fractions ($\Phi < 0.0053$). But, above volume fraction of 0.0053, the transmitted light intensity increased with increase in magnetic field strength. The field above which the intensity starts increasing is defined as the first critical field ($H_{c1}$). The transmitted intensity reaches a maximum at another critical field called second critical field ($H_{c2}$), beyond which the transmitted light intensity decreases with magnetic field strength and reaches a plateau at a higher magnetic field strength. This behavior was observed for all volume fractions of nanoemulsion except for $\Phi < 0.0053$.

Here, we analyze why the transmittance increased above certain volume fractions and critical field. The IPS (given in Eqn. 1.25) for volume fractions 0.0021, 0.0053, 0.0105, 0.0117, 0.0174, 0.0208, and 0.0339 was estimated as 1100, 767.8, 572.3, 545.2, 453.7, 416.3, and 324.6 nm, respectively.

*Table 5.1 The volume fraction, the corresponding IPS (calculated using Eqn. 1.25), experimental critical magnetic fields ($H_{c1}$, $H_{c2}$) and the corresponding theoretical coupling constants ($\Lambda_{c1}$, $\Lambda_{c2}$).*

| Volume fraction (Φ) | IPS (nm) Theory | $H_{c1}$ (G) Expt. | $H_{c2}$ (G) Expt. | $\Lambda_{c1}$ (theory) | $\Lambda_{c2}$ (theory) |
|---|---|---|---|---|---|
| 0.0021 | 1100 | 56 | 110.5 | 8.63 | 33.6 |
| 0.0053 | 767.8 | 42 | 90.23 | 4.85 | 22.4 |
| 0.0105 | 572.3 | 31.9 | 66.08 | 2.80 | 12 |
| 0.0117 | 545.2 | 25.9 | 64.9 | 1.85 | 11.6 |
| 0.0174 | 453.7 | 23.6 | 59 | 1.53 | 9.58 |
| 0.0208 | 416.3 | 20.3 | 54.28 | 1.13 | 8.11 |
| 0.0339 | 324.6 | 18.8 | 49.56 | 0.97 | 6.76 |

**Table 5.1** shows the volume fraction, experimentally observed critical magnetic fields ($H_{c1}$, $H_{c2}$) and the corresponding theoretical IPS and coupling constants ($\Lambda_{c1}$, $\Lambda_{c2}$). The experimentally observed values of $H_{c1}$ and $H_{c2}$ are taken from the **Fig. 5.1**. The magnetic attraction force between two identical droplet having $m_1 = m_2 = m_0$ with a separation $r$ is expressed as $F_m = -\frac{6m_0^2}{r^4}$. As the attractive force is inversely proportional to the fourth power of separation between the droplets, the smaller the separation between the droplets, the larger is the attractive force. As Φ increases, the distance between the droplets becomes smaller (i.e., IPS), therefore a smaller magnetic field is required to form linear chains. When $\Lambda_{c1} < 1$, the droplets are under random motion and hence there are no

large linear scatterers in the fluid and hence no variation in light intensity was observed up to $H_{c1}$. When $\Lambda_{c1} > 1$ droplets begin to form dimers, trimers, short chains, etc. The aspect ratio of the chains increases with the applied magnetic field. The chains are oriented parallel to the magnetic field direction but are in random positions mimicking a 'nematic liquid like structure'. Due to this increase in the anisotropy, the intensity of transmitted light increases sharply. The second coupling constant, corresponds to the formation of long chains that serves as the nucleation centers for thicker columns that are formed by lateral coarsening of individual chains. When the applied magnetic field exceeds $H_{c2}$, the number of columns increase and they become more rigid. The gap between the columns increases and become saturated at higher magnetic field strength. **Fig. 5.1** shows that the sample with highest volume fraction of droplets have the highest optical transparency at $H_{c2}$, as compared to the lower volume fraction. Since the IPS at low concentration is large, interaction force between the droplets is weak. The number of chains per unit area increase as the concentration of magnetic droplets increases, which contributes to a high degree of structure anisotropy while the critical magnetic fields were found to decrease with increase in volume fraction.

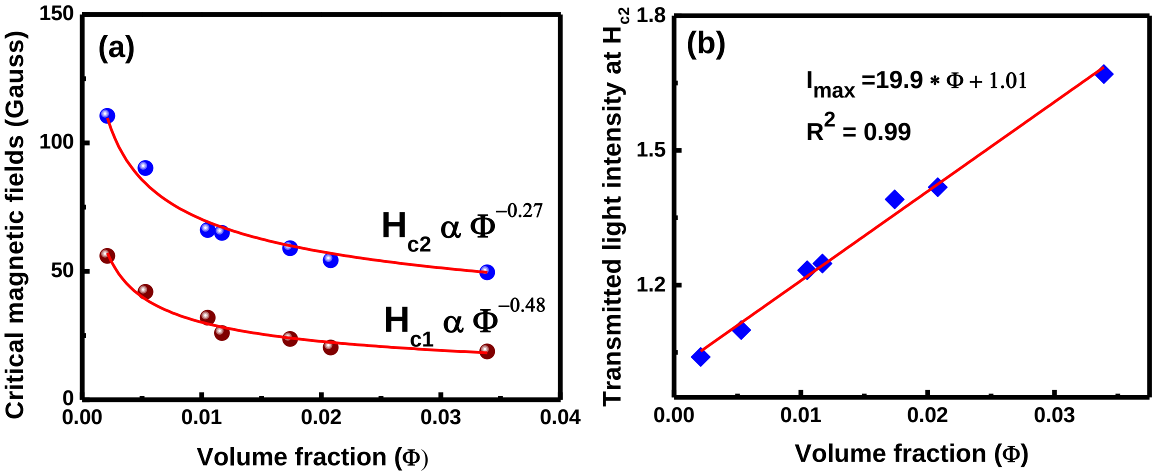

*Figure 5.2 (a) The critical magnetic fields as a function of droplet volume fraction. (b) The transmitted light intensity at $H_{c2}$ as a function of droplet volume fraction.*

**Figure 5.2 (a)** shows the critical magnetic fields as a function of droplet volume fraction. As Φ increases from 0.0021 to 0.0339, $H_{c1}$ decreases from 56.4 to 18.8 G and corresponding $H_{c2}$ drops from 110.5 to 49.56 G, respectively. Interestingly, $H_{c1}$ and $H_{c2}$ follow a power law decay with the volume fraction ($\sim \Phi^{-\mathrm{x}'}$), where the exponents were found to be 0.48 and 0.27, respectively. **Fig. 5.2 (b)** shows the transmitted light intensity at $H_{c2}$ as a function of Φ. The light intensity increases from 1.04 to 1.67 as Φ increases from 0.0021 to 0.0339, respectively. The intensity data is fitted with a linear equation, where slope is found to be 19.9 with a best fit ($R^2$) of 0.99. To obtain further insight into the internal microstructure at different magnetic fields, the light scattered from the samples is projected onto a screen placed perpendicular to the direction of incident light. The scattered patterns were recorded using a charge-coupled device (CCD) camera.

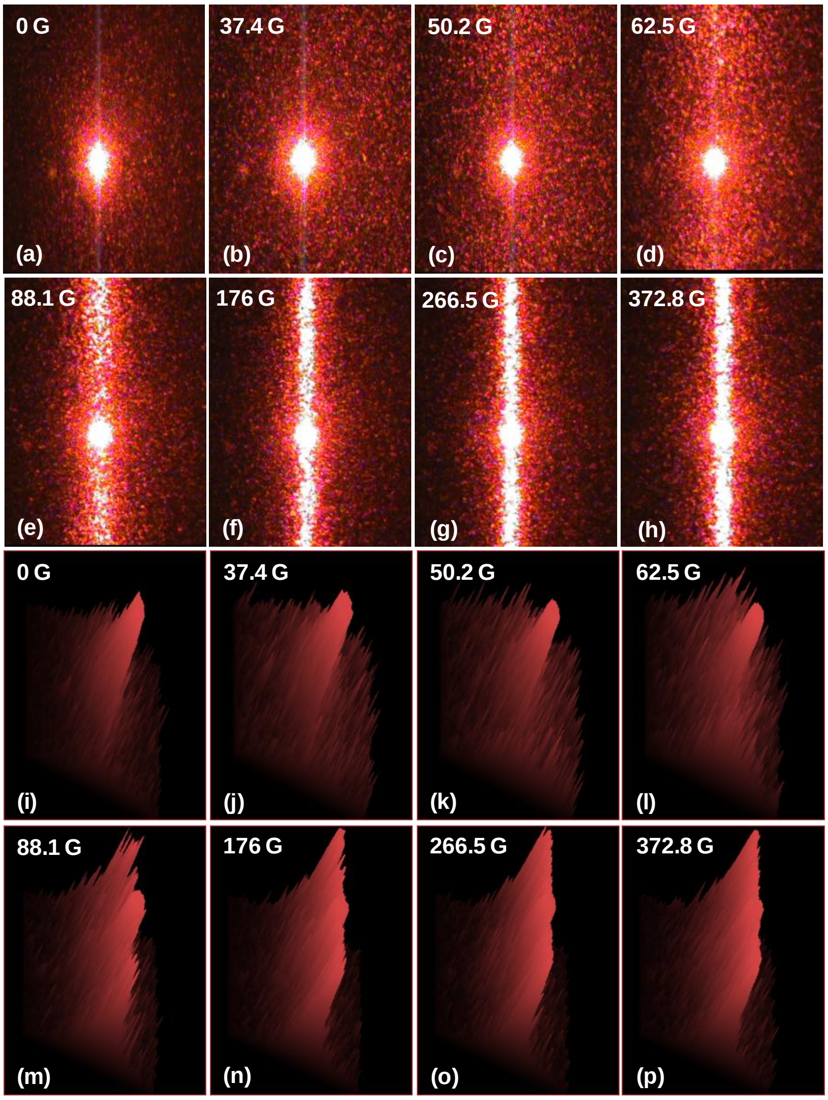

*Figure 5.3 (a - h) Scattered light intensity patterns from ferroemulsion and their corresponding surface plots for* $\Phi = 0.0339$ *at different magnetic fields (0, 37.4, 50.2, 62.5, 88.1, 176, 266.5, and 372.8 G). The magnetic field strength values are indicated in each image. (i - p) Surface plots of transmitted intensity patterns at different magnetic field strengths.*

**Figure 5.3 (a - h)** shows the forward scattered pattern at different magnetic field strengths (0, 37.4, 50.2, 62.5, 88.1, 176, 266.5, and 372.8 G) and (i - p) shows the corresponding surface plot from ferroemulsion of $\Phi = 0.0339$. In the absence of magnetic field, only a diffused spot was observed. As the field increases, the spot is transformed into a straight line. $H_{c1}$ occurs at 18.8 G for $\Phi = 0.0339$. **Fig. 5.3 (b)** shows the intensity pattern taken at 37.4 G, where more speckles are observed around the spot as compared to **Fig. 5.3 (a)** where field was zero. It was seen that the randomness of the media decreases with application of magnetic field. As the Brownian particles assembled to an ordered state, the scattered wavelets from media will be in phase rather than de-phased, which increases the probability of constructive interference of the scattered wave. The diffused speckles are oriented in a straight line after $H_{c2}$ and become sharp with no further change with increasing magnetic fields, which indicates the formation of well ordered structures.

In the absence of magnetic field, the droplets are in Brownian motion due to thermal energy, and are in a disordered state, where speckles are formed around the spot [226-228]. The droplets start to interact with each other after the $H_{c1}$ and form small aggregates like doublet, triplet and small chains in the direction of magnetic field [66]. As the field increases, small aggregates are transformed into long chains and then form column like structures due to lateral aggregation [68]. The scattering pattern arises due to interaction between electromagnetic wave and infinite long cylinder, which was studied for both normal and oblique incidences [229, 230]. The reason for the formation of straight line scattered pattern is explained in chapter 3. These experiments confirm the anisotropic structures formed under magnetic field.

### 5.3.2. Magnetic birefringence

To study the magnetic birefringence in nanoemulsion, a linearly polarized light was passed through a sample of thickness, 1 mm, placed between the poles of an electromagnet. The transmitted ray is divided into two rays with different velocities of propagation and with their direction of vibration perpendicular to each other. The polarizer and analyzer were crossed and the vibration components of transmitted light are perpendicular to each other as shown in **Fig. 5.4**.

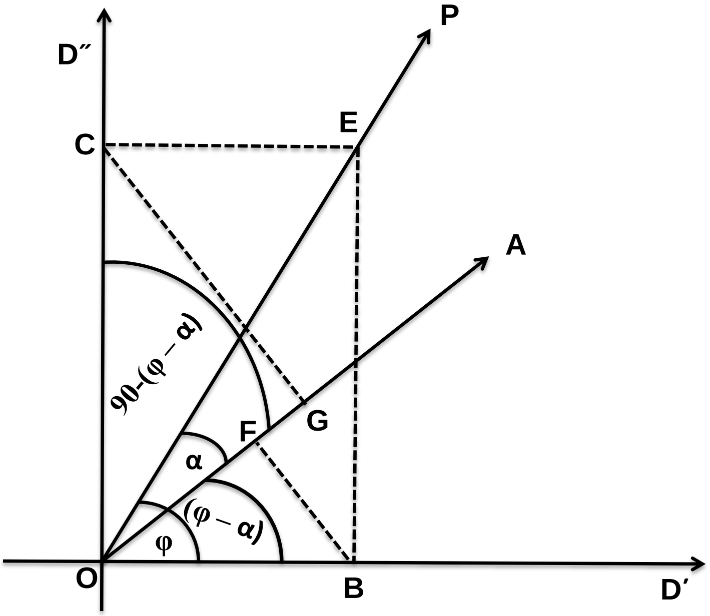

*Figure 5.4 Schematic representation of the vibration components transmitted by polarizer and analyzer. P - polarizer, A - analyzer, D′ and D″ represent the two mutually orthogonal direction of vibrations of the transmitted light in the sample. OP and OA are the direction of vibrations of polarizer and analyzer, respectively.*

In **Fig. 5.4,** φ is the angle that OP makes with D′ and α is the angle between OP and OA. The amplitude of the light incident on the sample is represented by the vector OE and its component in the directions of D′ and D″ are $OB = E\cos\varphi$ and $OC = E\sin\varphi$, respectively. The analyzer transmits only the components parallel to OA axis i.e., OF and OG lies on the axis of analyzer which is given by $OF = E\cos\varphi\cos(\varphi-\alpha)$ and $OG = E\sin\varphi\sin(\varphi-\alpha)$, respectively. The two components differ in phase ($\delta_p$) defined as $\delta_p = \frac{2\pi(\Delta n)L}{\lambda}$, where $\Delta n$ is the birefringence. The resultant intensity arises from the interference of two monochromatic waves with phase difference $\delta_p$ and it is given by

$$I_R = I_1 + I_2 + 2\sqrt{I_1 I_2}\cos\delta_p \tag{5.1}$$

where $I_1$ and $I_2$ are the intensities of two waves corresponding to OF and OG, respectively. By using the above expression in Eqn. (5.1), we have

$$I_R = E^2 \left[\cos^2\alpha - \sin 2\varphi \sin 2(\varphi - \alpha)\, sin^2\frac{\delta_p}{2}\right] \tag{5.2}$$

There are two special cases depending on the orientation of polarizer and analyzer:

Case-I: The analyzer and polarizer are parallel (i.e., $\alpha = 0$). Here, Eqn. (5.2) reduces to

$$(I_R)_{\parallel} = E^2 \left[1 - sin^2 2\varphi\, sin^2\frac{\delta_p}{2}\right] \tag{5.3}$$

Case-II: The analyzer and polarizer are mutually perpendicular (i.e., $\alpha = \frac{\pi}{2}$). Now Eqn. (5.2) reduces to

$$(I_R)_{\perp} = E^2 sin^2 2\varphi\, sin^2\frac{\delta_p}{2} \tag{5.4}$$

The resultant intensity ($I_R$) is proportional to $sin^2\delta_p/2$ where the phase difference depends on the magnetic birefringence.

$$I_R \propto\ sin^2\frac{\delta_p}{2} \tag{5.5}$$

The magnetic birefringence is expressed as [213]

$$\Delta n = A_2 \beta \Phi \tag{5.6}$$

where, $A_2$ is the anisotropy constant, $\beta$ is the proportionality constant which depends on the shape of the droplet as well as the electric polarizability of both droplets and carrier liquids and $\Phi$ is the volume fraction. $\beta$ given by [154]

$$\beta = \left[1 - \frac{3L(\xi)}{\xi}\right]\left[\frac{d}{d\sigma_a}\ln R(\sigma_a) - \frac{1}{3}\right] \tag{5.7}$$

where $\sigma_a = \frac{E_a}{k_B T}$; $E_a$ is the anisotropic energy. The coefficient $A_2$ is given as $A_2 = \frac{1}{2n_e}(\chi_{\parallel} - \chi_{\perp})$; $n_e$ is the refractive index of the carrier liquid, $\chi_{\parallel}$ and $\chi_{\perp}$ are the effective dielectric susceptibility of the nanoemulsion along a direction which is parallel and perpendicular to its anisotropy axis, respectively. $(\chi_{\parallel} - \chi_{\perp})$ is optical anisotropy factor due to the oscillating dipole-interaction anisotropy [141].

In the weak-field region, i.e., $\xi \ll 1$, Eqn. (5.6) can be written as

$$\Delta n = \Delta \mathrm{n}_0 \Phi \frac{\xi^2}{15} \tag{5.8}$$

In the high field region i.e. $\xi \gg 1$, Eqn. (5.6) can be written as

$$\Delta n = \Delta n_0 \Phi \left(1 - \frac{3}{\xi}\right) \tag{5.9}$$

where, $\Delta n_0$ is the maximum birefringence.

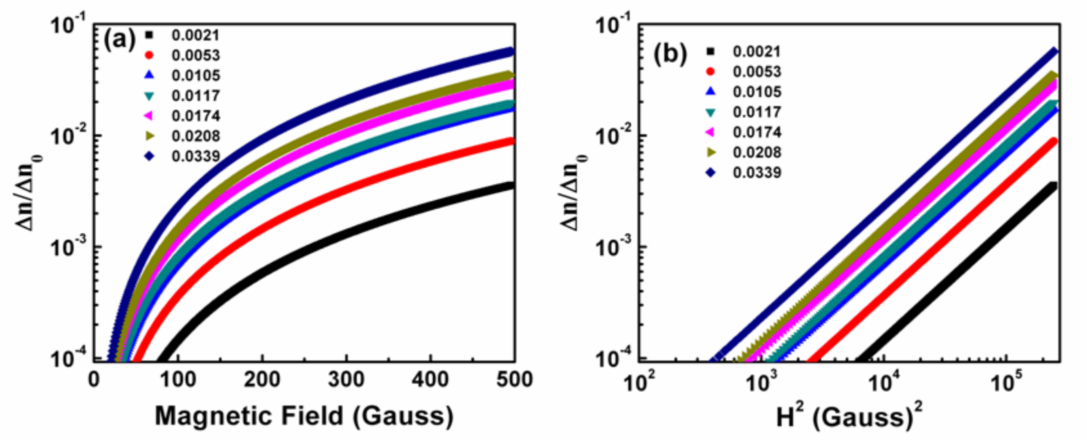

*Figure 5.5 Reduced magnetic birefringence ($\Delta n/\Delta n_0$) as a function of (a) applied magnetic field and (b) square of the magnetic field, at $\xi < 0$ for different volume fractions $\Phi$ = 0.0021, 0.0053, 0.0105, 0.0117, 0.0174, 0.0208, and 0.0339.*

**Figure 5.5** shows the reduced magnetic birefringence as a function of applied magnetic field and the square of magnetic field at different volume fractions of 0.0021, 0.0053, 0.0105, 0.0117, 0.0174, 0.0208, and 0.0339. The reduced magnetic birefringence ($\Delta n/\Delta n_0$) is defined as the ratio between birefringence at a certain magnetic field to its saturation value. It can be seen that the reduced birefringence increases linearly with magnetic field strength at lower values. In the lower field strength region, $\Delta n/\Delta n_0$ scales with $H^2$.

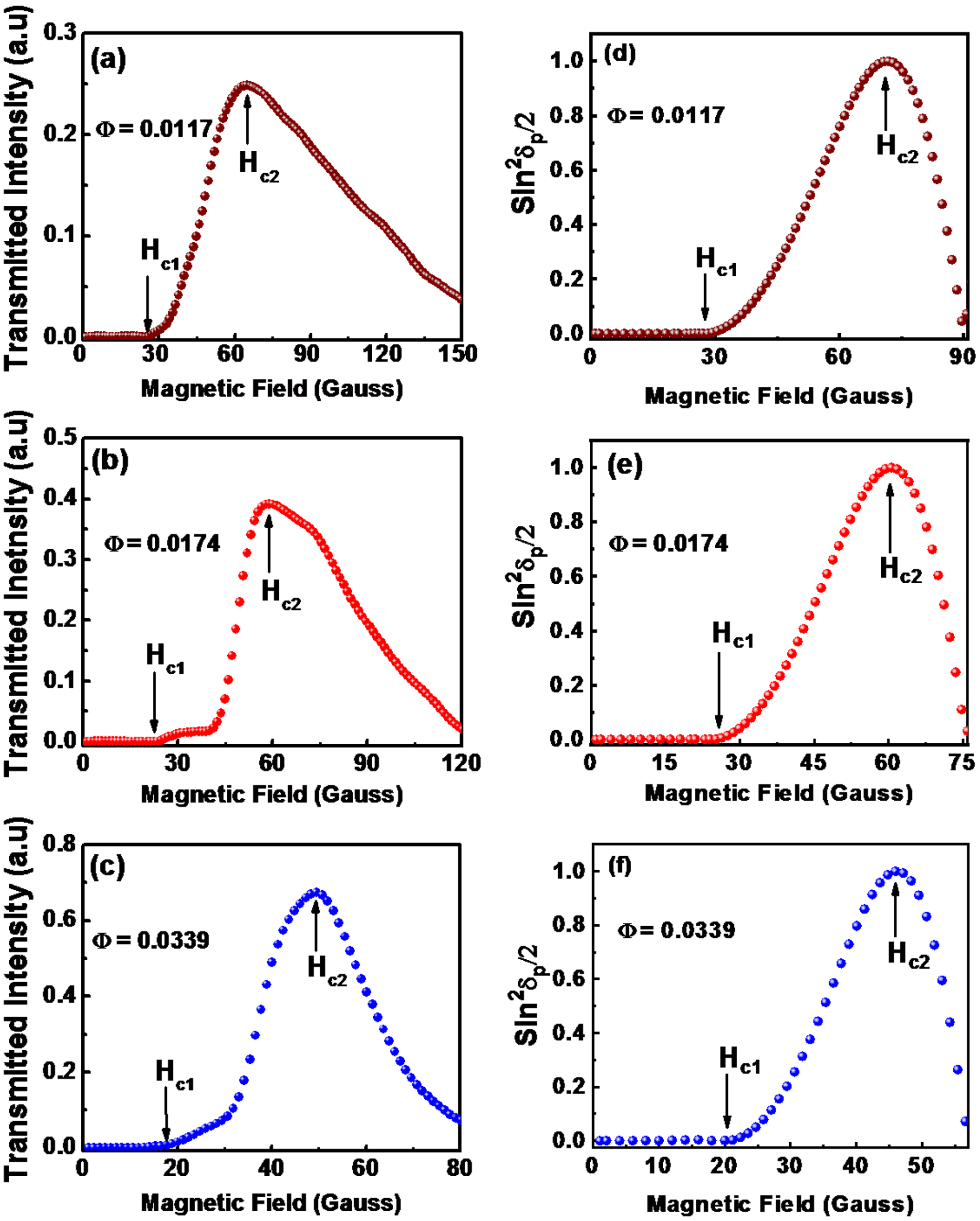

*Figure 5.6 (a - c) Transmitted light intensity as a function of magnetic field and (d - f)* $\sin^2\delta_p/2$ *as a function of applied magnetic field for* $\Phi$ = *0.0117, 0.0174 and 0.0339.*

**Figure 5.6 (a - c)** shows the variation of transmitted light intensity (experimental results) with the magnetic field and **Fig. 5.6 (d - f)** the intensity $sin^2\delta_p/2$ corresponding to crossed orientation of polarizer and analyzer as a function of magnetic field for Φ = 0.0117, 0.0174 and 0.0339, respectively. For Φ = 0.0117, the intensity remains constant up to 25.9 G, above which it increases rapidly, reaching a maximum at 64.9 G. After $H_{c2}$, it starts to decrease and becomes minimum at 173.46 G and then slowly increases with further increase in magnetic field strength. Similarly for Φ = 0.0174, the intensity remains constant up to 23.6 G, above which it increases rapidly reaching a maximum at 59 G. After $H_{c2}$, it starts to decrease and becomes minimum at 128.62 G. For the volume fraction 0.0339 the intensity remains constant up to 18.8 G, above which it increases rapidly, reaching a maximum at 49.56 G. After $H_{c2}$, the transmitted light intensity starts to decrease and becomes a minimum at 80 G and then slowly increases at higher magnetic field. The same behavior was observed in the experimental intensity profile with magnetic field where $H_{c1}$ and $H_{c2}$ were found to be 25.9 and 64.9 G for Φ = 0.0117, 23.6 and 59 G for Φ = 0.0174 and 18.8 and 49.56 G for Φ = 0.0339, respectively. The trend observed in both the experimental and theoretical curves remains similar and the values of $H_{c1}$ and $H_{c2}$ observed in the two cases showed remarkable agreement. This unambiguously confirm that the observed field induced transparency at lower magnetic field strength are indeed due to magnetic birefringence, which can be manifested only above a critical volume fraction of the droplets or critical inter-particle spacing. Our findings are consistent with the earlier study showing that magnetic birefringence in magnetic fluids can arise due to orientation of the particles, anisotropic spatial ordering and due to small aggregates [217] and the prediction that magnetic birefringence may occur at high volume fractions and in large sample thickness by Bukuzis et al.[134]. The perfectly reversible field induced transparency at very low magnetic field strength offer several new possibilities in tunable optical devices.

## 5.4. Conclusions

The field induced optical transparency and its origin in magnetic nanoemulsion containing droplets of average size ~200 nm is studied for the first time. The effect of volume fraction on critical magnetic fields and the transmitted light intensity were studied systematically. Beyond a volume fraction, the nanoemulsions showed a field induced transparency and the critical magnetic fields at which transparency was observed increased drastically, following a power law decay with Φ with distinct exponents. The field induced transparency in magnetic fluid was perfectly reversible. The observed field induced transparency in magnetic emulsions for $\Phi > 0.0021$ is attributed to the optical birefringence caused by the rod like nanostructures, which was further confirmed from the straight line scattering pattern observed on a screen placed perpendicular to the incident beam. The reduced birefringence is found to be proportional to the square of the applied magnetic field. The observed reversible field induced transparency in nanofluid may find potential applications in tunable optical devices.

## *Chapter 6*

# Influence of size polydispersity on magnetic field tunable structures in ferrofluids

## 6.1. Introduction

Colloidal suspensions of superparamagnetic particles (ferrofluids) exhibit fascinating physical properties with numerous applications, and they are wonderful model systems to probe microscopic phenomena such as order-disorder structural transitions, self-assembly, aggregation, and complex dynamics [18]. The field-induced aggregation and structural phase transitions in ferrofluids depend on the magnetic interaction strength between the particles, the magnetic field strength, the orientation of the field with respect to the sample, the rate of change of the field, the sample thickness, polydispersity, and volume fraction, the temperature, etc. [81, 231-236]. Particle-size polydispersity is inevitable in any ferrofluid, and it plays an important role in field-induced structure formation. A polydisperse fluid can be considered as a mixture of a large number of components, where the particle size, shape, or interaction strength may vary. This not only affects the equation of state for the system, but also the phase transitions. The initial susceptibility of a polydisperse ferrofluid is found to be larger than that of a monodisperse ferrofluid [237], and in general, the magnetic properties show a very strong dependence on the volume fraction of large particles. With an increase in the volume fraction of large particles, the magnetization increases much faster at weak fields due to the strong particle-field interaction, which leads to a larger initial susceptibility. Large particles act as nucleation sites and attract nearby particles to form chains via the dipolar head-tail interaction. Zippering of different chains is also more significant in polydisperse samples, and it occurs at lower field strengths as compared to more monodisperse samples.

Despite the vast number of studies on the field-dependent properties of ferrofluids, most of the research until now has been confined to equilibrium or steady-state properties. In many technological applications, ferrofluids are subjected to magnetic-field but the behavior of ferrofluids depends on the properties of suspended nanoparticles. However, the exact conditions at which different structures such as thin chains, thick chains, sheets, isotropic bubbles, hexagonal and lamellar/stripe structures are largely unknown. To the best of our knowledge, no systematic experimental study has been reported on the effect of particle-size polydispersity on field induced structures and structural transitions.

In this chapter, we detail the field-induced microstructures in ferrofluids with different polydispersity indices (PDIs), with either in-plane or out-of-plane fields with respect to the confining cell. Phase contrast optical microscopy, light scattering experiments are used to characterize the structures formed in three ferrofluids with various PDIs, and the experimental results for a high-PDI case are complemented by Brownian-dynamics simulations.

## 6.2. Materials and methods

### 6.2.1. Experimental

The magnetite nanoparticles were synthesized by co-precipitation technique which is detailed in section 2.2 of chapter 2. Three different magnetic nanofluids, M1, M2, and M3 were employed in this study. The volume fraction of all three ferrofluids was fixed at 0.037 (corresponding to 20 wt %). Table 6.1 summarizes the obtained results of ferrofluid characterization, details of which can be found in section 2.6 of chapter 2.

*Table 6.1 Sample name, crystallite size, hydrodynamic size, polydispersity index, magnetization, surfactant loss in samples M1, M2 and M3.*

| Sample name | Crystallite size [nm] | Hydrodynamic size [nm] | Polydispersity index | Magnetization [emu/g] | Surfactant weight loss [%] |
|---|---|---|---|---|---|
| M1 | 9.6 ± 0.7 | 10 ± 0.6 | 0.22 | 69 ± 0.6 | 24 |
| M2 | 8.3 ± 0.8 | 11.7 ± 0.9 | 0.23 | 66 ± 0.7 | 21 |
| M3 | 10.5 ± 1 | 20.9 ± 1 | 0.79 | 71 ± 0.7 | 19 |

### 6.2.2. Simulation

To complement the experimental study, and to gain additional insights on field-induced structure formation, Brownian dynamics simulations of sample M3 were carried out. This sample was selected because, as is shown in section 6.3, it shows the greatest diversity of structures. The simulations were carried out with $N_p = 12 \times 36 \times 36 = 15{,}552$ particles in a cuboidal cell with periodic boundary conditions, a constant *z* dimension (in the field direction) equal to 671 nm, and *x* and *y* cell dimensions set equal and to a value which gives the required volume fraction. A discretized particle-size distribution $N(d)$ was chosen to mimic the DLS results reported in section 6.3; more details are given in section 6.3.4. The short-range interactions between two particles *i* and *j* were given by the Weeks-Chandler-Andersen (WCA) potential [238], given by $u_{ij}^{\mathrm{WCA}}(r) = u_{ij}^{\mathrm{LJ}}(r) - u_{ij}^{\mathrm{LJ}}(r_0)$, where $u_{ij}^{\mathrm{LJ}}(r) = 4\varepsilon_1 \left[ \left(d_{ij}/r\right)^{12} - \left(d_{ij}/r\right)^{6} \right]$ is the Lennard-Jones (LJ) potential, $d_{ij} = \left(d_i + d_j\right)/2$ is the mean particle diameter, $r_0 = \sqrt[6]{2} d_{ij}$ is the position of the minimum of the LJ potential, and $\varepsilon_1 = k_{\mathrm{B}}T$ is an energy parameter, assumed to be the same for all pairs of particles, and equal to the thermal energy. The WCA potential is therefore a soft, purely repulsive potential which models the short-range, non-magnetic interactions between sterically stabilized nanoparticles. The magnetic interactions were computed using the particle-particle particle-mesh Ewald summation method [239] with conducting boundary conditions, to avoid any finite-size artifacts arising from demagnetization fields within the (small) simulation cell. The BD simulations were carried out at 300 K with a time step (in LJ units) of $\delta t^* = 0.00025$ (this being small to take account of the dynamics of the small-particles), and for at least $10^6$ timesteps, chosen so that the system reached a steady state. All simulations were performed using LAMMPS [240]. Details of computed observables are given in section 6.3.4.

## 6.3. Results and discussion

### 6.3.1. Effect of polydispersity on field-induced structural transformations in ferrofluids

The field-induced microstructures formed at different magnetic field strengths in samples M1, M2, and M3 were studied using a phase contrast optical microscope. The phase contrast optical microscopic images of samples M1, M2, and M3 at different magnetic field strengths of 0 G, 30 G, 80 G, 170 G, 280 G, and 550 G are shown in **Fig. 6.1.** The direction of the applied magnetic field $H$ is shown by an arrow in **Fig. 6.1 (m)**. In sample M1, no aggregates are observed even at the highest field strength of 550 G, indicating that any aggregates are nano-sized (smaller than the 100 nm resolution limit of the microscope). In sample M2, above a field strength of 280 G, submicron-sized aggregates are seen. At 280 G, the microscopy images of sample M2 show several short and thin chains with an average length and width around 12 µm to 0.9 µm, which increase to 37 and 1.6 µm, respectively as the magnetic field strength is increased to 550 G. In sample M3, very thick and long chains are observed at a field strength of 170 G, where the average length and width of the chains are 306 µm and 3.5 µm, respectively. As the field is increased to 280 G, adjacent chains coalesce to form thick sheets, which span the entire area being imaged.

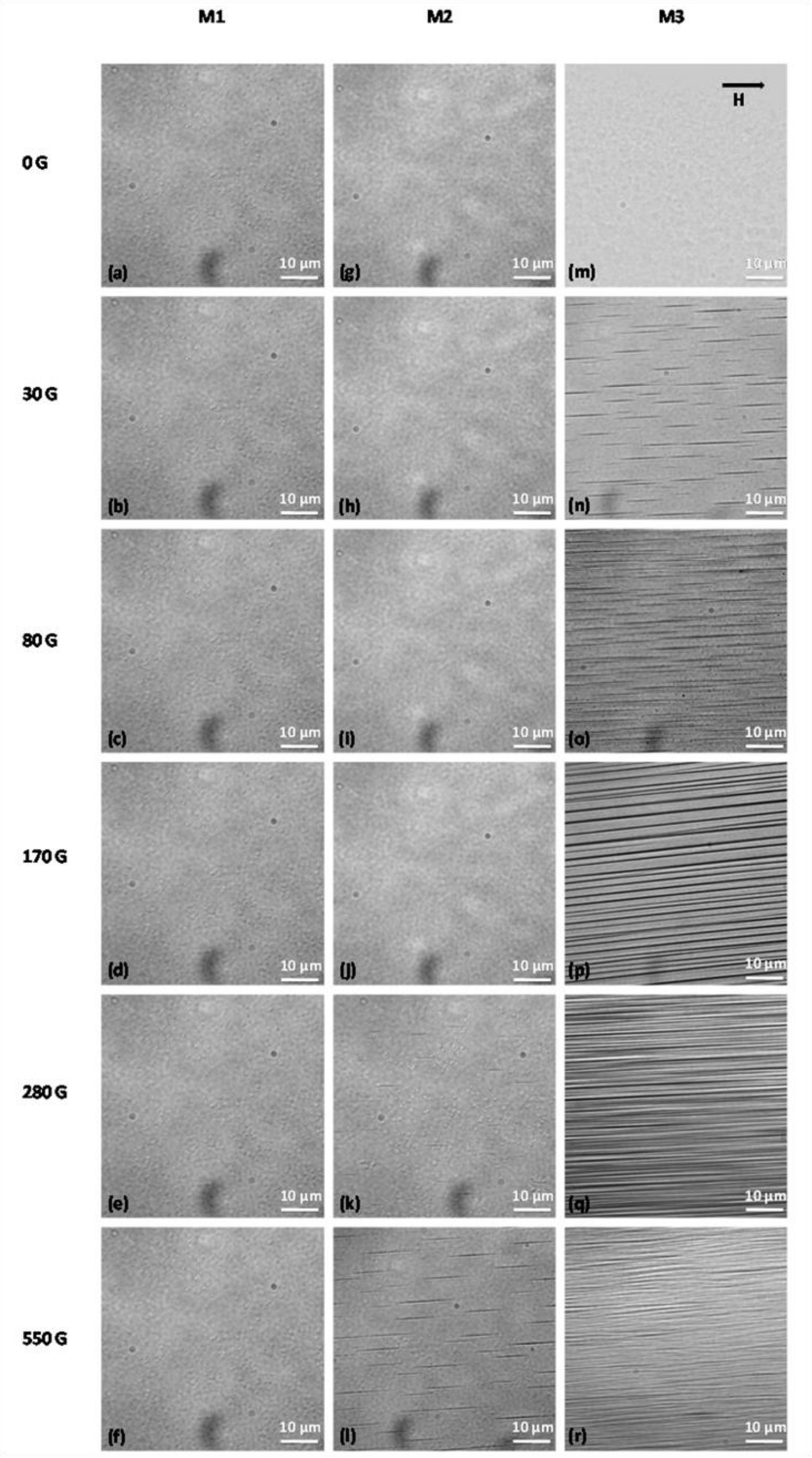

*Figure 6.1 Phase contrast optical microscope images showing field-induced aggregation of magnetic nanoparticles in samples M1 (a – f), M2 (g – l), and M3 (m – r), at different in-plane magnetic field strengths of 0 G, 30 G, 80 G, 170 G, 280 G, and 550 G. The volume fraction is $\Phi = 0.037$ in all three samples, and the direction of the magnetic field H is shown by an arrow in Fig. 6.1 (m).*

Cross-sectional views of magnetic field-induced microstructures in samples M1, M2, and M3 at different magnetic field strengths of 0 G, 30 G, 80 G, 170 G, 280 G, and 550 G are shown in **Fig. 6.2**. Here, the external magnetic field was applied perpendicular to the sample plane (out-of-plane). Cross-sectional views of columns and sheets appear as bubbles and stripes, respectively. Similar to **Fig. 6.1**, no such bubbles are observed in sample M1 at any magnetic field strength up to 550 G, which indicates that any aggregates are less than 100 nm in size. In sample M2, only a few bubbles are seen at the highest field strengths of 280 G and 550 G. Although the polydispersity is very high in sample M3, in zero field, all particles are well dispersed in the sample, and even if there are aggregates of larger particles, their size is much less than the 100 nm resolution limit of the microscope. Hence, no structures are observed in the absence of a magnetic field, but bubbles appear even at the very low magnetic field strength of 30 G. In this case, the bubbles are randomly positioned in the plane, with an average intercolumn spacing of 3 μm. There are more columns at a field strength of 80 G, with a smaller intercolumn spacing of 1.5 μm. Hexagonal close packed columnar structures are apparent above a magnetic field strength of $H = 170$ G, with an even smaller intercolumn spacing of 0.6 μm. Overall, the average intercolumn spacing is found to vary inversely with the external magnetic field strength ($\propto H^{-1}$ with $R^2 \simeq 0.99$) up to a field strength of 170 G, beyond which the columns coalesce and form stripe patterns. This is in agreement with an earlier report by Horng *et al.* [241]. At a field strength of 280 G, columns coalesce through lateral interactions to form stripe patterns (lamellar structures), with the stripes being extended perpendicular to the direction of the external magnetic field. The average width of a stripe at 280 G is 1.6 μm. As the field is increased further to 550 G, the number of stripes increases, the thickness of the stripes decreases, and the distance between the stripes decreases to 0.7 μm. At 280 G, the stripes are parallel to each other without significant bending. At 550 G, however, the stripes show a zig-zag modulation. This instability or undulation at 550 G can be understood as follows. As the field is increased, the width of the stripes decreases, while the length of the stripes increases (**Fig. 6.2**). In addition, since the ferrofluid is a paramagnetic substance, the local concentration of magnetic material in the cell volume should increase with increasing field strength, with particles being supplied by the surrounding ferrofluid reservoir. Since the stripe structures are confined in the field direction (the cell thickness was approximately 21 μm), the simplest way to increase the length is through undulation. The zig-zag pattern gives rise to a larger area of interaction between the stripes, which leads to stabilization through the long-range magnetic interaction between stripes [242].

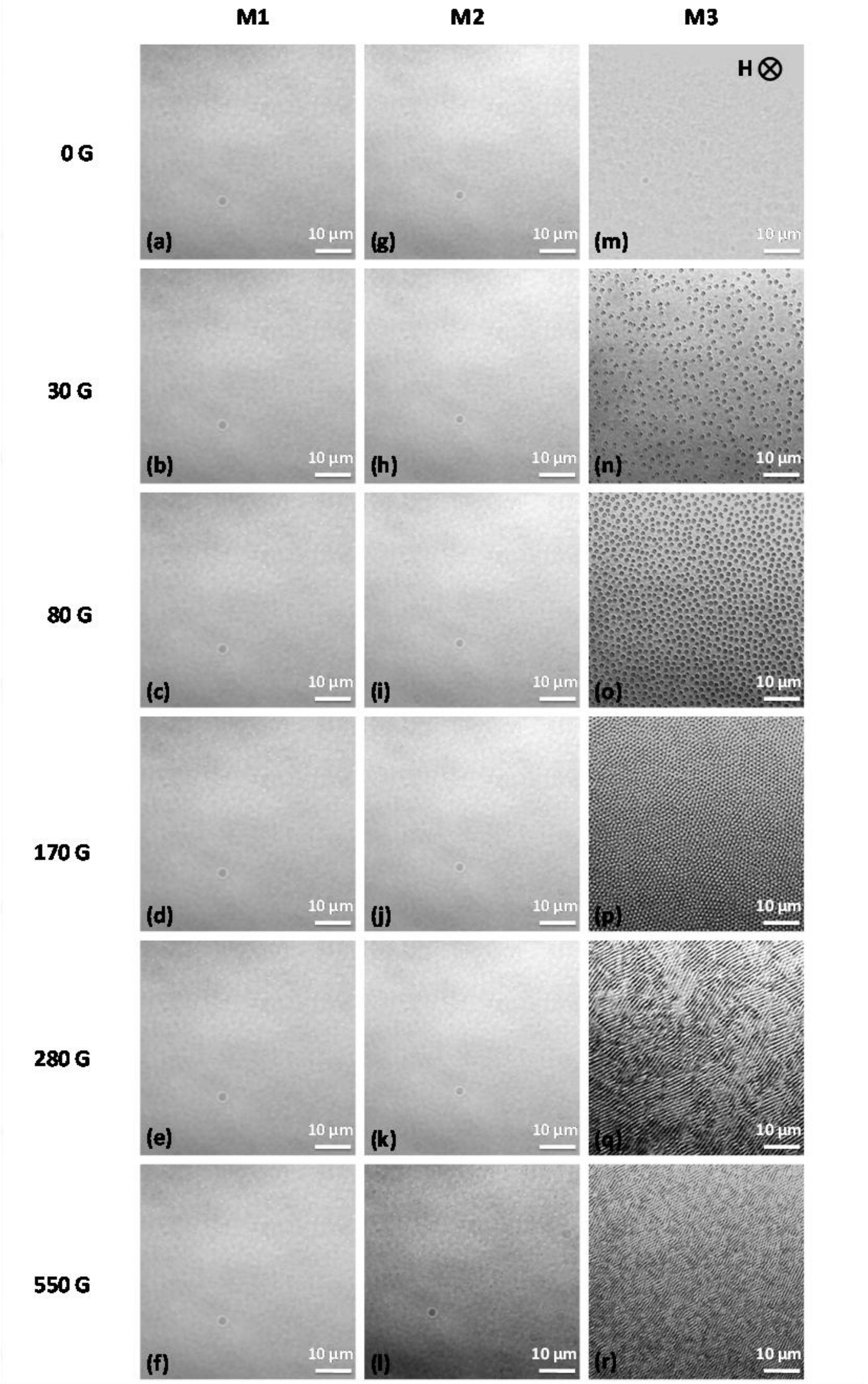

*Figure 6.2 Phase contrast optical microscopy images showing cross-sectional views (top views) of field-induced microstructures in samples M1 (a – f), M2 (g – l), and M3 (m – r), at different out-of-plane magnetic field strengths of 0 G, 30 G, 80 G, 170 G, 280 G, and 550 G. The volume fraction is $\Phi = 0.037$ in all three samples, and the direction of the magnetic field $H$ is perpendicular to the plane, as shown by an arrow in Fig. 6.2 (m).*

To sum up, in sample M3, three different structural arrangements of columns occurred in the presence of an out-of-plane field, these being isotropic, hexagonal, and stripe/lamellar structures with increasing magnetic field. These structures are shown in more detail in **Fig. 6.3**.

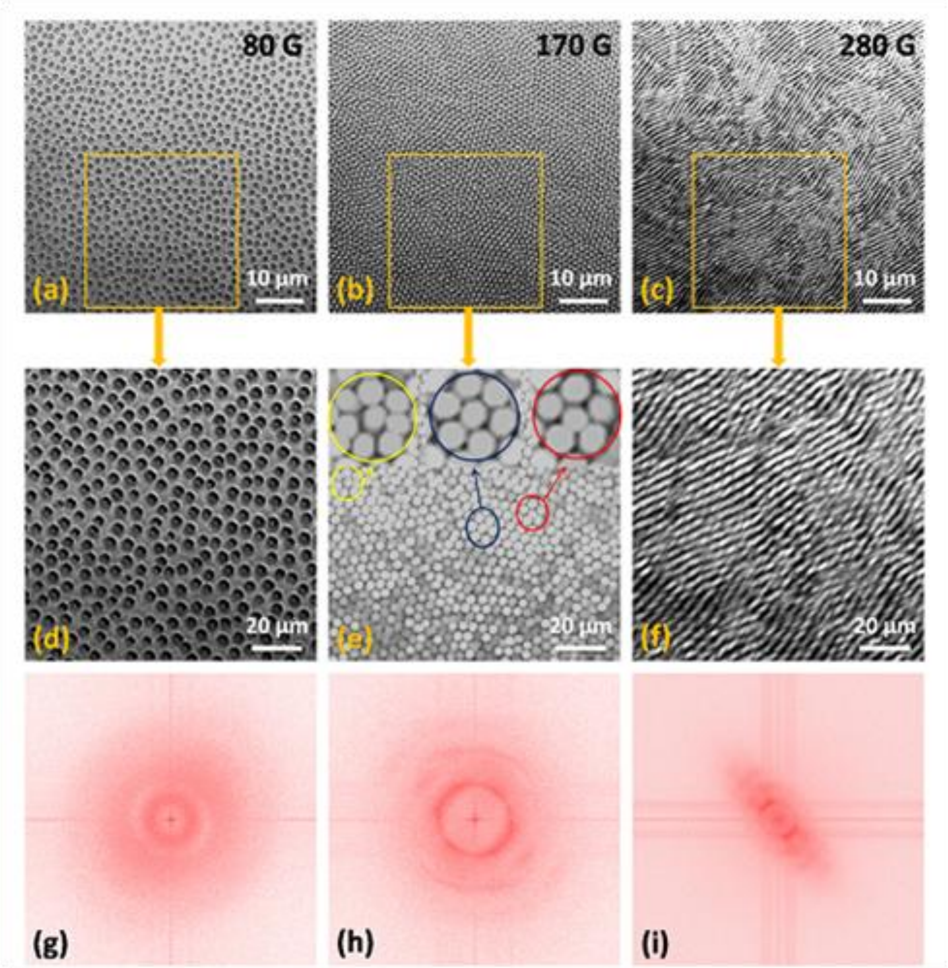

*Figure 6.3 (a – c) Phase contrast optical microscopy images of sample M3 showing the isotropic, hexagonal, and stripe/lamellar phases with out-of-plane magnetic field strengths of 80 G, 170 G, and 280 G, respectively. (d – f) Enlarged views of the images in (a – c). (g – i) FFT images of selected areas from (d – f).*

**Figure 6.3 (a – c)** shows the structural progression between isotropic, hexagonal, and stripe patterns in sample M3 with magnetic field strengths of 80 G, 170 G, and 280 G. **Fig. 6.3 (d – f)** shows enlarged views, and **Fig. 6.3 (g – i)** shows corresponding fast Fourier transform (FFT) images of the isotropic columnar distribution, hexagonal arrangement of columns, and stripe patterns. At $H = 80$ G, all columns are distributed randomly, and hence the FFT gives a circular pattern as shown in **Fig. 6.3 (g).** At $H = 170$ G, the columns are closer to one another, and adopt local 2D hexagonal coordination but without long-range order. Close inspection of the FFT patterns reveals that the enlarged image [**Fig. 6.3 (e)**] contains both five-fold and seven-fold coordination sites, along with the expected six-fold coordination sites. Five-fold and seven-fold coordination sites coincide with the positions of bubbles that are, respectively, smaller and larger than the bubbles that surround the six-fold coordination sites. It is known that size polydispersity creates dislocations and bubble-area mismatches, leading to size adjustment of the five-fold and seven-fold coordinated bubbles [243]. Due to the misorientation of columns, a hexagonal pattern is seen in **Fig. 6.3 (h)**, instead of the six diffraction spots expected for a perfect hexagonal structure [244]. Similar hexagonal patterns have also been seen in other systems such as a charged superparamagnetic colloid of $Fe_3O_4$ nanoparticles coated with silica [245], and a ferrofluid with magnetic holes (nonmagnetic particles dispersed in a magnetized ferrofluid solution) [246]. The stripe pattern [**Fig. 6.3 (i)**] indicates periodic ordering of the domains along the longitudinal direction of the pattern, and the angular distribution indicates the directionality of the stripe pattern. When stripes are parallel to each other, two spots are seen in **Fig. 6.3 (i)**. The increased magnetic moment and decreased column separation at 280 G cause a stronger repulsion between the columns, which results in the aggregation of columns into lamellar structures in order to minimize the free energy.

To help us to understand the effect of polydispersity on the field-induced structural transformations in magnetic colloids, a bidisperse approximation can be used [247]. In a bidisperse system, two additional parameters are introduced: the particle-size ratio, and the volume fraction of the larger particles. From the size distribution curve obtained by DLS, as given in the chapter 2, it was found that samples M1, M2, and M3 contained particles with diameters in the ranges of 7 nm–21 nm, 7 nm–28 nm, and 15 nm–44 nm, respectively. Here we consider a bidisperse system composed of small particles with diameter $\sigma_\mathrm{S}$, and large particles with diameter $\sigma_\mathrm{L}$, defined as shown in **Fig. 4**. The magnetic moments of the two types of particles are referred to as $m_\mathrm{S}$ and $m_\mathrm{L}$.

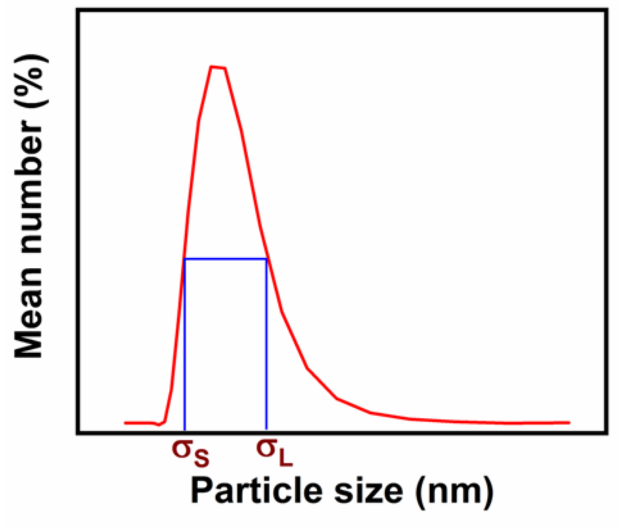

*Figure 6.4 The particle-size distribution curve and the full width at half of the maximum intersect at two points, which define the hydrodynamic diameters of the small particles ($\sigma_S$) and the large particles ($\sigma_L$).*

In such a bidisperse system, three different coupling constants can be defined: large-large (LL), large-small (LS), and small-small (SS). The magnetic field induced microstructures in such a system should somehow correspond to different values of the coupling constants $\Lambda_\mathrm{LL} = \frac{\pi\mu_0\sigma_\mathrm{L}^3\chi^2H^2}{72k_\mathrm{B}T}$, $\Lambda_\mathrm{LS} = \frac{\pi\mu_0\sigma_\mathrm{L}^3\sigma_\mathrm{S}^3\chi^2H^2}{9k_\mathrm{B}T(\sigma_\mathrm{L}+\sigma_\mathrm{S})^3}$, and $\Lambda_\mathrm{SS} = \frac{\pi\mu_0\sigma_\mathrm{S}^3\chi^2H^2}{72k_\mathrm{B}T}$ [248]. These constants describe the strengths of the magnetic dipole interactions between the various components, and some illustrative values are provided in Table 6.2.

*Table 6.2 The three coupling constants $\Lambda_{LL}$, $\Lambda_{LS}$, and $\Lambda_{SS}$ calculated at different magnetic field strengths and at temperature $T = 300\ K$. The diameters of the small and large particles in each of the three samples M1, M2, and M3 are taken from the particle size distributions obtained from DLS, as presented in the chapter 2. The experimental values of the initial susceptibility for the three samples are also given.*

| **Sample name** | $\sigma_{\mathrm{S}}$ **(nm)** | $\sigma_{\mathrm{L}}$ **(nm)** | $\chi$ | $H$ **(G)** | $\Lambda_{\mathrm{LL}}$ | $\Lambda_{\mathrm{LS}}$ | $\Lambda_{\mathrm{SS}}$ |
|---|---|---|---|---|---|---|---|
| M1 | 9 | 16 | 5.6 | 30 | 0.009 | 0.004 | 0.002 |
| | | | | 80 | 0.07 | 0.03 | 0.01 |
| | | | | 120 | 0.2 | 0.06 | 0.03 |
| | | | | 170 | 0.3 | 0.1 | 0.06 |
| | | | | 280 | 0.85 | 0.3 | 0.15 |
| | | | | 550 | 3.3 | 1.2 | 0.58 |
| M2 | 10 | 20 | 6.4 | 30 | 0.03 | 0.007 | 0.003 |
| | | | | 80 | 0.17 | 0.05 | 0.02 |
| | | | | 120 | 0.4 | 0.1 | 0.05 |
| | | | | 170 | 0.8 | 0.2 | 0.1 |
| | | | | 280 | 2.18 | 0.6 | 0.3 |
| | | | | 550 | 8.4 | 2.49 | 1.05 |
| M3 | 20 | 34 | 7.4 | 30 | 0.2 | 0.07 | 0.03 |
| | | | | 80 | 1.17 | 0.48 | 0.24 |
| | | | | 120 | 2.6 | 1.07 | 0.5 |
| | | | | 170 | 5.3 | 2.1 | 1.1 |
| | | | | 280 | 14.3 | 5.82 | 2.91 |
| | | | | 550 | 55.2 | 22.4 | 11.2 |

In sample M1, since the number of the large-sized particles is relatively small, the average separation between large-sized particles is much larger than the diameter of the small ones. The large number of small particles provides a magnetic background for the large ones. If the large-small particle interactions are neglected, this background field can be assumed as a continuous magnetic medium with an effective magnetic permeability $\mu_{\mathrm{eff}}$. The dipolar interaction energy between two large particles in such a magnetic medium is therefore $\mu_{\mathrm{eff}}$ times smaller than that in a nonmagnetic medium [249]. This weakening of the interaction energy will effectively reduce the aggregation probability of the large particles. At $H = 550$ G, $\Lambda_{\mathrm{LL}}$ and $\Lambda_{\mathrm{LS}}$ are greater than one, while $\Lambda_{\mathrm{SS}}$ is less than one, indicating favorable conditions for the formation of aggregates through large-large and large-small particle interactions. Since $\Lambda_{\mathrm{SS}} < 1$, the small particles may attach to chains formed by large particles due to their dipole-dipole interaction in two possible ways: by approaching from a direction perpendicular to the chain axis, and getting trapped in a triangular arrangement by two large particles at contact; or by attaching to the ends of the chains.

The chains made by larger particles are assumed to be linear with all the dipole moments well aligned. The optimum attractive energy is attained when the dipole moments of the small particles are oriented parallel to the chain axis. However, this energy is not stronger than $k_{\mathrm{B}}T$ in the case of transversely attaching particles. Hence, the small particles tend to attach at the ends of the chains of large particles due to relatively strong attraction. The attractive energy is not very sensitive to the chain length, due to the $r^{-3}$ decay of the dipolar potential energy. If the number of small particles is high, then there is a high probability for them to be attached to the ends of the chains. When two short chains with small particles at their ends approach each other, and combine into a longer chain, the smaller ones in the middle make the composite chain less stable as compared to a chain formed only by large particles, and as a result of thermal fluctuations, the composite chain may break at the location of the small particles [249]. This restricts the further growth of the chains, and also prevents lateral coalescence of chains or columns, which can lead to a decrease in chain length with an increase in the volume fraction of small particles (poisoning effect) [249, 250]. The field-induced aggregation in sample M1 is very slow and any chains would have to be nanosized, because they are not discernible in the phase contrast optical microscopy images, even at a magnetic field strength of 550 G (**Fig. 6.1** and **Fig. 6.2**).

In sample M2, the number of large-sized particles is higher than in sample M1. Only above $H = 280$ G is $\Lambda_{\mathrm{LL}} > 1$, where larger sized particles should form aggregates in the direction of magnetic field, and hence a few small chains appear as shown in **Fig. 6.1 (k)** and **Fig. 6.2 (k)**. At $H = 550$ G, all three coupling constants are greater than or equal to one, and hence the number of chains is larger, and they are randomly distributed throughout the sample.

Sample M3 contains significantly more large-sized particles than samples M1 and M2. Larger particles have larger dipolar strength in the dispersion. The initial susceptibility and the magnetization curve of this system show a strong dependence on the number of larger particles. With an increase in the number of larger particles, the magnetization of the system increases faster at weak fields, and this leads to a larger initial susceptibility. At $H = 280$ G, all three interaction parameters are much larger than one. The potential energy of a dipole moment in an external magnetic field is given by $U_H = -\mu_0 m \cdot H$, and the gradient of the magnetic field induces a magnetic packing force $F_H = -\nabla U_H$, which drives magnetic particles towards regions with the maximum local magnetic field strength. It has been reported that larger particles play an important role as condensation centers for the formation of nuclei [251]. Once the chain length is above a critical length, it attracts the nearest small cluster (containing both large and small particles) towards it, and forms a thicker column. Hence, this can be viewed as a kind of heterogeneous nucleation, where clusters of large particles act as nucleation points, and the rate is fast as compared to homogeneous nucleation. This mechanism enhances the degree of particle-size polydispersity within the columns. The introduction of small magnetic nanoparticles in a column induces a local magnetic field gradient, similar to the introduction of non-magnetic particles in a magnetic dispersion [71]. The magnetic moments of the large particles, and consequently those of the small particles in a column, increase under a strong magnetic field, which further increases the concentration of small particles in regions with a high local magnetic field strength. Due to the increased magnetic moment, small-small particle interactions lead to the formation of chains with smaller intercolumn separation. So, the increased magnetic moments and decreased chain separation cause stronger repulsion (i.e., due to steric hinderance) between the chains, which eventually results in the aggregation of chains into lamellar structures to minimize the free energy [71]. This occurs by shifting a neighboring chain by a distance $a$ corresponding to the radius of the nanoparticles.

### 6.3.2. Effect of volume fraction of large particles on field-induced microstructures

To study the effect of volume fraction of large particles ($\Phi_L$) on field-induced microstructures in ferrofluids, we prepared binary mixtures of samples M1 and M3 with various compositions. In total, five different samples named M1, A, B, C, and M3 were prepared. The volume fractions of small and large particles in the samples (based on the bidisperse model presented in Table 6.2), and the polydispersity indices, are given in Table 6.3.

*Table 6.3 The volume fractions of small particles ($\Phi_S$) and large particles ($\Phi_L$), and the polydispersity indices (PDIs) of samples M1, A, B, C, and M3, based on the bidisperse model presented in Table 6.2.*

| **Sample name** | **$\Phi_S$** | **$\Phi_L$** | **Polydispersity index (PDI)** |
|---|---|---|---|
| M1 | 0.017 | Nil | 0.22 |
| A | 0.008 | 0.008 | 0.47 |
| B | 0.004 | 0.012 | 0.60 |
| C | 0.00198 | 0.0148 | 0.71 |
| M3 | Nil | 0.017 | 0.79 |

The field-induced microstructures in all five samples were studied at different magnetic field strengths using a phase contrast optical microscope. The resulting images at magnetic field strengths of 80 G (a, e, i, m, q), 170 G (b, f, j, n, r), 280 G (c, g, k, o, s), and

550 G (d, h, l, p, t) are shown in **Fig. 6.5.** The direction of $H$ is shown by an arrow in **Fig. 6.5 (d)**. Similar to **Fig. 6.1**, no visible aggregates or chains are seen in sample M1 at any magnetic field strength. In sample A, with half of the total volume fraction containing large particles (i.e., $\Phi_\mathrm{L} = 0.008$), chains are formed in the direction of magnetic field even at a small field strength of 80 G, where the larger sized particles act as nucleation centers. The average length of the chains increases from 20 µm to 225 µm as the magnetic field strength increases from 80 G to 550 G. Zippering of chains is seen above a field strength of 170 G, and progressive growth of small chains, through long chains, to zippered columns is seen on increasing the magnetic field from 80 G to 550 G. In sample B, the average length of the chains increases from 32 µm to 305 µm, as the magnetic field strength is increased from 80 G to 550 G. Similarly, in samples C and M3, with $\Phi_\mathrm{L} = 0.0148$ and 0.017, respectively, short chains, longs chains, zippered columns, and finally magnetic sheets are formed when the field strength is increased from 80 G to 550 G.

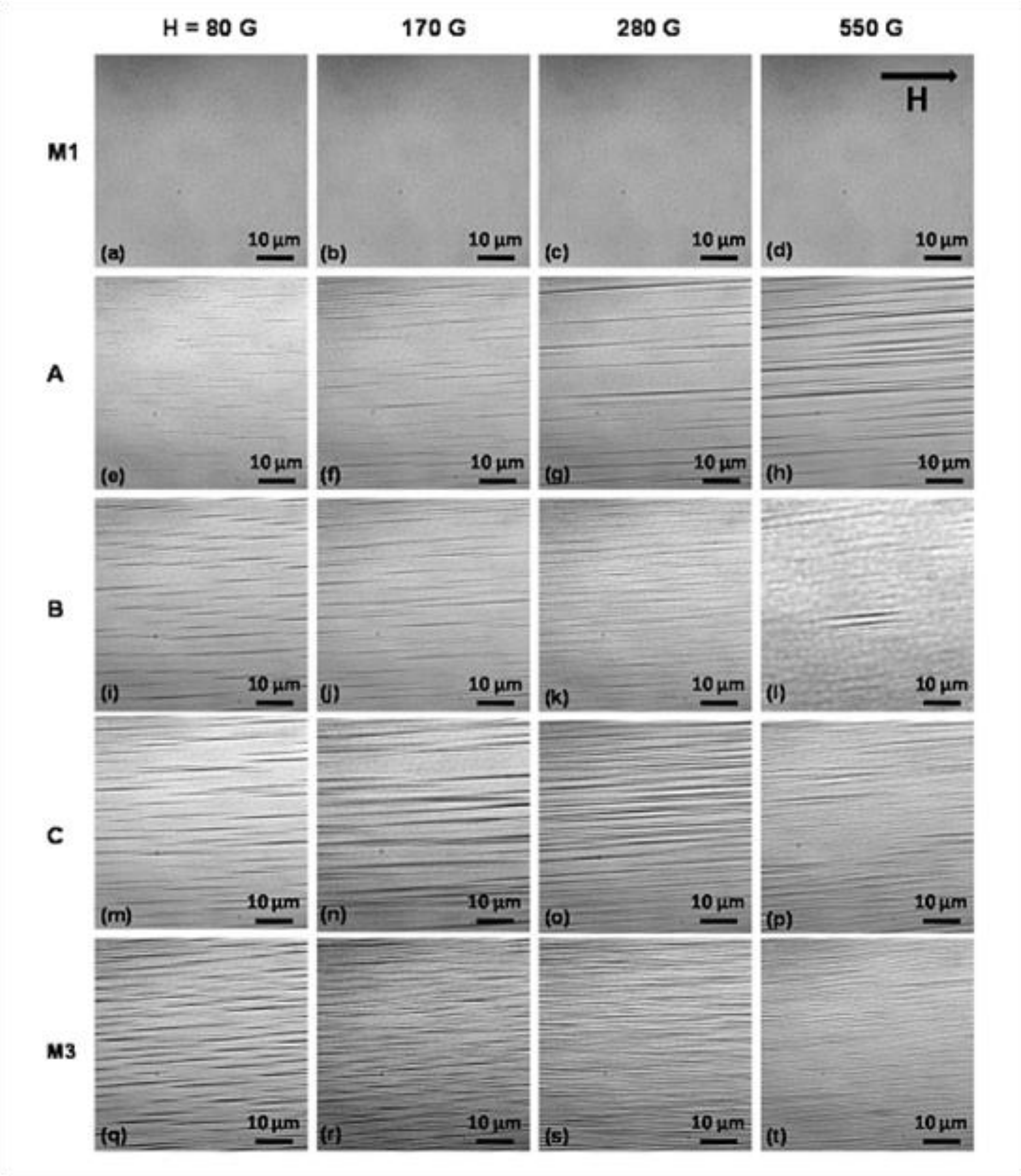

*Figure 6.5 Phase contrast optical microscopy images (side view) of magnetic field induced microstructures in samples M1, A, B, C, and M3 at different magnetic field strengths of 80 G (a, e, i, m, q), 170 G (b, f, j, n, r), 280 G (c, g, k, o, s), and 550 G (d, h, l, p, t). The direction of the magnetic field H is shown in Fig. 6.5 (d).*

The cross-sectional (top) view of field induced structures in samples M1, A, B, C, and M3 at magnetic field strengths of 80 G (a, e, i, m, q), 170 G (b, f, j, n, r), 280 G (c, g, k, o, s), and 550 G (d, h, l, p, t) are shown in **Fig. 6.6**.

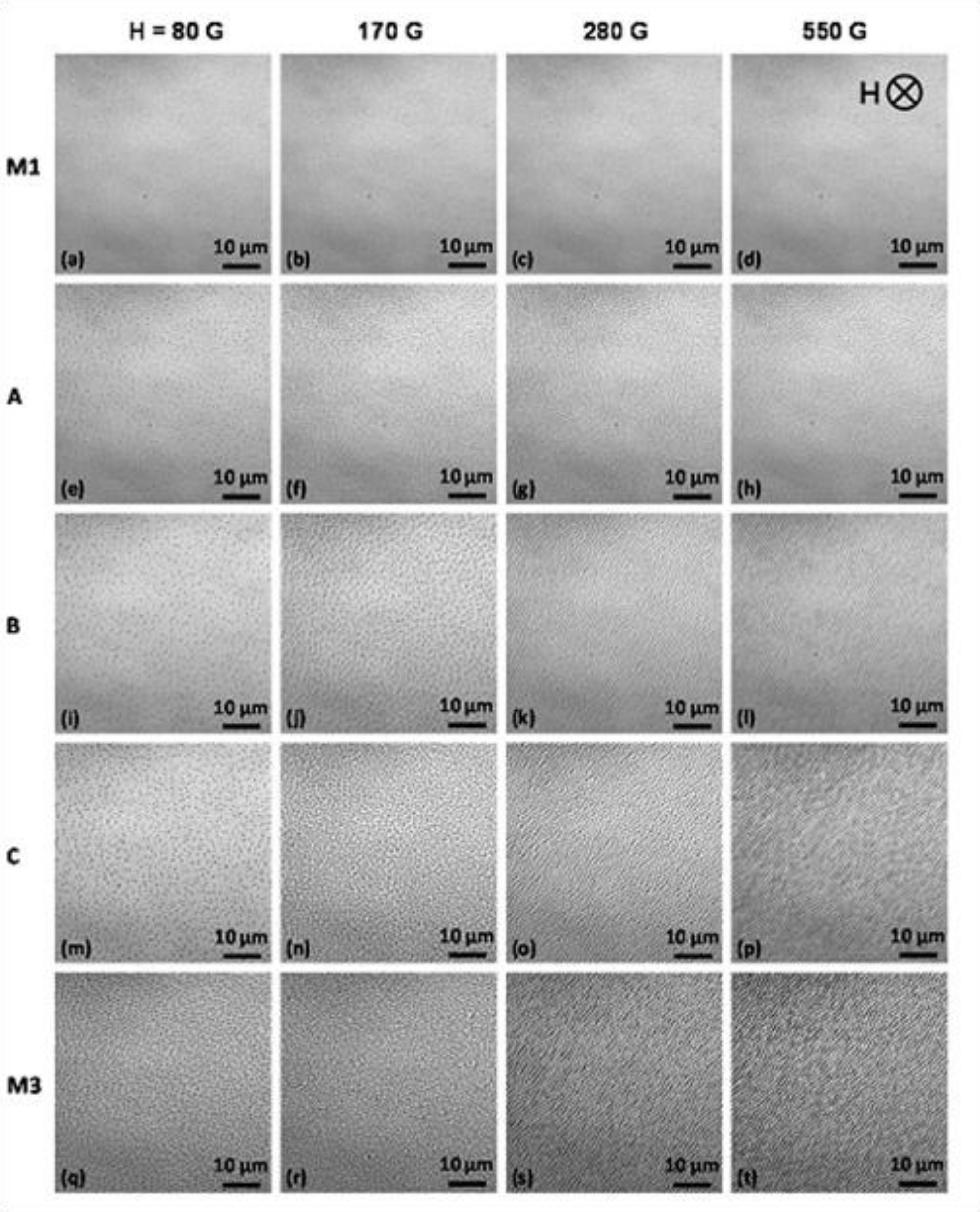

*Figure 6.6 Phase contrast optical microscopy images (top view) of magnetic field induced microstructures in samples M1, A, B, C, and M3 at different magnetic field strengths of 80 G (a, e, i, m, q), 170 G (b, f, j, n, r), 280 G (c, g, k, o, s), and 550 G (d, h, l, p, t). The direction of the magnetic field H is shown in Fig. 6.6 (d).*

Here, the orientation of the magnetic field is normal to the sample plane. In sample A, a large number of bubbles are seen at 80 G. The number of bubbles increases within the field of view, and the interbubble spacing decreases, with increasing magnetic field. The bubbles are distributed randomly in the dispersions even at 550 G. However, in samples B, C, and M3, above a certain magnetic field strengths, hexagonal close packed structures and finally lamellar structures (formed by lateral aggregation of columns) are observed. The isotropic, hexagonal columnar, and lamellar/stripe patterns observed in samples B, C, and M3 indicate the prominent roles of the larger sized particles and the applied magnetic field strength in structural transitions in ferrofluids. The lamellar structures are formed only at high volume fraction and high magnetic field strength.

The average intercolumn spacing, determined from the microscopy images using *IMAGE J* software, as a function of both the volume fraction of large particles and the applied magnetic field strength, are shown in **Fig. 6.7.** The magnetic field strengths considered are below that at which stripe patterns start to form. **Fig. 6.7 (a)** shows that the intercolumn spacing decreases with increasing $\Phi_{\mathrm{L}}$, and follows a power-law dependence (i.e., $\sim\Phi_{\mathrm{L}}^{-x'}$) where the exponent $x'$ has values of 1.17 ($R^2 = 0.98$), 0.95 ($R^2 = 0.99$), 1.08 ($R^2 = 0.98$), and 1.006 ($R^2 = 0.80$) at magnetic field strengths of 50 G, 80 G, 120 G, and 170 G, respectively. **Fig. 6.7 (b)** shows that the intercolumn spacing decreases and follows a power-law dependence with magnetic field strength ($\sim H^{-y'}$) where the exponent $y'$ is found to be 0.99 ($R^2 = 0.97$), 0.88 ($R^2 = 0.96$), 0.81 ($R^2 = 0.98$), and 0.94 ($R^2 = 0.97$) for samples A, B, C, and M3, respectively. **Fig. 6.7 (c)** and **(d)** shows the dependence of the intercolumn spacing on $\Phi_{\mathrm{L}}^{-1}$ and $H^{-1}$, respectively, confirming the roughly inverse dependence of the spacing on volume fraction and field strength.

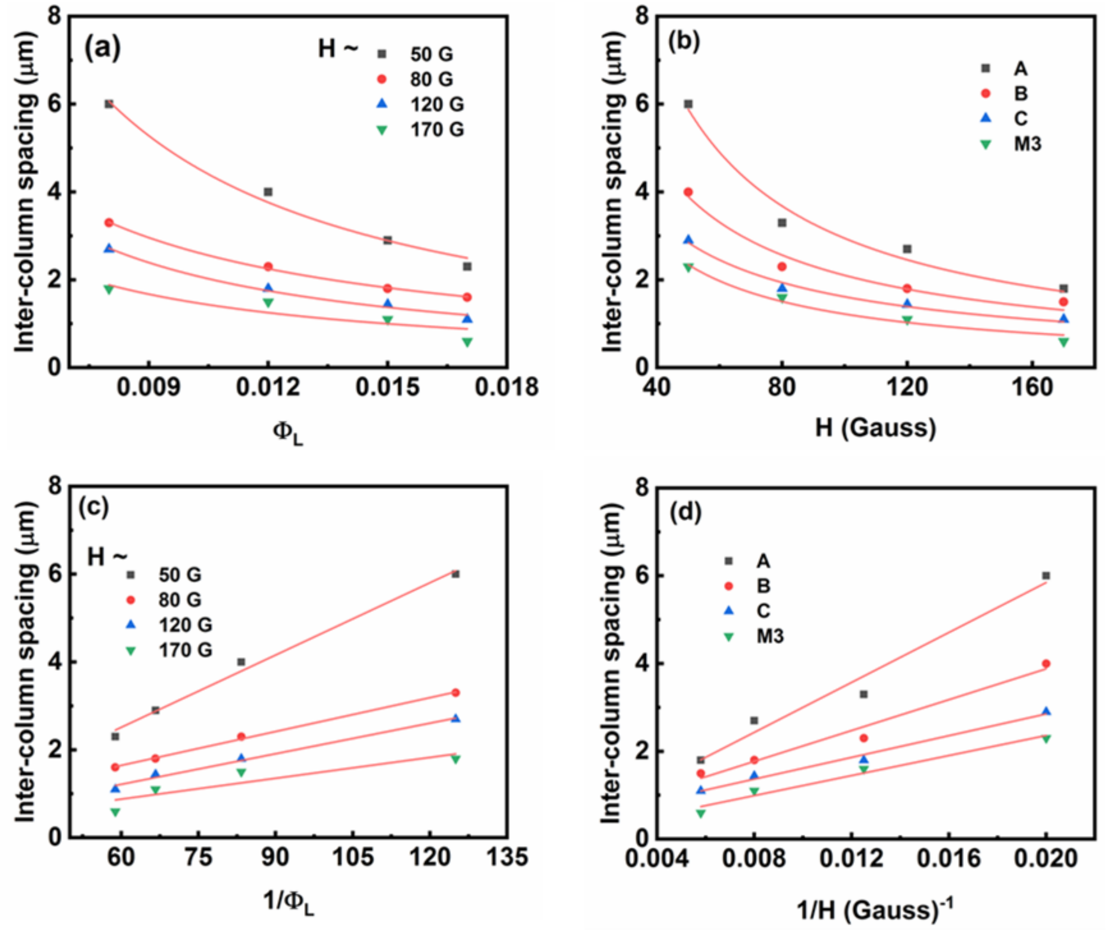

*Figure 6.7 Average intercolumn spacing as functions of (a) and (c) the volume fraction of large particles, and (b) and (d) the external magnetic field strength, in ferrofluid samples A, B, C, and M3. All results are with out-of-plane magnetic fields with strengths 50 G, 80 G, 120 G, and 170 G.*

From the microscopy results, a phase diagram is constructed on the basis of the volume fraction of the larger particles, and the applied magnetic field strength. The phase diagram showing the regions of isotropic (I), hexagonal (H), and stripe (S) phases is shown in **Fig. 6.8**. In the blue region of the graph, short chains and columns are randomly positioned throughout the sample, and this is called the isotropic phase. In the green and red regions, respectively, hexagonal close packed columnar structures and stripe patterns are formed. Under a high magnetic field, and with a high volume fraction of large particles, a stripe/lamellar pattern is observed. At intermediate magnetic fields, and a moderate volume fraction of large particles, hexagonal structures are formed. When the concentration of large particles is low, no hexagonal or stripe structures are observed, even under a strong magnetic field.

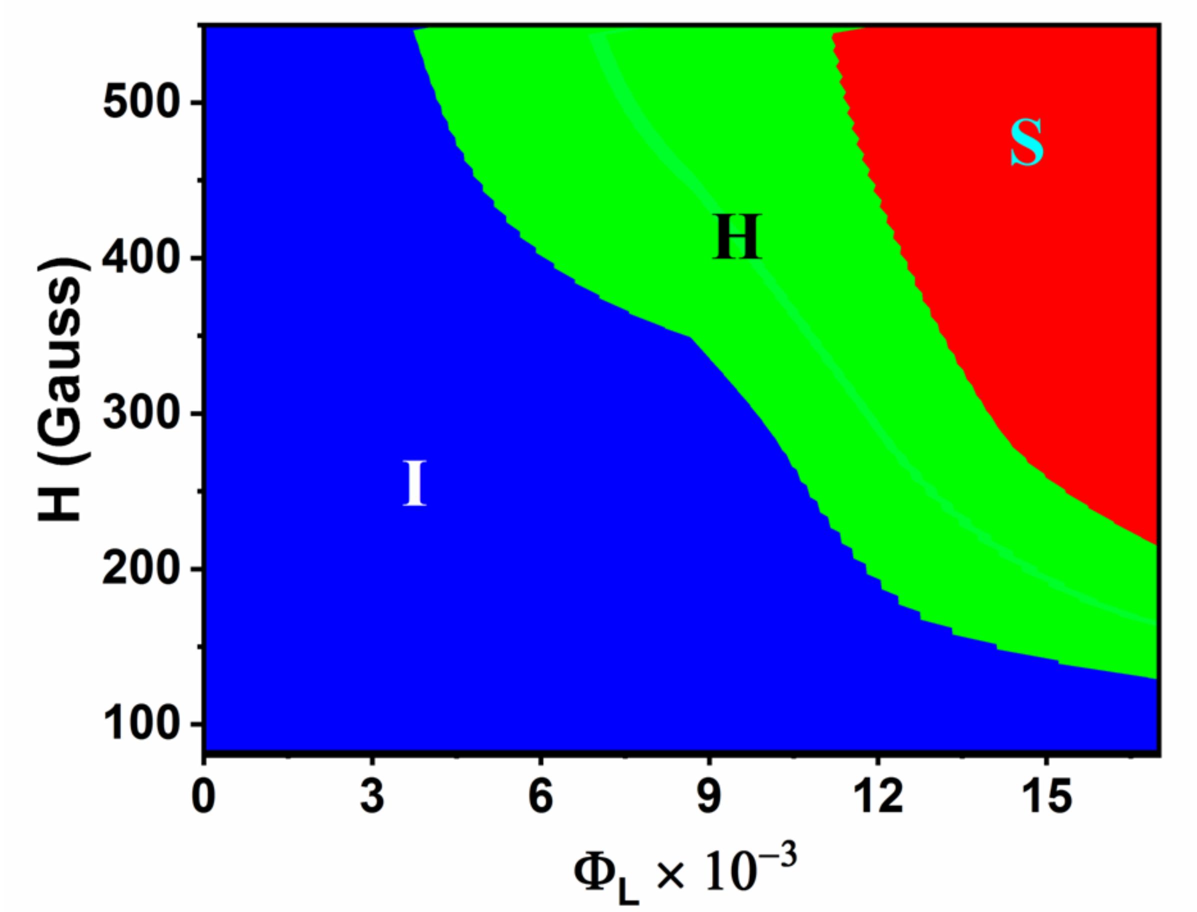

*Figure 6.8 Phase diagram of magnetic nanofluids with large-particle volume fraction $\Phi_L$ and magnetic field strength $H$, showing the structural boundaries between isotropic (I), hexagonal (H), and stripe (S) phases.*

### 6.3.3. Scattered pattern and the light transmission through magnetic nanofluids

The scattered light intensity pattern from samples M1, M2, and M3 at magnetic field strengths of 0 G, 80 G, 170 G, and 550 G are shown in **Fig. 6.9**. The magnetic field direction is parallel to the direction of light propagation.

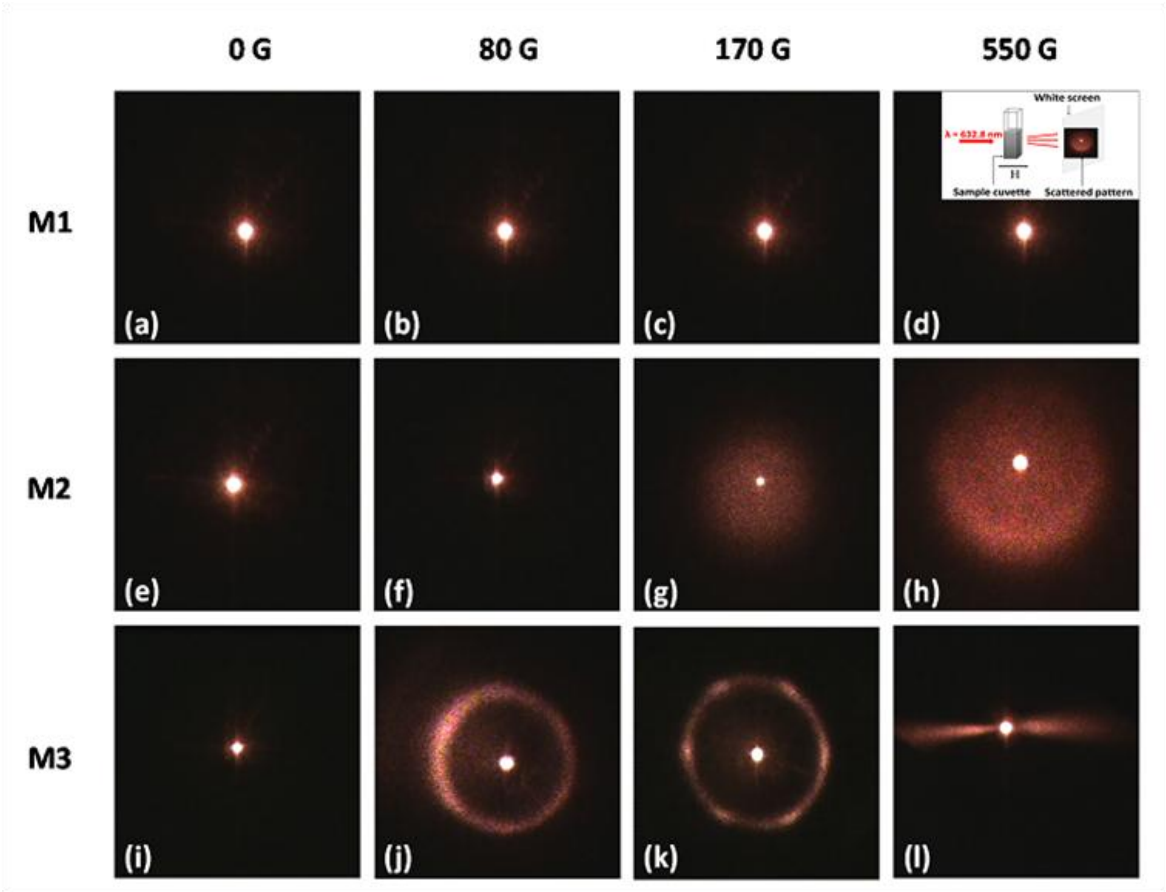

*Figure 6.9 Scattered light intensity pattern from samples M1, M2, and M3 at magnetic field strengths of 0 G (a, e, i), 80 G (b, f, j), 170 G (c, g, k), and 550 G (d, h, l). The inset of Fig. 6.9 (d) shows the schematic representation of light scattering measurement.*

In the absence of a magnetic field, there is no clustering of the magnetic nanoparticles, and since the particles are smaller than the wavelength of incident light ($d \ll \lambda$), Rayleigh scattering gives rise to one central spot on the screen. When the size of the scatterers is comparable to the wavelength of incident light, the scattering changes from the Rayleigh to the Mie regime. In case of sample M1, the spot intensity remains unchanged with an increase of the magnetic field strength, indicating that the scatterer size remains within the Rayleigh regime. **Fig. 6.1** shows that no micron-sized chains are visible in sample M1, even at the highest magnetic field strength of 550 G. Due to the presence of only smaller aggregates such as pairs, triplets, and other small chains, no changes in the intensity of the transmitted light spot are observed. In sample M2, there is a slight decrease in light intensity at 80 G. At 170 G, intense speckles of white spots and dark spots appear around the central spot. The scattered waves from ordered media remain in phase rather than be dephased, which increases the probability of constructive interference of scattered wave. As the field increases, the number of single chains increases in the direction of the magnetic field. At 550 G, the system contains isolated particles, pairs, triplets, small chains, and large chains, as shown in **Fig. 6.1**. The number of speckles and the speckle contrast both increase, and the speckles are arranged in a circle indicating that linear aggregates are formed along the light-propagation direction. The increase in speckle contrast indicates a decrease in the mobility of the growing aggregates on increasing the magnetic field strength [160]. In sample M3, the transmitted light spot at zero field is transformed into a circular pattern at 80 G, where the speckles are distributed on the circumference of circle, indicating the formation of long chains and zippered columns that are distributed randomly in the sample, as shown in **Fig. 6.1** and **Fig. 6.2.** The reason for the formation of a circular pattern can be explained on the basis of light scattered by cylindrical surfaces which is discussed in chapter 3. For $\zeta_c = 0°$, the scattered pattern will be a circle as shown for sample M3 at 80 G in **Fig. 6.9 (j)**. In sample M3 at 170 G, six bright spots with some speckles are observed at the circumference of the circular pattern, indicating the presence of a short-range ordered hexagonal pattern. At 550 G, a straight-line pattern is observed due to the scattering of light from stripe-like structures, which is analogous to the scattering pattern form a straight line when the incident-light direction is normal to the cylinder axis.

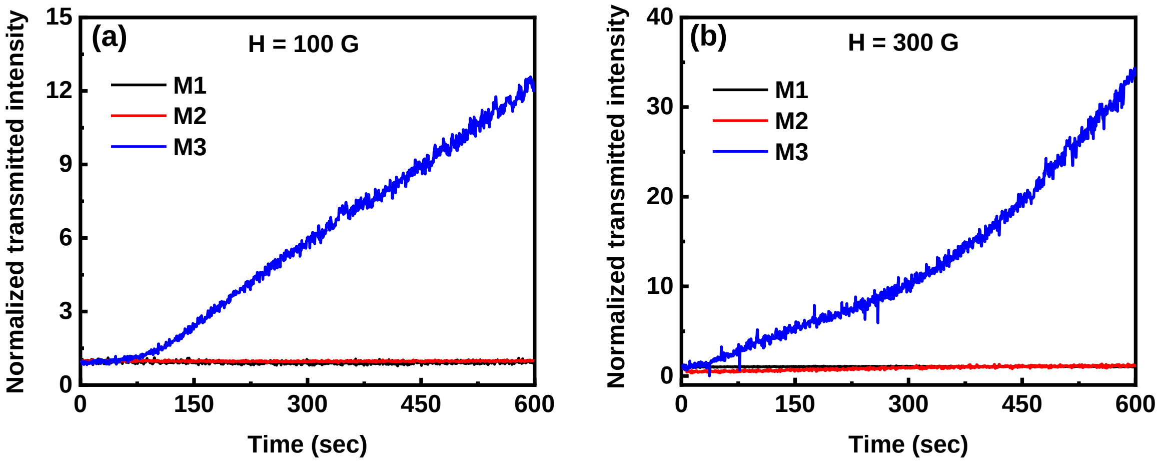

*Figure 6.10 Normalized transmitted light intensity as a function of time for samples M1, M2, and M3 at magnetic field strengths of (a) 100 G and (b) 300 G.*

**Figure 6.10** shows the normalized transmitted light intensity as a function of time for samples M1, M2, and M3 at magnetic field strengths of 100 G and 300 G. The magnetic field was switched on at time $t = 0$ s, and kept constant up to $t = 600$ s. The transmitted light intensity through samples M1 and M2 in the presence of a magnetic field remains invariant with time. However, sample M3 shows drastic changes in the transmitted intensity in the presence of a magnetic field. At 100 G, the transmitted intensity remains constant during the initial time interval ($t = 0\ \mathrm{s} - 75\ \mathrm{s}$), and after that it increases linearly with time with a slope of about $0.02\ \mathrm{s}^{-1}$ ($R^2 = 0.99$). At 300 G, the transmitted light intensity starts to increase after 35 s, and ultimately follows a power-law increase with time ($\sim t^{x'}$), where the exponent $x'$ is found to be 1.5 ($R^2 = 0.98$). Similar trends in the temporal variation of the transmitted light intensity were observed for a ferrofluid emulsion. Sample M3 contains larger sized particles that act as nucleation centers, which initiate chain formation even at low magnetic field strength. With a further increase in the magnetic field strength, the aspect ratio of the chains increases. Once the chains reach the maximum length, the lateral interaction between chains leads to zippering. As the number density of chains decreases, and the spacing between the chains increases, more light is transmitted. This explains the growth in transmitted light intensity in sample M3 with a strong magnetic field. Due to the presence of nanosized aggregates with high diffusion coefficients, no changes in the transmitted light intensity as a function of time are observed in samples M1 and M2.

**Figure 6.11 (a – c)** shows the variation of the normalized transmitted light intensity as a function of magnetic field strength at a ramp rate of $2\ \mathrm{G\ s^{-1}}$, during both the increase and decrease, for samples M1, M2, and M3.

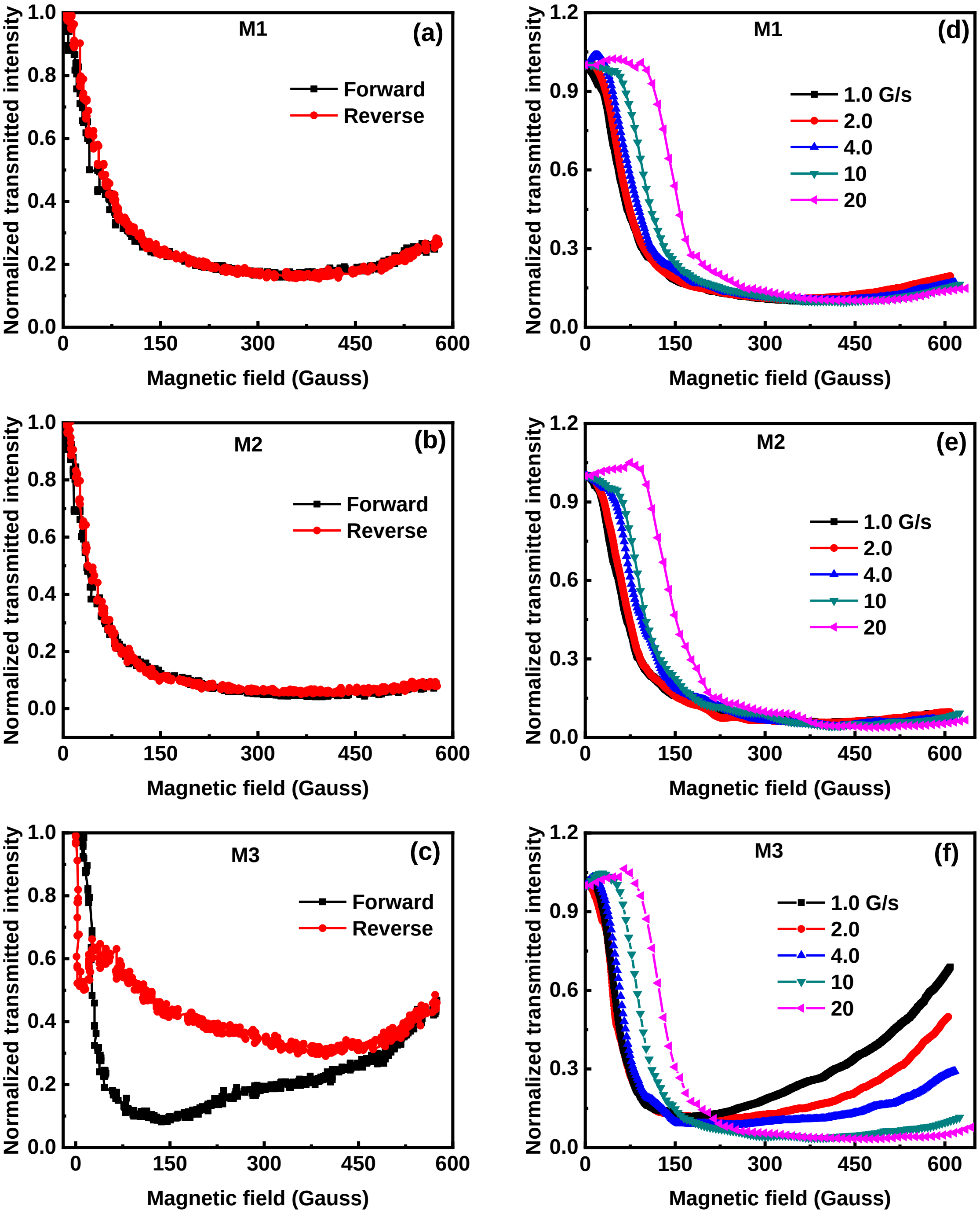

*Figure 6.11 (a – c) Transmitted light intensity as a function of external magnetic field during increase and decrease at a ramp rate of 2 G s$^{-1}$. (d – f) Transmitted light intensity as a function of the external magnetic field strength at ramp rates of 1, 2, 4, 10, and 20 G s$^{-1}$. (a) and (b) are for sample M1, (c) and (d) are for sample M2, and (e) and (f) are for sample M3.*

For sample M3, a large hysteresis in the transmitted light intensity curve is observed during the increase and decrease of magnetic field. However, for samples M1 and M2, no hysteresis is observed during the increase and decrease of the field, which indicates rapid aggregation and disaggregation processes. The significant hysteresis area observed with sample M3 indicates slow field-induced aggregation arising from the higher polydispersity. This observation shows that the polydispersity plays an important role in the aggregation and disaggregation processes. The transmitted light intensity returns to its initial value after switching off the magnetic field, indicating that the particles are redispersed after removing the applied magnetic field. **Fig. 6.11 (d – f)** shows the variation of the transmitted light intensity as a function of magnetic field at different ramp rates of 1, 2, 4, 10 and $20\ \mathrm{G\,s^{-1}}$ for samples M1, M2, and M3. For all ramp rates, the transmitted light intensity through samples M1 and M2 is found to decrease with increasing magnetic field, and reach a plateau at high magnetic field strength. The transmitted light intensity through sample M3 increases after reached at a minimum in the presence of the magnetic field strength for all ramp rates, except $20\ \mathrm{G\,s^{-1}}$, indicating the formation of long chains and columns in the direction of the magnetic field, which scatter more light in the forward direction.

### 6.3.4. Insights on chain and sheet formation from Brownian dynamics simulations

Brownian dynamics simulations are used to gain further insight on the crossover between columnar and stripe patterns in sample M3. **Fig. 6.12 (a)** shows the particle-size distribution from the DLS study, along with a discretized version containing 11 fractions for use in the simulations. As explained in section 6.3.1, the ferrofluid is a paramagnetic substance, and hence it is attracted to a region with high magnetic field intensity. As a result, the exact volume fraction of particles within the experimental observation region is not known, and neither is the local particle-size distribution. So for the purposes of illustration, it is assumed that the particle size distribution in the observation region is the same as that for the bulk sample, and the volume fraction is scanned between 1 and 6 times the stock value, meaning $\Phi = 0.037 - 0.222$. The third moment of the particle-size distribution is $\langle \sigma^3 \rangle = 1.23 \times 10^4$ nm$^3$, and so with $N_p = 15552$ particles, and a fixed $z$ dimension of 671 nm, the $x$ and $y$ dimensions of the cell ranged from 2014 nm at the lowest volume fraction to 822 nm at the highest volume fraction. Since the average particle diameter is 22 nm, the box dimensions are at least 30 times bigger in all cases.

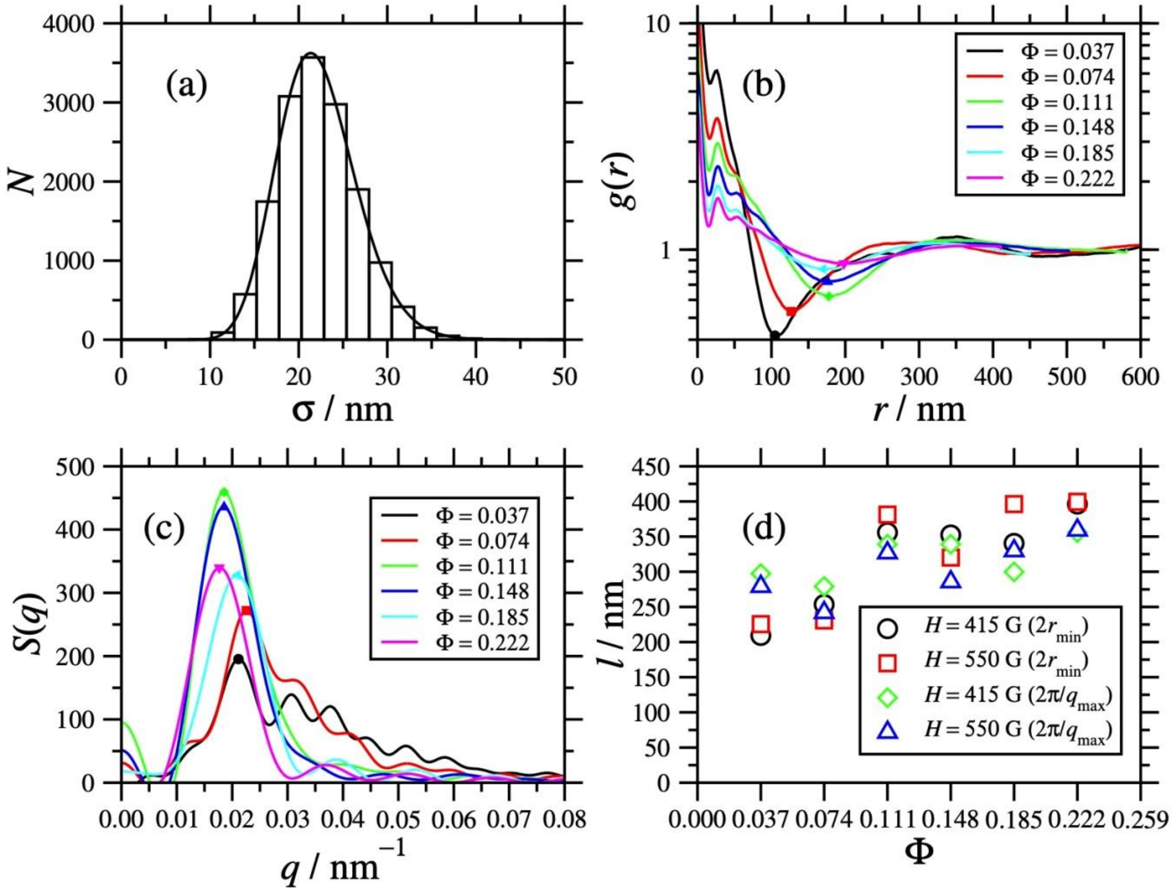

*Figure 6.12 (a) The particle-size distribution mimicking sample M3. (b) The two-dimensional radial distribution function $g(r)$ of particle positions projected onto the* xy *plane (perpendicular to the field direction). (c) The static structure factor $S(q)$ corresponding to the radial distribution function in (b). (d) Characteristic length scales extracted from the minima in the radial distribution function, and the maxima in the static structure factor. The points in (b) and (c) indicate the first minima and primary maxima, respectively.*

**Figure 6.13** shows top-down views of systems corresponding to $H = 280$ G, and $\Phi = 0.037$ and 0.222. For each system, an orthographic view and a perspective view are shown, so that the presence of chains in the field direction can be discerned. In the case of the orthographic view, four periodic replicas are shown in the *xy* plane, so that any clusters cut by the box edge can be distinguished. At $\Phi = 0.037$, it is clear that long chains of large particles have formed in the field direction, but many of the small particles are not part of any cluster. Some chains are one-particle thick, and others are zippered. The orthographic view – where the particle positions are projected on the plane – shows some clustering, but the distinction between clusters and free particles is not very clear. Increasing the volume fraction does not produce any interesting structure. As shown in **Fig. 6.13**, at $\Phi = 0.222$, no distinct clusters can be identified clearly from either view.

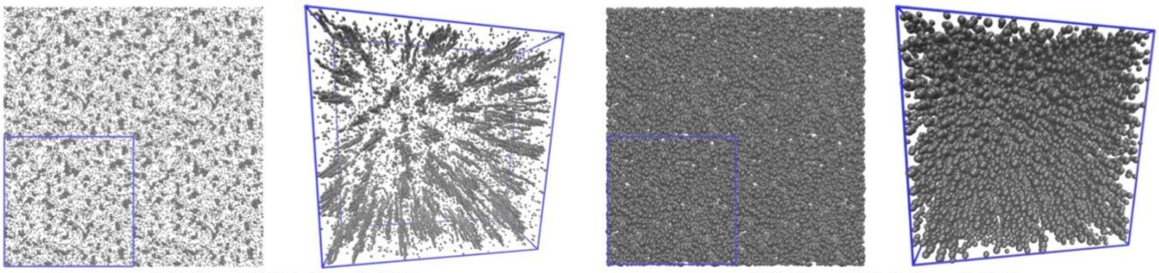
(a) $H = 280$ G, $\Phi = 0.037$ (b) $H = 280$ G, $\Phi = 0.222$

*Figure 6.13 Snapshots from simulations with $H = 280$ G and (a) Φ = 0.037, and (b) Φ = 0.222. In each case, an orthographic view (with 4 periodic replicas) and a perspective view are shown.*

Higher field strengths are required to produce more distinct clusters. **Fig. 6.14** shows snapshots from simulations at a field of 415 G (halfway between the experimental values of 280 G and 550 G), and at six volume fractions in the range $\Phi = 0.037 - 0.222$. The results are dramatically different from those at the lower magnetic field strength. Firstly, a much greater proportion of particles are now associated with columns, meaning that the clusters are much more distinct in the snapshots. At the three lowest volume fractions ($\Phi = 0.037$, $0.074$, and $0.111$) the columns mostly have cylindrical symmetry, and are evenly spaced in the *xy* plane, but without long-range ordering. At higher volume fractions ($\Phi \geq 0.148$) the columns have coalesced to form structures that are more extended in the direction perpendicular to the field, and as the volume fraction is increased, they begin to connect up further to form something resembling a continuous, labyrinthine structure. The perspective views clearly show the sheet-like structures formed by the coalescence of the columns.

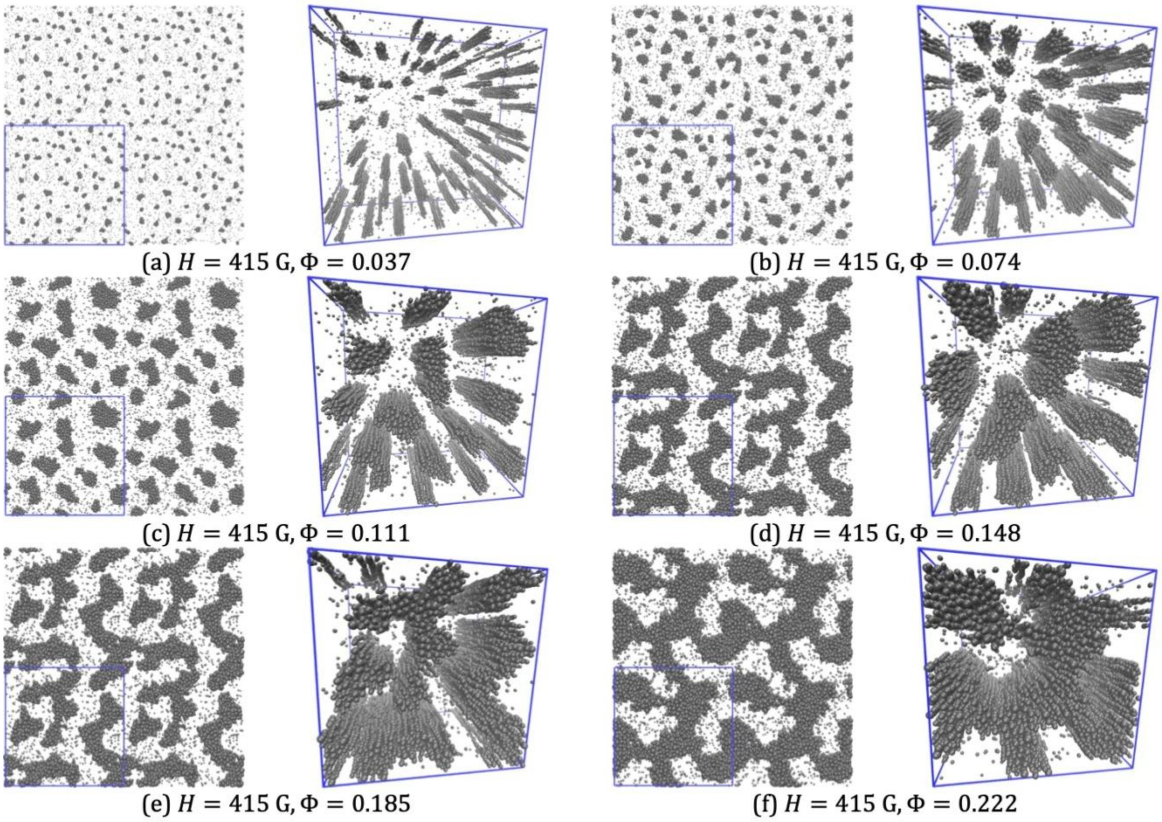

(a) $H = 415$ G, $\Phi = 0.037$ (b) $H = 415$ G, $\Phi = 0.074$

(c) $H = 415$ G, $\Phi = 0.111$ (d) $H = 415$ G, $\Phi = 0.148$

(e) $H = 415$ G, $\Phi = 0.185$ (f) $H = 415$ G, $\Phi = 0.222$

*Figure 6.14 Snapshots from simulations with* $H = 415$ *G and (a)* $\Phi = 0.037$*, (b)* $\Phi = 0.074$*, (c)* $\Phi = 0.111$*, (d)* $\Phi = 0.148$*, (e)* $\Phi = 0.185$*, and (f)* $\Phi = 0.222$*. In each case, an orthographic view (with 4 periodic replicas) and a perspective view are shown.*

**Figure 6.15** shows similar results but for a field strength of 550 G. The qualitative picture is very similar to that at 415 G. At low volume fractions, the particles are clustered into columns. There are fewer free, small particles at this field strength because of the increased magnetization and hence coupling constants of the particles. As the volume fraction is increased, the columns start to coalesce in the lateral dimension, forming sheet-like structures. At the highest volume fraction, these sheets connect up to form a labyrinthine structure; the snapshots very clearly show the two-dimensional nature of the sheets.

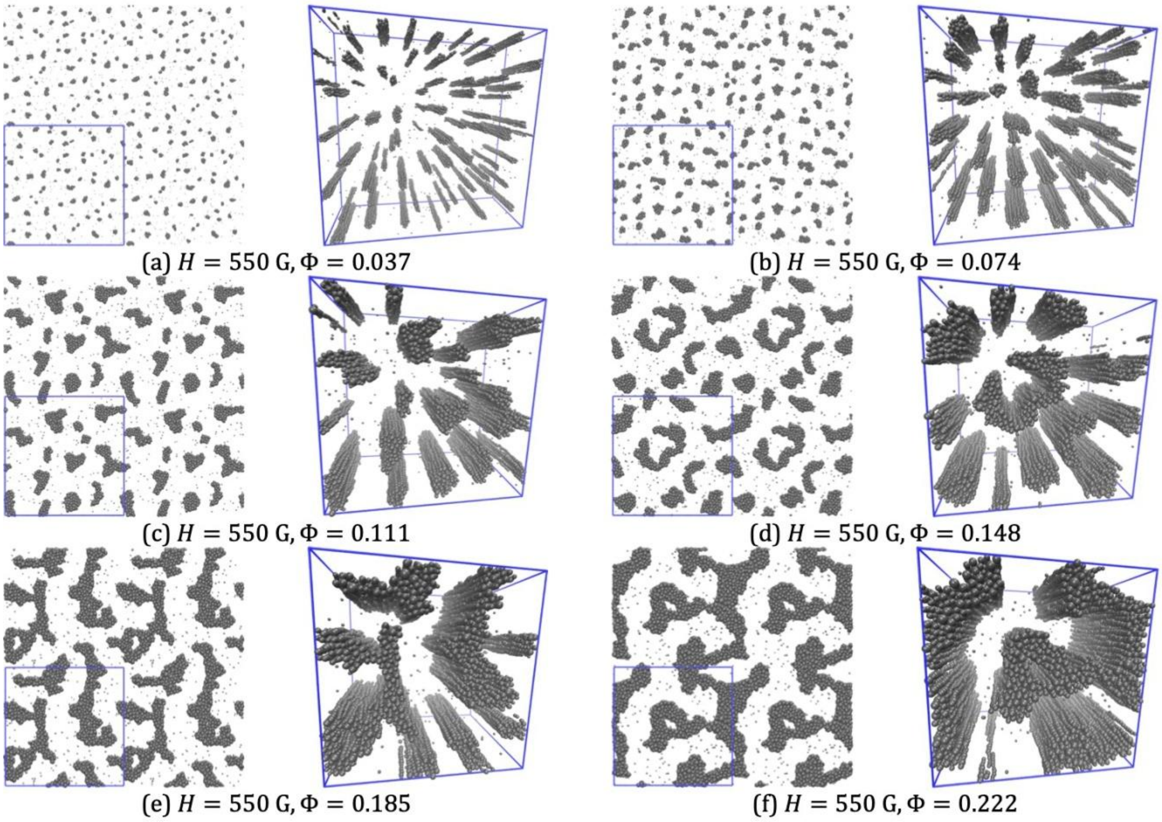

(a) $H = 550$ G, $\Phi = 0.037$

(b) $H = 550$ G, $\Phi = 0.074$

(c) $H = 550$ G, $\Phi = 0.111$

(d) $H = 550$ G, $\Phi = 0.148$

(e) $H = 550$ G, $\Phi = 0.185$

(f) $H = 550$ G, $\Phi = 0.222$

*Figure 6.15 Snapshots from simulations with* $H = 550$ *G and (a)* $\Phi$ *= 0.037, (b)* $\Phi$ *= 0.074, (c)* $\Phi$ *= 0.111, (d)* $\Phi$ *= 0.148, (e)* $\Phi$ *= 0.185, and (f)* $\Phi$ *= 0.222. In each case, an orthographic view (with 4 periodic replicas) and a perspective view are shown.*

To estimate the length scales of the various structures being formed, the two-dimensional radial distribution function $g(r)$ was computed by projecting all particle positions onto the *xy* plane. This is given by

$$g(r) = \lim_{\delta r \to 0} \frac{n(r, r + \delta r)}{2\pi N \varrho r \delta r} \tag{6.1}$$

where $n(r, r + \delta r)$ is the number of pairs of particles separated by a distance between $r$ and $r + \delta r$, the denominator is the number of such pairs expected for a completely random array of positions, and $\varrho$ is the total number of particles per unit area. As defined, $g(r) \to 1$ as $r \to \infty$ if there is no long-range order. The results for systems at 415 G and 550 G are shown in **Fig. 6.12 (b)**. The first minimum in $g(r)$ should occur at a distance ($r_{\min}$) roughly half-way between different clusters [highlighted by points in **Fig.**

**6.12 (b)**], and hence one estimate of the characteristic length scale in the system is $l = 2r_{\min}$. Another estimate of this length scale can be obtained by finding the primary peak in the static structure factor

$$S(q) = 1 + \varrho \int [g(r) - 1] \exp(-i\boldsymbol{q} \cdot \boldsymbol{r}) d\boldsymbol{r} = 1 + 2\pi\varrho \int_0^\infty r J_0(qr)[g(r) - 1] dr \qquad (6.2)$$

where $\boldsymbol{q}$ is a wave vector, $q = |\boldsymbol{q}|$, and $J_0(qr)$ is a Bessel function of the first kind. In the absence of any order, $S(q) = 1$, while the presence of large-scale structures are indicated by peaks at low values of $q$. The results are shown in **Fig. 6.12 (c)**, and the primary peaks ($q_{\max}$) are highlighted by points. The characteristic length scale corresponds to $l = 2\pi/q_{\max}$.

**Figure 6.12 (d)** shows the characteristic length scales obtained from both $g(r)$ and $S(q)$, as functions of the volume fraction, and for the field strengths $H = 415$ G and 550 G (no structure being discernible at 280 G). Firstly, the two routes give broadly similar results. Secondly, as the volume fraction increases (corresponding to the ingress of magnetic nanoparticles), the characteristic length scales approach values in the range 300 nm – 400 nm, irrespective of the field strength. This suggests that the natural length scale of the stripe-like patterns should be in the region of 0.4 μm. In Section 6.3.1, it was observed that the distance between stripes at the highest field strength was about 0.7 μm. There are several unknown factors at play here (local size distribution, volume fraction, and magnetic field strength and gradient). Moreover, the simulations can only capture a very small volume, and over much shorter timescales than in experiments (on the timescale of minutes). Nonetheless, the simulations show how columns coalesce to form sheets, and that the spacing between sheets is at least of the right order of magnitude as compared to experiment.

## 6.4. Conclusions

The effect of size polydispersity on field-induced equilibrium and non-equilibrium structures in ferrofluids was probed systematically. Three different ferrofluids – labelled M1, M2, and M3 – containing magnetic nanoparticles with average crystallite diameters 9.6 nm, 8.3 nm, and 10.5 nm, and with different polydispersities, respectively, were studied. Phase contrast optical microscopy images revealed that sample M3 showed structural transitions from isotropic columnar, through hexagonal close packed, to striped patterns on increasing the magnetic field between 0 G and 500 G. In contrast, samples M1 and M2 showed no such structural transitions. The formation of stripe/lamellar structures was completely reversible upon switching on and off the external magnetic field. The lamellar structures obtained in strong fields were dynamic, and disappeared upon the removal of the external magnetic field. In sample M3, bubbles were formed at a very low magnetic field strength of 30 G, with an average intercolumn spacing of 3 μm, which was found to decrease with increasing magnetic field. Hexagonal close packed columnar structures were formed with an intercolumn spacing of 0.6 μm at 170 G. The average intercolumn spacing was found to vary inversely with the external magnetic field up to 170 G, beyond which the columns coalesced and formed striped patterns. At very high magnetic field strength, an undulation due to the long-range magnetic coupling interaction between stripes gave rise to a zig-zag pattern. The isotropic, hexagonal columnar, and lamellar/stripe patterns observed in sample M3 indicate the prominent roles of larger sized particles and the applied magnetic field strength in structural transitions in ferrofluids. The lamellar structures were formed only at high volume fraction of large particles and with strong magnetic fields. The intercolumn spacing decreased with $\Phi_L$ and followed a power-law dependence. The intercolumn spacing varied inversely with the magnetic field strength. A phase diagram was constructed containing the different structures seen with different volume fractions and field strengths. The structural transitions observed with microscopy were also confirmed using light-scattering techniques, with each structure giving rise to characteristic features in the scattering pattern. In addition, time-resolved experiments showed that the aggregation and disaggregation kinetics are slow, but that the processes are essentially reversible. Finally, Brownian dynamics simulations were used to gain some insights on the formation of the magnetic sheets which give rise to the stripe-like patterns in the high-polydispersity sample (M3) seen with very strong magnetic fields. It was shown how thin chains coalesce to form sheets with increasing magnetic field, and although the ultimate equilibrium structures cannot be obtained on the simulation timescale, the emerging characteristic length scales were in approximate agreement with those seen in the microscopy experiments. Our work not only provide new insights into the role of PDI on structural transitions but also opens up new opportunities to develop optical devices and accessing diverse structures by tuning size polydispersity. The obtained results are useful for the design of light-controllable magnetic-fluid-based devices such as light modulators and light switches, where the light transmission through magnetic fluid can be controlled by an external magnetic field, size polydispersity and volume fraction of larger sized particles. The reversible and fast response of polydisperse sample will also be beneficial for microfluidics applications such as ferrofluid-based robots and lab-on-chip devices.

# *Chapter 7*

# Conclusions and recommendations for future work

## 7.1. Summary and conclusions

The parameters such as volume fraction, size polydispersity, surfactant concentration, magnetic field strength, field ramp rate, field orientation, and switching conditions, etc., influencing the field driven structures in magnetic fluids (ferrofluids and ferrofluid emulsions), its temporal evolution and dynamics were studied systematically. The important results are summarized below.

The role of surface charge on the critical magnetic field for various structural transitions in magnetic nanoemulsion of different volume fractions is studied for the first time. Three distinct critical magnetic fields are identified from the changes in the field dependent transmitted forward scattering light intensity, which correspond to the commencement of small aggregate formation, complete formation of linear aggregates before the commencement of lateral coalescence of individual chains, and the formation of densely packed columnar solid like structures through zippering of individual chains. The field induced anisotropic structure formation in the emulsion was evident from the ring like pattern observed. With decreasing Debye screening length, the aggregation rate was found to increase linearly. The experimentally observed critical fields were in good agreement with theoretical predictions at lower surfactant concentrations.

The effect of volume fraction of magnetic droplets, magnetic field strength, and surfactant concentration on the temporal evolution of magnetic field induced structures, is studied using time dependent transmitted intensity measurement and phase contrast optical microscopy. The transmitted light intensity through ferrofluid emulsion is found to decrease after a certain critical field ($H_{c1}$) and reaches a minimum at a higher magnetic field. At low magnetic field strength ($H$ = 50 G), the long chains and zippered structures are formed by lateral chain aggregation where the spacing among the chains is found to increase with time. At higher magnetic field strength ($H$ = 300 G), the chains are interconnected to each other and the spacing between the chains remains constant with time, which was consistent with the observed time independent transmitted light intensity. With increased volume fraction of droplet and surfactant concentration, a larger number of individual non-zippered chains are observed at higher magnetic field strength due to the reduction of lateral diffusion of magnetic chains in the dispersion. These results confirm that the lateral diffusion of chains is hindered at high magnetic field strength due to reduced thermal fluctuation.

The field induced optical transparency and its origin in magnetic nanoemulsion containing droplets of average size ~200 nm is studied for the first time. The effect of volume fraction on critical magnetic fields and the transmitted light intensity were studied systematically. Beyond a volume fraction, the nanoemulsions showed a field induced transparency and the critical magnetic fields at which transparency was observed increased drastically, following a power law decay with $\Phi$ with distinct exponents. The field induced transparency in magnetic fluid was perfectly reversible. The observed field induced transparency in magnetic emulsions for $\Phi > 0.0021$ is attributed to the optical birefringence caused by the rod like nanostructures, which was further confirmed from the straight line scattering pattern observed on a screen placed perpendicular to the incident beam. The reduced birefringence is found to be proportional to the square of the applied magnetic field.

The effect of size polydispersity on field-induced equilibrium and non-equilibrium structures in ferrofluids was probed systematically. Phase contrast optical microscopy images revealed that sample with high polydispersity (M3) showed structural transitions from isotropic columnar, through hexagonal close packed, to striped patterns on increasing the magnetic field between 0 G and 500 G. In contrast, samples with low polydispersity showed no such structural transitions. The formation of stripe/lamellar structures was completely reversible upon switching on and off the external magnetic field. The lamellar structures obtained in strong fields were dynamic, and disappeared upon the removal of the external magnetic field. In sample with high polydispersity, bubbles were formed at a very low magnetic field strength of 30 G, with an average intercolumn spacing of 3 μm, which was found to decrease with increasing magnetic field. Hexagonal close packed columnar structures were formed with an intercolumn spacing of 0.6 μm at 170 G. The average intercolumn spacing was found to vary inversely with the external magnetic field up to 170 G, beyond which the columns coalesced and formed striped patterns.

At very high magnetic field strength, an undulation due to the long-range magnetic coupling interaction between stripes gave rise to a zig-zag pattern. The isotropic, hexagonal columnar, and lamellar/stripe patterns observed in sample M3 indicate the prominent roles of larger sized particles and the applied magnetic field strength in structural transitions in ferrofluids. The lamellar structures were formed only at high volume fraction of large particles and with strong magnetic fields. The intercolumn spacing decreased with $\Phi_L$ and followed a power-law dependence. The intercolumn spacing varied inversely with the magnetic field strength. The structural transitions observed with microscopy were also confirmed using light-scattering techniques, with each structure giving rise to characteristic features in the scattering pattern. In addition, time-resolved experiments showed that the aggregation and disaggregation kinetics are slow, but that the processes are essentially reversible. Finally, Brownian dynamics simulations were used to gain some insights on the formation of the magnetic sheets which give rise to the stripe-like patterns in the high-polydispersity sample seen with very strong magnetic fields. It was shown how thin chains coalesce to form sheets with increasing magnetic field, and although the ultimate equilibrium structures cannot be obtained on the simulation timescale, the emerging characteristic length scales were in approximate agreement with those seen in the microscopy experiments. Our work not only provide new insights into the role of PDI on structural transitions but also opens up new opportunities to develop optical devices and accessing diverse structures by tuning size polydispersity.

The results of this study provide better insights into the field induced structure formation and are useful for the design of light-controllable magnetic-fluid-based devices such as light modulators, light switches, ferrofluid-based robots and lab-on-chip devices.

## 7.2. Major contributions

- The role of surface charge on the critical magnetic field for various structural transitions in magnetic nanoemulsion of different volume fractions is studied for the first time. Three distinct critical magnetic fields are identified from the changes in the field dependent transmitted light intensity, corresponding to the commencement of small aggregate formation, complete formation of linear aggregates and the formation of densely packed columnar solid like structures through zippering of individual chains.
- The field induced anisotropic structure formation in the emulsion is demonstrated from the ring like pattern.
- Obtained a relationship between Debye screening length and the aggregation rate.
- The dependence of transmitted light intensity in ferrofluid emulsion on critical field and volume fraction is established.
- The field induced optical transparency and its origin in magnetic nanoemulsion is demonstrated for the first time. Correlation between the field induced transparency, magnetic fields and $\Phi$ is established.

- New insights into the size polydispersity on field-induced equilibrium and non-equilibrium structures in ferrofluids are obtained.
- Structural transitions from isotropic columnar, through hexagonal close packed, to striped patterns on increasing the magnetic field is demonstrated in the sample with high polydispersity.
- The results from this study are useful for the design of light-controllable magnetic-fluid-based devices such as light modulators, light switches, ferrofluid-based robots and lab-on-chip devices.

## 7.3. Recommendations for future work

Recommendations for future work include:

- ✓ Probing the effect of temperature on field induced structural transitions in magnetic fluids (ferrofluids and magnetic nanoemulsions).
- ✓ Probing the role of viscosity of carrier liquid on the aggregation kinetics and magneto-optical properties in magnetic fluids.
- ✓ Probing the role of non-magnetic particles in magnetic fluids on magnetic field induced structural transitions and associated magneto-optical properties.
- ✓ Development of optical modulator, switches, field sensors, etc., using magnetic fluids

# References

[1] R.A.L. Jones, Soft Condensed Matter, Oxford University Press, Oxford, 2002.

[2] G. Gompper, M. Schick, An Introduction to Soft Matter, in: Soft Matter, Wiley-VCH Verlag GmbH & Co. KGaA, Weinheim, 2005, pp. 1-16.

[3] Y. Singh, J.G. Meher, K. Raval, F.A. Khan, M. Chaurasia, N.K. Jain, M.K. Chourasia, Nanoemulsion: Concepts, development and applications in drug delivery, J. Control. Release, 252 (2017) 28-49.

[4] D.T. Piorkowski, D.J. McClements, Beverage emulsions: Recent developments in formulation, production, and applications, Food Hydrocoll., 42 (2014) 5-41.

[5] M.M. Fryd, T.G. Mason, Advanced Nanoemulsions, Annu. Rev. Phys. Chem., 63 (2012) 493-518.

[6] M.S. El-Aasser, E.D. Sudol, Miniemulsions: overview of research and applications, JCT Res., 1 (2004) 21-32.

[7] J. Bibette, Depletion interactions and fractionated crystallization for polydisperse emulsion purification, J. Colloid Interface Sci., 147 (1991) 474-478.

[8] T. Tadros, P. Izquierdo, J. Esquena, C. Solans, Formation and stability of nano-emulsions, Adv. Colloid Interface Sci, 108 (2004) 303-318.

[9] K. Landfester, M. Willert, M. Antonietti, Preparation of polymer particles in nonaqueous direct and inverse miniemulsions, Macromolecules, 33 (2000) 2370-2376.

[10] W. Li, H. Chen, Z. He, C. Han, S. Liu, Y. Li, Influence of surfactant and oil composition on the stability and antibacterial activity of eugenol nanoemulsions, LWT - Food Sci. Technol., 62 (2015) 39-47.

[11] U. Buranasuksombat, Y.J. Kwon, M. Turner, B. Bhandari, Influence of emulsion droplet size on antimicrobial properties, Food Sci. Biotechnol., 20 (2011) 793-800.

[12] S. Hak, Z. Garaiova, L.T. Olsen, A.M. Nilsen, C.d.L. Davies, The effects of oil-in-water nanoemulsion polyethylene glycol surface density on intracellular stability, pharmacokinetics, and biodistribution in tumor bearing mice, Pharm. Res., 32 (2015) 1475-1485.

[13] K. Mortensen, J.S. Pedersen, Structural study on the micelle formation of poly (ethylene oxide)-poly (propylene oxide)-poly (ethylene oxide) triblock copolymer in aqueous solution, Macromolecules, 26 (1993) 805-812.

[14] R. Kumar, A.M. Ketner, S.R. Raghavan, Nonaqueous photorheological fluids based on light-responsive reverse wormlike micelles, Langmuir, 26 (2010) 5405-5411.

[15] R. Li, C.C. Horgan, B. Long, A.L. Rodriguez, L. Mather, C.J. Barrow, D.R. Nisbet, R.J. Williams, Tuning the mechanical and morphological properties of self-assembled peptide hydrogels via control over the gelation mechanism through regulation of ionic strength and the rate of pH change, RSC Adv., 5 (2015) 301-307.

[16] J.P. McTague, Magnetoviscosity of magnetic colloids, J. Chem. Phys., 51 (1969) 133-136.

[17] S. Fraden, A.J. Hurd, R.B. Meyer, Electric-Field-Induced Association of Colloidal Particles, Phys. Rev. Lett., 63 (1989) 2373.

[18] R.E. Rosensweig, Ferrohydrodynamics, Dover Publications, Inc. New York, 1997.

[19] L.J. Felicia, S. Vinod, J. Philip, Recent advances in magnetorheology of ferrofluids (magnetic nanofluids)—a critical review, J. Nanofluids, 5 (2016) 1-22.

[20] I. Nkurikiyimfura, Y. Wang, Z. Pan, Heat transfer enhancement by magnetic nanofluids—a review, Renew. Sustainable Energy Rev., 21 (2013) 548-561.

[21] J. Philip, J.M. Laskar, Optical properties and applications of ferrofluids—A review, J. Nanofluids, 1 (2012) 3-20.

[22] S.S. Papell, Low viscosity magnetic fluid obtained by the colloidal suspension of magnetic particles, in: in: U.S.P. Office (Ed.), United States, 1965.

[23] R.E. Rosensweig, Fluid Dynamics and Science of Magnetic Liquids, in: Adv. Electron. Electron Phys., Academic Press, 1979, pp. 103-199.

[24] C. Kittel, Theory of the structure of ferromagnetic domains in films and small particles, Phys. Rev., 70 (1946) 965.

[25] C. Kittel, Physical theory of ferromagnetic domains, Rev. Mod. Phys., 21 (1949) 541.

[26] A.P. Guimaraes, Principles of nanomagnetism, Springer-Verlag, Berlin, Heidelberg, 2009.

[27] C.A.F. Vaz, J.A.C. Bland, G. Lauhoff, Magnetism in ultrathin film structures, Rep. Prog. Phys., 71 (2008) 056501.

[28] W.T. Coffey, Y.P. Kalmykov, Thermal fluctuations of magnetic nanoparticles: Fifty years after Brown, J. Appl. Phys., 112 (2012) 121301.

[29] I. Torres-Díaz, C. Rinaldi, Recent progress in ferrofluids research: novel applications of magnetically controllable and tunable fluids, Soft Matter, 10 (2014) 8584-8602.

[30] W.F.B. Jr, Thermal fluctuations of a single-domain particle, Phys. Rev., 130 (1963) 1677.

[31] D.H. Everett, Basic Principles of Colloid Science, The Royal Society of Chemistry, London, 1988.

[32] D.F. Evans, H. Wennerstrom, The Colloidal Domain, Wiley-VCH, New York, 1999.

[33] C. Scherer, A.M.F. Neto, Ferrofluids: properties and applications, Braz. J Phys., 35 (2005) 718-727.

[34] L. Vékás, D. Bica, O. Marinica, Magnetic nanofluids stabilized with various chain length surfactants, Rom. Rep. Phys., 58 (2006) 257.

[35] A. Joseph, S. Mathew, Ferrofluids: synthetic strategies, stabilization, physicochemical features, characterization, and applications, ChemPlusChem, 79 (2014) 1382-1420.

[36] C.F. Kernizan, K.J. Klabunde, C.M. Sorensen, G.C. Hadjipanayis, Magnetic properties of nanometer-scale iron particles generated by iron atom clustering in cold pentane, Chem. Mater., 2 (1990) 70-74.

[37] P.C. Hiemenz, Principles of Colloid and Surface Chemistry, Marcel Dekker New York, 1986.

[38] G. Gnanaprakash, J. Philip, T. Jayakumar, B. Raj, Effect of digestion time and alkali addition rate on physical properties of magnetite nanoparticles, J. Phys. Chem. B, 111 (2007) 7978-7986.

[39] M. Wu, G. Liu, M. Li, P. Dai, Y. Ma, L. Zhang, Magnetic field-assisted solvothermal assembly of onedimensional nanostructures of Ni–Co alloy nanoparticles, J. Alloys Compd., 491 (2010) 689-693.

[40] S. Xuan, L. Hao, W. Jiang, X. Gong, Y. Hu, Z. Chen, Preparation of water-soluble magnetite nanocrystals through hydrothermal approach, J. Magn. Magn. Mater., 308 (2007) 210-213.

[41] T. Muthukumaran, J. Philip, A single pot approach for synthesis of phosphate coated iron oxide nanoparticles, J. Nanosci. Nanotechnol., 15 (2014) 2715-2725.

[42] K.D. Kim, S.S. Kim, Y.-H. Choa, H.T. Kim, Formation and surface modification of $Fe_3O_4$ nanoparticles by co-precipitation and sol-gel method, J. Ind. Eng. Chem., 13 (2007) 1137-1141.

[43] Z.G. Estephan, H.H. Hariri, J.B. Schlenoff, One-pot, exchange-free, room-temperature synthesis of sub-10 nm aqueous, noninteracting, and stable zwitterated iron oxide nanoparticles, Langmuir, 29 (2013) 2572-2579.

[44] R. Giernoth, Task-specific ionic liquids, Angew. Chem. Int. Ed., 49 (2010) 2834-2839.

[45] X. Xu, S.A. Majetich, S.A. Asher, Mesoscopic monodisperse ferromagnetic colloids enable magnetically controlled photonic crystals, J. Am. Chem. Soc., 124 (2002) 13864-13868.
[46] S.S. Nair, J. Thomas, C.S.S. Sandeep, M.R. Anantharaman, R. Philip, An optical limiter based on ferrofluids, Appl. Phys. Lett., 92 (2008) 171908.
[47] J. Philip, T. Jaykumar, P. Kalyanasundaram, B. Raj, A tunable optical filter, Meas. Sci. Technol. , 14 (2003) 1289-1294.
[48] R. Dreyfus, J. Baudry, M.L. Roper, M. Fermigier, H.A. Stone, J. Bibette, Microscopic artificial swimmers, Nature, 437 (2005) 862-865.
[49] J. Bibette, T.G. Mason, H. Gang, D.A. Weitz, Kinetically induced ordering in gelation of emulsions, Phys. Rev. Lett., 69 (1992) 981.
[50] A. Koenig, P. Hébraud, C. Gosse, R. Dreyfus, J. Baudry, E. Bertrand, J. Bibette, Magnetic force probe for nanoscale biomolecules, Phys. Rev. Lett., 95 (2005) 128301.
[51] L. Boitard, D. Cottinet, C. Kleinschmitt, N. Bremond, J. Baudry, G. Yvert, J. Bibette, Monitoring single-cell bioenergetics via the coarsening of emulsion droplets, Proc. Natl. Acad. Sci., 109 (2012) 7181-7186.
[52] V. Mahendran, J. Philip, Nanofluid based optical sensor for rapid visual inspection of defects in ferromagnetic materials, Appl. Phys. Lett., 100 (2012) 073104.
[53] V. Mahendran, J. Philip, Sensing of biologically important cations such as $Na^+$, $K^+$, $Ca^{2+}$, $Cu^{2+}$, and $Fe^{3+}$ using magnetic nanoemulsions, Langmuir, 29 (2013) 4252-4258.
[54] H.J. Butt, K. Graf, M. Kappl, Physics and Chemistry Interfaces (Wiley-VCH Verlag & Co.), 2003.
[55] D. Myers, Surfaces, Interfaces, and Colloids: Principles and Applications (John Wiley & Sons), 1999.
[56] R.J. Hunter, Zeta potential in colloid science: principles and applications, Academic Press, London, 1981.
[57] H.-J. Butt, K. Graf, M. Kappl, Physics and chemistry of interfaces, Wiley-VCH Verlag GmbH & Co. KGaA, Weinheim, 2003.
[58] T.F. Tadros, Applied surfactants: principles and applications, Wiley-VCH Verlag GmbH & Co. KGaA, Weinheim, 2005.
[59] E.J.W. Verwey, J.T.G. Overbeek, Theory of stability of lyophobic colloids: the interaction of sol particles having an electric double layer., Elsevier, Amsterdam, 1948.
[60] B.V. Derjaguin, On the repulsive forces between charged colloid particles and on the theory of slow coagulation and stability of lyophobe sols, Trans. Faraday Soc., 35 (1940) 203-215.
[61] C.E. Mullins, Magnetic susceptibility of the soil and its significance in soil science-a review, J. Soil Sci., 28 (1977) 223-246.
[62] S. Chikazumi, Physics of ferromagnetism, Oxford science publication, 1997.
[63] Q. Cao, Q. Fan, Q. Chen, C. Liu, X. Han, L. Li, Recent advances in manipulation of micro-and nano-objects with magnetic fields at small scales, Mater. Horiz., 7 (2020) 638-666.
[64] J. Faraudo, J.S. Andreu, C. Calero, J. Camacho, Predicting the self-assembly of superparamagnetic colloids under magnetic fields, Adv. Funct. Mater. , 26 (2016) 3837-3858.
[65] M. Wang, L. He, Y. Yin, Magnetic field guided colloidal assembly, Mater. Today, 16 (2013) 110-116.
[66] M. Ivey, J. Liu, Y. Zhu, S. Cutilas, Magnetic-field -induced structural transitions in a ferrofluid emulsion, Phys. Rev. E, 63 (2000) 011403.
[67] G.A. Flores, J. Liu, M. Mohebi, N. Jamasbi, Magnetic-field-induced nonequilibrium structures in a ferrofluid emulsion, Phys. Rev. E, 59 (1999) 751.

[68] J.M. Laskar, J. Philip, B. Raj, Experimental evidence for reversible zippering of chains in magnetic nanofluids under external magnetic fields, Phys. Rev. E, 80 (2009) 041401.
[69] Q. Zhang, M. Janner, L. He, M. Wang, Y. Hu, Y. Lu, Y. Yin, Photonic labyrinths: two-dimensional dynamic magnetic assembly and in situ solidification, Nano Lett., 13 (2013) 1770-1775.
[70] K. Giżynski, T. Lee, B.A. Grzybowski, Dynamic aelf-assembly of magnetic/polymer composites in rotating frames of reference, Advanced Materials, 29 (2017) 1700614.
[71] L. He, Y. Hu, H. Kim, J. Ge, S. Kwon, Y. Yin, Magnetic assembly of nonmagnetic particles into photonic crystal structures, Nano Lett., 10 (2010) 4708-4714.
[72] J. Richardi, M.P. Pileni, J.J. Weis, Self-organization of confined dipolar particles in a parallel field, J. Chem. Phys., 130 (2009) 124515.
[73] A.-P. Hynninen, M. Dijkstra, Phase diagram of dipolar hard and soft spheres: manipulation of colloidal crystal structures by an external field, Phys. Rev. Lett., 94 (2005) 138303.
[74] J.W. Swan, J.L. Bauer, Y. Liu, E.M. Furst, Directed colloidal self-assembly in toggled magnetic fields, Soft Matter, 10 (2014) 1102-1109.
[75] X. Xu, G. Friedman, K.D. Humfeld, S.A. Majetich, S.A. Asher, Superparamagnetic photonic crystals, Adv. Mater., 13 (2001) 1681-1684.
[76] J. Liu, E.M. Lawrence, A. Wu, M.L. Ivey, G.A. Flores, K. Javier, J. Bibette, J. Richard, Field-induced structures in ferrofluid emulsions, Phys. Rev. Lett., 74 (1995) 2828-2831.
[77] M.F. Islam, K.H. Lin, D. Lacoste, T.C. Lubensky, A.G. Yodh, Field-induced structures in miscible ferrofluid suspensions with and without latex spheres, Phys. Rev. E, 67 (2003) 021402.
[78] Y.H. Hwang, X.-l. Wu, Quasi-two-dimensional domain structures of magnetic particles in a static field, Phys. Rev. E, 49 (1994) 3102.
[79] J.E. Martin, E. Venturini, J. Odinek, R.A. Anderson, Anisotropic magnetism in field-structured composites, Phys. Rev. E, 61 (2000) 2818-2830.
[80] V. Germain, M.P. Pileni, Size distribution of cobalt nanocrystals: A key parameter in formation of columns and labyrinths in mesoscopic structures, Adv. Mater., 17 (2005) 1424-1429.
[81] A.J. Dickstein, S. Erramilli, R.E. Goldstein, D.P. Jackson, S.A. Langer, Labyrinthine Pattern Formation in Magnetic Fluids, Science, 261 (1993) 1012-1015
[82] F.M. Ytreberg, S.R. McKay, Calculated properties of field-induced aggregates in ferrofluids, Phys. Rev. E, 61 (2000) 4107.
[83] D. Lacoste, T.C. Lubensky, Phase transitions in a ferrofluid at magnetic-field-induced microphase separation, Phys. Rev. E, 64 (2001) 041506.
[84] J. Richardi, D. Ingert, M.P. Pileni, Theoretical study of the field-induced pattern formation in magnetic liquids, Phys. Rev. E, 66 (2002) 046306.
[85] J. Richardi, M.P. Pileni, Nonlinear theory of pattern formation in ferrofluid films at high field strengths, Phys. Rev. E, 69 (2004) 016304.
[86] C. Rablau, P. Vaishnava, C. Sudakar, R. Tackett, G. Lawes, R. Naik, Magnetic-field-induced optical anisotropy in ferrofluids: A time-dependent light-scattering investigation, Phys. Rev. E, 78 (2008) 051502
[87] N.S.S. Mousavi, S.D. Khapli, S. Kumar, Direct observations of field-induced assemblies in magnetite ferrofluids, J. Appl. Phys., 117 (2015) 103907.
[88] S. Pu, X. Chen, Z. Di, Y. Xia, Relaxation property of the magnetic-fluid-based fiber-optic evanescent field modulator, J. Appl. Phys., 101 (2007) 053532.

[89] J.J. Chieh, S.Y. Yang, H.E. Horng, C.Y. Hong, H.C. Yang, Magnetic-fluid optical-fiber modulators via magnetic modulation, Appl. Phys. Lett., 90 (2007) 133505.

[90] A. Ray, V.B. Varma, P.J. Jayaneel, N.M. Sudharsan, Z.P. Wang, R.V. Ramanujan, On demand manipulation of ferrofluid droplets by magnetic fields, Sens. Actuator B-Chem., 242 (2017) 760-768.

[91] T. Liu, X. Chen, Z. Di, J. Zhang, X. Li, J. Chen, Tunable magneto-optical wavelength filter of long-period fiber grating with magnetic fluids, Appl. Phys. Lett., 91 (2007) 121116.

[92] H.E. Horng, C.S. Chen, K.L. Fang, S.Y. Yang, J.J. Chieh, C.Y. Hong, H.C. Yang, Tunable optical switch using magnetic fluids, Appl. Phys. Lett., 85 (2004) 5592.

[93] S. Pu, X. Chen, L. Chen, W. Liao, Y.Chen, Y.Xia, Tunable magnetic fluid grating by applying a magnetic field, Appl. Phys. Lett., 87 (2005) 021901.

[94] A.W. Zaibudeen, J. Philip, Thermally tunable grating using thermo-responsive magnetic fluid, Opt. Mater., 66 (2017) 117-121.

[95] V. Mahendran, J. Philip, A methanol sensor based on stimulus-responsive magnetic nanoemulsions, Sens. Actuators B, 185 (2013) 488-495.

[96] F. Choueikani, F. Royer, D. Jamon, A. Siblini, J.J. Rousseau, S. Neveu, J. Charara, Magneto-optical waveguides made of cobalt ferrite nanoparticles embedded in silica/zirconia organic-inorganic matrix, Appl. Phys. Lett., 94, (2009) 051113.

[97] J. Masajada, M. Bacia, S. Drobczyński, Cluster formation in ferrofluids induced by holographic optical tweezers, Opt. Lett., 38 (2013) 3910-3913.

[98] S. Pu, S. Dong, J. Huang, Tunable slow light based on magnetic-fluid-infiltrated photonic crystal waveguides, J. Opt., 16 (2014) 045102.

[99] S. Brojabasi, J. Philip, Magnetic field dependant backscattering of light in water based ferrofluid containing polymer covered Fe3O4 nanoparticles, J. Appl. Phys., 113 (2013) 054902.

[100] P.D. Shima, J. Philip, B. Raj, Magnetically controllable nanofluid with tunable thermal conductivity and viscosity, Appl. Phys. Lett., 95 (2009) 133112.

[101] A. Dadwal, P.A. Joy, Influence of chain length of long-chain fatty acid surfactant on the thermal conductivity of magnetite nanofluids in a magnetic field, Colloids Surf. A Physicochem. Eng. Asp. , 555 (2018) 525-531.

[102] N.S.S. Mousavi, S. Kumar, Effective in-field thermal conductivity of ferrofluids, J. Appl. Phys., 123 (2018) 043902.

[103] R. Kappiyoor, M. Liangruksa, R. Ganguly, I.K. Puri, The effects of magnetic nanoparticle properties on magnetic fluid hyperthermia, J. Appl. Phys. , 108 (2010) 094702

[104] S. Ranoo, B.B. Lahiri, T. Muthukumaran, J. Philip, Enhancement in hyperthermia efficiency under in situ orientation of superparamagnetic iron oxide nanoparticles in dispersions, Appl. Phys. Lett., 115 (2019) 043102.

[105] D. Serantes, D. Baldomir, C. Martinez-Boubeta, K. Simeonidis, M. Angelakeris, E. Natividad, M. Castro, A. Mediano, D.-X. Chen, A. Sanchez, L. Balcells, B. Martínez, Influence of dipolar interactions on hyperthermia properties of ferromagnetic particles, J. Appl. Phys. , 108 (2010) 073918

[106] J.B. Mathieu, S. Martel, Aggregation of magnetic microparticles in the context of targeted therapies actuated by a magnetic resonance imaging system, J. Appl. Phys., 106 (2009) 044904.

[107] N. Pekas, M.D. Porter, M. Tondra, A. Popple, A. Jander, Giant magnetoresistance monitoring of magnetic picodroplets in an integrated microfluidic system, Appl. Phys. Lett., 85 (2004) 4783.

[108] D.W. Inglis, R. Riehn, R.H. Austin, J.C. Sturm, Continuous microfluidic immunomagnetic cell separation, Appl. Phys. Lett., 85 (2004) 5093.
[109] M.F.d. Silva, A.M.F. Neto, Optical- and x-ray-scattering Studies of ionic ferrofluids of $MnFe_2O_4$, $\gamma$-$Fe_2O_3$, and $CoFe_2O_4$, Phys. Rev. E, 48 (1993) 4483.
[110] P.D. Duncan, P.J. Camp, Structure and dynamics in a monolayer of dipolar spheres, J. Chem. Phys., 121 (2004) 11322.
[111] M. Mohebi, N. Jamasbi, J. Liu, Simulation of the formation of nonequilibrium structures in magnetorheological fluids subject to an external magnetic field, Phys. Rev. E 54 (1996) 5407
[112] A. Wiedenmann, U. Keiderling, M. Meissner, D. Wallacher, R. Gähler, R.P. May, S. Prévost, M. Klokkenburg, B.H. Erné, J. Kohlbrecher, Low-temperature dynamics of magnetic colloids studied by time-resolved small-angle neutron scattering, Phys. Rev. B, 77 (2008) 184417.
[113] A.V. Teixeira, I. Morfin, F. Ehrburger-Dolle, C. Rochas, E. Geissler, P. Licinio, P. Panine, Scattering from dilute ferrofluid suspensions in soft polymer gels, Phys. Rev. E, 67 (2003) 021504.
[114] M. Klokkenburg, B.H. Erné, A. Wiedenmann, A.V. Petukhov, A.P. Philipse, Dipolar structures in magnetite ferrofluids studied with small-angle neutron scattering with and without applied magnetic field, Phys. Rev. E, 75 (2007) 051408.
[115] R. Pynn, J.B. Hayter, S.W. Charles, Determination of ferrofluid structure by neutron polarization analysis, Phys. Rev. Lett., 51 (1983) 710-713.
[116] A. Wiedenmann, A. Hoell, M. Kammel, P. Boesecke, Field-induced pseudocrystalline ordering in concentrated ferrofluids, Phys. Rev. E, 68 (2003) 031203.
[117] B.J. Lemaire, P. Davidson, P. Panine, J.P. Jolivet, Magnetic-field-induced nematic-columnar phase transition in aqueous suspensions of Goethite ($\alpha$-FeOOH) nanorods, Phys. Rev. Lett., 93 (2004) 267801.
[118] S. Melle, M.A. Rubio, G.G. Fuller, Time scaling regimes in aggregation of magnetic dipolar particles: scattering dichroism results, Phys. Rev. Lett., 87 (2001) 115501.
[119] D. Heinrich, A.R. Goñi, C. Thomsen, Dynamics of magnetic-field-induced clustering in ionic ferrofluids from Raman scattering, J. Chem. Phys., 126 (2007) 124701.
[120] J. Promislow, A.P. Gast, M. Fermigier, Aggregation kinetics of paramagnetic colloidal particles, J. Chem. Phys. , 102 (1995) 5492.
[121] F.M. Pedredo, A.E. Harrak, J.C.F. Tolenado, M.Tirado-Miranda, J. Baudry, A. Schmitt, J. Bibette, J.C. Fernandez, Kinetic study of coupled field-induced aggregation and sedimentation processes arising in magnetic fluids, Phys. Rev. E, 78 (2008) 011403
[122] Á. Sanz-Felipe, J.C. Martín, Numerical method for analysis of the correlation between ferrofluid optical transmission and its intrinsic properties, J. Magn. Magn. Mater., 474 (2019) 613-618.
[123] R. Tao, J.M. Sun, Three-dimensional structure of induced electrorheological solid, Phys. Rev. Lett., 67 (1991) 398-401.
[124] R. Tao, Q. Jiang, Simulation of structure formation in an electrorheological fluid, Phys. Rev. Lett., 73 (1994) 205-208.
[125] T. Ukai, T. Maekawa, Patterns formed by paramagnetic particles in a horizontal layer of a magnetorheological fluid subjected to a dc magnetic field, Phys. Rev. E, 69 (2004) 032501.
[126] J.J. Weis, D. Levesque, Chain formation in low density dipolar hard spheres: A Monte Carlo study, Phys. Rev. Lett. , 71 (1993) 2729-2732.
[127] P.J. Camp, G.N. Patey, Structure and scattering in colloidal ferrofluids, Phys. Rev. E, 62 (2000) 5403-5408.

[128] J. Richardi, M.P. Pileni, Self-organization of magnetic nanoparticles: A Monte Carlo study, Phys. Rev. E 77 (2008) 061510.
[129] M.C. Miguel, R. Pasto-Satorras, Kinetic growth of field-oriented chains in dipolar colloidal solutions, Phys. Rev. E 59 (1999) 826
[130] P.D. Duncan, P.J. Camp, Aggregation kinetics and the nature of phase separation in two-dimensional dipolar fluids, Phys. Rev. Lett., 97 (2006) 107202.
[131] D. Zablotsky, E. Blums, H.J. Herrmann, Self-assembly and rheology of dipolar colloids in simple shear studied using multi-particle collision dynamics, Soft Matter, 13 (2017) 6474-6489.
[132] D. Heinrich, A.R. Goñi, T.M. Osan, L.M.C. Cerioni, A. Smessaert, S.H.L. Klapp, J. Faraudo, D.J. Pusiol, C. Thomsen, Effects of magnetic field gradients on the aggregation dynamics of colloidal magnetic nanoparticles, Soft Matter, 11 (2015) 7606-7616.
[133] Z.M. Sherman, D. Ghosh, J.W. Swan, Field-directed self-assembly of mutually polarizable nanoparticles, Langmuir, 34 (2018) 7117-7134.
[134] A.F. Bakuzis, K.S. Neto, P.P. Gravina, L.C. Figueiredo, P.C. Moraisa, L.P. Silva, R.B. Azevedo, O. Silva, Magneto-optical properties of a highly transparent cadmium ferrite-based magnetic fluid, Appl. Phys. Lett., 84 (2004) 2355.
[135] M.T.A. Eloi, J.L. Santos, P.C. Morais, A.F. Bakuzis, Field-induced columnar transition of biocompatible magnetic colloids: an aging study by magnetotransmissivity, Phys. Rev. E, 82 (2010) 021407.
[136] C. Sena, M.H. Godinho, A.M.F. Neto, Optical characterization of urethane/urea elastomers undoped and doped with magnetic nanoparticles subjected to a uniaxial strain, J. Appl. Phys., 102 (2007) 073524.
[137] T.-Z. Zhang, J. Li, H. Miao, Q.-M. Zhang, J. Fu, B.-C. Wen, Enhancement of the field modulation of light transmission through films of binary ferrofluids, Phys. Rev. E, 82 (2010) 021403.
[138] J.M. Laskar, J. Philip, B. Raj, Experimental investigation of magnetic-field-induced aggregation kinetics in nonaqueous ferrofluids, Phys. Rev. E, 82 (2010) 021402.
[139] H. Bhatt, R. Patel, R.V. Mehta, Magnetically induced Mie resonance in a magnetic sphere suspended in a ferrofluid, J. Opt. Soc. Am. A, 27 (2010) 873-877.
[140] D.K. Mohapatra, J. Philip, Effect of surface charge screening on critical magnetic fields during field induced structural transitions in magnetic fluids, J. Appl. Phys., 125 (2019) 244301.
[141] M. Xu, P.J. Ridler, Linear dichroism and birefringence effects in magnetic fluids, J. Appl. Phys., 82 (1997) 326.
[142] K.S. Neto, A.F. Bakuzis, A.R. Pereira, P.C. Morais, Magnetic aging in magnetic fluids: a static magnetic birefringence investigation, J. Magn. Magn. Mater., 226-230 (2001) 1893-1895.
[143] N.A. Yusuf, A.A. Rousan, H.M. El-Ghanem, The wavelength dependence of Faraday rotation in magnetic fluids J. Appl. Phys., 64 (1988) 2781.
[144] D. Lacoste, F. Donatini, S. Neveu, J.A. Serughetti, B.A.V. Tiggelen, Photonic Hall effect in ferrofluids: Theory and experiments, Phys. Rev. E, 62 (2000) 3934.
[145] F. Martinez-Pedredo, A. El-Harrak, J.C. Fernandez-Tolenado, M.Tirado-Miranda, J. Baudry, A. Schmitt, J. Bibette, J.C. Fernandez, Kinetic study of coupled field-induced aggregation and sedimentation processes arising in magnetic fluids, Phys. Rev. E, 78 (2008) 011403
[146] W.D. Young, D.C. Prieve, Initial rate of flocculation of magnetic dispersions in an applied magnetic field, Ind. Eng. Chem. Res., 35 (1996) 3186-3194.

[147] J.J.M. Janssen, J.J.M. Baltussen, A.P.V. Gelder, J.A.A.J. Prenboom, Kinetics of magnetic flocculation. I: Flocculation of colloidal particles, J. Phys. D: Appl. Phys., 23 (1990) 1447-1454.
[148] R.V. Mehta, R. Patel, R. Desai, R.V. Upadhyay, K. Parekh, Experimental evidence of zero forward scattering by magnetic spheres, Phys. Rev. Lett., 96 (2006).
[149] J.E. Martin, K.M. Hill, C.P. Tigges, Magnetic-field-induced optical transmittance in colloidal suspensions, Phys. Rev. E, 59 (1999) 5676.
[150] S. Radha, S. Mohan, C. Pai, Diffraction patterns in ferrofluids: Effect of magnetic field and gravity, Phys. B: Condens. Matter, 448 (2014) 341-345.
[151] C.F. Hayes, Observation of Association in a Ferromagnetic Colloid, J. Colloid Interface Sci., 52 (1975) 239-243.
[152] W. Reed, J.H. Fendler, Anisotropic aggregates as the origin of magnetically induced dichroism in ferrofluids, J. Appl. Phys., 59 (1986) 2914-2924.
[153] J.C. Bacri, R. Perzynski, D. Salin, J. Servais, Magnetic transient birefringence of ferrofluids : particle size determination, J. Physique, 48 (1987) 1385-1391.
[154] E. Hasmonay, E. Dubois, J.C. Bacri, R. Perzynski, Y.L. Raikher, V.I. Stepanov, Static magneto-optical birefringence of size-sorted $\gamma$-$Fe_2O_3$ nanoparticles, Eur. Phys. J. B, 5 (1998) 859-867.
[155] J. Li, X. Liu, Y. Lin, L. Bai, Q. Li, X. Chen, A. Wang, Field modulation of light transmission through ferrofluid film, Appl. Phys. Lett., 91 (2007) 253108.
[156] S.I. Shulyma, B.M. Tanygin, V.F. Kovalenko, M.V. Petrychuk, Magneto-optical extinction trend inversion in ferrofluids, J. Magn. Magn. Mater., 416 (2016) 141-149.
[157] Z. Di, X. Chen, S. Pu, X. Hu, Y. Xia, Magnetic-field-induced birefringence and particle agglomeration in magnetic fluids, Appl. Phys. Lett., 89 (2006) 211106.
[158] M.-F. Chung, S.E. Chou, C.-M. Fu, Time-dependent dynamic behavior of light diffraction on ferrofluid, J. Appl. Phys., 111 (2012) 07B333.
[159] J. Jin, D. Song, J. Geng, D. Jing, Time-dependent scattering of incident light of various wavelengths in ferrofluids under external magnetic field, J. Magn. Magn. Mater., 447 (2018) 124-133.
[160] S. Brojabasi, T. Muthukumaran, J.M. Laskar, J. Philip, The effect of suspended $Fe_3O_4$ nanoparticle size on magneto-optical properties of ferrofluids, Opt. Commun., 336 (2015) 278-285.
[161] P. Zu, C.C. Chan, W.S. Lew, Y. Jin, H.F. Liew, W.C. Wong, X. Dong, C.Z. Foo, Laser self-induced tunable birefringence of magnetic fluid, Appl. Phys. Lett., 102 (2013) 181116.
[162] L. Sakhnini, J. Popplewell, Interaction effects on magneto-optical birefringence in magnetic fluids, J. Magn. Magn. Mater., 122 (1993) 142-145.
[163] T. Du, W. Luo, Intensity dependent transmission dynamics in magnetic fluids, J. Appl. Phys, 85 (1999) 5953.
[164] B.R. Jennings, M. Xu, P.J. Ridler, Ferrofluid structures: a magnetic dichroism study, Proc. R. Soc. Lond. A, 456 (2000) 891-907.
[165] J. Philip, J.M. Laskar, B. Raj, Magnetic field induced extinction of light in a suspension of $Fe_3O_4$ nanoparticles, Appl. Phys. Lett., 92 (2008) 221911.
[166] S. Brojabasi, V. Mahendran, B.B. Lahiri, J. Philip, Temperature dependent light transmission in ferrofluids, Opt. Commun., 342 (2015) 224-229.
[167] J.M. Laskar, B. Raj, J. Philip, Path length tunable light-matter interaction in magnetic nanofluid based field-induced photonic crystal-glass structure, New J. Phys. , 18 (2016 ) 103037.
[168] M. Shalaby, M. Peccianti, Y. Ozturk, M. Clerici, I. Al-Naib, L. Razzari, T. Ozaki, A. Mazhorova, M. Skorobogatiy, R. Morandotti, Terahertz Faraday rotation in a magnetic

liquid: high magneto-optical figure of merit and broadband operation in a ferrofluid, Appl. Phys. Lett., 100 (2012) 241107.

[169] M. Hagenbüchle, P. Sheaffer, Y. Zhu, J. Liu, Static and dynamic light scattering of dilute magnetorheolgical emulsions, Int. J. Mod. Phys. B, 10 (1996) 3057-3065.

[170] J.M. Laskar, B. Raj, J. Philip, Enhanced transmission with tunable Fano-like profile in magnetic nanofluids, Phys. Rev. E 84 (2011) 051403.

[171] S. Brojabasi, V. Mahendran, B.B. Lahiri, J. Philip, Near infrared light absorption in magnetic nanoemulsion under external magnetic field, Opt. Commun., 323 (2014) 54–60.

[172] P.D. Shima, J. Philip, B. Raj, Synthesis of aqueous and nonaqueous iron oxide nanofluids and study of temperature dependence on thermal conductivity and viscosity, J. Phys. Chem. C, 114 (2010) 18825-18833.

[173] T. Muthukumaran, G. Gnanaprakash, J. Philip, Synthesis of stable magnetic nanofluids of different particle sizes, J. Nanofluid, 1 (2012) 85-92.

[174] J. Bibette, Monodisperse ferrofluid emulsions, J. Magn. Magn. Mater. , 122 (1993) 37-41.

[175] J. Philip, T. Jaykumar, P. Kalyanasundaram, B. Raj, Effect of polymer-surfactant association on colloidal force, Phys. Rev. E, 66 (2002) 011406.

[176] J. Philip, G.G. Prakash, T. Jaykumar, P. Kalyanasundaram, O. Mondain-Monval, B. Raj, Interaction between emulsion droplets in the presence of polymer-surfactant complexes, Langmuir, 18 (2002) 4625-4631.

[177] B.D. Cullity, S.R. Stock, Elements of X-Ray Diffraction, Prentice Hall, New Jersey, 2001.

[178] O. Glatter, O. Kratky, Small angle X-ray scattering, Academic Press, London, 1982.

[179] A. Guinier, G. Fournet, Small-angle scattering of X-rays, John Wiley and Sons, New York, 1955.

[180] B.J. Berne, R. Pecora, Dynamic Light Scattering With Applications to Chemistry, Biology, and Physics, Dover Publications, Inc., New York, 2000.

[181] P.A. Hassan, S. Rana, G. Verma, Making sense of brownian motion: colloid characterization by dynamic light scattering, Langmuir, 31 (2015) 3-12.

[182] S. Foner, Versatile and Sensitive Vibrating-Sample Magnetometer, Rev. Sci. Instrum., 30 (1959) 548-557.

[183] A.W. Coats, J.P. Redfern, Thermogravimetric analysis. A review, Analyst, 88 (1963) 906-924.

[184] F. Zernike, Phase contrast, a new method for the microscopic observation of transparent objects, Physica, 9 (1942) 686-698.

[185] G. Gnanaprakash, S. Ayyappan, T. Jayakumar, J. Philip, B. Raj, Magnetic nanoparticles with enhanced $\gamma$-$Fe_2O_3$ to $\alpha$-$Fe_2O_3$ phase transition temperature, Nanotechnology, 17 (2006) 5851-5857.

[186] V. Mahendran, J. Philip, Macromolecular conformation changes at oil-water interface in the presence of cations, Colloids Surf. A, 497 (2016) 90-100.

[187] A. Yethiraj, Tunable colloids: control of colloidal phase transitions with tunable interactions, Soft Matter, 3 (2007) 1099-1115.

[188] T.C. Halsey, W. Toor, Fluctuation-induced couplings between defect lines or particle chains, J. Stat. Phys. , 61 (1990) 1257-1281.

[189] J.E. Martin, J.Odinek, T.C.Halsey, Evolution of structure in a quiescent electrorheological fluid, Phys. Rev. Lett., 69 (1992) 1524

[190] M. Gross, Ground state of a dipolar fluid film, Phys. Rev. E, 58 (1998) 6124.

[191] R. Haghgooie, P.S. Doyle, Transition from two-dimensional to three-dimensional behavior in the self-assembly of magnetorheological fluids confined in thin slits, Phys. Rev. E, 75 (2007) 061406.

[192] R. Tao, Q. Jiang, Structural transitions of an electrorheological and magnetorheological fluid, Phys. Rev. E, 57 (1998) 5761-5765.

[193] Y. Zhu, E. Haddadian, T. Mou, M. Gross, J. Liu, Role of nucleation in the structure evolution of a magnetorheological fluid, Phys. Rev. E, 53 (1996) 1753-1759.

[194] T.C. Halsey, W. Toor, Structure of electrorheological fluids, Phys. Rev. Lett., 65 (1990) 2820.

[195] A.W. Zaibudeen, J. Philip, Multi-stimuli responsive nanofluid with easy-to-visualize structural color patterns, Colloids Surf. A, 518 (2017) 98-108.

[196] C.F. Bohren, D.R. Huffman, Absorption and scattering of light by small particles, Wiley, New York, 1983.

[197] J.M. Laskar, S. Brojabasi, B. Raj, J. Philip, Comparison of light scattering from self assembled array of nanoparticle chains with cylinders Opt. Commun. , 285 (6) (2012) 1242 - 1247.

[198] M. Klokkenburg, B.H. Erne, J.D. Meeldijk, A. Wiedenmann, A.V. Petukhov, R.P.A. Dullens, A.P. Philipse, In situ imaging of field-induced hexagonal columns in magnetite ferrofluids, Phys. Rev. Lett., 97 (2006) 185702.

[199] E.M. Furst, A.P. Gast, Dynamics and lateral interactions of dipolar chains, Phys. Rev. E 62 (2000) 6916.

[200] M. Fermigier, A.P. Gast, Structure evolution in a paramagnetic latex suspension, J. Colloid Interface Sci. , 154 (1992) 522-539.

[201] S. Cutillas, J. Liu, Experimental study on the fluctuations of dipolar chains, Phys. Rev. E, 64 (2001) 011506.

[202] D. Liu, M.R. Maxey, G.E. Karniadakis, Simulations of dynamic self-assembly of paramagnetic microspheres in confined microgeometries, J. Micromech. Microeng. , 15 (2005) 2298-2308.

[203] K.I. Morozov, Gradient diffusion in concentrated ferrocolloids under the influence of a magnetic field, Phys. Rev. E, 53 (1996) 3841-3846.

[204] A. Mertelj, L. Cmok, M. Čopič, Anomalous diffusion in ferrofluids, Phys. Rev. E, 79 (2009) 041402.

[205] J.C. Bacri, A. Cebers, A. Bourdon, G. Demouchy, B.M. Heegaard, B. Kashevsky, R. Perzynski, Trasient grating in a ferrolfuid under magnetic field: Effect of magnetic interactions on the diffusion coefficient of translation, Phys. Rev. E, 52 (1995) 3936.

[206] G.K. Batchelor, Slender-body theory for particles of arbitrary cross-section in Stokes flow, J. Fluid Mech., 44 (1970) 419-440.

[207] A.H. Krall, D.A. Weitz, Internal dynamics and elasticity of fractal colloidal gels, Phys. Rev. Lett., 80 (1998) 778-781.

[208] M. Hagenbüchle, J. Liu, Chain formation and chain dynamics in a dilute magnetorheological fluid, Appl. Opt., 36 (1997) 7664-7671.

[209] E.M. Lawrence, M.L. Ivey, G.A. Flores, J. Liu, J. Bibette, J. Richard, Field induced structure of confined ferrofluid emulsion, Int. J. Mod. Phys. B 08 (1994) 2765-2777.

[210] J.E. Martin, R.A. Anderson, C.P. Tigges, Thermal coarsening of uniaxial and biaxial field-structured composites, J. Chem. Phys., 110 (1999) 4854-4866.

[211] A.W. Zaibudeen, J. Philip, Magnetic nanofluid based non-enzymatic sensor for urea detection, Sens Actuators B: Chem., 255 (2018) 720-728.

[212] S. Kralj, D. Makovec, Magnetic assembly of superparamagnetic iron oxide nanoparticle clusters into nanochains and nanobundles, ACS Nano, 9 (2015) 9700-9707.

[213] Y.N. Skibin, V.V. Chekanov, Y.L. Raker, Birefringence in a ferromagnetic liquid, Sov. Phys. JETP, 45 (1977) 949-955

[214] H.W. Davies, J.P. Llewellyn, Magnetic birefringence of ferrofluids. II. pulsed field measurements, J. Phys. D: Appl. Phys., 12 (1979) 1357.

[215] S. Taketomi, Magnetic fluid's anomalous pseudo-cotton mouton effects about $10^7$ times larger than that of nitrobenzene, Jpn. J. Appl. Phys. , 22 (1983) 1137.
[216] S. Neveu-Prin, F.A. Tourinho, J.C. Bacri, R. Perzynski, Magnetic birefringence of cobalt ferrite ferrofluids, Colloids Surf. A Physicochem. Eng. Asp, 80 (1993) 1-10.
[217] P.C. Scholten, The origin of magnetic birefringence and dichroism in magnetic fluids, IEEE Trans. Magn. , 16 (1980 ).
[218] M. Rasa, Magnetic properties and magneto-birefringence of magnetic fluids, Eur. Phys. J. E, 2 (2000) 265-275.
[219] X. Wang, S. Pu, H. Ji, G. Yu, Enhanced magnetic-field-induced optical properties of nanostructured magnetic fluids by doping nematic liquid crystals, Nanoscale Res Lett 7(2012) 249.
[220] M. Cui, X. Tian, G. Zou, B. Zhu, Q. Zhang, Composite optical fiber polarizer with ternary copolymer overlay for large range modulation of phase difference, Opt. Mater., 66 (2017) 415-421.
[221] J. Konieczkowska, E. Schab-Balcerzak, M. Siwy, K. Switkowski, A. Kozanecka-Szmigiel, Large and highly stable photoinduced birefringence in poly(amideimide)s with two azochromophores per structural unit, Opt. Mater., 39 (2015) 199-206.
[222] J.P. Llewellyn, Form birefringence in ferrofluids, J. Phys. D: Appl. Phys., 16 (1983) 95.
[223] Y.T. Pan, C.W. Du, J. Liu, B. Li, R. Birngruber, Monte Carlo simulation of magnetobirefringence in magnetic fluids, J. Appl. Phys., 73 (1993) 6142-6144.
[224] A.O. Ivanov, O.B. Kuznetsova, Nonmonotonic field-dependent magnetic permeability of a paramagnetic ferrofluid emulsion, Phys. Rev. E, 85 (2012) 041405.
[225] S. Brojabasi, B.B. Lahiri, J. Philip, External magnetic field dependent light transmission and scattered speckle pattern in a magnetically polarizable oil-in-water nanoemulsion, Physica B, 454 (2014) 272-278.
[226] M.S. Singh, K. Rajan, R.M. Vasu, Estimation of elasticity map of soft biological tissue mimicking phantom using laser speckle contrast analysis, J. Appl. Phys., 109 (2011) 104704.
[227] M. Rosenbluh, M. Hoshen, I. Freund, Dynamic backscattered speckle in multiply scattering fluids, Phil. Mag. B, 56 (1987) 705-715.
[228] U. Bortolozzo, S. Residori, P. Sebbah, Experimental observation of speckle instability in kerr random media, Phys. Rev. Lett., 106 (2011) 103903.
[229] L. Rayleigh, On the electromagnetic theory of light, Phil. Mag. , 12 (1881) 81-101.
[230] J.R. Wait, Scattering of a plane wave from a circular dielectric cylinder at oblique incidence, Can. J. Phys., 33 (1955) 189-195.
[231] C. Holm, J.J. Weis, The structure of ferrofluids: A status report, Curr. Opin. Colloid Interface Sci, 10 (2005) 133-140.
[232] G.A. Flores, M.L. Ivey, J. Liu, M. Mohebi, N. Jamasbi, Field induced labyrinthine patterns in ferrofluid emulsions, Int. J. Mod. Phys. B, 10 (1996) 3283-3292.
[233] F. Donado, J.M. Sausedo-Solorio, R.E. Moctezuma, Dynamical and structural properties of a granular model for a magnetorheological fluid, Phys. Rev. E, 95 (2017) 022601.
[234] S.L. Saville, R.C. Woodward, M.J. House, A. Tokarev, J. Hammers, B. Qi, J. Shaw, M. Saunders, R.R. Varsani, T.G.S. Pierre, O.T. Mefford, The effect of magnetically induced linear aggregates on proton transverse relaxation rates of aqueous suspensions of polymer coated magnetic nanoparticles, Nanoscale, 5 (2013) 2152-2163.
[235] A.B. Dobroserdova, S.S. Kantorovich, Self-diffusion in bidisperse systems of magnetic nanoparticles, Phys. Rev. E, 103 (2021) 012612.

[236] J. Vessaire, N. Plihon, R. Volk, M. Bourgoin, Sedimentation of a suspension of paramagnetic particles in an external magnetic field, Phys. Rev. E, 102 (2020) 023101.
[237] P.J. Camp, E.A. Elfimova, A.O. Ivanov, The effects of polydispersity on the initial susceptibilities of ferrofluids, J. Phys. Condens. Matter 26 (2014) 456002.
[238] J.D. Weeks, D. Chandler, H.C. Andersen, Role of repulsive forces in determining the equilibrium structure of simple liquids, J. Chem. Phys., 54 (1971) 5237-5247.
[239] J.J. Cerdà, V. Ballenegger, O. Lenz, C. Holm, $P^3M$ algorithm for dipolar interactions, J. Chem. Phys., 129 (2008) 234104.
[240] S. Plimpton, Fast parallel algorithms for short-range molecular dynamics, J. Comp. Phys., 117 (1995) 1-19.
[241] H.-E. Horng, C.-Y. Hong, W.B. Yeung, H.-C. Yang, Magnetochromatic effects in magnetic fluid thin films, Appl. Opt., 37 (1998) 2674-2680
[242] F. Elias, C. Flament, J.-C. Bacri, S. Neveu, Macro-organized patterns in ferrofluid layer: Experimental studies, J. Phys. France, 7 (1997) 711-728.
[243] M. Seul, C.A. Murray, Scale transformation of magnetic "bubble" arrays: coupling of topological disorder and polydispersity, Science, 262 (1993) 558.
[244] H.-E. Horng, C.-Y. Hong, S.L. Lee, C.H. Ho, S.Y. Yang, H.C. Yang, Magnetochromatics resulted from optical gratings of magnetic fluid films subjected to perpendicular magnetic fields, J. Appl. Phys., 88 (2000) 5904-5908.
[245] L. He, V. Malik, M. Wang, Y. Hu, F.E. Anson, Y. Yin, Self-assembly and magnetically induced phase transition of three-dimensional colloidal photonic crystals, Nanoscale, 4 (2012) 4438-4442.
[246] A.T. Skjeltorp, One- and two-dimensional crystallization of magnetic holes, Phys. Rev. Lett., 51 (1983) 2306-2309.
[247] A.O. Ivanov, E.V. Novak, Phase separation of ferrocolloids: The role of van der Waals interaction, Colloid J., 69 (2007) 302-311.
[248] E.S. Minina, A.B. Muratova, J.J. Cerda, S.S. Kantorovich, Microstructure of bidisperse ferrofluids in a thin layer, J. Exp. Theor. Phys., 116 (2013) 424-441.
[249] Z. Wang, C. Holm, Structure and magnetic properties of polydisperse ferrofluids: A molecular dynamics study, Phys. Rev. E, 68 (2003) 041401.
[250] A.O. Ivanov, S.S. Kantorovich, Chain aggregate structure and magnetic birefringence in polydisperse ferrofluids, Phys. Rev. E, 70 (2004) 021401.
[251] H. Ezzaier, J.A. Marins, I. Razvin, M. Abbas, A.B.H. Amara, A. Zubarev, P. Kuzhir, Two-stage kinetics of field-induced aggregation of medium-sized magnetic nanoparticles, J. Chem. Phys., 146 (2017) 114902.